Self-bearing permanent magnet synchronous machine configurations and control for high-speed applications

Dem Fachbereich Elektrotechnik und Informationstechnik
der Technischen Universität Darmstadt
zur Erlangung des akademischen Grades eines
Doktor-Ingenieurs (Dr.-Ing.)
genehmigte Dissertation

von

Gael Messager, M. Sc.
geboren am 18. Mai 1987 in Cannes la Bocca

Referent:	Prof. Dipl.-Ing. Dr.techn. Andreas Binder
Korreferent:	Prof. Dr.-Ing. Ulrich Konigorski
Tag der Einreichung:	04.09.2018
Tag der mündlichen Prüfung:	18.01.2019

D17
Darmstadt 2018

Gael Messager: Self-bearing permanent magnet synchronous machine configurations and control for high-speed applications
Darmstadt, Technische Universität Darmstadt,
Jahr der Veröffentlichung der Dissertation auf TUprints: 2019
Tag der mündlichen Prüfung: 18.01.2019

Ich versichere hiermit, dass ich die vorliegende Dissertation allein und nur unter Verwendung der angegebenen Literatur verfasst habe. Die Arbeit hat bisher noch nicht zu Prüfungszwecken gedient.

Gael Messager 04.09.2018

Motivation - The principle of magnetic levitation is thriving thanks to recent technical breakthroughs in the field of power electronics and digital signal processors. Beside the widely spread magnetic bearing technologies, present in industrial and transportation applications, alternative magnetic levitation principles arise with different advantages and drawbacks. Among those, the so-called bearingless topologies are catching the interest of the scientific community. Indeed, they offer new exploration opportunities in the field of electrical machines. The bearingless motors, or more appropriately called active self-bearing motor, use the additional available degrees of freedom of multi-phase and or multi-winding configurations to control not only the rotational position but also the axial and radial displacements of an unfastened rotor. Many topologies can be found today, depending on the rotational speed and the power range of application.

Motivation - Das Prinzip der Magnetschwebetechnik ist aufgrund technischer Durchbrüche in der Leistungselektronik und bei der digitalen Signalverarbeitung aktuell ein spannendes, viel beachtetes und bearbeitetes Feld. Neben der weit verbreiteten Nutzung der Magnetlagertechnologie in der Industrie und im Transportwesen verbreiten sich alternative Anwendungen mit unterschiedlichen Vor- und Nachteilen. Unter diesen Anwendungen sind Auslegungen lagerloser Motoren wissenschaftlich besonders interessant. Tatsächlich bieten sie neue Möglichkeiten für elektrische Maschinen. Lagerlose Motoren, auch bezeichnet als aktiv selbstgelagerte Motoren, nutzen die zusätzlich verfügbaren Freiheitsgrade von Mehrphasen- oder Mehrwicklungskonfigurationen, um nicht nur die Rotationsposition, sondern auch die axiale und radiale Auslenkung eines schwebenden Rotors zu regeln. Mittlerweile existieren viele verschiedene Auslegungen, abhängig von der Rotationsgeschwindigkeit und der Leistungsklasse der jeweiligen Anwendung.

Abstract - In this thesis, the active self-bearing topologies relevant for high-speed motors are investigated. From the conventional double isolated winding topology toward more sophisticated winding configurations, two active self-bearing principles are examined. For each configuration, this thesis focuses on the modelling and the control aspects. The advantages and drawbacks, as well as the relevant field of applications are also addressed. The first part deals with the working principle of magnetic levitation force generation with superposition of field components. A qualitative comparison between self-bearing motors and magnetic bearings follows to present the fundamental differences between DC and AC based electromagnetic actuators. Since the drive is actively controlled, a revision of the relevant sensors for this particular application is given. Particular attention is given at the characteristic and limitations of the sensors. The modelling part follows with the analytical calculation of the motor electromagnetic model starting from the *Maxwell* equations. The non-linear torque and force components that act as disturbance on the model are also evaluated. A general position control scheme is then presented and derived with several feedback control. It is shown that, given an appropriate control reference frame, the mechanical control scheme is very similar to the one with magnetic bearings. Given that, the active self-bearing motor differs from its counter part with active magnetic bearing only from the electrical point of view. Then a double conical self-bearing motor is presented and modelled. A second self-bearing motor with split winding is presented. First the working principle as well as the control is detailed. The design and modelling is done for a prototype rated at 60 krpm and 0.66 kW. The prototype is then built and measured. Finally the presented controllers are experimented on a testbench. The design of the hardware and software parts is presented as well as the performances obtained with the double-conical self-bearing motor.

Kurzfassung - In dieser Arbeit sollen verschiedene Auslegungen aktiv selbst gelagerter Hochdrehzahlmotoren untersucht werden. Von der üblichen, getrennten Wicklung hin zu komplexeren Wicklungskonfigurationen werden zwei aktiv selbst gelagerte Modelle untersucht. Für beide Konfigurationen konzentriert sich diese Arbeit auf die Aspekte der Modellierung und Regelung. Die jeweiligen Vor- und Nachteile sowie verschiedene Anwendungsmöglichkeiten werden diskutiert. Der erste Teil der Arbeit beschäftigt sich mit dem Prinzip der Erzeugung von Magnetschwebekraft durch die Überlappung von Feldkomponenten. Im Folgenden wird ein qualitativer Vergleich zwischen einem aktiv selbst gelagerten Motor und Magnetlagern gezogen, um den fundamentalen Unterschied zwischen Gleich- und Wechselstrom basierten Antriebselementen darzustellen. Ein Überblick über die relevanten Sensoren wird gegeben, die für die aktive Regelung in der jeweiligen Anwendung benötigt werden. Besondere Aufmerksamkeit gilt hierbei den Eigenschaften und Beschränkungen der Sensoren. Im Weiteren folgt die analytische Berechnung des elektromagnetischen Motormodells ausgehend von den *Maxwell*-Gleichungen. Die nicht linearen Drehmoment- und Kraftkomponenten, die Störungen für das Modell darstellen, werden ebenfalls diskutiert. Eine allgemeine Übersicht zur Positionsregelung wird präsentiert, und verschiedene Rückführungen werden abgeleitet. Es wird gezeigt, dass das mechanische Regelungssystem innerhalb eines entsprechenden Regelungsreferenzrahmens einer Anordnung mit Magnetlagern sehr ähnlich ist. Unter diesem Gesichtspunkt unterscheidet sich ein aktiv selbst gelagerter Motor von einem Motor mit Magnetlagern nur in elektrischer Hinsicht. Ein doppelt konischer, selbst gelagerter Motor wird vorgestellt und modelliert. Ein zweiter selbst gelagerter Motor mit kombinierter, doppelt-dreiphasiger Wicklung wird beschrieben. Das Funktionsprinzip sowie die entsprechende Regelung werden dargelegt. Das Design und die Modellierung wurden für einen Prototyp mit Bemessungspunkt bei 60 krpm und 0,66 kW durchgeführt. Der Prototyp wurde dann gebaut und seine Eigenschaften vermessen. Zuletzt wurden die Regelungen experimentell an einem Prüfstand getestet. Das Design der Hardware- und Softwarekomponenten sowie die Ergebnisse für den doppelt konischen, selbst gelagerten Motor werden beschrieben und diskutiert.

Vorwort - Die vorliegende Arbeit entstand während meiner Tätigkeit als wissenschaftlicher Mitarbeiter zwischen den Jahren 2012 und 2017 am *Institut für Elektrische Energiewandlung* der *Technischen Universität Darmstadt.*

Zahlreiche Personen waren und sind in die Entstehung dieser Dissertation direkt oder indirekt eingebunden, und ich nutze die Gelegenheit, mich herzlich zu bedanken. Besonders möchte ich der gesamten Mannschaft des Instituts für die vielseitige Unterstützung danken. Zunächst meinem Doktorvater *Prof. Dr.-Ing. habil. Andreas Binder*, der mich zuerst in die sehr interessante Welt der magnetischen Lagerung eingeführt hat. Mit Blick auf die vergangenen Jahre war das Thema für mich die richtige Wahl. Dankbar bin ich auch für die wissenschaftliche Unterstützung und sein persönliches Engagement für die Finanzierung und Realisierung meiner Arbeit, meiner Veröffentlichungen und meiner Weiterbildung. Ich danke *Fabian Mink* und *Gabriel Bergmann* für die Einführung in die Regelung und Auslegung von Elektromotoren und das Teilen ihrer Fachkenntnisse. Ich bedanke mich bei meinen Kollegen, mit denen ich gearbeitet und gelernt habe: *Bogdan Funieru, Marco Susic, Mirco Strauch, Nam Anh Dinh Ngoc, Stefan Dewenter, Boris Dotz, Yves Gemeinder, Kersten Reis, Jinou Wang, Jeongki An, Marcel Lehr, Björn Deusinger, Sascha Neusüs, Martin Schuster, Nicolas Erd* und *Daniel Dietz.* Glücklich bin ich über die vielen wissenschaftlichen Diskussionen, aber auch über die privaten Aktivitäten in der Gruppe, die viele Freundschaften hervorbrachten. Ich danke den administrativen Mitarbeitern, die an der Realisierung der Prototypen beteiligt waren. Einen herzlichen Dank an *Anette Ptaschek* für die Zeichnungen und an *Annette Siler* für die Buchhaltung meines DFG-Projekts, *Klaus Gütlich* für die Realisierung des Prüfstands und *Andreas Fehringer* und *Markus Lohnes* für die Fertigung der Prototypen. Ich danke der *Deutschen Forschungsgemeinschaft* für die finanzielle Unterstützung meiner Arbeit unter der Projektnummer BI 701/12-1. Für die Bereitstellung des Magnetlagers, der Magnetlagerelektronik und verschiedener Motorteile und Software möchte ich mich bei Herrn *Dr. Christian Redemann* sowie bei *Timo Michel* und *Johannes von Löwis* der Firma *LTI Motion,*

Lahnau, bedanken. Für die Bachelor- und Masterarbeiten, die eine Unterstützung bei der Durchführung für Teile dieser Arbeit waren, möchte ich meinen Dank an *Juri Liebhart*, *Javier Valverde*, *Philipp Kappes*, *Sridahr Balasubramanian*, *Panagiotis Mouratidis*, *Philipp Hörner* und *Yann Cedric Devisscher* richten. Ein persönliches Dankeschön richte ich an meine Eltern, die mich im Studium unterstützt haben, um bis zu dieser Arbeit zu kommen. Ein persönliches Dankeschön an meine Freundin *Daniela Loos* für die Geduld und die Hilfe bei der Korrektur dieses Textes.

Gael Messager, im September 2018

Contents

Applied Notations and Symbols

Abbreviations

ADC	Analogue-to-Digital Converter
AMB	Active Magnetic Bearing
BM	Self-bearing motor
CMB	Combined radial and axial Magnetic Bearing
DE (NDE)	Drive-End (Non-Drive-End)
DFT	Discrete *Fourier* Transformation
DOF	Degree Of Freedom
EMI	ElectroMagnetic Interferences
FEM	Finite Element Method
FIR	Finite Impulse Response
FPGA	Field Programmable Gate Array
IGBT	Insulated Gate Bipolar Transistor
MMF	Magneto-Motive Force
MOSFET	Metal Oxide Semiconductor Field Effect Transistor
PCI	Peripheral Component Interconnect
PD (PID)	Proportional (Integral) Derivative controller
PMSM	Permanent Magnet Synchronous Motor
PWM	Pulse-Width Modulation
RTAI	Real-Time Application Interface
SISO	Single-Input Single-Output
SPI	Serial Peripheral Interface
TLC	Target Language Code

VHDL	Very high speed integrated circuit Hardware Description Language

List of symbols

α	rad	Conus angle
α	-	Pole coverage ratio
γ	rad	Eccentricity angle.
δ	m	Air gap
ϵ	m	Eccentricity amplitude
ζ	-	Damping ratio
θ	rad	Angle
θ	°C	Temperature
λ	$\mathrm{rad\,s^{-1}}$	Eigenvalue
μ	$\mathrm{V\,s\,A^{-1}\,m^{-1}}$	Permeability
ν	-	Harmonic order
ρ	$\Omega\,\mathrm{m}$	Specific resistivity
τ_p	m	Pole pitch
τ	s	Time constant
φ	°	Electrical angle
$\mathit{\Psi}$	Wb	Magnetic flux linkage
ψ	A	Magnetic scalar potential
ω	$\mathrm{rad\,s^{-1}}$	Angular velocity
d	m	Diameter
d_e	m	Penetration depth
f	Hz	Frequency
f	$\mathrm{N\,m^{-2}}$	Force density
h_Q	m	Slot height
h_B	m	Height of the bandage
h_M	m	Magnet height
k_C	-	*Carter* coefficient

k_{w}	-	Winding factor
k	-	Control coefficient
l	m	Length
l_{Fe}	m	Iron length
m	-	Number of phases
n	s^{-1}	Rotational speed
p	-	Number of pole pairs
p	$\mathrm{rad\,s}^{-1}$	Pole of a system
q	-	Slots per pole and phase
r	m	Radius
s_{Q}	m	Slot opening
u_{i}	V	Induced voltage
A	$\mathrm{A\,m}^{-1}$	Current loading
$\boldsymbol{A}$	$\mathrm{V\,s\,m}^{-1}$	Magnetic vector potential
A	m^2	Area
B	T	Magnetic flux density
F	N	Force
$\boldsymbol{G}$	-	Gyroscopic matrix
G	-	Transfer function
$G(\mathrm{j}\omega)$	-	Frequency response
H	$\mathrm{A\,m}^{-1}$	Magnetic field strength
I	A	Current
$\boldsymbol{I}_n$	-	Identity matrix of order n
J	$\mathrm{A\,m}^{-2}$	Current density
J_{i}	$\mathrm{kg\,m}^2$	Moment of inertia along the axis i
L	H	Inductance
$\boldsymbol{M}$	$\mathrm{A\,m}^{-1}$	Magnetisation
$\boldsymbol{M}$	$\mathrm{kg\,m}^2$ and kg	Inertia matrix
M_{e}	$\mathrm{N\,m}$	Electromagnetic torque
N_{s}	-	Number of turns per phase
P	W	Active power
Q	VAr	Reactive power
R	Ω	Phase resistance

$\lvert \underline{S} \rvert$	VA	Apparent power
S_w	-	Output sensitivity function
T	s	Period
T_s	s	Settling time
U	V	Voltage
V	A	Magneto-motive force
W	m	Pitch of coil
W_m	J	Magnetic energy

Subscripts and superscripts

0	No-load value
0	Rotor related quantity
0	Open loop
1	Quantity related to the stator drive winding
2	Quantity related to the stator levitation winding
act	Actual
crit	Critical
d	d-axis
dem	Demodulation
dist	Disturbance
q	q-axis
e	Electric
ex	Excitation
i	Related to the current i
m	Mechanical
m	Overshoot
max	Maximum
mea	Measured
mo	Magnet outer
r	Rotor

rem	Remanence
ro	Rotor outer
s	Stator
si	Stator inner
samp	Sampling
surf	Surface
w	Winding
w	Closed-loop
Cu	Copper
D	Differential part
Fe	Iron
I	Integral part
L	Load
P	Proportional part
U, V, W	Phase U, V and W

Notations

$\boldsymbol{M}$, $\boldsymbol{q}$	Matrix, vector
$\boldsymbol{I}_{\mathbf{n}}$	Identity matrix of order n
$\boldsymbol{q}^{\mathsf{T}}$	Matrix/vector transpose
$x[n]$	n-th element of the digital signal x
$*$	Convolution operator
$\boldsymbol{a} \times \boldsymbol{b}$	Cross product of the two vectors $\boldsymbol{a}$ and $\boldsymbol{b}$
$\delta_{i,j}$	*Kronecker* Delta of the variable i and j
$\dot{q}$	Time derivative of q
$f(x)\Big\vert_{x=0}$	Expression $f(x)$ evaluated at $x = 0$
$\arg G(\mathrm{j}\omega)$	Phase of the frequency response $G(\mathrm{j}\omega)$
$\lvert G(\mathrm{j}\omega)\rvert$	Magnitude of the frequency response $G(\mathrm{j}\omega)$

1. Introduction

1.1. Background and motivation

The recent breakthroughs in semiconductor technologies, especially in power switching applications and signal processing, gave lots of opportunities to develop more sophisticated electronically controlled systems. The field of magnetic levitation, also fostered by these breakthroughs, gained industrial interest. In fact, the active magnetic suspension is an expensive and complex solution to levitate a shaft in comparison to conventional mechanical bearings. In some applications however, it is preferred due to its particular advantages with regards to:

- Mechanical wear and contact friction losses
- Rotor vibration and rotor balance requirements
- Contamination due to presence of lubrication or metal dust
- Presence of electrical discharge in mechanical bearings
- Contribution to system diagnostic due to sensing capability

Several industrial branches already adopted magnetic bearing technology to manipulate fluid at high speed and without contamination. Worth mentioning are vacuum pumps, which are widely established in the food, the pharmaceutical and the semiconductor industry. The tolerance of rotor imbalance and the mandatory rotor position monitoring of magnetically suspended drives loosen the restrictions on rotor balancing [1] and can be used to monitor the process quality such as to evaluate the wear of a machine tool in a spindle application. Other applications are to be found for example in transportation, where the magnetic levitation enables to transit people faster with reduced noise emission [2]. The high cost and the lack of trust in inherent unstable systems are the two main objections that prevent the general use of active magnetic suspension.

1.2. Magnetically levitated drive categories

Magnetically levitated drives are rotating field motors where the rotor is suspended at the center of the stator by means of electromagnetic forces. While the forces originate from both electric field and magnetic field, a magnetically levitated drive, as disclosed by its name, is of magnetic origin only. Indeed, at the low voltages commonly encountered in these applications, the electromagnetic forces due to the electric field are negligibly small.

In the group of magnetically levitated systems, a distinction in three families can be made, depending on the nature of the magnetic forces:

- Electro-magnetic levitation: This family relies on two forces of different natures. First, the reluctance force that relies on material permeability. A ferromagnetic material, penetrated by a magnetic field, experiences a force oriented parallel to the magnetic field toward the direction of minimum permeability. According to *Earnshaw*'s theorem [3], any magnetic levitation, utilising magnetic forces on ferromagnetic materials, is unstable by nature and needs to be stabilised with the help of active control. Second, the *Lorentz*-force is used, that acts on a conductor penetrated by a magnetic field and in which a current is flowing. As for conventional electrical machines, its amplitude is usually small compared to the reluctance forces. As good conducting materials are not ferromagnetic, *Lorentz*-forces require much more magnetising currents than reluctance forces. They are still useful in superconducting applications where high magnetising currents are realisable and where high magnetic fields are employed. Magnetic bearings and self-bearing motors belong to this electro-magnetic levitation family.

- Electro-dynamic levitation: This family relies on the *Lenz*'s law. Any varying magnetic flux on a conductive surface induces eddy-currents at its surface, generating themselves a flux counteracting the original flux variation. The two opposing fluxes together produce a repulsive force. Magnetic levitation systems based on electro-dynamic levitation is passively stable.

- Diamagnetic levitation: This family is also composed of forces of reluctance nature. However, the materials to be levitated are, in this case, diamagnetic. Diamagnetic materials, with permeability less that of vacuum, squeeze the magnetic field out of the material, simultaneously generating repulsive forces. Strong diamagnetism, encountered for example in materials in super-conducting state, can be used for magnetic levitation. Due to the repulsive nature of the forces, this family is self-stable.

This thesis focuses exclusively on the electro-magnetic levitation family. Apart from some rare high-speed coreless motors, most of magnetically levitated drives are based on reluctance forces, as the magnetising current requirements are, in contrast to *Lorentz*-forces, much easier manageable.

In a magnetically levitated drive, the rigid rotor has six degrees of freedom. A general representation is given in Figure 1.1. In order to ensure controllability of its position, three forces and three torque components are to be applied on the rotor. The equation of motion of a rigid body is usually obtained with the *Newton-Euler*'s equations in a coordinate frame whose origin is set at the rotor center of mass. However, in levitated drives, an equivalent description with five forces (four radial forces and an axial force) and one torque is preferred for convenience. Indeed, the precession and the nutation angles of the levitated rotor (respectively the first and second *Euler* angle) are very small in practice so that their values are difficult to

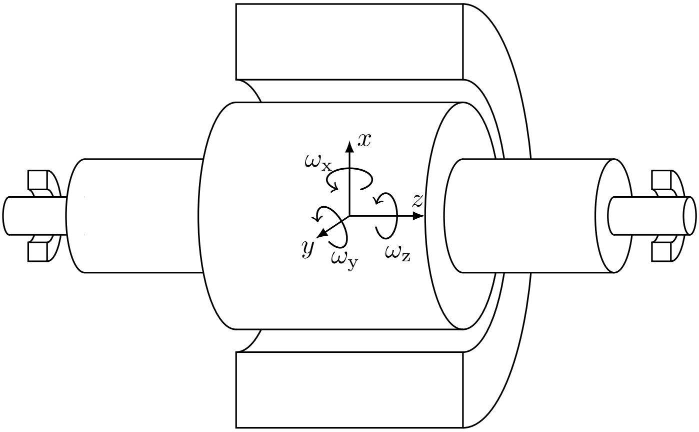

Figure 1.1.: Schematic representation of a rigid rotor with its six degrees of freedom: The rigid rotor can rotate and translate along the three axes x, y and z.

apprehend. Furthermore, the torque components that affect the precession and the nutation angles result from two sets of distinct actuator forces. In this thesis, the rotor position is expressed with proper *Euler*'s angles when dealing with the control, whereas the second representation with five forces and one torque is preferred for the motor design parts.

1.3. Rotor suspension with magnetic bearings

A magnetic bearing is an electromechanical system that is able to generate attractive magnetic forces between a fixed part (stator) and a free moving part (rotor) when magnetised. In its simplest form, the stator is composed of two ferromagnetic C-cores, placed on each side of the ferromagnetic rotor part, each surrounded by one magnetising coil. A schematic representation is given in Figure 1.2 where the two stator C-cores can pull the rotor in the respective directions. The coil 1 on the left magnetises the left stator C-core and the air gap 1 between the core and the rotor. It pulls the rotor to the left. If the same current is fed in the second coil 2 on the right, and if the air

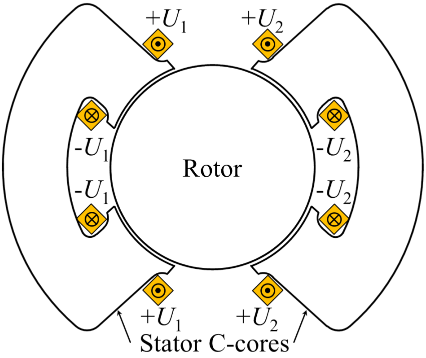

Figure 1.2.: Simple horizontal magnetic bearing: The left C-core pulls the rotor to the left when coil 1 is fed, whereas the right C-core pulls the rotor to the right when coil 2 is fed.

gaps 1 and 2 are equal, the pulling force on the right is equal and opposed to the one on the left. A resulting force (e.g. on the right) is obtained by reducing the magnetising current on one core (e.g. 1) and increasing the one on the other core (e.g. 2). For further information on drives with magnetic bearings, the following references are recommended [4], [5], [6] and [7].

1.4. Active self-bearing suspension

The term active self-bearing suspension is often referred to as bearingless motor in the literature. The latter term is misleading since the rotor needs a bearing mechanism to be suspended. Owing to its prevalence in publications, the name settled in the scientific community. An active self-bearing suspension describes a magnetically levitated rotor where the radial levitation forces are generated in the motor active part itself. It uses the same magnetic active parts to generate both the torque and the levitation forces. For nominal operation, no additional suspension system is required. However, to insure fail-safe operation, additional emergency mechanical bearings are inserted on both sides of the stator, as for a magnetically levitated drive.

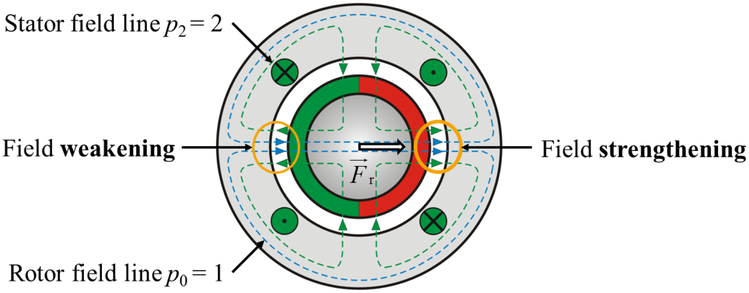

Figure 1.3.: Working principle of a self-bearing motor: The stator levitation field (in green) strengthens the rotor field (in blue) in the air gap portion on the right and weakens the rotor field in the air gap portion on the left. It results a rotor magnetic pull to the right.

The lateral suspension force results from the superposition of the rotor field with p_0 pole pairs and stator levitation field with p_2 pole pairs. In order to obtain radial forces, the pole pair relation $p_2 = p_0 \pm 1$ must be fulfilled [8]. A schematic representation is given in Figure 1.3. In this example, $p_0 = 1$ and $p_2 = 2$ which is the preferred configuration for high-speed low-power self-bearing motors. The stator levitation field (in green) and rotor field (in blue) are superposed in the air gap. The stator levitation field strengthens the rotor field in the air gap portion on the right and weakens the rotor field in the air gap portion on the left, so that the rotor experiences a resulting magnetic pull to the right. As the rotor rotates, the stator field must rotate with the same electrical angle so that the magnetic pull in the stator reference frame remains unchanged.

2. Magnetic levitation working principle

2.1. Control scheme overview of magnetically levitated systems

In this section, the basics of magnetic levitation control are introduced. It is shown later that most magnetically levitated systems can be simplified to the presented models. The magnetic levitation and self-bearing levitation are compared to explore the advantages and disadvantages of each system. Commonly, the control of a magnetically levitated drive consists of two cascaded closed-loop controls. The position controller, on the outer loop, is responsible for the calculation of the reference forces required to stabilise the rotor position at the center of the stator. The feedback signals, required by the position controller, are given by several position sensors, placed at defined locations. The electromagnetic actuators, used to generate forces, are current-force transducers. As a consequence, the reference forces are converted into reference currents that are impressed in the actuators by switching power amplifiers. In the inner loop, the current controllers are responsible for the calculation of the reference voltages, required to set proper phase currents. It calculates the firing instants of the power switches so that the phase current follows the reference given by the position control. The current feedback signals are provided by current sensors. The actuators are voltage-source inverters. A general representation of the control scheme is given in Figure 2.1. Although the electrical model is different for the

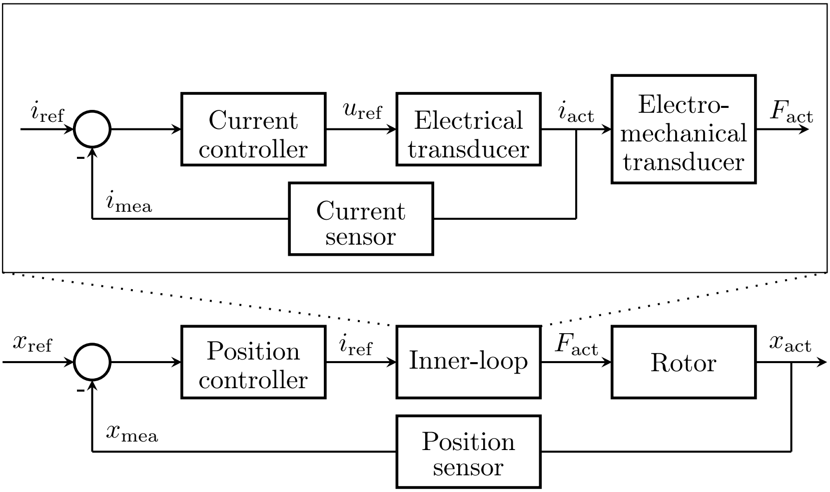

Figure 2.1.: General representation of a magnetically levitated system: The inner-loop (top) is formed by the electrical model and the current control loop. The outer-loop (bottom) is composed of the mechanical model and the position control loop.

magnetic bearing and self bearing motor, it is largely an inductive model. The mechanical model is identical in both cases. Sometimes, the electrical and mechanical models are combined to obtain a single control scheme with interesting properties. One application of this combined model worth mentioning is for the voltage controlled magnetic bearing [6]. With the integration of the voltage induction due to rotor displacement, the system becomes marginally stable (i.e. the three poles of the plant are all equal to zero).

2.2. Generation of magnetic forces

2.2.1. Simple electromagnetic actuator

The force-displacement characteristic of a ferromagnetic C-core, with a variable air gap δ, as displayed in Figure 2.2a, is non-linear. As long as the magnetic core is unsaturated, the electromagnetic force F, acting on the surface S of the core and generated by the magneto-motive force $N \cdot i$, is anti-proportional to the square of the air gap width δ according to 2.1. Furthermore, the current-force characteristic is also non-linear since the force F, in the unsaturated case and for a given air gap δ, is proportional to the square of the magneto-motive force $N \cdot i$. Finally, only attraction forces can take place so that the force-displacement characteristic is not bidirectional. In order to overcome these limitations, the magnetic bearings are designed with two symmetrically mounted ferromagnetic C-cores as displayed in Figure 2.2b. The magnetic circuits are characterised by the air gaps δ_1, δ_2 and the currents i_1, i_2 following equation 2.2. The air gap magnetisation can be done with a single coil carrying the total current i. This magnetic bearing type is called differential feeding bearing. However it can also be done with two coils, one carrying the magnetisation current i_0, and the second carrying the control current Δi. This differential winding magnetic bearing has more resistive losses. By summing the two electromagnetic forces F_1 and F_2, with their respective orientations, a (within certain limits) linear net force-displacement characteristic can be achieved, described by the force-displacement factor k_{sr} as (2.3). This coefficient characterises the equivalent spring of the rotor model in Figure 2.1. The same consideration is repeated to obtain a linear net force-current characteristic, with a force-current factor k_{ir} as (2.4). This second coefficient characterises the electro-mechanical transducer in Figure 2.1. The last characteristic coefficient in the electrical model is the voltage-velocity factor k_{u} defined by (2.5).

$$F(\delta, i) \approx \frac{\mu_0 \cdot S \cdot N^2 \cdot i^2}{4\delta^2} \tag{2.1}$$

$$\begin{aligned} \delta_1 &= \delta_0 + \Delta x, \delta_2 = \delta_0 - \Delta x \\ i_1 &= i_0 + \Delta i, i_2 = i_0 - \Delta i \end{aligned} \tag{2.2}$$

$$k_{\mathrm{sr}} = -\frac{\partial F}{\partial \delta}\bigg|_{i=i_0,\delta=\delta_0} = -\frac{\mu_0 \cdot S \cdot N^2 \cdot i_0^2}{\delta_0^3} \tag{2.3}$$

$$k_{\mathrm{ir}} = \frac{\partial F}{\partial i}\bigg|_{i=i_0,\delta=\delta_0} \approx \frac{\mu_0 \cdot S \cdot N^2 \cdot i_0}{\delta_0^2} \tag{2.4}$$

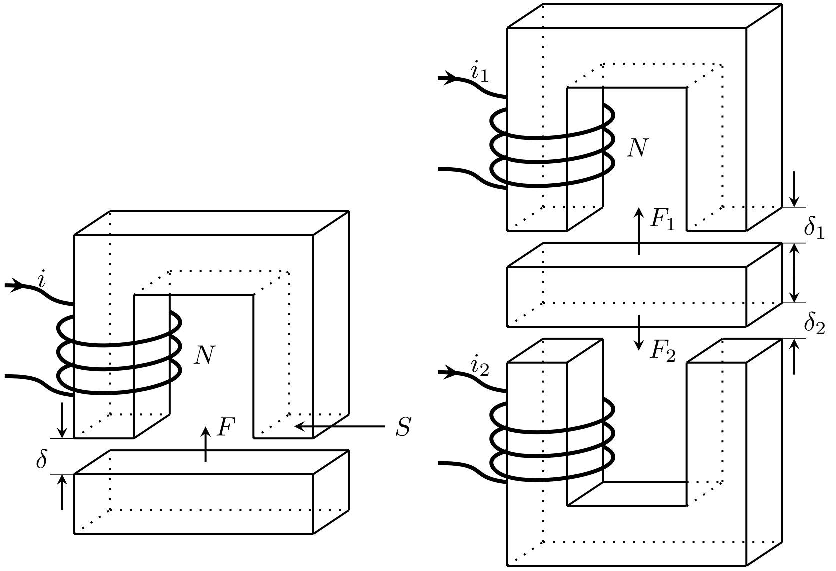

(a) Single-sided magnetic bearing (b) Double-sided magnetic bearing

Figure 2.2.: Geometry and parameters of a single-sided magnetic bearing (left) and double-sided magnetic bearing (right).

$$u_{\mathrm{i}} = -\frac{\partial \Psi}{\partial \delta} \cdot \frac{\partial \delta}{\partial t}\bigg|_{i=i_0, \delta=\delta_0} = k_{\mathrm{u}} \cdot \frac{\partial \delta}{\partial t} \text{ where } k_{\mathrm{u}} = k_{\mathrm{ir}} \tag{2.5}$$

An important aspect to be noticed in equation (2.3) is that the single sided magnetic pull, resulting from the misalignment from the center position, points toward the misalignment direction ($k_{\mathrm{sr}} < 0$). It is equivalent to a spring with a negative stiffness. This negative stiffness describes the inherent instability of reluctance based magnetically levitated systems, expressed in the *Earnshaw*'s theorem [3]. The very low equivalent damping of the actuator, mainly provided by the eddy-current losses in the core, is also an aspect that needs to be considered during control design.

2.2.2. Principle of field superposition in self-bearing machines

The principle of force generation in a self-bearing machine is based on the superposition of two fields with different number of pole pairs [9]. A machine cross section is depicted in Figure 1.3 for illustration. The considered rotating machine is composed of two distributed stator windings: A drive winding, with p_1 pole pairs and $N_{\mathrm{s},1}$ winding turns per phase and a levitation winding, with p_2 pole pairs and $N_{\mathrm{s},2}$ winding turns per phase. For simplicity, the drive winding is disregarded. In case of a PM self-bearing machine, the rotor magnetic flux density with the amplitude B_0 at the stator inner radius r_{si} with p_0 pole pairs is generated by surface mounted permanent magnets. For the sake of simplicity, only the fundamental of the rotor magnetic field is considered. The calculation of the electromagnetic forces is more complicated than previously and is thoroughly detailed in Chapter 4. For a two pole rotor ($p_0 = 1$) and four pole levitation winding ($p_2 = 2$), the derivative of the force with regard to the eccentricity ϵ at zero stator current is given by (2.6) where l_{Fe} is the equivalent iron length, r_{si} the stator inner-radius and r_{ro} the rotor outer-radius. The derivative of the force with regard to the stator levitation current i_2 at the rotor concentric position is given by (2.7) where m is the number of phases, $N_{\mathrm{s},2}$ the number of turns per phase and $k_{\mathrm{w},2}$ the fundamental winding factor of the levitation winding. Both equations are valid for a magnet relative permeability μ_{PM} which equals one.

$$k_{\mathrm{sr}} = -\frac{\partial F}{\partial \epsilon}\bigg|_{i_2=0,\epsilon=0} \approx -\frac{\pi \cdot l_{\mathrm{Fe}}}{\mu_0} \cdot \frac{r_{\mathrm{si}}^4}{r_{\mathrm{si}}^4 - r_{\mathrm{ro}}^4} \cdot B_0^2 \tag{2.6}$$

$$k_{\mathrm{ir}} = \frac{\partial F}{\partial i_2}\bigg|_{\epsilon=0} \approx m \cdot N_{\mathrm{s},2} \cdot k_{\mathrm{w},2} \cdot l_{\mathrm{Fe}} \cdot B_0 \cdot \frac{r_{\mathrm{si}}^4}{r_{\mathrm{si}}^4 - r_{\mathrm{ro}}^4} \tag{2.7}$$

Comparing the two equations (2.6) and (2.7) with the equations for the magnetic bearing (2.3) and (2.4), it should be noticed that the magnetising task of the current i_0 is taken by the permanent magnet flux density B_0. In both cases, the increase of air gap length leads to a decrease of the negative

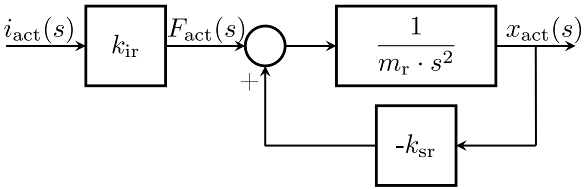

Figure 2.3.: Single axis equivalent model in *Laplace* domain of a magnetically levitated rotor of mass m_{r}, suspended with the current i_{act}. The control force F_{act} is proportional to the current i_{act} with the force-current factor k_{ir}. x_{act} is the rotor position, oriented in the same direction as the control force F_{act}. The positive feedback with $-k_{\mathrm{sr}}$ is responsible for the inherent system instability.

stiffness k_{sr} and force-current coefficient k_{ir}. Given a rotor mass m_{r}, both magnetic bearing and self-bearing motors can be modelled with the model in Figure 2.3.

2.3. Comparison between magnetic bearings and active self-bearing suspension

2.3.1. Mechanical properties

From the mechanical point of view, suspension systems based on magnetic bearings and active self-bearings share very similar models. The rotor has according to Figure 1.1 a rotor polar moment of inertia J_{z}, two transverse moments of inertia J_{x}, J_{y} and a rotor mass m_{r}. It is levitated by magnetic forces at the drive-end and the non-drive-end F_{DE}, F_{NDE}, effective in the magnetic active parts. Both transducers display linear current-force and displacement-force characteristics within certain limits of x, y and i. As a consequence, most of the already thoroughly investigated mechanical control concepts for magnetic bearings can be transposed on the control of active self-bearing systems.

2.3.2. Electrical properties

From the electrical point of view, an analogy can be drawn between the active magnetic bearing and the DC motor and between the active self-bearing motor and the synchronous motor. The similarities concern firstly the type of excitation. The DC motor, as for the magnetic bearing, is excited via the stator while the excitation of the synchronous motor, as for the active self-bearing motor, is excited via the rotor. As a consequence, the control reference frame is for the magnetic bearing and the DC motor the stator reference frame, whereas the synchronous motor and the active self-bearing motor are controlled in a two-pole rotor-fixed reference frame rotating with electrical frequency. The same full bridge power converters are used for the DC motor and the magnetic bearing whereas three-phase inverters are used for the synchronous motor and the active self-bearing motor. The magnetic bearing air gap flux linkage Ψ_c is governed by a very simple equation (2.8) in stator coordinate system, where the voltage u is applied to one coil c with a resistance R_c. In stationary operation, the derivative of the air gap flux is zero so that the bearing voltage u only overcomes the voltage drop due to phase resistance R_c.

$$u = R_\mathrm{c} \cdot i + \frac{\mathrm{d}\,\Psi_\mathrm{c}}{\mathrm{d}t} \tag{2.8}$$

The same equation governs the levitation flux linkage Ψ_2 of the self-bearing motor. However, the derivative of the flux in stationary operation is zero in the synchronous levitation reference frame, so that the voltage equation in synchronous reference frame is (2.9).

$$u_{\mathrm{d},2} + \mathrm{j}u_{\mathrm{q},2} = R_{\mathrm{s},2}\,(i_{\mathrm{d},2} + \mathrm{j}i_{\mathrm{q},2}) + \mathrm{j}\omega_\mathrm{e}\,(\Psi_{\mathrm{d},2} + \mathrm{j}\,\Psi_{\mathrm{q},2}) + \frac{\mathrm{d}}{\mathrm{d}t}\,(\Psi_{\mathrm{d},2} + \mathrm{j}\,\Psi_{\mathrm{q},2}) \tag{2.9}$$

2.3.3. Force densities

While the active magnetic bearings exclusively use the radial component of the magnetic flux densities to produce forces, the self-bearing motors are combining the radial and tangential components of the air gap magnetic flux densities to produce forces. In order to get synergy of the force components, the relation between the number of pole pairs of the levitation winding p_2 and the rotor number of pole pairs p_0 should be $p_2 = p_0 + 1$ [9].

In the case of the double-sided magnetic bearing, the bias magnetising flux density is high. In absence of magnets, it can overcome 1 T [4], while with permanent magnet bias, it usually ranges from 0.5 T to 1 T. In contrast to self-bearing machines, magnetic bearings do not require a bandage on the rotor, leading to a small magnetic air gap volume. In active magnetic bearings, the control magnetic flux, that interacts with the air gap magnetising flux to generate radial levitation forces, is ranging from 0 to the amplitude of the bias magnetising flux. In case of low permanent magnet bias, it can overcome the bias magnetising flux until tooth saturation occurs. Their superposition results in magnetic force densities ranging from 40 $\mathrm{N/cm^2}$ at 1 T with permanent magnets up to 160 $\mathrm{N/cm^2}$ with coil excitation and 2 T magnetic flux density [5]. In contrast, the levitation magnetic flux density in active self-bearing machines is much smaller than the permanent magnet bias. As an illustration, the maximum radial magnetic flux components of the self-bearing motors, presented in the following sections, are below 150 mT. The maximum force densities are consequently not exceeding 4 $\mathrm{N/cm^2}$. There are two reasons for this difference. First the rotor of low power high speed permanent magnet synchronous motors is commonly not laminated in order to keep the first bending mode frequency of the rotor above the rated frequency. As the levitation field is asynchronous to the rotor, the induced eddy currents on the rotor surface must be kept small. To that end, the amplitude of the levitation magnetic flux is kept small. The second reason is the increased effective magnetic air gap due to the non-magnetic bandage and the magnets with a recoil permeability close to one. The required magneto-motive force to generate the levitation field is substantial so that the magnetic flux density is kept small. As a result, a large iron length l_{Fe} is necessary in active self-bearing machines to obtain a sufficiently big levitation force. Therefore, it is suitable for applications where the required radial forces and stiffnesses are low while the torque is high (e.g. pump applications). It is also proven later that self-bearing motors with high levitation fields behave non-linear even when considering ideal ferromagnetic materials with $\mu_{\mathrm{Fe}} \to \infty$.

2.3.4. Power electronic for actuator feeding

Each coil of active magnetic bearings is usually fed with a full H-bridge while each phase of self-bearing motors is fed with a half-bridge. For one radial force, a magnetic bearing requires two full bridges and eight power switches. The levitation winding requires only three half-bridges and six power switches. Bulky analogue power amplifiers have been replaced by much more compact switched power supplies with much higher efficiency [4]. Since switching frequencies of several tens of kHz are easily obtained with MOSFET switches, the inherent control delay, caused by the voltage modulation, is not a limiting factor. The power converters must be designed to provide a nominal reactive power that depends on the force and design of the actuator.

2.3.5. Reactive power requirement

2.3.5.1. Reactive power requirement under static load

Under static load, the levitated drive is in stationary condition. From (2.8) it is clear that the magnetic bearing with its low phase resistance R_{c} needs little active power P_1 and no reactive power Q_1 to maintain a constant magnetic force F. For both differential feeding and differential winding excitation, the active power is given by (2.10). However, the phase resistance R_{c} of the differential winding magnetic bearing is higher than the one of the differential feeding, since two coils are inserted in the same slot cross-section. For example, a cross-section share of 50% for the excitation coil and 50% for the control coil leads to doubled ohmic losses.

$$P_1(i_0, \Delta i) = 2R_{\mathrm{c}} \cdot (i_0^2 + \Delta i^2), \quad Q_1(i_0, \Delta i) = 0 \tag{2.10}$$

From (2.9) the active power P_2, which is required to maintain a constant force in an active self-bearing motor with m phases, is calculated as (2.11). As for the magnetic bearing, the force amplitude is constant, however the reactive power Q_2 is linearly increasing with the electrical frequency $f = \omega/(2\pi)$ (2.11).

$$P_2(\omega, i_{\mathrm{s},2}) = m \cdot R_{\mathrm{s},2} \cdot i_{\mathrm{s},2}^2, \quad Q_2(\omega, i_{\mathrm{s},2}) = m \cdot \omega \cdot L_{\mathrm{s},2} \cdot i_{\mathrm{s},2}^2 \tag{2.11}$$

As illustrated later in the design examples, the reactive power Q_2, which is required to rotate the levitation field at high frequency, is much bigger than the small active power P_2, so that the self-bearing motor needs a power amplifier with higher ratings compared to drives with active magnetic bearings to compensate static loads. In order to design the power converter, the reactive power requirement under dynamic load is required [4].

2.3.5.2. Reactive power requirement under dynamic load

The shaft is coupled to a mechanical process (e.g. to a compressor wheel) and is subjected to disturbance forces, whose amplitudes and frequencies must be estimated to design the power supply. The dynamic performance of an actuator describes the maximum variation of the levitation force that can be achieved for a given amplifier's apparent power, given that the actuator is not in magnetic saturation. The straight comparison of a magnetic bearing dynamic performance with the one of a self-bearing motor is not easy since they are different in terms of force density and geometry. However the involved forces are of reluctance origin in both cases. In case of a flux density B in air between materials of high permeability $\mu_\mathrm{h} \gg \mu_0$, the magnetic force per area on the material surface f is equal to the magnetic energy density w_m per volume (2.12).

$$f = w_\mathrm{m} = \frac{B^2}{2\mu_0} \tag{2.12}$$

In order to obtain a desired magnetic force F in the air gap, a certain magnetic flux density B is required at the material surface enclosing the rotor in the air gap. This magnetic flux density B leads to a stored magnetic energy $W_\mathrm{m} = \int w_\mathrm{m} \mathrm{d}V$ which is the integral of (2.12) in the air gap volume V surrounding the rotor part. If the magnetic force F is varying with the angular frequency ω, the reactive power, which is necessary to change the magnetic energy W_m, is simply $Q = \omega \cdot W_\mathrm{m}$. In order to get the maximum force amplitude F at the angular frequency ω, and assuming a limited apparent power S, the stored magnetic energy W_m must be minimised. Since the material's surface at the air gap and magnetic flux density B are already fixed to get the required force F, the only possibility to reduce the volume V and hence the magnetic stored energy W_m is by decreasing the air gap width δ. This is the reason why magnetic bearings are designed with small air gap width δ. The feeding type (differential feeding or differential winding) has a decisive influence on the required reactive power. In case of a differential feeding, the voltage equations (2.8) at the terminals of the two electromagnets 1 and 2 in Figure 2.2b are expressed as a function of the currents i_1 and i_2 in (2.13).

$$\begin{aligned} u_1 &= R_\mathrm{c} \cdot i_1 + \frac{\mu_0 \cdot N^2 \cdot S}{2\delta_1} \cdot \frac{\mathrm{d}i_1}{\mathrm{d}t} \\ u_2 &= R_\mathrm{c} \cdot i_2 + \frac{\mu_0 \cdot N^2 \cdot S}{2\delta_2} \cdot \frac{\mathrm{d}i_2}{\mathrm{d}t} \end{aligned} \tag{2.13}$$

With the magnetic energy increment $\mathrm{d}W_\mathrm{m} = i \cdot \mathrm{d}\Psi$ and the co-energy increment $\mathrm{d}W_\mathrm{m}^* = \Psi \cdot \mathrm{d}i$ in case of linear magnetic circuits $\Psi = L \cdot i$, the numerical equality (2.14) is true.

$$W_\mathrm{m} = \int_0^{\Psi} i \cdot \mathrm{d}\Psi = \Psi^2/(2L) = W_\mathrm{m}^* = \int_0^{i} \Psi \cdot \mathrm{d}i = Li^2/2 \tag{2.14}$$

At the center position $\delta_1 = \delta_2 = \delta_0$, the energy W_1, which is necessary to increase i_1 from i_0 to $i_0 + \Delta i$ as well as to reduce i_2 from i_0 to $i_0 - \Delta i$, is given by (2.15).

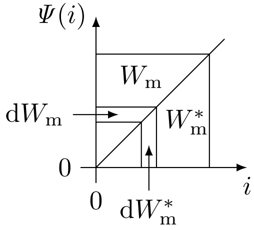

Figure 2.4.: Magnetic energy W_m and co-energy W_m^* in a linear magnetic circuit with air gap. The magnetic co-energy variation is given by $\mathrm{d}W_\mathrm{m}^* = \Psi(i)\mathrm{d}i$, whereas the magnetic energy variation is given by $\mathrm{d}W_\mathrm{m} = i(\Psi)\mathrm{d}\Psi$.

$$\begin{aligned}
W_{\mathrm{m},1}^* &= \int_{\mathrm{i}_0}^{i_0+\Delta i} \frac{\mu_0 \cdot N^2 \cdot S}{2\delta_0} \cdot i \cdot \mathrm{d}i = \frac{\mu_0 \cdot N^2 \cdot S}{4\delta_0} \cdot (2i_0 + \Delta i) \cdot \Delta i = W_{\mathrm{m},1} \\
W_{\mathrm{m},2}^* &= \int_{\mathrm{i}_0}^{i_0-\Delta i} \frac{\mu_0 \cdot N^2 \cdot S}{2\delta_0} \cdot i \cdot \mathrm{d}i = -\frac{\mu_0 \cdot N^2 \cdot S}{4\delta_0} \cdot (2i_0 - \Delta i) \cdot \Delta i = W_{\mathrm{m},2}
\end{aligned} \tag{2.15}$$

In case of a differential winding, the two coils in Figure 2.2b are split in two. One magnetising coil with N_0 turns is fed by i_0, while the second control coil with N_c turns is fed by i_c in the top electro-magnet and by $-i_\mathrm{c}$ in the bottom one. Both magnetising coils are connected in series and are fed by a constant terminal voltage u_0. Both control coils are connected in series but with interchanged coil terminals in order to get a differential winding and are fed by the control voltage u_c. The flux linkage of the control flux with the two magnetic coils cancels completely due to the interchanged control coil terminals. In the same way the flux linkage of the magnetising coils with the control coils cancels for the same reason so there is no mutual coupling between control and magnetising coils. The equations of u_0 and u_c at the center position $\delta_1 = \delta_2 = \delta_0$ are thus given by (2.16) only with self-inductances.

$$\begin{aligned} u_0 &= R_0 \cdot i_0 + \frac{\mu_0 \cdot N_0^2 \cdot S}{\delta_0} \cdot \frac{\mathrm{d}i_0}{\mathrm{d}t} \\ u_\mathrm{c} &= R_\mathrm{c} \cdot i_\mathrm{c} + \frac{\mu_0 \cdot N_\mathrm{c}^2 \cdot S}{\delta_0} \cdot \frac{\mathrm{d}i_\mathrm{c}}{\mathrm{d}t} \end{aligned} \tag{2.16}$$

The two voltage equations (2.16) are thus magnetically independent as the magnetising coil does not induce any voltage in the control coil and vice versa. The corresponding magnetic co-energy to increase the control current i_c from 0 to Δi is given by (2.17).

$$W_\mathrm{c}^* = \int_0^{\Delta i} \frac{\mu_0 \cdot N_\mathrm{c}^2 \cdot S}{\delta_0} \cdot i \cdot \mathrm{d}i = \frac{\mu_0 \cdot N_\mathrm{c}^2 \cdot S}{2\delta_0} \cdot \Delta i^2 \ll W_1^* + W_2^* \tag{2.17}$$

Despite their higher ohmic losses, magnetic bearings with differential windings require less reactive power compared to differential feeding in particular when the control current Δi is low compared to the magnetising current i_0.

2.3.6. Comparison by an example

A comparison between a magnetic bearing and a self-bearing motor is given to illustrate the observations of 2.3.1 ... 2.3.5. A magnetic bearing with differential feeding is considered with the parameters in Table 2.1, which are taken from [5]. It is compared to a two-pole self-bearing motor with diametrically magnetised rotor magnets and with the parameters in Table 2.2.

The differential magnetic flux density ΔB (in Table 2.1) and the levitation field current loading A_2 (in Table 2.2) are calculated so that the nominal levitation force equals 9.8 N with an assumed sufficiently big force reserve. The average force densities in the two magnetic bearing air gaps are $f = 12.6\ \mathrm{N/cm^2}$ and $f = 7.6\ \mathrm{N/cm^2}$ respectively. The force density distribution in the self-bearing motor has a local maximum at the rotor outer radius

Table 2.1.: Magnetic bearing parameters

Parameter	**Symbol**	**Value**	**Unit**
Surface area of C-core	S	100	mm^2
Air gap width	δ	0.5	mm
Magnetisation flux density	B_0	0.5	T
Differential flux density	ΔB	62	mT

Table 2.2.: Self-bearing motor parameters

Parameter	**Symbol**	**Value**	**Unit**
Rotor outer radius	r_{ro}	12.25	mm
Magnet outer radius	r_{mo}	15	mm
Stator inner radius	r_{si}	17.5	mm
Rotor axial length	l_{Fe}	40	mm
Permanent magnet remanence	B_{rem}	0.96	T
Permanent magnet recoil permeability	$\mu_{\mathrm{r,m}}$	1.2	p.u.
Levitation field current loading	A_2	133	A/cm

r_{ro} of $\hat{f}(r_{\mathrm{ro}}) = 37\ \mathrm{N/cm^2}$, but a maximum of only $\hat{f}(r_{\mathrm{si}}) = 7.2\ \mathrm{N/cm^2}$ at the stator inner radius r_{si}. The volume V to be magnetised is $V = 0.2\ \mathrm{cm^3}$ for the magnetic bearing and $V = 19.6\ \mathrm{cm^3}$ for the self-bearing motor. Therefore, the self-bearing air gap volume V to be magnetised is 100 times bigger than the one of the magnetic bearing. The total magnetic energy W_{m} stored in the magnetic bearing air gap is $W_{\mathrm{m}} = 20$ mJ. Approximately 60% of W_{m} is stored in the first (e.g. upper) air gap (see Figure 2.2b), while the rest is stored in the second (lower) air gap (see Figure 2.2b). In contrast, the total magnetic energy W_{m} in the self-bearing motor is $W_{\mathrm{m}} = 3.6$ J. The total energy variation, which is necessary to reverse the levitation force in the magnetic bearing is 4.9 mJ whereas the total energy variation in the self-bearing motor air gap is 5.6 mJ. In order to impress a force of the same amplitude, which is pulsating with $f = 1$ kHz, the average reactive power requirement is $Q = 31$ VAr for the magnetic bearing and $Q = 35$ VAr for the self-bearing motor. This surprising result of nearly equality is simply explained by the fact that the two coils of the magnetic bearings bear the magnetising flux as well as the control flux whereas the levitation winding, with a pole pair p_2, which is different from the rotor field p_0, is not induced by the rotor magnetising field of p_0 pole pairs. In contrast, a magnetic bearing with differential winding and the same parameters as in Table 2.1 would require only $Q = 1.9$ VAr to obtain the same force variation. To conclude, the self-bearing motor is able to get similar dynamic performances compared to magnetic bearings with differential feeding since the big air gap volume to be magnetised is compensated by the low magnetisation requirement of the levitation field. However, it is not able to compete with magnetic bearings with permanent magnet bias magnetisation or with differential winding. Therefore, self-bearing motors are not suited for applications requiring high mechanical stiffness such as spindle machines.

3. Sensor signal processing and transformations

As explained previously, magnetic levitation systems based on reluctance forces, are unstable and require a suitable closed-loop control for stable operation. A closed-loop control needs some feedback information of the plant state variables in order to estimate and compensate the deviation between reference and actual value. For this purpose, sensors are necessary to transform the information into a signal that is used by the controller. Commonly, the signal is transformed into an electrical form (such as electrical voltage) and digitised before being used by the digital controller. In addition to the position sensors, which are required to control the rotor position in magnetically levitated drives, other sensors are needed, such as current sensors for a proper feeding of the actuators with voltage source converters and rotational position sensors for a proper air gap magnetic field orientation. In this chapter, the employed sensors are presented, together with their limitations and issues which they cause in active self-bearing motors.

3.1. Current sensors for magnetically levitated drives

The electromagnetic actuators are usually voltage-fed. The generated forces and torque are related to actuator currents, so that force and torque controllers require the measurement of the actuator currents. Several physical

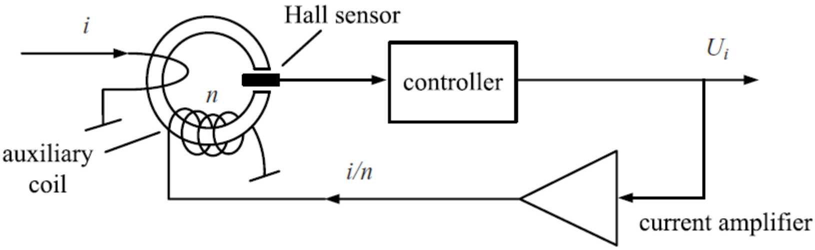

Figure 3.1.: Closed-loop *Hall*-sensor based current sensor working principle [4]. The controller generates a voltage reference signal U_i, converted into a balancing current i/n by the current amplifier, to regulate the magnetic flux in the C-shaped core to zero.

properties can be used to transform a current signal into a voltage signal. The closed-loop *Hall*-sensor technology is a well established and low cost solution in order to obtain a low noise current transducer that operates from DC up to several kilo Hertz. The working principle of a closed-loop *Hall*-sensor is illustrated in Figure 3.1. It is based on a zero flux closed-loop control. A C-shaped magnetic core surrounding the wire is magnetised by the wire current i to be measured. A second balancing coil (auxiliary coil) with n turns is inserted on the same core to compensate within the C-core the magnetisation of the wire current. A *Hall*-sensor is inserted in the air gap of the C-core to measure the residual magnetic flux density in the core. The obtained *Hall* voltage signal is proportional to the residual magnetic flux and is used by the balancing controller (differential operational amplifier) to produce a counteracting magnetising current so that the resulting magnetic flux is zero. The voltage output U_i is proportional to the current i. A cheaper realisation is possible with open-loop *Hall*-effect sensors where no compensation of the magnetisation is present. Since these sensors have lower accuracy, they are not recommended for magnetically levitated applications. Alternatively, the current-shunt for current measurement is slightly more difficult to use, since the measured shunt voltage is at the phase potential, hence it is experiencing high voltage transients. Analogue isolated amplifiers with high voltage transient immunity such as the HCPL-7840 suffer from a significant noise-floor, due to the analogue-digital-analogue conversion. Recently, some alternatives were proposed by integrated circuit manufacturers, where a sigma-delta modulator and a digital isolator are present on a single chip. Such isolated modulators provide a digital signal with high precision and low noise. The controller needs a sigma-delta demodulator to convert the pulse train in a usable signal. The important drawback of such a solution is that it is not possible to sample the current at particular current-ripple-free instants to reduce signal noise without additional filtering.

3.1.1. Employed current sensors and limitations

In this work, the PWM frequencies f_{PWM} of the MOSFET-based voltage source converters range from 20 kHz to 62.5 kHz. The current sensor frequency bandwidth should cover at least the frequency range of the converter. The phase of the current sensor transfer function should be small at frequency f_{PWM}, so that the phase current ripple, resulting from the voltage pulse-width modulation of the voltage source converter, does not appear in the sampled current signal. The linearity error of most closed-loop current sensors is sufficiently low and suited for this application. The chosen current sensors to be implemented in the current control on the investigated motors belong to the family *CASR* from the company *LEM*. They are based on the flux-gate working principle, which is slightly more complex than the one presented in Figure 3.1, but is less sensitive to temperature variation and offset than the *Hall*-effect sensors. With a frequency bandwidth (defined by an attenuation of -3 dB) of 300 kHz, with a reaction time below 0.3 µs and with a linearity error below 0.1%, these sensors exceed the requirements that are set by the application.

3.1.2. Current signal processing

The achievable precision and dynamic of a controlled system is closely related to the quality of the feedback information signals. Whereas signal processing cannot improve the absolute signal quality, it enables to highlight the frequency or the frequency range of interest. To do so, some prior knowledge on the signal properties, which shall be evaluated, is necessary. The bandwidth of the chosen current sensor largely covers the frequency range of interest for the current control of up to 8 kHz, so that the insertion of the current sensors in the current control loop is of little effect on the control phase. It is common practice to limit the signal bandwidth with a low-pass filter in order to attenuate the sensor noise at higher frequency and its subsequent actuator loading. A compromise must be found between the reduction of signal noise and inserted delay in the control. The current ripple, which is present in continuous time domain and which is resulting from the chopped voltage feeding, should not be filtered. Indeed, the filter that would be necessary to attenuate the current ripple in time domain is too slow and would limit significantly the current control performances. For example, the cut-off frequency f_c of a second order filter with a damping ratio $\zeta = 1$ (ratio of actual damping to critical damping, *Lehr*'s damping ratio) must be lower than 1.1 kHz to attenuate the signal ripple by at least 50 dB at $f_\mathrm{PWM} = 20$ kHz. Instead, the current signals should be synchronously sampled at moments, where the current ripple is zero. These instants are present twice per PWM period at the middle of the symmetrical pulse pattern. If the signals are moderately filtered, the delayed signals contain a fraction of the current ripple at the sampling instants. This fraction is reduced by slightly delaying the sampling instant to account for signal delay. For the considered *CASR* sensor, the flux-gate technique operates at a high carrier frequency (ca. 450 kHz) that induces a small out-of-band voltage ripple at the signal output [10]. If not filtered in time continuous domain, this disturbance is reflected in the first *Nyquist*-zone and is visible in the sampled signal. The output ripple of the chosen current sensor has an amplitude of 20 mV at 450 kHz. It should be reduced below the quantization level of the 12-bit analog-to-digital converter, which is 5 $\mathrm{V}/2^{12} = 1.2$ mV. For a PWM frequency of 20 kHz, a second order filter with a cut-off frequency of $f_\mathrm{C} = 100$ kHz and a damping ratio of $\zeta = 1$ is sufficient. It inserts a phase shift of -22° at 20 kHz. In contrast, the attenuation of the current ripple in continuous time domain requires a filter with a cut-off frequency f_C well below 20 kHz. The resolution of the analog-to-digital converters, which are used to sample the current signals, does not need to be high, since the full converter measurement range is utilised, and the voltage source converter linearity is low. In practice, a 12-bit resolution with a signal-to-noise ratio of about 70 dB is sufficient.

3.2. Rotor angle sensors for magnetically levitated drives

3.2.1. Employed rotor angle sensors

In contrast to drives with magnetic bearings, the rotor angle sensor is mandatory in self-bearing machines not only for the drive but also for the correct orientation of the stator levitation field with respect to the rotor field. A perturbation of this sensor signal potentially leads to levitation instability. Several technologies are available for rotor angle measurement. The most commonly used are:

- Rotary encoders, that can be absolute or incremental. The delivered signal is analogue or digital. They can be of mechanical, optical, magnetic or of capacitive nature.
- Resolvers, mostly analogue, that are equivalent to a two phase rotary electrical transformer. They require a modulation and demodulation of an excitation signal, where the phase is modulated in the amplitude.

Active self-bearing high-speed drives require absolute, contact-free, wide frequency range (DC to maximum rotational speed) rotor angle sensors with sufficiently high resolution. Therefore, combinations of two rotor angle sensors are common. In this work, the following combination of sensors is considered:

- Digital *Hall*-sensors, whose discrete and coarse angle resolution is improved by increasing the number of mounted *Hall*-sensors. The *Hall*-sensors are fast switching and enable high noise immunity due to their digital nature. They are particularly suited for high-speed operation.
- Analogue two-dimensional *Hall*-sensors, whose angle resolution is limited by the signal noise. Even though the bandwidth is not limiting, they are more noise sensitive compared to the digital *Hall*-sensors.

This sensor selection is discussed in the coming section.

3.2.2. Rotor angle resolution and stability issues

In a drive with active magnetic bearings, the misalignment angle θ_e between the actual θ_act and measured rotor position θ_mea is of little consequence. Whereas the positioning control stability of magnetic bearings is not influenced by the angle misalignment θ_e, the electrical torque M_e generated by the motor is decreasing according to $\cos\theta_\mathrm{e}$. Consequently, significant errors up to $\pm\pi/2$ can be tolerated without any stability issue. In contrast, the rotor position misalignment affects the stability of the position control loop in active self-bearing drives [5]. In order to understand and illustrate the influence of the misalignment between the actual and measured rotor field, the determination of the poles in the s-plane of the transfer function of a simplified two dimensional active self-bearing motor stabilised with a simple proportional derivative controller is derived. For illustration purpose, a numerical application is presented with the motor and control parameters given in Table 3.1. The position of the rotor is given by the vector $\boldsymbol{q} = (q_\mathrm{x}\ q_\mathrm{y})^\mathsf{T}$. A simple proportional derivative controller, tuned according to the design rule of "natural" stiffness [4], is inserted to stabilise the system. The second *Newton*'s law of motion that governs the mechanical plant

Table 3.1.: Motor and control parameters of a simplified levitated drive with PD controller

Parameter	**Symbol**	**Value**	**Unit**
Rotor mass	m_r	1.12	kg
Force-displacement coefficient	k_sr	-50	N/mm
Force-current coefficient	k_ir	1.74	N/A
Proportional coefficient	k_P	57.3	A/mm
Damping coefficient	k_D	0.136	A s/mm
Critical damping coefficient	$k_\mathrm{D,crit}$	0.271	A s/mm

(left hand side) and the control equation (right hand side) are combined in (3.1), with consideration of the rotor misalignment θ_e with the rotation matrix $\boldsymbol{R_2}$.

$$m_\mathrm{r} \cdot \boldsymbol{I_2} \cdot \ddot{\boldsymbol{q}} + k_\mathrm{sr} \cdot \boldsymbol{I_2} \cdot \boldsymbol{q} = -k_\mathrm{P} \cdot k_\mathrm{ir} \cdot \boldsymbol{R_2} \cdot \boldsymbol{q} - k_\mathrm{D} \cdot k_\mathrm{ir} \cdot \boldsymbol{R_2} \cdot \dot{\boldsymbol{q}},$$
$$\text{where } \boldsymbol{I_2} = \begin{pmatrix} 1 & 0 \\ 0 & 1 \end{pmatrix} \text{ and } \boldsymbol{R_2}(\theta_\mathrm{e}) = \begin{pmatrix} \cos\theta_\mathrm{e} & \sin\theta_\mathrm{e} \\ -\sin\theta_\mathrm{e} & \cos\theta_\mathrm{e} \end{pmatrix}. \tag{3.1}$$

The equation (3.1) describes a two-dimension second order system. It is transformed in a state space representation with a system matrix $\boldsymbol{A}$ given by (3.2). Due to the non-diagonal elements b and d for $\theta_\mathrm{e} \neq 0$, the horizontal and vertical position controllers are coupled. The four eigenvalues of the system matrix $\boldsymbol{A}$ are the mentioned poles and are determined analytically with (3.3).

$$\boldsymbol{A} = \begin{pmatrix} 0 & 0 & 1 & 0 \\ 0 & 0 & 0 & 1 \\ a & b & c & d \\ -b & a & -d & c \end{pmatrix}, \text{ where } \begin{cases} a = -\dfrac{k_\mathrm{P} \cdot k_\mathrm{ir} \cdot \cos\theta_\mathrm{e} + k_\mathrm{sr}}{m_\mathrm{r}} \\ b = -\dfrac{k_\mathrm{P} \cdot k_\mathrm{ir} \cdot \sin\theta_\mathrm{e}}{m_\mathrm{r}} \\ c = -\dfrac{k_\mathrm{D} \cdot k_\mathrm{ir} \cdot \cos\theta_\mathrm{e}}{m_\mathrm{r}} \\ d = -\dfrac{k_\mathrm{D} \cdot k_\mathrm{ir} \cdot \sin\theta_\mathrm{e}}{m_\mathrm{r}} \end{cases} \tag{3.2}$$

$$\begin{cases} \underline{\lambda}_1 = 0.5\left(c - \mathrm{j}d - \sqrt{4a - \mathrm{j}4b + c^2 - \mathrm{j}2c \cdot d - d^2}\right) \\ \underline{\lambda}_3 = 0.5\left(c + \mathrm{j}d - \sqrt{4a + \mathrm{j}4b + c^2 + \mathrm{j}2c \cdot d - d^2}\right) \\ \underline{\lambda}_2 = 0.5\left(c - \mathrm{j}d + \sqrt{4a - \mathrm{j}4b + c^2 - \mathrm{j}2c \cdot d - d^2}\right) \\ \underline{\lambda}_4 = 0.5\left(c + \mathrm{j}d + \sqrt{4a + \mathrm{j}4b + c^2 + \mathrm{j}2c \cdot d - d^2}\right) \end{cases} \tag{3.3}$$

The positions of the poles that characterise the parallel rigid body mode of the drive, are numerically derived with the parameters from Table 3.1 and (3.3). The calculated root locus in Figure 3.2a depicts the dependency of the poles $\underline{\lambda}_1, ..., \underline{\lambda}_4$ with respect to the misalignment electrical angle θ_e, for a misalignment increasing from 0° to 30°. It can be noticed that the system damping is quickly reduced as the misalignment increases toward 30°. Indeed, two of the four poles $(\underline{\lambda}_2, \underline{\lambda}_4)$ are moving toward the right half plane in the s-domain. In order to increase the robustness against rotor misalignment, the differential coefficient k_D of the PD controller should be increased to reach the critically damped control setting $k_{\mathrm{D,crit}}$. The root locus with critical damping ratio $\zeta = 1$ is represented in Figure 3.2b. In absence of misalignment, the four poles are lying on the negative part of the real axis. The plant remains mathematically stable up to a misalignment of 60°. Whereas the critically damped control displays the highest resilience against sensor misalignment, it is not suited to actual implementation with noisy position signals. This is, because a high differential coefficient k_D magnifies position sensor noise in the controller output, loading the actuators likewise [4]. It should be noted that in actual magnetically levitated drives a control phase margin reserve is necessary to ensure stability so that only small misalignments of typically 10° are possible. This simple example neglects many physical control aspects. For example, the low-pass filter that is present after the PD controller in actual implementations to limit the action of the differentiator at high frequencies, reduces the phase margin. The dynamic behaviour of the current control is also neglected and must be considered when a high stiffness is aimed at.

From these results, it is clear that the use of three digital *Hall*-sensors, com-

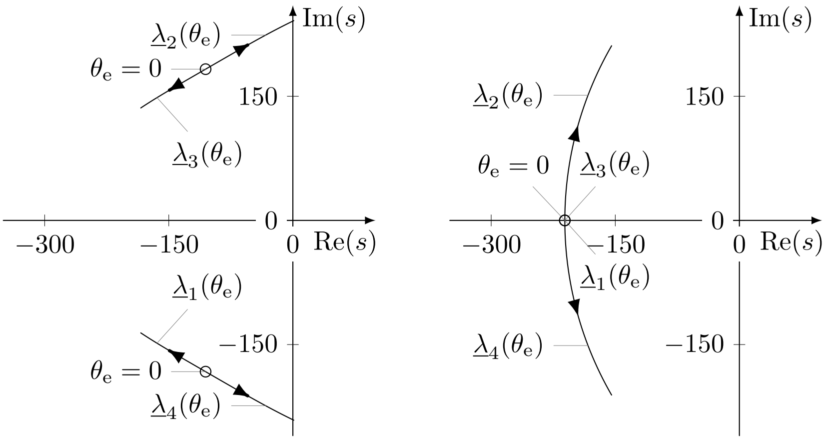

(a) PD controller tuned with half-critical damping $k_\mathrm{D} = 0.5 \cdot k_\mathrm{D,crit}$. The system is unstable as the rotor angle misalignment θ_e reaches 30°.

(b) PD controller tuned with critical damping $k_\mathrm{D,crit}$. The system is much more robust against rotor angle misalignment. It is stable for $\theta_\mathrm{e} < 60°$.

Figure 3.2.: Root loci of a simplified self-bearing levitated drive with the parameters in Table 3.1 as the rotor angle misalignment θ_e, between measured and actual rotor position, increases from 0° to 30°. The poles for zero misalignment $\theta_\mathrm{e} = 0$ are marked with "o".

monly found in low-cost brushless DC motors and giving a rotor angle misalignment of ± 30°, is infeasible in levitated drives with active self-bearings. A more precise analogue position sensor must be provided. Despite its inherently low angle resolution, the digital *Hall*-sensors are preferred at high-speed operation. To understand why it is so, let us consider a magnetically levitated rotor with a principal axis inertia J, operating in steady state at rotational speed $\omega_{\mathrm{r},0}$. The rotor angle θ_r is measured with n digital *Hall*-sensors, giving an absolute resolution of $\Delta R = \pi/n$. As the rotor rotates, the *Hall*-sensors deliver a new position signal every time instant $\Delta T = \pi/(n \cdot \omega_{\mathrm{r},0})$. After a signal transition at the instant t_0, the rotor position angle θ_mea is extrapolated according to (3.4), assuming a constant rotational speed $\omega_\mathrm{r}(t_0)$.

$$\theta_\mathrm{mea}(t) = \theta_\mathrm{mea}(t_0) + \omega_\mathrm{r}(t_0) \cdot (t - t_0) \tag{3.4}$$

The disturbing shaft torque M_{dist}, bounded by $\pm M_{\max}$ and acting during the interval ΔT, leads to a speed variation $\omega_{\mathrm{r}}(t_0+\Delta T)-\omega_{\mathrm{r}}(t_0)$. By integrating the maximum speed deviation during ΔT, the maximal angle error $\theta_{\mathrm{e,max}}$, caused by the disturbance torque $\pm M_{\max}$ before the next position signal transition at $t_0+\Delta T$, is given by (3.5).

$$\theta_{\mathrm{e,max}} = \frac{M_{\max}}{2J}\cdot\left(\frac{\pi}{n\cdot\omega_{\mathrm{r},0}}\right)^2 \tag{3.5}$$

This means that the rotor misalignment θ_{e}, caused by a torque disturbance M_{dist}, using a first order angle extrapolation (3.4), is decreasing with the square of the rotational speed $\omega_{\mathrm{r},0}$ and with the number of *Hall*-sensors n. As the noise from the analogue *Hall*-sensor is largely speed-independent, the resulting rotor misalignment angle from the noise is approximately constant. Therefore, there is a rotational speed, at which the digital *Hall*-sensors, with rotor angle extrapolation, give a more precise rotor position than their analogue counterpart. At this rotational speed, the controller usually changes the position signal from the analogue to the digital *Hall*-sensors. The resolution is still limited by the jitter of the *Hall*-sensor hysteresis and the switching lag. The sensor circuit used for the presented prototypes is shown in Figure A.1.

Some improvement is given by weighting the two signals, depending on the speed and the analogue signal noise. Additionally the motor rotational mechanical equation and the rotor back-EMF equations can be integrated, for example within a *Kalman*-filter, to improve the rotor angle signal. Experimental evaluations revealed that even though the digital *Hall*-sensors lead to a quieter operation at high-speed, rotor levitation of the investigated prototype drives with analogue sensors and proper filtering is manageable with a rotational speed above 30 000 rpm.

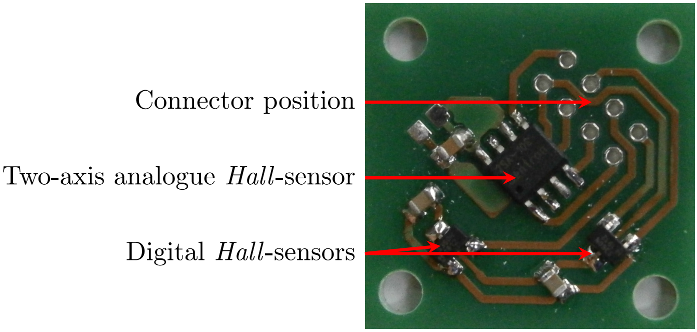

Figure 3.3.: Sensor circuit board with a two-axis analogue *Hall*-sensor (type Melexis MLX91204) and two digital *Hall*-sensors (type Honeywell SS360NT) spatially shifted by 90°. The rotor magnet is diametrically magnetised and rotates on top of the two-axis *Hall*-sensor.

3.2.3. Rotor angle sensor and speed calculation

Indeed, the digital *Hall*-sensors are particularly of interest when the levitated drive operates in speed control. From the cosine and sine of the angle of the analogue position sensor, the rotor angle θ is obtained using the atan2 function defined in (3.6).

$$\operatorname{atan2}(y, x) = \begin{cases} 2 \arctan\left(\dfrac{y}{\sqrt{x^2 + y^2} + x}\right) & \text{if } x > 0 \text{ or } y \neq 0, \\ \pi & \text{if } x < 0 \text{ and } y = 0, \\ \text{undefined} & \text{if } x = 0 \text{ and } y = 0. \end{cases} \tag{3.6}$$

The two real cosine and sine signals of amplitude U_1 contain a small amount of harmonics (with amplitudes U_n with $n > 1$) principally due to misalignment of the rotor magnet and the stator sensor circuit and due to imperfections in the rotor magnet magnetization pattern. These harmonics pass through the non-linear function atan2, leading to distortion of the sawtooth position signal. The amplitude of the angle distortion signal is small, as it is for the resulting rotor misalignment angle θ_e. As the rotational speed $\omega_{\mathrm{r},0}$ increases, the positions of the resulting harmonics in the frequency spectrum are shifted toward higher frequencies. The rotational speed ω_0 is calculated by differentiation of the rotor position angle signal θ. As a consequence, the rotor angle signal harmonics are magnified in the speed signal with increasing speed at a rate of 20 dB/decade. The speed controller outputs correspondingly high torque reference values to compensate the harmonics in the measured rotational speed signal. Instead, when using a single transition edge of one digital *Hall*-sensor, this distortion is inherently absent so that the torque reference signal keeps smooth at high-speed. The mentioned lack of position resolution at low rotational speed with digital *Hall*-sensors is also true for the speed resolution. Therefore analogue signals are preferred at low speed and digital signals at high speed operations. For speed calculation, one digital *Hall*-sensor is sufficient. The analogue-to-digital converter, that samples the analogue *Hall*-sensors, can be of low resolution, since the harmonics (with amplitudes U_n, $n > 1$) in the sinusoidal position angle signals (with a fundamental amplitude U_1) are the limiting factors for the accuracy of measured signal. A -40 dB total harmonic distortion $(20 \log(\frac{\sqrt{U_2^2+U_3^2+\ldots+U_\mathrm{n}^2}}{U_1}))$ is realistic for a good position signal. For this, a 10-bit resolution is largely sufficient.

3.3. Rotor displacement sensors

3.3.1. Displacement sensors for contact-free position measurement

Displacement transducers for the levitated body can be realised out of almost any physical property. A non-exhaustive list of contactless displacement-sensors, commonly found in magnetically levitated drive, encompass:

- Optical sensors, based on light intensity (photonic sensors)
- Analogue *Hall*-effect sensors

- Capacitive sensors, which rely on the capacity change due to the proximity of a conductive material
- Inductive respectively eddy-current based sensors, that rely on the magnetic respectively conductive properties of the rotor surface

Whereas the optical sensors can reach very high immunity against electromagnetic interferences, since the electrical machines are not polluting in the frequency spectrum of light, the diffraction of light limits the achievable resolution [4]. Therefore, these sensors are mainly found in levitated demonstrators. They are also very sensitive to environment contaminants and to the optical quality of the target surface [11]. The analogue *Hall*-effect sensors are sometimes used as position sensors in low-cost applications where high linearity and resolution is not critical. In magnetic bearings however, they are very interesting when used as magnetic flux sensors in the air gap. It enables to implement air gap flux control. Their integration in small air gaps is still a current field of research [12]. While the sensor miniaturisation, which is necessary to fit into the drive, is challenging (a sensor thickness below 0.25 mm is required), the disturbances introduced by the inverter feeding are limiting factors. In contrast, the capacitive, inductive and eddy-current sensors are very common. They defer in terms of measuring range, linearity, sensitivity, resolution and frequency bandwidth.

The capacitive sensors can reach a very high resolution together with wide measuring ranges (such as a subnanometre resolution with a submillimetre measurement range). The position signal is obtained by evaluating the capacity formed between the sensor head and the conductive rotor surface. This evaluation is commonly done at a fixed carrier frequency, with a modulation-demodulation scheme. The change of capacitance due to rotor displacement is non-linear by nature, but the sensor's capacitance-displacement characteristic is evaluated and stored in a look-up table. Since the sensor generates an electrical field between the sensor and the levitated target (the rotor), the rotor cannot be electrically isolated. This is in contradiction with contact-free levitation. In order to overcome this issue, capacitive sensor manufacturers recommend to use two sensor-heads fed in phase opposition. In this case, the capacitive current flows from one sensor head, through the shaft of the rotor and back to the second sensor head. This current coupling is responsible for a differential-mode interference between the two position signals that elevates significantly the noise floor. The immunity against rotor electrical potential variations is weak. As a consequence, the zero-sequence voltage, injected by the inverter and transferred capacitively onto the rotor, significantly disturbs the position signals. Additionally, the sensors are calibrated for a given gap dielectric (generally this is clean air). The presence of dust or oil on the measuring surface modifies the dielectric parameter of the capacitance significantly, so that a good sealing of the machine is mandatory to ensure a high sensor precision. Since the levitated rotor can move up to a fraction of millimetre, the sealing is commonly realised with air purge systems.

The inductive sensors are based on the change of reluctance of a magnetic path, due to the change of position of a ferromagnetic material as levitated body. In order to evaluate its reluctance, an alternative current magnetises the sensor via an excitation coil, and the induced voltage on a second coil (pick-up coil) is measured to obtain the magnetic flux. An alternative evaluation consists in measuring the impedance of the excitation coil. The signal dynamic range (that is the variation of impedance) related to the signal amplitude (that is the impedance at zero-position of the levitated body) is usually small, and the characteristic is non-linear, so that the resolution of such sensors is limited [5]. Several signal conversion principles are commonly used to increase the signal dynamic range, for example, with resonant circuits, or to improve the linearity, for example with a balanced differential configuration. Unfortunately, all ferromagnetic materials (iron, nickel and cobalt) are also conducting materials where eddy-currents are induced at the surface. At increasing frequency, the eddy-currents, caused at the measurement surface, act by their opposing self-field as an equivalent diamagnetic material whose influence predominates in the MHz range. This is the reason, why inductive sensors are excited at rather low frequencies (typically below 200 kHz).

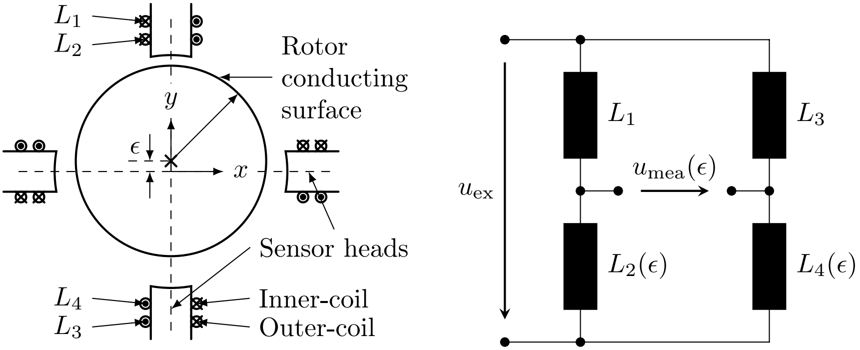

(a) Disposition of the differential eddy-current sensors according to patent [13]. Here, the rotor eccentricity is ϵ in the positive y-direction.

(b) Connection of the sensor coils as a *Wheatstone* bridge for the vertical axis (the same holds also for the horizontal axis).

Figure 3.4.: The sensor heads at the top and bottom (resp. left and right) are responsible for the measurement of the rotor displacement in vertical direction y (resp. horizontal direction x). The coils L_1 and L_2 belong to the sensor head at the top, and the two coils L_3 and L_4 belong to the opposite one at the bottom. The coils L_2 and L_4 are the inner-coils that experience the change of impedance with rotor displacement ϵ. The reference coils L_1 and L_3 are the outer-coils (see page 42).

Eddy-current based sensors are also based on the change of reluctance, but of a diamagnetic path. A stator coil, excited by an AC current, generates a pulsating magnetic field on the levitated rotor conducting surface. Eddy-currents are induced at the rotor surface, which excite an opposing magnetic field, according to *Lenz*'s law. The closer the rotor surface is positioned to the sensor, the higher the eddy-current amplitude on the rotor surface. The resulting reduction of the air gap field for a given impressed AC current in the excitation coil is equivalent to an increase of the reluctance of the field path. This increased reluctance is also manifested in the stator excitation coil inductance, as its inductance is inversely proportional to the reluctance. Hence, the stator coil inductance is evaluated to obtain the position information. Again the signal dynamic measurement range of such a sensor is limited (the impedance changes only by a few percent) and is usually improved, using differential topologies (e.g. with a *Wheatstone* bridge as in Figure 3.4b). In Figure 3.4a the excitation coils are split into two half coils (outer-coil and inner-coil) for the use of the circuit Figure 3.4b. Several patented realisations exist, that differ in terms of integration, sensitivity and noise immunity. Both inductive sensors and eddy-current sensors are insensitive to non-conductive and non-magnetic pollution on the measurement surface. Therefore, they are generally preferred for magnetic levitation.

3.3.2. Employed eddy-current sensors and limitations

As the rotor is usually made of ferromagnetic material, the field of the eddy-current sensor must be focused on a particular rotor section where only non-magnetic conductive materials are present. An aluminium ring is usually shrink-fitted on the rotor for this purpose. In order to influence the penetration of the field into the conducting target, the frequency of the injected signal can be modified. The choice of this frequency is not simple, since many limiting factors are to be considered: The excitation magnetic field from the sensor coil should not reach the inner rotor ferromagnetic part under the Aluminium ring in order to prevent the high iron relative permeability to counteract the change of inductance due to eddy-currents. In order to fulfil this condition, the penetration depth d_{e}, as defined in (3.7), should be chosen at least three time smaller than the thickness of the non-magnetic conducting measurement ring. For example, the use of an aluminium rotor ring with a thickness $h = 1$ mm limits the minimum excitation frequency f_{e} to about 60 kHz. With an electrical conductivity of $\kappa_{\mathrm{Alu}} = 34$ MS/m, the penetration depth d_{e} is lower than 1/3 for f_{e} greater than 60 kHz.

$$d_{\mathrm{e}} = \sqrt{\frac{2}{\omega_{\mathrm{e}} \cdot \mu_0 \cdot \kappa_{\mathrm{Alu}}}} \tag{3.7}$$

The sensor sensitivity is also influenced by the excitation frequency f_{e}. According to *Faraday*'s law of induction, the impressed field on the rotor surface induces a voltage u_{i} whose amplitude is proportional to the frequency f_{e}. This voltage u_{i} is responsible for the circulation of the eddy-currents i_{Ft}

at the rotor surface. The higher the frequency f_e, the bigger the amplitude $\hat{I}_\mathrm{Ft}$ of surface eddy-currents, and the bigger the impedance change of the excitation coil of the sensor. In other words, the higher the frequency f_e, the closer the target surface "appears" to the sensor head. As a consequence, the sensitivity of the sensor increases with the frequency f_e, so that higher frequencies f_e are desirable. The sensor dimensions must be considered as well. The sensing surface speed is $\omega_\mathrm{r} \cdot r_\mathrm{surf}$ where r_surf is the radius of the sensing surface, and ω_r is the rotational speed. The sensor head generates a pulsating field on the sensing surface with the angular frequency ω_e. At the rotor surface, the magnetic flux density vector is mainly composed of a radial component, as can be seen in Figure 3.5a. The variation of the radial flux density distribution $B_\mathrm{r}(x,t)$ over time of one sensor head L_1, L_2 (see Figure 3.4a) at the stationary rotor surface ($\omega_\mathrm{r} = 0$) is displayed in Figure 3.5b. It is composed of two main lobes with maxima that are distant by approximately the sensor diameter $d \approx d_\mathrm{head}$. In order that the moving rotor surface ($\omega_\mathrm{r} > 0$) does not influence significantly the eddy-currents formed at the rotor surface, the time it needs to travel between the two maxima $d_\mathrm{head}/(\omega_\mathrm{r} \cdot r_\mathrm{surf})$ should be much longer than the time π/ω_e where the flux density distribution reverses. This condition leads to the frequency condition (3.8) and sets an excitation frequency minimum $f_\mathrm{e,min}$ depending on the rotor radius r_surf and sensor diameter d_head. If not fulfilled, the sensitivity of the sensor drops. Thus, it reduces the feedback of the position controller, leading to a potential levitation instability. In the literature, this effect is referred to as "eddy-current drag" [11]. The sensor diameter d_head can not be chosen arbitrarily big because of two reasons:

- The sensors are usually calibrated for a flat target surface ($r_\mathrm{surf} \to \infty$). If the sensor diameter is bigger than one tenth of the rotor diameter ($d_\mathrm{head} > 0.2 \cdot r_\mathrm{surf}$), the target curvature reduces significantly the sensor sensitivity [11].

- By increasing the sensor diameter d_head, the leakage fields of neighbouring sensors become more disturbing (see Figure 3.4a). It results in crosstalk between the two position signals.

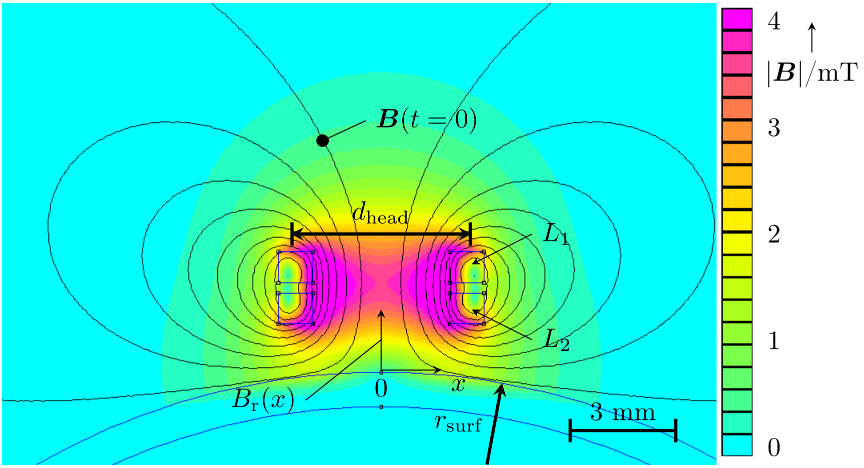

(a) FEMM simulation of the magnetic flux density absolute value, resulting from the excitation coil of one sensor head (see Figure 3.4a) (L_1, L_2) excited at $f_{\mathrm{e}} = 200$ kHz on an aluminium rotor ring as target. The opposing self-field of the eddy-currents in the aluminium target squeeze the sensor magnetic field out of the measurement surface.

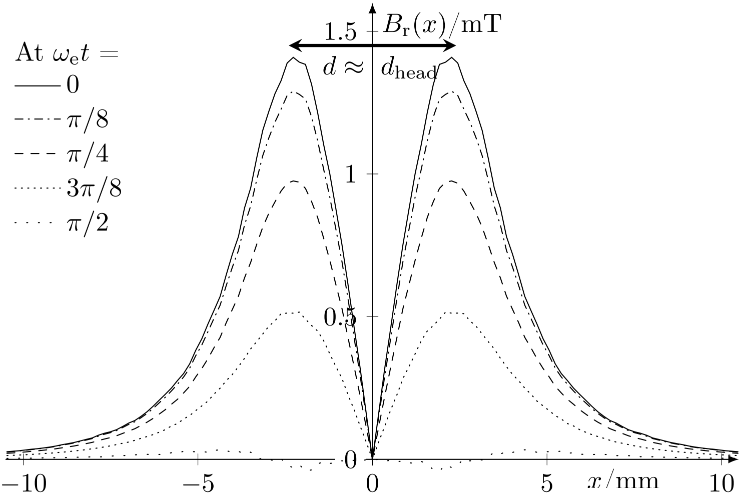

(b) Evaluation of the real part of the radial magnetic flux density B_{r} at the rotor surface at $\omega_{\mathrm{r}} = 0$ for different instants from $t = 0$ to $t = \pi/(2\omega_{\mathrm{e}})$.

Figure 3.5.: The calculated magnetic flux density at the rotor surface r_{surf} is mainly composed of a radial component B_{r}, pulsating with excitation angular frequency ω_{e}.

$$\omega_{\mathrm{e}} \gg \omega_{\mathrm{r}} \cdot \pi \cdot \frac{r_{\mathrm{surf}}}{d_{\mathrm{head}}} \tag{3.8}$$

At a nominal rotational speed $\omega_{\mathrm{r}}/(2\pi) = n_{\mathrm{N}} = 1\ 000\ \mathrm{s}^{-1}$ and for a sensor-to-rotor diameter ratio of $d_{\mathrm{head}}/(2 \cdot r_{\mathrm{surf}}) = 0.1$, the condition (3.8) gives $f_{\mathrm{e}} \gg 15.7$ kHz. A good choice for f_{e} would be at least 10 times of 15.7 kHz, hence 160 kHz. Sensor manufacturers recommend much higher ratios $\omega_{\mathrm{e}}/\omega_{\mathrm{r}}$ to get small sensitivity variations with varying rotor speed. Those ratios can be difficult to be fulfilled in the actual high speed drive. The recommendations [11] for this particular example lead to $f_{\mathrm{e}} > 1.6$ MHz, while their sensor products are operating below 1 MHz. The excitation frequency f_{e} cannot be chosen arbitrarily high, either, for several reasons. Despite the difficulty to realise sensors with high frequency excitation, several physical aspects are limiting the highest excitation frequency $f_{\mathrm{e,max}}$ as well. One of the limits is set by the achievable minimum rotor surface roughness. As previously mentioned, the penetration depth characterises the thickness of the flux path below the rotor surface. According to (3.7), the penetration depth d_{e} decreases with increasing frequency f_{e}. As the eddy-currents flow only in a depth of around 3 d_{e}, any groove on the rotor surface whose dimension is in the order of the penetration depth d_{e}, perturbs significantly the sensor impedance and consequently the measured position, when the rotor rotates. This phenomenon is very well-known in the field of mechanical engineering, where non-destructive surface quality control of conducting materials are making extensive use of this effect. In this application, the signal quality degrades with increasing frequency due to the decreasing value d_{e}. The limit of f_{e} depends on the achievable minimum roughness during rotor surface polishing and the metal quality (such as crystallographic defects), used as target surface. Though, excitation frequencies of several MHz are possible [5] with acceptable sensor signal quality.

A second limitation is set by the cable, which is used for the signal transmission between the sensor and the signal processing unit. The parasitic capacitance of the cable is loading the measurement line with a capacitive current component. As the frequency increases, the sensor impedance increases while the cable parasitic impedance decreases. At high frequency, hence the position signal nearly vanishes. This aspect is particularly limiting when a long cable of several meters and frequencies f_e of several MHz are used. Impedance matching or pre-amplification with instrumentation amplifiers of the sensor signal mitigate the problem. In order to limit the higher frequency components of the maximal signal and the subsequent voltage reflection problems on the cable terminals, a sinus sensor excitation should be preferred to square wave excitation when using a long cable.

In the prototypes presented later, a particular differential eddy-current sensor from the company *LTI-Motion* is used. The sensor heads are composed of an inner-coil (measurement coil, e.g. L_2) and an outer-coil (reference coil, e.g. L_1) as shown in Figure 3.4a. The inner-coil inductance changes with the rotor displacement due to the eddy-current self-field while the outer-coil inductance, more distant from the rotor surface, is almost constant. The two coils are connected in series as displayed in Figure 3.4b to form an variable inductive divider. They are fed by an alternative voltage u_ex. The two inductive dividers of two opposite sensor heads (e.g. L_1/L_2 and L_3/L_4) are connected in parallel to form a *Wheatstone* bridge (see Figure 3.4b). This configuration improves the linearity of the sensor characteristic and reduces the sensor signal drift with temperature [13]. When the rotor is equidistant to both opposing sensor heads (e.g. L_1/L_2 and L_3/L_4), the two inductive dividers have the same voltage ratio so that the differential voltage u_mea in Figure 3.4b is zero. When the rotor is displaced towards L_4, the ratio $L_2/(L_1{+}L_2)$ increases whereas the ratio $L_4/(L_3{+}L_4)$ decreases. The differential voltage u_mea is in phase with the AC excitation voltage u_ex, and its amplitude is proportional to the rotor displacement. The proportionality factor must be obtained experimentally. Before setting-up the test-bench, the appropriate excitation frequency f_e was investigated experimentally. The highest sensitivity was obtained for frequencies between $f_\mathrm{e} = 200$ kHz and 400 kHz.

3.3.3. Rotor displacement signal processing

The eddy-current position sensors deliver AC pulsating voltage signals u_{mea} according to the AC excitation voltage u_{ex}. From their amplitudes $\hat{U}_{\mathrm{mea}}$, $\hat{U}_{\mathrm{ex}}$ the position is obtained. There are many different types of signal processing algorithms, depending on the sensor type and sensor configuration. Since the presented prototypes exclusively use the differential eddy-current sensors from the company *LTI-Motion*, a dedicated signal processing algorithm is presented here.

The measured position voltage signal u_{mea} is a periodic AC signal with excitation frequency f_{ex}, and whose amplitude $\hat{U}_{\mathrm{mea}}$ is proportional to the rotor displacement from centre position. The position signal is obtained as the following:

- The coil excitation voltage signal u_{ex} and the position voltage signal u_{mea} are simultaneously sampled at the sampling frequency f_{samp}. Since the Shannon-Nyquist sampling criterion requires a relatively high sampling frequency ($f_{\mathrm{samp}} > 2f_{\mathrm{ex}}$) and as fast analogue-to-digital converters with high resolutions are expensive, the under-sampling technique is used ($f_{\mathrm{samp}} < 2f_{\mathrm{ex}}$).

- Each sampled signal passes through two orthogonal finite impulse bandpass filters that are tuned at the target frequency $f_{\mathrm{dem}} = f_{\mathrm{samp}}/N$, where the even number N sets the size of the demodulator filter. The coefficients of the digital filters are given by (3.9). In this fashion, two vector components are created out of each signal.

- The two components are concatenated in the vectors $\boldsymbol{u}_{\mathbf{ex}}[k]$ and $\boldsymbol{u}_{\mathbf{mea}}[k]$ respectively. Finally the vector $\boldsymbol{u}_{\mathbf{mea}}[k]$ is projected on the excitation vector $\boldsymbol{u}_{\mathbf{ex}}[k]$ using (3.10) to obtain a signal $x[k]$ proportional to the displacement from the sensor center position.

- The signal $x[k]$ is low-pass filtered to reduce the undesired high frequency noise.

$$\begin{aligned} h_{\cos,\mathrm{N}}[k] &= \frac{2}{N} \cdot \cos(\frac{\pi \cdot (2k+1)}{N} + \frac{\pi}{4}) \quad k = 1...N \\ h_{\sin,\mathrm{N}}[k] &= \frac{2}{N} \cdot \sin(\frac{\pi \cdot (2k+1)}{N} + \frac{\pi}{4}) \quad k = 1...N \end{aligned} \tag{3.9}$$

$$\begin{aligned} x[k] =& (h_{\cos,\mathrm{N}} * u_{\mathrm{ex}})[k] \cdot (h_{\cos,\mathrm{N}} * u_{\mathrm{mea}})[k] + \\ & (h_{\sin,\mathrm{N}} * u_{\mathrm{ex}})[k] \cdot (h_{\sin,\mathrm{N}} * u_{\mathrm{mea}})[k] \end{aligned} \tag{3.10}$$

The analogue-to-digital converters that sample the position signals should be of high resolution for two reasons. First the signals can reach high amplitudes when the shaft lies in the safety bearings, but they are small during operation (e.g. at ± 10 µm orbits in operation for a measurement range of ± 250 µm). Consequently, the most significant bits of the digitised signal are always constant during normal operation. The A/D-converter measurement range is inefficiently utilised. Secondly the damping part of the position controller (e.g. k_{D} in a PID-controller) magnifies the noise of the position signal in the current reference. Therefore, a low resolution position signal leads to increased actuator currents and consequently to audible noise due to magnetic forces and additional eddy-current losses during rotor levitation. For a stiff tuned controller, a 16-bit resolution with at least 80 dB signal-to-noise ratio is recommended. Softer (i.e. less stiff) controllers are realisable with a good signal quality with 12-bit resolution.

4. Classical self-bearing configuration

4.1. Motor description

The simplest active self-bearing motor with six DOF control consists of two motor parts that generate torque and two radial force components each on one side of the shaft, and an axial magnetic bearing, that generates an axial force. The disposition of the active part is given in Figure 4.1. The rotor (BM in Figure 4.1) is similar to the one of a high-speed PMSM. The surface-mounted magnets are glued onto the rotor and then pressed on the shaft by a carbon fibre bandage that ensures positive pressure between magnet and rotor iron. Additional details on the design of such a bandage are given in [14]. In the stator slots, two isolated distributed windings with different numbers of pole pairs are inserted. Despite their higher manufacturing complexity, distributed windings are preferred to tooth-wound windings in high-speed drives due to their lower iron losses, induced by field harmonics. The drive winding must have the same number of pole pairs p_1 as the rotor p_0 to produce torque while the levitation winding must have a pole pair number p_2 that differs from the rotor pole pair number by one ($p_2 = p_0 \pm 1$) to produce lateral forces.

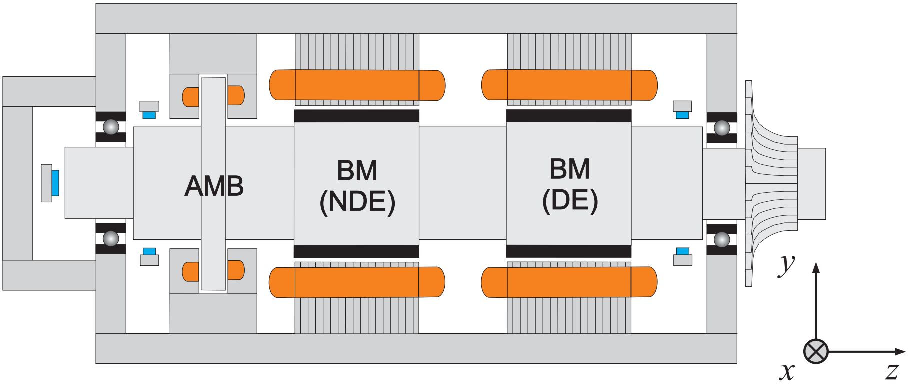

Figure 4.1.: Active self-bearing motor configuration for six-DOF control. The torque and radial forces are generated by the two self-bearing motors (BM). The axial force is generated by the thrust active magnetic bearing (AMB). (Orange: stator winding, black: rotor magnets).

4.2. Magnetic equations

The axial cross-section of a self-bearing motor with two isolated stator windings is displayed in Figure 4.2. In contrast to asynchronous motors, the magnetic equivalent air gap width δ_{eq}, formed by the magnet height h_{M}, the non-conductive and non-magnetic bandage thickness h_{b}, the mechanical air gap width δ_{m} and, to a certain extent, by the slot opening s_{o} [15], is not negligible compared to the rotor iron outer radius r_{ro}. Consequently, the influence of the magnetic flux density distribution $\boldsymbol{B}(r, \theta)$ with respect to its curvature in the air gap must be taken into consideration when calculating the motor characteristic parameters. Fortunately, the analytical determination of the magnetic flux densities in such motors is extensively documented in the literature for almost every PMSM geometry, with different degrees of complexity. Since the amplitudes of the magnetic flux densities, encountered in high-speed active self-bearing machines, are usually below the saturation level of magnetic steels (in order to avoid excessive iron losses), the iron saturation may be neglected in the analytical calculation. The analytically obtained results match well the ones obtained with numerical

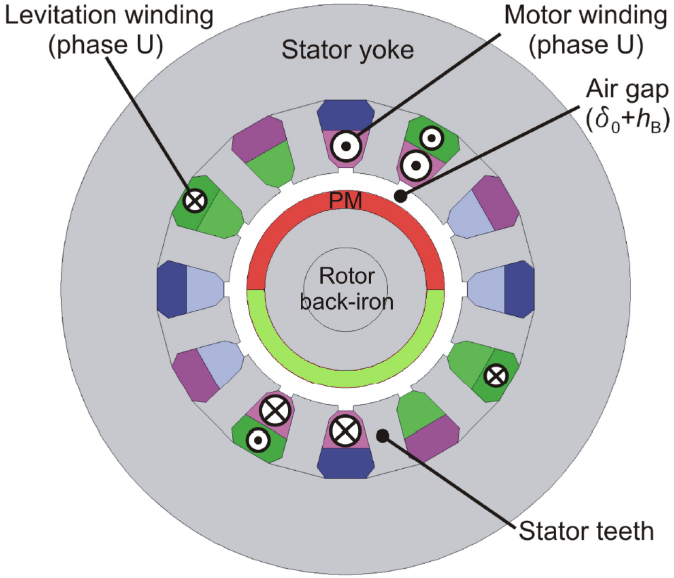

Figure 4.2.: Cross section of an active self-bearing motor with two isolated windings [14]. The drive and the levitation windings are inserted in the same stator slots. The rotor permanent magnet (PM) is surface-mounted on the rotor. A three-phase two-pole motor with $q = 2$ slots per pole and phase is shown. The air gap in the Figure is meaning here a sum of air gap of non-magnetic bandage thickness h_B and mechanical air gap width δ_0.

calculations with finite element models that consider a possibly occurring iron saturation. In this chapter, several analytical calculations are derived in order to determine the main design parameters of the active self-bearing motor. Among others, the force-current coefficient, the force-displacement coefficient, the torque-current coefficient and the induced voltage will be calculated analytically. The calculation is done with the following assumptions:

- The magnetic scalar potential ψ, defined in (4.1), is used to calculate the magnetic flux density distributions generated by the stator equivalent current loadings and by the rotor permanent magnets in the air gap region.

- The problem is derived in two dimensions, in a cylindrical coordinate system under quasi-static condition so that the border effects in axial direction are disregarded.
- The iron parts are considered magnetically linear. As a consequence, field superposition is allowed.

The air gap region is free of any current density since the equivalent stator current loadings are located at the stator bore. Therefore, the problem can be solved analytically with only the magnetic scalar potential ψ as no eddy currents are considered. The calculation can be also done with the magnetic vector potential $\boldsymbol{A}$ (4.1), giving in this case exactly the same analytical solutions.

$$\boldsymbol{H} = -\nabla\psi \text{ and } \boldsymbol{B} = \nabla \times \boldsymbol{A} \tag{4.1}$$

In order to derive the induced voltage in the stator winding and the force-displacement coefficient, the magnetic field components due to the rotor permanent magnets (subscript 0) are calculated a) at rotor concentric position and b) for a small rotor eccentricity ϵ. First the homogeneous and particular solutions of *Poisson*'s equation are determined. Then the boundary value problem is solved. In a second step, the magnetic field components excited by the driving (subscript 1) and levitation windings (subscript 2) are derived, again at a) rotor concentric position and b) for a small rotor eccentricity ϵ. The force-current coefficients and torque-current coefficients are then calculated by integration of the *Maxwell* stress components on a closed surface around the rotor, placed between the stator and rotor, considering the superposition of the rotor permanent magnet magnetic field, the stator levitation field and the stator driving field. The notation adopted for the coefficients $x^k_{i,j}$ that satisfy the boundary value problems, are defined as follows:

- a and b are the coefficients that satisfy the field boundary value problem due to rotor permanent magnets,

- c and d are the coefficients that satisfy the field boundary value problem due to the stator current loading A.

The subscripts i, j and k are defined as follows:

- i is the pole pair number of the solution,
- j is the region where the coefficient x is defined. It takes the value 1, 2, 3 and 4 for the rotor region, the rotor permanent magnet region, the air gap region and the stator iron region, respectively. The four regions 1 to 4 are defined in Figure 4.3.
- When the magnetic scalar potential ψ is calculated for an eccentric rotor, the solution is approximated with its *Taylor* expansion. In this case, the superscript k designates the order of the expansion term. Otherwise, when the eccentricity is zero, it is omitted.

For example, the coefficient $a^0_{i,j}$ (or $a_{i,j}$) characterises the rotor field solution with i pole pairs in the region j at rotor concentric position, while $a^1_{i,j}$ characterises the first order term of the rotor field *Taylor* expansion [18], when the rotor is not concentric to the stator.

4.2.1. Magnetic fields at no-load and without rotor eccentricity

The calculation of the air gap field follows the approach proposed in [16]. With this method, many permanent magnet magnetisation patterns can be considered. However, in order to limit the scope of this chapter, only the simplified two-pole motor geometry displayed in Figure 4.3 is treated. It is composed of a two-pole diametrically magnetised rotor magnet (in y-direction) with 100% pole coverage ratio. This model enables to obtain the model parameters of the actual prototype presented in Chapter 6. In order to adopt the calculation for another motor geometry, the detailed approach can be followed, with the help of the reference [16]. Some additional advice is given at the end of the chapter to facilitate the calculation. The magnetic

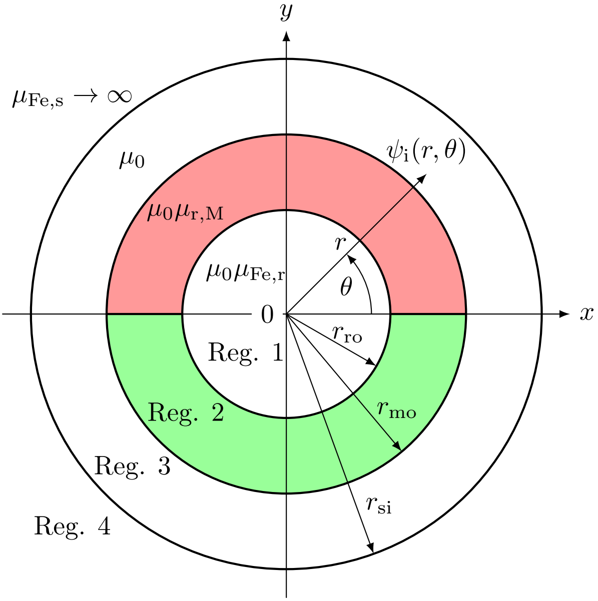

Figure 4.3.: Definition of the geometry with relevant machine parameters for the calculation of the 2D magnetic rotor field and the derivation of the no-load voltage.

flux densities are calculated in three regions. The region 1 constitutes the rotor iron part and has a finite relative permeability $\mu_{\text{Fe,r}}$. The region is delimited by its outer radius r_{ro}. The rotor is considered of finite permeability so that the magnetic flux density in this region can be defined as a function of the magnetic scalar potential ψ. The same calculation can be derived with infinite rotor permeability, however then the magnetic vector potential A must be used instead. The region 2, consisting of the rotor permanent magnet, has a permeability of $\mu_0\mu_{\text{r,M}}$ and a magnetisation vector $\boldsymbol{M}(r,\theta)$. It is delimited between the two radius values r_{ro} and r_{mo}. The region 3 encompasses the mechanical air gap and the non-magnetic, non-conductive carbon fibre bandage. This region has a permeability of μ_0. This region is delimited between the two radius values r_{mo} and r_{si}. The calculation of the fields in the region 4, consisting of the slotless stator with infinite permeability $\mu_{\text{Fe,s}} = \infty$, is not necessary, but the boundary conditions at the inner edge of region 4 r_{si} must be considered. The calculation is done with cylindrical coordinates, so that each point is described by its coordinates (r, θ). A cross section of the model, with the related parameters, is given in Figure 4.3. The influence of the stator slot opening s_{Q} on the field distribution is not considered in this calculation. If needed, it can be considered with the use of conformal mapping to transform the stator slots in a slotless configuration. The increased equivalent air gap width δ'_{eq} due to the slot openings s_{Q}, which has to be magnetised by the two stator fundamental fields, can be approximated with the help of *Carter*'s coefficient k_{C} [15]. Considering the relative recoil permeability of the rare earth permanent magnet $\mu_{\mathrm{r,M}} \approx 1$ (e.g. NdFeB or $\mathrm{Sm_2Co_{17}}$), the increase of the equivalent air gap width can be obtained with (4.2) where τ_{Q} is the slot pitch. However this increase is negligible in the considered machines since the magnetic air gap width δ_{eq} is considerably bigger than the slot opening s_{Q} of the stator semi-closed slots.

$$\frac{\delta'_{\mathrm{eq}}}{\delta_{\mathrm{eq}}} = k_{\mathrm{C}} = \frac{\tau_{\mathrm{Q}}}{\tau_{\mathrm{Q}} - \zeta(h) \cdot \delta_{\mathrm{eq}}} \text{ with } \zeta(h) \approx \frac{h^2}{h+5} \text{ and } h = \frac{s_{\mathrm{Q}}}{\delta_{\mathrm{eq}}} \tag{4.2}$$

In the region 1 and 3, the magnetic scalar potential satisfies *Laplace*'s equation (4.3), and in region 2 it satisfies *Poisson*'s equation (4.4).

$$\Delta\psi = 0 \Rightarrow \frac{\partial^2 \psi_i}{\partial r^2} + \frac{1}{r}\frac{\partial \psi_i}{\partial r} + \frac{1}{r^2}\frac{\partial^2 \psi_i}{\partial \theta^2} = 0, \text{ with } i \in \{1,3\} \tag{4.3}$$

$$\Delta\psi = \frac{1}{\mu_{\mathrm{r,M}}}\nabla\cdot\boldsymbol{M} \Rightarrow \frac{\partial^2 \psi_2}{\partial r^2} + \frac{1}{r}\frac{\partial \psi_2}{\partial r} + \frac{1}{r^2}\frac{\partial^2 \psi_2}{\partial \theta^2} = \frac{1}{\mu_{\mathrm{r,M}}}\cdot\left(\frac{M_{\mathrm{r}}}{r} + \frac{\partial M_{\mathrm{r}}}{\partial r} + \frac{1}{r}\frac{\partial M_{\theta}}{\partial \theta}\right) \tag{4.4}$$

The first step of the method proposed in [16] consists in the decomposition of the scalar potential and of the radial and tangential magnetisation distributions M_{r} and M_{θ} into *Fourier* series [18]. The magnet has two poles and is diametrically magnetised with a 100% coverage ratio so that the magnetisation distribution follows (4.5) where B_{rem} is the remanence and θ_0 the orientation of the magnetisation with respect to the stator coordinate frame. The magnetic flux density distribution of this particular geometry is simple to calculate with the decomposition in *Fourier* series since it displays only a fundamental.

$$M_{\mathrm{r}}(r,\theta) = \frac{B_{\mathrm{rem}}}{\mu_0} \cdot \cos(\theta - \theta_0), \text{ and } M_{\Theta}(r,\theta) = -\frac{B_{\mathrm{rem}}}{\mu_0} \cdot \sin(\theta - \theta_0) \quad (4.5)$$

The number of functions that satisfy *Laplace*'s equation [18] (4.3) is infinite. Some of them do not fulfil the field continuity condition such as $f(r,\theta) = \theta$, or do not satisfy *Gauss*'s law [18] such as $f(r,\theta) = \ln(r)$. The solutions of interest can be arranged in sets as (4.6) where n is the pole pair number of the field described by the set.

$$\begin{cases} f_{1,n}(r,\theta) = r^n \cdot \cos(n\theta) & f_{2,n}(r,\theta) = r^{-n} \cdot \cos(n\theta) \\ f_{3,n}(r,\theta) = r^n \cdot \sin(n\theta) & f_{4,n}(r,\theta) = r^{-n} \cdot \sin(n\theta) \end{cases} \quad (4.6)$$

In order to reduce the number of coefficients, that are necessary to solve the boundary value problem, the calculation is done in the frame oriented in the direction of the rotor magnetisation θ_0. Doing so, the solutions become orthogonal to $f_{3,n}(r,\theta)$ and $f_{4,n}(r,\theta)$, simplifying the expressions to a great extent. Taking into account the previous considerations, the solution in the regions 1 and 3 and the solution in region 2 can be factorised in the form (4.7) and (4.8), respectively, where the constants $a_{n,i}$ and $b_{n,i}$ must satisfy the magnetic field boundary conditions at the boundaries of region i, and where the coefficients $k_n(r)$ are part of the particular solution of *Poisson*'s equation [18] (4.4). They are given by (4.9) [16].

$$\psi_i(r,\theta) = \sum_{n=1}^{\infty} (a_{n,i} r^n + b_{n,i} r^{-n}) \cdot \cos(n\theta - \theta_0), \text{ with } i \in \{1,3\} \quad (4.7)$$

$$\psi_2(r,\theta) = \sum_{n=1}^{\infty} \left(a_{n,2} r^n + b_{n,2} r^{-n} + \frac{k_n(r)}{\mu_{\mathrm{r,M}}} r \right) \cdot \cos(n\theta - \theta_0) \quad (4.8)$$

$$k_1(r) = \frac{M_{\mathrm{r},1} + M_{\Theta,1}}{2} \cdot \ln(r) \text{ and } k_n(r) = \frac{n \cdot M_{\mathrm{r,n}} + M_{\Theta,\mathrm{n}}}{1 - n^2} \text{ for } n > 1 \quad (4.9)$$

In the considered problem, the right hand side of the equation (4.4) in the magnet region is zero. Indeed the divergence $\nabla \cdot \boldsymbol{M}$ is zero so that $k_i(r) = 0$ for all positive integers i. As a consequence, the problem is pathological and its solution can not be factorised in the forms commonly found in the literature [16], [14], [17]. Still the solution of the boundary value problem $\psi(r, \theta)$, is not zero since its coefficients $\{a_{1,1},\ b_{1,1},\ a_{1,2},\ b_{1,2},\ a_{1,3},\ b_{1,3}\}$ in (4.7) and (4.8) must fulfil the non-zero boundary conditions (4.10). The boundary conditions are the following:

- At the center of the rotor, the amplitude of the magnetic flux density $\boldsymbol{B}$ is finite.
- The tangential component of the magnetic field strength H_θ is, in absence of any surface current at the boundary between two neighbouring regions, identical between the two regions.
- The radial component of the magnetic flux density B_r is identical at the boundary between two neighbouring regions.

These conditions are written mathematically as (4.10).

$$\begin{cases} \forall \theta \in [0, 2\pi]\,, \lim\limits_{r \to 0} \|\boldsymbol{B}(r, \theta)\|_2 < \infty \\ \forall i \in \{1, 2, 3\}, \forall \theta \in [0, 2\pi]\,, H_{\theta,i}(\theta, r = r_{i,i+1}) = H_{\theta,i+1}(\theta, r = r_{i,i+1}) \\ \forall i \in \{1, 2, 3\}, \forall \theta \in [0, 2\pi]\,, B_{\mathrm{r},i}(\theta, r = r_{i,i+1}) = B_{\mathrm{r},i+1}(\theta, r = r_{i,i+1}) \end{cases} \tag{4.10}$$

In order to translate (4.10) into a system of equations for the magnetic scalar potential $\psi(r, \theta)$, the tangential component of the magnetic field strength $H_\theta(r, \theta)$ and the radial component of the magnetic flux density $B_\mathrm{r}(r, \theta)$ are derived in (4.11) and (4.12) as function of the magnetic scalar potential ψ in the regions 1, 2 and 3.

$$H_{\theta,i}(r, \theta) = -\frac{1}{r}\frac{\partial \psi_i(r, \theta)}{\partial \theta} \quad \text{for } i \in \{1, 2, 3\} \tag{4.11}$$

$$\begin{cases} B_{\mathrm{r},1}(r,\theta) = -\mu_0\mu_{\mathrm{Fe,r}} \cdot \dfrac{\partial\psi_1(r,\theta)}{\partial r} \\ B_{\mathrm{r},2}(r,\theta) = -\mu_0\mu_{\mathrm{r,M}} \cdot \dfrac{\partial\psi_2(r,\theta)}{\partial r} + \mu_0 M_\mathrm{r}(\theta) \\ B_{\mathrm{r},3}(r,\theta) = -\mu_0 \cdot \dfrac{\partial\psi_3(r,\theta)}{\partial r} \end{cases} \tag{4.12}$$

Each set of six coefficients $\{a_{\mathrm{n},1},\ b_{\mathrm{n},1},\ a_{\mathrm{n},2},\ b_{\mathrm{n},2},\ a_{\mathrm{n},3},\ b_{\mathrm{n},3}\}$, describing the n^{th} term of the *Fourier* series of $\psi(r,\theta)$ in the three regions 1, 2, 3, can be factorised in a linear system of order six as for example (4.13) for $n = 1$, where the boundary conditions (4.10) define the right hand side of the system. The solution for the fundamental $n = 1$ is obtained using *Cramer*'s rule [18]. All coefficients of higher order $n > 1$ are zero, since due to (4.5) the right hand side for each system is always zero. As a consequence, the vector of magnetic flux density distribution $\boldsymbol{B}(r,\theta)$ in this particular problem displays only a fundamental in all three regions in Figure 4.3. Even though the field solution in each region can only be obtained by considering all the three regions 1, 2 and 3, only the field in the air gap region 3 is actually of interest for the functions of the levitated and drive rotor.

$$\begin{pmatrix} 0 & 1 & 0 & 0 & 0 & 0 \\ -\mu_{\mathrm{Fe,r}} & \mu_{\mathrm{Fe,r}} r_{\mathrm{ro}}^{-2} & \mu_{\mathrm{r,M}} & -\mu_{\mathrm{r,M}} r_{\mathrm{ro}}^{-2} & 0 & 0 \\ 1 & r_{\mathrm{ro}}^{-2} & -1 & -r_{\mathrm{ro}}^{-2} & 0 & 0 \\ 0 & 0 & \mu_{\mathrm{r,M}} & -\mu_{\mathrm{r,M}} r_{\mathrm{mo}}^{-2} & -1 & r_{\mathrm{mo}}^{-2} \\ 0 & 0 & 1 & r_{\mathrm{mo}}^{-2} & -1 & -r_{\mathrm{mo}}^{-2} \\ 0 & 0 & 0 & 0 & 1 & r_{\mathrm{si}}^{-2} \end{pmatrix} \cdot \begin{pmatrix} a_{1,1}^{0} \\ b_{1,1}^{0} \\ a_{1,2}^{0} \\ b_{1,2}^{0} \\ a_{1,3}^{0} \\ b_{1,3}^{0} \end{pmatrix} = \begin{pmatrix} 0 & B_{\mathrm{rem}}/\mu_0 & 0 & B_{\mathrm{rem}}/\mu_0 & 0 & 0 \end{pmatrix}^{\mathsf{T}} \tag{4.13}$$

The superscript 0 of the coefficients denote, that the rotor is at its concentric position and that any eccentricity is zero. The two coefficients $\{a_{1,3}^{0}, b_{1,3}^{0}\}$

that describe the air gap field are given in (4.14), considering $\mu_{\mathrm{Fe,r}} \gg 1$.

$$
\begin{aligned}
a_{1,3}^{0} &= -\frac{1}{\mu_0} \cdot \frac{B_{\mathrm{rem}} \cdot \left(\dfrac{r_{\mathrm{mo}}^2}{r_{\mathrm{si}}^2} - \dfrac{r_{\mathrm{ro}}^2}{r_{\mathrm{si}}^2} \right)}{(1+\mu_{\mathrm{r,M}}) \cdot \left(1 - \dfrac{r_{\mathrm{ro}}^2}{r_{\mathrm{si}}^2} \right) + (1-\mu_{\mathrm{r,M}}) \cdot \left(\dfrac{r_{\mathrm{mo}}^2}{r_{\mathrm{si}}^2} - \dfrac{r_{\mathrm{ro}}^2}{r_{\mathrm{mo}}^2} \right)} \\
b_{1,3}^{0} &= -r_{\mathrm{si}}^2 \cdot a_{1,3}
\end{aligned}
\tag{4.14}
$$

Finally, by calculating the gradient of the magnetic scalar potential $\psi_3(r,\theta)$ with (4.1) in the air gap region 3 considering $\mu_{\mathrm{Fe,r}} \gg 1$, the expressions of the magnetic flux densities $B_{\mathrm{r},3}$ and $B_{\theta,3}$ in the air gap region simplify to (4.15).

$$
\begin{aligned}
B_{\mathrm{r},3}(r,\theta) &= \frac{B_{\mathrm{rem}} \cdot \left(\dfrac{r_{\mathrm{mo}}^2}{r_{\mathrm{si}}^2} - \dfrac{r_{\mathrm{ro}}^2}{r_{\mathrm{si}}^2} \right) \cdot \left(1 + \dfrac{r_{\mathrm{si}}^2}{r^2} \right)}{(1+\mu_{\mathrm{r,M}}) \cdot \left(1 - \dfrac{r_{\mathrm{ro}}^2}{r_{\mathrm{si}}^2} \right) + (1-\mu_{\mathrm{r,M}}) \cdot \left(\dfrac{r_{\mathrm{mo}}^2}{r_{\mathrm{si}}^2} - \dfrac{r_{\mathrm{ro}}^2}{r_{\mathrm{mo}}^2} \right)} \cdot \cos(\theta - \theta_0) \\
B_{\theta,3}(r,\theta) &= \frac{B_{\mathrm{rem}} \cdot \left(\dfrac{r_{\mathrm{mo}}^2}{r_{\mathrm{si}}^2} - \dfrac{r_{\mathrm{ro}}^2}{r_{\mathrm{si}}^2} \right) \cdot \left(-1 + \dfrac{r_{\mathrm{si}}^2}{r^2} \right)}{(1+\mu_{\mathrm{r,M}}) \cdot \left(1 - \dfrac{r_{\mathrm{ro}}^2}{r_{\mathrm{si}}^2} \right) + (1-\mu_{\mathrm{r,M}}) \cdot \left(\dfrac{r_{\mathrm{mo}}^2}{r_{\mathrm{si}}^2} - \dfrac{r_{\mathrm{ro}}^2}{r_{\mathrm{mo}}^2} \right)} \cdot \sin(\theta - \theta_0)
\end{aligned}
\tag{4.15}
$$

It can be verified mathematically that the obtained field expressions (4.15) comply with the *Taylor* expansion of the fundamental component of the field expressions given in [16] for the case where the two-pole magnet is diametrically magnetised and the pole coverage ratio is $\alpha < 1$, when α tends to 1^-. It can also be verified that the calculation with the magnetic vector potential $\boldsymbol{A}$ with $\mu_{\mathrm{Fe,r}} \to \infty$ leads to the same results (4.15).

The calculation of the induced voltage U_{i} in the stator drive winding is done as follows: First the magnetic flux linked to a single stator coil is obtained by integrating the magnetic flux density $B_{\mathrm{r},3}(r_{\mathrm{si}},\theta)$ at r_{si} over the coil surface A_{coil}. The rotor angle θ is set at $\theta_0 + \omega \cdot t$, where ω is the electrical angular frequency. The magnetic flux is derived with respect to time t to get the induced voltage in that coil according to *Faraday*'s law. Then the sum of induced voltages in the q series connected coils is calculated considering their respective phases. This gives (4.16), where $N_{\mathrm{s},1}$ is the number of turns per phase, $k_{\mathrm{w},1}$ the resulting fundamental winding factor, $\tau_{\mathrm{p},1}$ the pole pitch, and l_{Fe} the equivalent axial iron length.

$$\hat{U}_{\mathrm{i}} = \omega \cdot N_{\mathrm{s},1} k_{\mathrm{w},1} \cdot \frac{2}{\pi} \tau_{\mathrm{p},1} l_{\mathrm{Fe}} \cdot B_{\mathrm{r},3}(r_{\mathrm{si}}, \theta_0) \tag{4.16}$$

The curvature effect is present in $B_{\mathrm{r},3}(r_{\mathrm{si}}, \theta_0)$. By assuming $\mu_{\mathrm{r,M}} \approx 1$, the induced voltage in the drive winding simplifies to (4.17).

$$\hat{U}_{\mathrm{i}} \approx \omega \cdot N_{\mathrm{s},1} k_{\mathrm{w},1} \cdot \frac{2}{\pi} \tau_{\mathrm{p},1} l_{\mathrm{Fe}} \cdot B_{\mathrm{rem}} \cdot \frac{r_{\mathrm{mo}}^2 - r_{\mathrm{ro}}^2}{r_{\mathrm{si}}^2 - r_{\mathrm{ro}}^2} \tag{4.17}$$

4.2.2. Magnetic pull at no-load due to rotor eccentricity

The magnetic pull, resulting from the rotor eccentricity in radial direction, is an important effect that must be evaluated during the design of self-bearing motors as it gives the minimum required control gain that ensures stability of the position control. Together with the current-force coefficient, it gives also a first estimation of the reachable closed-loop dynamic of the position control [4]. The problem of magnetic pull has been already addressed for some time for the asynchronous machines since the small magnetic air gap makes the asynchronous machine particularly sensitive to magnetic pull [19], [20]. The use of the single-sided magnetic pull equation in [20], derived for asynchronous machines, gives however important deviations when used for the determination of the negative stiffness of surface mounted PMSM [53]. This deviation is due to the distribution of the magnetic flux density in the air gap that plays a major effect for surface mounted PMSM what is not the case for induction motors. The determination of this magnetic pull is evaluated analytically for the geometry given in Figure 4.3. Different methods can be found in the literature to determine analytically the magnetic field in a PMSM under rotor eccentricity condition. A particular type of conformal mapping called bilinear mapping is particularly suited to transform circular non-concentric problems into circular concentric problems [21].

This method consists in transforming the actual motor geometry in a new concentric model, in a canonical domain. The magnetic field distribution solution obtained in this canonical domain is then transformed back to the actual motor geometry domain, with the bilinear mapping. From the expression of the magnetic field distribution, which expressions depend on the eccentricity, the *Maxwell* stress tensor has to be calculated and integrated over a closed surface in the air gap. The force expression obtained with this method has to be differentiated with regard to the eccentricity ϵ at the concentric rotor position $\epsilon = 0$ in order to get the force-displacement coefficient k_{sr}. Unfortunately, due to the size of the obtained expressions, this straightforward analytical determination is very difficult. A simpler and exact calculation method is proposed here, where the magnetic flux density distribution $B(r, \theta)$ is approximated with its first order *Taylor* expansion with regard to the rotor eccentricity ϵ. In [17], the calculation of the magnetic field distribution is described for an outer rotor PMSM with $p > 1$ and radial magnetisation. The same method is used here but for an inner rotor PMSM with $p = 1$, where the rotor magnet is diametrically magnetised and the geometry given in Figure 4.4. When the field distributions are obtained, the *Maxwell* stress tensor is calculated and integrated over a closed surface in the air gap. Finally the force expression is derived with respect to the rotor eccentricity ϵ to get the negative stiffness coefficient k_{sr}. Again, the magnetic scalar potential ψ_i, $i = 1, 2, 3$ is used to solve *Laplace*'s equation (4.3) in region $i = 1$ and $i = 3$, and *Poisson*'s equation (4.4) in region $i = 2$. The boundary conditions are non-linear since the problem has no rotational symmetry. As a consequence, the two-pole magnetisation $\boldsymbol{M}$ of the rotor induces field harmonics that result from the modulation of the MMF distribution with the varying air gap width $\delta(\theta)$. Now that the rotor is not concentric with the stator, two polar coordinate systems are defined. The polar coordinates in the stator fixed cylindrical coordinate system are defined as (r, θ). In the rotor cylindrical coordinate system, they are defined with (ξ, φ). The two coordinate systems are displayed in Figure 4.4, where ϵ is the rotor eccentricity distance and γ the direction angle of the rotor eccentricity at origin 0. The first order approximation of the coordinate

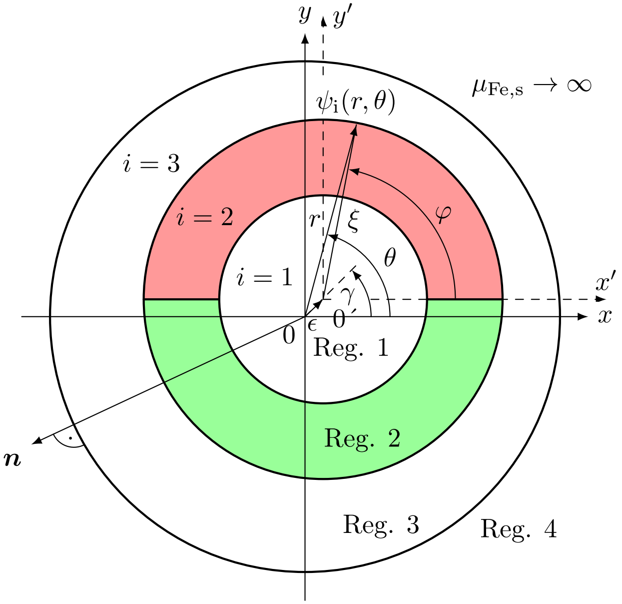

Figure 4.4.: Definition of the geometry with relevant machine parameters for the calculation of the single-sided magnetic pull. The stator coordinates are (r, θ) resp. (x, y) and the rotor coordinates are (ξ, φ) resp. (x', y'). The two coordinate centres 0 and 0' are distant by the rotor eccentricity ϵ in the direction of angle γ, centred at 0.

transformation from stator (r, θ) to rotor (ξ, φ) coordinates with respect to the eccentricity ϵ (see Figure 4.4) is given with the radius r from origin 0 by (4.18) [17].

$$\begin{cases} \xi \approx r - \epsilon \cdot \cos(\theta - \gamma) \\ \varphi \approx \theta + (\epsilon/r) \cdot \sin(\theta - \gamma) \end{cases} \tag{4.18}$$

The vector $\boldsymbol{n}(\xi, \varphi, \epsilon)$ orthogonal to the stator inner surface is expressed in the rotor coordinate system by calculating the normalised gradient of the first order approximation of the stator boundary expression in rotor coordinate system $g(\xi, \varphi, \epsilon) \approx \xi + \epsilon \cdot \cos(\varphi - \gamma)$ with $\nabla = (\frac{\partial}{\partial \xi}, \frac{1}{\xi}\frac{\partial}{\partial \varphi})$ and $(\epsilon/\xi)^2 \ll 1$ as (4.19) [17].

$$\boldsymbol{n}(\xi,\varphi,\epsilon)=\nabla g/\|\nabla g\|_2=\frac{(\frac{\partial g}{\partial\xi},\frac{1}{\xi}\cdot\frac{\partial g}{\partial\varphi})^{\mathsf{T}}}{\sqrt{(\frac{\partial g}{\partial\xi})^2+(\frac{1}{\xi}\cdot\frac{\partial g}{\partial\varphi})^2}}\approx(1,-\epsilon/\xi\cdot\sin(\varphi-\gamma))^{\mathsf{T}} \tag{4.19}$$

In contrast to the previous calculation without rotor eccentricity, the determination of the magnetic field distribution differs in the rotor coordinate system only at the stator boundary where the boundary condition of H_θ changes. As for the previous calculation, due to $\mu_{\mathrm{Fe,s}}\rightarrow\infty$ the continuity of the radial flux density B_r at the stator boundary does not give any useful expression. The expression of the continuity of the tangential magnetic field strength H_θ at the border between Region 3 and 4 $\xi_{3,4}=r_{\mathrm{si}}-\epsilon\cdot\cos(\varphi-\gamma)$ is formulated in (4.20) with the help of the vector $\boldsymbol{n}(\xi,\varphi,\epsilon)$ obtained in (4.19). The expression, calculated with $\boldsymbol{H_4}=\boldsymbol{0}$ due to $\mu_{\mathrm{Fe,s}}\rightarrow\infty$ and $\boldsymbol{H_3}=(H_{\xi,3},H_{\varphi,3})^{\mathsf{T}}$, and with the simplified $\boldsymbol{n}$ according to (4.19), becomes (4.21).

$$|\boldsymbol{n}(\xi,\varphi,\epsilon)\times\boldsymbol{H_3}(\xi,\varphi,\epsilon)|=|\boldsymbol{n}(\xi,\varphi,\epsilon)\times\boldsymbol{H_4}(\xi,\varphi,\epsilon)|\Big|_{\xi=\xi_{3,4}}=0 \tag{4.20}$$

$$1\cdot H_{\varphi,3}(\xi,\varphi,\epsilon)+(\epsilon/\xi)\cdot\sin(\varphi-\gamma)\cdot H_{\xi,3}(\xi,\varphi,\epsilon)\Big|_{\xi=\xi_{3,4}}\approx 0 \tag{4.21}$$

As proposed in [17], the magnetic scalar potential ψ is decomposed as *Taylor* expansion with ending after first order terms with respect to the eccentricity ϵ at the center point $\epsilon=0$ in the rotor coordinate system with (4.22).

$$\psi_\mathrm{i}(\xi,\varphi,\epsilon)\approx\psi_\mathrm{i}(\xi,\varphi,0)+\epsilon\cdot\frac{\partial\psi_\mathrm{i}(\xi,\varphi,0)}{\partial\epsilon},\ \text{with } i\in\{1,2,3\} \tag{4.22}$$

From (4.1), left equation, the decomposition of the magnetic field strength via the $-\nabla\psi$-operation with $\nabla=(\frac{\partial}{\partial\xi},\frac{1}{\xi}\frac{\partial}{\partial\varphi})$ follows in (4.23).

$$\begin{aligned} H_{\xi,\mathrm{i}}(\xi,\varphi,\epsilon) &\approx -\frac{\partial\psi_\mathrm{i}(\xi,\varphi,0)}{\partial\xi} - \epsilon\cdot\frac{\partial^2\psi_\mathrm{i}(\xi,\varphi,0)}{\partial\xi\partial\epsilon},\ \text{with } i\in\{1,2,3\} \\ H_{\varphi,\mathrm{i}}(\xi,\varphi,\epsilon) &\approx -\frac{1}{\xi}\cdot\frac{\partial\psi_\mathrm{i}(\xi,\varphi,0)}{\partial\varphi} - \epsilon\cdot\frac{1}{\xi}\cdot\frac{\partial^2\psi_\mathrm{i}(\xi,\varphi,0)}{\partial\varphi\partial\epsilon},\ \text{with } i\in\{1,2,3\} \end{aligned} \tag{4.23}$$

The boundary equation (4.21), defined at $\xi_{3,4} = r_\mathrm{si} - \epsilon\cdot\cos(\varphi-\gamma)$, is expressed as a function of the magnetic field strength components at $\xi = r_\mathrm{si}$ with the help of the *Taylor* expansion (4.24). Note that at $\xi = \xi_{3,4}$, $-\frac{\partial^2\psi_3(\xi,\varphi,0)}{\partial\xi\partial\epsilon} = \frac{\partial H_{\xi,3}(\xi,\varphi,0)}{\partial\epsilon} = \frac{\partial H_{\xi,3}}{\partial\xi}\cdot\frac{\partial\xi}{\partial\epsilon} = \frac{\partial H_{\xi,3}}{\partial\xi}\cdot\frac{\partial}{\partial\epsilon}(r_\mathrm{si} - \epsilon\cdot\cos(\varphi-\gamma)) = \frac{\partial H_{\xi,3}}{\partial\xi}\cdot(-\cos(\varphi-\gamma))$.

$$\begin{aligned} H_{\xi,3}(\xi,\varphi,\epsilon)\Big|_{\xi=\xi_{3,4}} &\approx H_{\xi,3}(r_\mathrm{si},\varphi,0) - \epsilon\cdot\cos(\varphi-\gamma)\cdot\frac{\partial H_{\xi,3}(r_\mathrm{si},\varphi,0)}{\partial\xi} \\ H_{\varphi,3}(\xi,\varphi,\epsilon)\Big|_{\xi=\xi_{3,4}} &\approx H_{\varphi,3}(r_\mathrm{si},\varphi,0) - \epsilon\cdot\cos(\varphi-\gamma)\cdot\frac{\partial H_{\varphi,3}(r_\mathrm{si},\varphi,0)}{\partial\xi} \end{aligned} \tag{4.24}$$

By inserting the equations (4.23) in (4.24), and neglecting the term of second order $\sim \epsilon^2$ with respect to the rotor eccentricity ϵ, the expression (4.21) becomes (4.25).

$$\begin{aligned} \frac{\partial\psi_3(r_\mathrm{si},\varphi,0)}{\partial\varphi} + \epsilon\cdot\frac{\partial^2\psi_3(r_\mathrm{si},\varphi,0)}{\partial\varphi\partial\epsilon} + \epsilon\cdot\sin(\varphi-\gamma)\cdot\frac{\partial\psi_3(r_\mathrm{si},\varphi,0)}{\partial\xi} \\ +\epsilon\cdot\cos(\varphi-\gamma)\cdot\left[\frac{1}{r_\mathrm{si}}\frac{\partial\psi_3(r_\mathrm{si},\varphi,0)}{\partial\varphi} - \frac{\partial^2\psi_3(r_\mathrm{si},\varphi,0)}{\partial\xi\partial\varphi}\right] = 0 \end{aligned} \tag{4.25}$$

At the concentric position $\epsilon = 0$, the expression (4.25) simplifies to (4.26). This result is the continuity of the tangential magnetic field strength at r_si already obtained in the previous part at (4.10), second equation.

$$\frac{\partial\psi_3(r_\mathrm{si},\varphi,0)}{\partial\varphi} = 0 \tag{4.26}$$

Finally, inserting (4.26) into (4.25), the first order stator boundary condition simplifies to (4.27), being independent of ϵ.

$$\frac{\partial^2\psi_3(r_{\mathrm{si}},\varphi,0)}{\partial\varphi\partial\epsilon} = -\sin(\varphi-\gamma)\cdot\frac{\partial\psi_3(r_{\mathrm{si}},\varphi,0)}{\partial\xi} + \cos(\varphi-\gamma)\cdot\frac{\partial^2\psi_3(r_{\mathrm{si}},\varphi,0)}{\partial\xi\partial\varphi} \tag{4.27}$$

The expression (4.27) gives a relation between the magnetic scalar potential in the concentric configuration and its first partial derivative with regard to the eccentricity ϵ at $\epsilon = 0$. The multiplication of the magnetic scalar potential ψ (its difference between two points called MMF) with the sinus and cosine functions of $(\varphi - \gamma)$ in (4.27) expresses the modulation of the rotor field with the varying air gap width. The other first-order boundary conditions with the radius values of Figure 4.3 and $\mu_{\mathrm{Fe,r}} \to \infty$ are straightforward according to (4.10), second and third equations and are given in (4.28).

$$\begin{aligned}
&\text{Tangential } H\text{-component: } \frac{\partial^2\psi_2(r_{\mathrm{ro}},\varphi,0)}{\partial\varphi\partial\epsilon} = 0\\
&\text{Radial } B\text{-component: } \mu_0\cdot\frac{\partial^2\psi_3(r_{\mathrm{mo}},\varphi,0)}{\partial\xi\partial\epsilon} = \mu_0\mu_{\mathrm{r,M}}\cdot\frac{\partial^2\psi_2(r_{\mathrm{mo}},\varphi,0)}{\partial\xi\partial\epsilon}\\
&\text{Tangential } H\text{-component: } \frac{\partial^2\psi_3(r_{\mathrm{mo}},\varphi,0)}{\partial\varphi\partial\epsilon} = \frac{\partial^2\psi_2(r_{\mathrm{mo}},\varphi,0)}{\partial\varphi\partial\epsilon}
\end{aligned} \tag{4.28}$$

Since the magnetic scalar potential ψ fulfils *Poisson*'s equations (4.3) and (4.4) independently from the eccentricity ϵ, the partial derivative of the magnetic scalar potential $\partial\psi/\partial\epsilon$ with regard to the eccentricity ϵ must also fulfil these equations. Its general solution is therefore of similar form as (4.7) and is defined in (4.29) where a_n^1 and b_n^1 are the coefficients of the first order expansion solution (superscript 1) of $\partial\psi/\partial\epsilon$.

$$\frac{\partial\psi_3(\xi,\varphi,0)}{\partial\epsilon} = \sum_{n=1}^{\infty}(a_{n,3}^1\cdot\xi^n + b_{n,3}^1\cdot\xi^{-n})\cos(n\cdot\varphi-\gamma-\theta_0) \tag{4.29}$$

As already done previously, the general solution is expressed in the rotor coordinate system rotated by $\gamma + \theta_0$, with θ_0 as magnetisation angle of the permanent magnet, in order to reduce the number of coefficients which are necessary to solve the boundary value problem. For every field harmonic component of order n, the boundary conditions (4.27) and (4.28) are set in a system. For $n = 2$, the system becomes (4.30) and the coefficients $a^1_{2,3}$ and $b^1_{2,3}$ are solved using the *Cramer*'s rule. They are given in (4.31).

$$\begin{pmatrix} r_{\mathrm{si}}^{2} & r_{\mathrm{si}}^{-2} & 0 & 0 \\ 0 & 0 & r_{\mathrm{ro}}^{2} & r_{\mathrm{ro}}^{-2} \\ r_{\mathrm{mo}}^{2} & -r_{\mathrm{mo}}^{-2} & -\mu_{\mathrm{r,M}} r_{\mathrm{mo}}^{2} & \mu_{\mathrm{r,M}} r_{\mathrm{mo}}^{-2} \\ r_{\mathrm{mo}}^{2} & r_{\mathrm{mo}}^{-2} & -r_{\mathrm{mo}}^{2} & -r_{\mathrm{mo}}^{-2} \end{pmatrix} \cdot \begin{pmatrix} a^1_{2,3} \\ b^1_{2,3} \\ a^1_{2,2} \\ b^1_{2,2} \end{pmatrix} = \begin{pmatrix} a^0_{1,3} \\ 0 \\ 0 \\ 0 \end{pmatrix} \tag{4.30}$$

For the system with order $n = 1$, which describes the permanent magnet fundamental component ($p_0 = 1$), and for all the systems of higher order $n > 2$ (harmonic fields with more than four poles), the system right hand side is always zero. In the considered case here, $p_0 = 1$ so the modulation of the rotor field with the air gap width gives rise to a four pole parasitic eccentricity field $p_0^+ = 2$ only. Indeed, the homo-polar eccentricity field with $p_0^- = 0$ does not fulfil the *Gauss*'s law in two dimensions. In the case $p_0 > 1$, the modulation would generate two parasitic eccentricity fields with $p_0^- = p_0 - 1$ and $p_0^+ = p_0 + 1$, characterised by two sets of coefficients $\{a^1_{p_0-1}, b^1_{p_0-1}\}$ and $\{a^1_{p_0+1}, b^1_{p_0+1}\}$.

$$\begin{aligned} a^1_{2,3} &= \frac{a^0_{1,3}}{r_{\mathrm{si}}^2 r_{\mathrm{mo}}^4} \cdot \frac{(1+\mu_{\mathrm{r,M}}) \cdot r_{\mathrm{mo}}^4 - (1-\mu_{\mathrm{r,M}}) \cdot r_{\mathrm{ro}}^4}{(1+\mu_{\mathrm{r,M}}) \cdot \left(1 - \frac{r_{\mathrm{ro}}^4}{r_{\mathrm{si}}^4}\right) + (1-\mu_{\mathrm{r,M}}) \cdot \left(\frac{r_{\mathrm{mo}}^4}{r_{\mathrm{si}}^4} - \frac{r_{\mathrm{ro}}^4}{r_{\mathrm{mo}}^4}\right)} \\ b^1_{2,3} &= \frac{a^0_{1,3}}{r_{\mathrm{si}}^2} \cdot \frac{(1-\mu_{\mathrm{r,M}}) \cdot r_{\mathrm{mo}}^4 - (1+\mu_{\mathrm{r,M}}) \cdot r_{\mathrm{ro}}^4}{(1+\mu_{\mathrm{r,M}}) \cdot \left(1 - \frac{r_{\mathrm{ro}}^4}{r_{\mathrm{si}}^4}\right) + (1-\mu_{\mathrm{r,M}}) \cdot \left(\frac{r_{\mathrm{mo}}^4}{r_{\mathrm{si}}^4} - \frac{r_{\mathrm{ro}}^4}{r_{\mathrm{mo}}^4}\right)} \end{aligned} \tag{4.31}$$

The first order approximation of the magnetic flux density with respect to the eccentricity ϵ is finally obtained in (4.32). It is for a two-pole permanent magnet field an additional parasitic four-pole eccentricity field distribution.

$$\begin{aligned}\frac{\partial B_{\xi,3}(\xi,\varphi,0)}{\partial\epsilon} &= -2\mu_0\cdot\left(a^1_{2,3}\xi - b^1_{2,3}\xi^{-3}\right)\cdot\cos(2\varphi-\gamma-\theta_0)\\ \frac{\partial B_{\varphi,3}(\xi,\varphi,0)}{\partial\epsilon} &= 2\mu_0\cdot\left(a^1_{2,3}\xi + b^1_{2,3}\xi^{-3}\right)\cdot\sin(2\varphi-\gamma-\theta_0)\end{aligned} \tag{4.32}$$

Finally, the magnetic flux density in the air gap region is expressed as a function of the eccentricity ϵ in (4.33).

$$\begin{aligned}B_{\xi,3}(\xi,\varphi,\epsilon) &\approx B_{\xi,3}(\xi,\varphi,0)+\epsilon\cdot\frac{\partial B_{\xi,3}(\xi,\varphi,0)}{\partial\epsilon}\\ B_{\varphi,3}(\xi,\varphi,\epsilon) &\approx B_{\varphi,3}(\xi,\varphi,0)+\epsilon\cdot\frac{\partial B_{\varphi,3}(\xi,\varphi,0)}{\partial\epsilon}\end{aligned} \tag{4.33}$$

In order to obtain the single-sided magnetic pull resulting from the eccentricity ϵ, the *Maxwell* force density $\boldsymbol{f} = (f_\xi, f_\varphi, 0)^T$, whose radial component f_ξ and tangential component f_φ are defined in (4.34) for two dimensions, is integrated over a closed surface $S(\xi)$ surrounding the rotor in the air gap region 3 at the radius ξ. The result is the force vector $(F_\mathrm{x}, F_\mathrm{y})$ of single-sided (or imbalanced) magnetic pull for a two-pole-magnetised rotor magnet ring at the rotor eccentricity ϵ and can be seen in (4.35). In order to get a convenient equation for $(F_\mathrm{x}, F_\mathrm{y})$, the expression is derived as a function of the maximum flux density at the stator inner radius in the concentric configuration at $\epsilon = 0$, occuring at $\theta = \theta_0$ as $B_{\mathrm{r},3}(r_\mathrm{si}, \theta_0)$ of (4.15).

$$\left\{\begin{aligned} f_\xi(\xi,\varphi,\epsilon) &= \frac{B^2_\xi(\xi,\varphi,\epsilon)-B^2_\varphi(\xi,\varphi,\epsilon)}{2\mu_0}\\ f_\varphi(\xi,\varphi,\epsilon) &= \frac{B_\xi(\xi,\varphi,\epsilon)\cdot B_\varphi(\xi,\varphi,\epsilon)}{\mu_0}\end{aligned}\right. \tag{4.34}$$

$$F_\mathrm{x} = \frac{\pi l_\mathrm{Fe}\cdot\left[1-\dfrac{1-\mu_\mathrm{r,M}}{1+\mu_\mathrm{r,M}}\cdot\dfrac{r^4_\mathrm{ro}}{r^4_\mathrm{mo}}\right]\cdot B^2_{\mathrm{r},3}(r_\mathrm{si},\theta_0)\cdot\cos\gamma}{\mu_0\cdot\left[\left(1-\dfrac{r^4_\mathrm{ro}}{r^4_\mathrm{si}}\right)+\dfrac{1-\mu_\mathrm{r,M}}{1+\mu_\mathrm{r,M}}\cdot\left(\dfrac{r^4_\mathrm{mo}}{r^4_\mathrm{si}}-\dfrac{r^4_\mathrm{ro}}{r^4_\mathrm{mo}}\right)\right]}\cdot\epsilon \tag{4.35a}$$

$$F_{\mathrm{y}} = \frac{\pi l_{\mathrm{Fe}} \cdot \left[1 - \dfrac{1-\mu_{\mathrm{r,M}}}{1+\mu_{\mathrm{r,M}}} \cdot \dfrac{r_{\mathrm{ro}}^4}{r_{\mathrm{mo}}^4}\right] \cdot B_{\mathrm{r},3}^2(r_{\mathrm{si}},\theta_0) \cdot \sin\gamma}{\mu_0 \cdot \left[\left(1 - \dfrac{r_{\mathrm{ro}}^4}{r_{\mathrm{si}}^4}\right) + \dfrac{1-\mu_{\mathrm{r,M}}}{1+\mu_{\mathrm{r,M}}} \cdot \left(\dfrac{r_{\mathrm{mo}}^4}{r_{\mathrm{si}}^4} - \dfrac{r_{\mathrm{ro}}^4}{r_{\mathrm{mo}}^4}\right)\right]} \cdot \epsilon \tag{4.35b}$$

$$F = \frac{\pi l_{\mathrm{Fe}} \cdot \left[1 - \dfrac{1-\mu_{\mathrm{r,M}}}{1+\mu_{\mathrm{r,M}}} \cdot \dfrac{r_{\mathrm{ro}}^4}{r_{\mathrm{mo}}^4}\right] \cdot B_{\mathrm{r},3}^2(r_{\mathrm{si}},\theta_0)}{\mu_0 \cdot \left[\left(1 - \dfrac{r_{\mathrm{ro}}^4}{r_{\mathrm{si}}^4}\right) + \dfrac{1-\mu_{\mathrm{r,M}}}{1+\mu_{\mathrm{r,M}}} \cdot \left(\dfrac{r_{\mathrm{mo}}^4}{r_{\mathrm{si}}^4} - \dfrac{r_{\mathrm{ro}}^4}{r_{\mathrm{mo}}^4}\right)\right]} \cdot \epsilon \tag{4.35c}$$

$$\boldsymbol{F} = (F_{\mathrm{x}}, F_{\mathrm{y}}),\ F_{\mathrm{x}} = \cos\gamma,\ F_{\mathrm{y}} = \sin\gamma \tag{4.35d}$$

The obtained expressions (4.35) are independent from the chosen integration surface $S(\xi)$ in the air gap region as long as it is a closed surface within that region around the rotor. It has to be noticed that the force amplitude F (4.35c) is proportional to the eccentricity ϵ and the force vector $\boldsymbol{F}$ points into the eccentricity direction γ. The force amplitude $F = \sqrt{F_{\mathrm{x}}^2 + F_{\mathrm{y}}^2}$ is independent of the actual direction of the permanent magnet field θ_0, but depends on its field value $B_{\mathrm{r},3}^2(r_{\mathrm{si}},\theta_0)$. The stiffness coefficient k_{sr} for the single-sided magnetic pull is finally obtained by derivation of the force expressions (4.35) with regard to the eccentricity ϵ as $k_{\mathrm{sr}} = \mathrm{d}F/\mathrm{d}\epsilon$ and is given by (4.36).

$$k_{\mathrm{sr}} = -\frac{\pi l_{\mathrm{Fe}} \cdot \left[(1+\mu_{\mathrm{r,M}}) - (1-\mu_{\mathrm{r,M}}) \cdot \dfrac{r_{\mathrm{ro}}^4}{r_{\mathrm{mo}}^4}\right] \cdot B_{\mathrm{r},3}^2(r_{\mathrm{si}},\theta_0)}{\mu_0 \cdot \left[(1+\mu_{\mathrm{r,M}}) \cdot \left(1 - \dfrac{r_{\mathrm{ro}}^4}{r_{\mathrm{si}}^4}\right) + (1-\mu_{\mathrm{r,M}}) \cdot \left(\dfrac{r_{\mathrm{mo}}^4}{r_{\mathrm{si}}^4} - \dfrac{r_{\mathrm{ro}}^4}{r_{\mathrm{mo}}^4}\right)\right]} \tag{4.36}$$

The stiffness coefficient k_{sr} leads to an increase of attracting force $F = k_{\mathrm{sr}} \cdot \epsilon$ of rotor to the stator with increasing ϵ, hence is acting opposite to a mechanical spring stiffness, and is therefore for a direction of decreasing ϵ a negative value. The expression (4.36) can be simplified in order to highlight the curvature effect on the negative stiffness k_{sr}. The commonly used rare-earth magnets (NdFeB and SmCo) display a relative recoil permeability of the magnet $\mu_{\mathrm{r,M}} \approx 1$. The expression of the negative stiffness under this assumption is given with (4.15) by (4.37).

$$k_{\mathrm{sr}} = -\frac{\pi l_{\mathrm{Fe}}}{\mu_0} \cdot \frac{r_{\mathrm{si}}^4 \cdot \left(r_{\mathrm{mo}}^2 - r_{\mathrm{ro}}^2\right)^2}{\left(r_{\mathrm{si}}^2 + r_{\mathrm{ro}}^2\right) \cdot \left(r_{\mathrm{si}}^2 - r_{\mathrm{ro}}^2\right)^3} \cdot B_{\mathrm{rem}}^2 \tag{4.37}$$

4.2.3. Induced voltage in the levitation winding due to rotor eccentricity

At rotor eccentricity , ϵ, the two-pole rotor field of the permanent magnet ($p_0 = 1$) is modulated by the varying air gap width $\delta(\varphi)$, giving rise to an additional parasitic eccentricity four-pole field $p_0^+ = 2$ according to (4.33). Since the levitation winding has two pole pairs $p_2 = 2$, this eccentricity field induces a voltage in the levitation winding at rotor movement. This induced voltage is calculated by integration of the radial magnetic flux density $B_{\mathrm{r},3}$ at $r = r_{\mathrm{si}}$. In order to calculate $B_{\mathrm{r},3}$, two possibilities are offered: The expressions (4.22) are transformed into the stator coordinate system (r, θ) with the help of (4.18) and are then differentiated or the magnetic flux densities are calculated directly using the chain rule (4.38).

$$\begin{aligned} B_{\mathrm{r},3} &= -\mu_0 \cdot \left(\frac{\partial\psi}{\partial\xi} \cdot \frac{\partial\xi}{\partial r} + \frac{\partial\psi}{\partial\varphi} \cdot \frac{\partial\varphi}{\partial r}\right) \\ B_{\theta,3} &= -\frac{\mu_0}{r} \cdot \left(\frac{\partial\psi}{\partial\xi} \cdot \frac{\partial\xi}{\partial\theta} + \frac{\partial\psi}{\partial\varphi} \cdot \frac{\partial\varphi}{\partial\theta}\right) \end{aligned} \tag{4.38}$$

The first order *Taylor* expansion with regard to the eccentricity ϵ of the magnetic flux density components at $r = r_{\mathrm{si}}$ are obtained with (4.39).

$$\begin{aligned}
B_{\mathrm{r},3}(r_{\mathrm{si}},\theta,\epsilon) &\approx -\mu_0\cdot(a^0_{1,3}-\frac{b^0_{1,3}}{r^2_{\mathrm{si}}})\cdot\cos(\theta-\theta_0)\\
&-\frac{\mu_0\cdot\epsilon}{r_{\mathrm{si}}}\cdot\left(2\cdot(a^1_{2,3}-\frac{b^1_{2,3}}{r^2_{\mathrm{si}}})+\frac{1}{2}\cdot(a^0_{1,3}-3\frac{b^0_{1,3}}{r^2_{\mathrm{si}}})\right)\cdot\cos(2\theta-\gamma-\theta_0)\\
B_{\theta,3}(r_{\mathrm{si}},\theta,\epsilon) &\approx \mu_0\cdot(a^0_{1,3}+\frac{b^0_{1,3}}{r^2_{\mathrm{si}}})\cdot\sin(\theta-\theta_0)\\
&+\frac{\mu_0\cdot\epsilon}{r_{\mathrm{si}}}\cdot\left(2\cdot(a^1_{2,3}+\frac{b^1_{2,3}}{r^2_{\mathrm{si}}})-(a^0_{1,3}-\frac{b^0_{1,3}}{r^2_{\mathrm{si}}})\right)\cdot\sin(2\theta-\gamma-\theta_0)
\end{aligned}\tag{4.39}$$

The field expressions (4.39) agree for $\epsilon = 0$ with the expressions (4.15), which were already obtained for the concentric rotor $\epsilon = 0$. The coefficients in (4.31) are inserted in (4.39) to finally obtain the compact expression (4.40), where $B_{\theta,3}(r_{\mathrm{si}},\theta,\epsilon)$ is small of the order of ϵ^2.

$$\begin{aligned}
B_{\mathrm{r},3}(r_{\mathrm{si}},\theta,\epsilon) \approx &-2\cdot\mu_0\cdot a^0_{1,3}\cdot\cos(\theta-\theta_0)\\
&-4\cdot\mu_0\cdot\epsilon\cdot r_{\mathrm{si}}\cdot a^1_{2,3}\cdot\cos(2\theta-\gamma-\theta_0)\\
B_{\theta,3}(r_{\mathrm{si}},\theta,\epsilon) =&\mathcal{O}(\epsilon^2)
\end{aligned}\tag{4.40}$$

The first order approximation of $B_{\theta,3}(r,\theta,\epsilon)$ as $\sim\epsilon$ at $r = r_{\mathrm{si}}$ is zero, fulfilling the tangential magnetic field strength continuity at the stator boundary r_{si}. The induced voltage $U_{\mathrm{i},2}$ in the levitation winding due to the rotor field under eccentricity ϵ is obtained as done previously in (4.16) by integration of (4.40), where only the radial component $B_{\mathrm{r},3}$ contributes to the coil flux linkage. The parasitic induced voltage due to the eccentricity field is given by (4.41) where $N_{\mathrm{s},2}$ is the number of turns per phase and $k_{\mathrm{w},2,1}$ the winding factor of the levitation winding.

$$\hat{U}_{\mathrm{i},2}(\epsilon,\omega) = \omega\cdot N_{\mathrm{s},2}\cdot k_{\mathrm{w},2,1}\cdot\frac{8}{\pi}\cdot\tau_{\mathrm{p},2}\cdot l_{\mathrm{Fe}}\cdot\mu_0\cdot r_{\mathrm{si}}\cdot a^1_{2,3}\cdot\epsilon \tag{4.41}$$

In order to compare this parasitic induced voltage $U_{\mathrm{i},2}$ in the levitation winding to the no-load voltage $U_{\mathrm{i},1}$ in the drive winding of (4.16), the relative recoil permeability of the magnet $\mu_{\mathrm{r,M}}$ is set to 1 such as in (4.17) and the equivalent air gap width $\delta_{\mathrm{eq}} = r_{\mathrm{si}} - r_{\mathrm{ro}}$ is considered small compared to r_{si}. The ratio of the induced voltages $\hat{U}_{\mathrm{i},2}/\hat{U}_{\mathrm{i},1}$ then simplifies to the expression (4.42).

$$\frac{\hat{U}_{\mathrm{i},2}}{\hat{U}_{\mathrm{i},1}} \approx \frac{N_{\mathrm{s},2} \cdot k_{\mathrm{w},2,1}}{N_{\mathrm{s},1} \cdot k_{\mathrm{w},1,1}} \cdot \frac{\epsilon}{4\delta_{\mathrm{eq}}} \tag{4.42}$$

The two windings, namely the levitation and the drive winding, form a transformer system, coupled by the eccentric permanent magnet rotor, where the transformer voltage ratio is proportional to the rotor eccentricity ϵ. At $\epsilon = 0$, no transformer coupling exits via the rotor magnet movement. The amplitude and the phase of the induced voltage $U_{\mathrm{i},2}$ in the levitation winding depend on ϵ and enable us theoretically to obtain the rotor eccentricity position information without any radial position sensor. As the ratio (4.42) is small, and the induced voltage $U_{\mathrm{i},1}$ is also small at low speed, an induced voltage-based rotor position observer may be difficult to realise due to the low voltage amplitude to be observed.

4.2.4. Magnetic field due to stator current without rotor eccentricity

In order to produce torque and radial forces, the torque winding (pole pair count p_1) and the suspension (or levitation) winding (pole pair count p_2) are fed by a three-phase current system with a torque current component i_1 and a radial force component i_2, respectively. These two current systems excite via *Ampère*'s law additional stator field components in the self-bearing motor air gap. In order to simplify the calculation, the magneto-motive forces as the difference of the magnetic scalar potential ψ at different points in the slots, resulting from the Ampere-turns in the stator slots, are considered to be generated from an equivalent current loading A_1 and A_2 at the stator inner diameter r_{si}. By that we neglect the slotting permeance ripple of the air gap region. The slots are reduced to points at the stator bore with infinite slot current density and local infinite current loading. The resulting MMF $V(x,t)$ from a three phase symmetrical six-zone winding system with a number of turns per phase N_s and a pole pair number p, fed by a positive sequence current system, expressed as space vector $\underline{i}(t) = \hat{I}_\mathrm{s} \cdot \exp(\mathrm{j}\omega t)$, is given in (4.43) where φ_ν is the phase of the MMF component of order ν at $t = 0$.

$$V(\theta,t) = \frac{3N_\mathrm{s}\hat{I}_\mathrm{s}}{\pi p} \cdot \sum_{\nu=1,-5,7\ldots} \frac{k_{\mathrm{w},\nu}}{\nu} \cdot \cos(\nu \cdot \theta \cdot p - \omega t - \varphi_\nu) \tag{4.43}$$

The series (4.43) of the form $\sum_\nu \mathrm{sgn}(k_{\mathrm{w},\nu})/\nu$ is conditional convergent (see *Riemann* series theorem [22] and *Fourier* series theorem [18]). The *Fourier* series of the equivalent current loading $A(\theta,t)$ is divergent, because it was assumed to have infinitely big current loading in the idealised point-like slots, which means infinite current loading there and zero between these slots. Therefore, as an approximation, the calculation of A can only be done for a finite number of harmonics (e.g. until $\nu_\mathrm{max} = N$ in (4.44)).

$$A(\theta,t) = -\frac{3N_\mathrm{s}\hat{I}_\mathrm{s}}{\tau_\mathrm{p} p} \cdot \sum_{\nu=1,-5,7\ldots}^{N} k_{\mathrm{w},\nu} \cdot \sin(\nu \cdot \theta \cdot p - \omega t - \varphi_\nu) \tag{4.44}$$

The calculation of the stator magnetic field follows the same procedure as for the calculation of the no-load magnetic field of Section 4.2.1. Similar to (4.13), but instead of a, b, here c, d, each set of coefficients $\{c_{\mathrm{n},1}, d_{\mathrm{n},1}, c_{\mathrm{n},2}, d_{\mathrm{n},2}, c_{\mathrm{n},3}, d_{\mathrm{n},3}\}$ that describes each stator harmonic field component of the order of n in the three regions 1, 2, 3, is set in a system of order six with the respective current loading harmonic component wave A_n as stator boundary condition. All the solutions are then superposed to get the resulting stator field. Since the *Fourier* series of discontinuous functions like the current-loading in point-like slots, is not pointwise convergent, the results obtained with this method are not fitting the numerical solutions with finite element method in the vicinity of the discontinuous boundaries. Moreover, the *Gibbs* phenomenon at the step-like MMF variations, occuring at the point-like slots, is responsible for local field variations in the solution that have no electromagnetic origin. The calculation is done therefore not for a complete *Fourier*-sum (4.43), but for the component ν of a p pole pair three-phase winding. The solution is then applied to the considered geometry with the drive and levitation current loading respectively. The system is considered like in Section 4.2.1 axial symmetric so that the field components have only radial $B_{\mathrm{r}}(r,\theta)$ and tangential components $B_{\theta}(r,\theta)$. As the actual winding Ampere-turns in the real stator slots are replaced by infinite current-loading in point-like slots, leading to an infinite sum of equivalent current loading waves $A_\nu(\theta,t)$, defined by (4.44) and (4.45), the magnetic fields in the regions 1, 2 and 3 are curl-free. Therefore the calculation is done again with the magnetic scalar potential ψ. The general solution of the differential equation is the same as in (4.7). Only the right hand side of the system is changing with the boundary conditions (4.46) at the stator inner radius r_{si}, which is valid for $\mu_{\mathrm{Fe,s}} \to \infty$.

$$A_\nu(\theta) = -\frac{3k_{\mathrm{w},\nu} N_{\mathrm{s}} \hat{I}_{\mathrm{s}}}{\pi r_{\mathrm{si}}} \cdot \sin(n\cdot\theta - \theta_{\mathrm{n}}) \text{ with } n = p\cdot\nu \text{ and } \theta_{\mathrm{n}} = \omega t + \varphi_\nu \quad (4.45)$$

$$\forall\theta \in [0,2\pi]\,, H_{\theta,3,\nu}(\theta, r = r_{\mathrm{si}}) = A_\nu(\theta) \quad (4.46)$$

The system is given by $c_{\mathrm{n},1} = 0$ due to $\mu_{\mathrm{Fe,s}} \to \infty$ and (4.47).

$$\begin{pmatrix} \mu_{\mathrm{Fe,r}} r_{\mathrm{ro}}^{-n-1} & \mu_{\mathrm{r,M}} r_{\mathrm{ro}}^{n-1} & -\mu_{\mathrm{r,M}} r_{\mathrm{ro}}^{-n-1} & 0 & 0 \\ r_{\mathrm{ro}}^{-n-1} & -r_{\mathrm{ro}}^{n-1} & -r_{\mathrm{ro}}^{-n-1} & 0 & 0 \\ 0 & \mu_{\mathrm{r,M}} r_{\mathrm{mo}}^{n-1} & -\mu_{\mathrm{r,M}} r_{\mathrm{mo}}^{-n-1} & -r_{\mathrm{mo}}^{n-1} & r_{\mathrm{mo}}^{-n-1} \\ 0 & r_{\mathrm{mo}}^{n-1} & r_{\mathrm{mo}}^{-n-1} & -r_{\mathrm{mo}}^{n-1} & -r_{\mathrm{mo}}^{-n-1} \\ 0 & 0 & 0 & r_{\mathrm{si}}^{n-1} & r_{\mathrm{si}}^{-n-1} \end{pmatrix} \begin{pmatrix} d_{\mathrm{n},1} \\ c_{\mathrm{n},2} \\ d_{\mathrm{n},2} \\ c_{\mathrm{n},3} \\ d_{\mathrm{n},3} \end{pmatrix} = \begin{pmatrix} 0 & 0 & 0 & 0 & A_\nu/n \end{pmatrix}^{\mathsf{T}} \quad (4.47)$$

Again the region of interest is the air gap region 3 where the radial and tangential magnetic flux densities are obtained similar to (4.13)...(4.15) for $\mu_{\mathrm{Fe,r}} \gg 1$ in (4.48).

$$
\begin{aligned}
B_{\mathrm{r},3,\nu}(r,\theta) &= \mu_0 \cdot \frac{3k_{\mathrm{w},\nu} N_{\mathrm{s}} \hat{I}_{\mathrm{s}}}{\pi r_{\mathrm{si}}} \cdot \cos(n \cdot \theta - \theta_{\mathrm{n}}) \cdot \\
&\frac{\left(\frac{r_{\mathrm{si}}^{n+1} r^{n-1}}{r_{\mathrm{ro}}^{2n}} + \frac{r_{\mathrm{si}}^{n+1}}{r^{n+1}}\right) - \frac{1-\mu_{\mathrm{r,M}}}{1+\mu_{\mathrm{r,M}}} \cdot \left(\frac{r_{\mathrm{si}}^{n+1} r^{n-1}}{r_{\mathrm{mo}}^{2n}} + \frac{r_{\mathrm{mo}}^{2n} r_{\mathrm{si}}^{n+1}}{r_{\mathrm{ro}}^{2n} r^{n+1}}\right)}{\left(1 - \frac{r_{\mathrm{si}}^{2n}}{r_{\mathrm{ro}}^{2n}}\right) + \frac{1-\mu_{\mathrm{r,M}}}{1+\mu_{\mathrm{r,M}}} \cdot \left(\frac{r_{\mathrm{si}}^{2n}}{r_{\mathrm{mo}}^{2n}} - \frac{r_{\mathrm{mo}}^{2n}}{r_{\mathrm{ro}}^{2n}}\right)} \\
B_{\theta,3,\nu}(r,\theta) &= \mu_0 \cdot \frac{3k_{\mathrm{w},\nu} N_{\mathrm{s}} \hat{I}_{\mathrm{s}}}{\pi r_{\mathrm{si}}} \cdot \sin(n \cdot \theta - \theta_{\mathrm{n}}) \cdot \\
&\frac{\left(\frac{r_{\mathrm{si}}^{n+1} r^{n-1}}{r_{\mathrm{ro}}^{2n}} - \frac{r_{\mathrm{si}}^{n+1}}{r^{n+1}}\right) - \frac{1-\mu_{\mathrm{r,M}}}{1+\mu_{\mathrm{r,M}}} \cdot \left(\frac{r_{\mathrm{si}}^{n+1} r^{n-1}}{r_{\mathrm{mo}}^{2n}} - \frac{r_{\mathrm{mo}}^{2n} r_{\mathrm{si}}^{n+1}}{r_{\mathrm{ro}}^{2n} r^{n+1}}\right)}{\left(1 - \frac{r_{\mathrm{si}}^{2n}}{r_{\mathrm{ro}}^{2n}}\right) + \frac{1-\mu_{\mathrm{r,M}}}{1+\mu_{\mathrm{r,M}}} \cdot \left(\frac{r_{\mathrm{si}}^{2n}}{r_{\mathrm{mo}}^{2n}} - \frac{r_{\mathrm{mo}}^{2n}}{r_{\mathrm{ro}}^{2n}}\right)}
\end{aligned}
\tag{4.48}
$$

The fundamental components $\nu = 1$ of the drive field with $p_1 = 1$ are given by (4.49), where $\theta_1 = \omega t + \varphi_1$ with an arbitrary phase angle φ_1.

$$
\begin{aligned}
B_{\mathrm{r},3,1}(r,\theta) &= -\mu_0 A_1 \cdot \frac{1 + \frac{r_{\mathrm{ro}}^2}{r^2} - \frac{1-\mu_{\mathrm{r,M}}}{1+\mu_{\mathrm{r,M}}} \cdot \left(\frac{r_{\mathrm{ro}}^2}{r_{\mathrm{mo}}^2} + \frac{r_{\mathrm{mo}}^2}{r^2}\right)}{1 - \frac{r_{\mathrm{ro}}^2}{r_{\mathrm{si}}^2} + \frac{1-\mu_{\mathrm{r,M}}}{1+\mu_{\mathrm{r,M}}} \cdot \left(\frac{r_{\mathrm{mo}}^2}{r_{\mathrm{si}}^2} - \frac{r_{\mathrm{ro}}^2}{r_{\mathrm{mo}}^2}\right)} \cdot \cos(\theta - \theta_1) \\
B_{\theta,3,1}(r,\theta) &= -\mu_0 A_1 \cdot \frac{1 - \frac{r_{\mathrm{ro}}^2}{r^2} - \frac{1-\mu_{\mathrm{r,M}}}{1+\mu_{\mathrm{r,M}}} \cdot \left(\frac{r_{\mathrm{ro}}^2}{r_{\mathrm{mo}}^2} - \frac{r_{\mathrm{mo}}^2}{r^2}\right)}{1 - \frac{r_{\mathrm{ro}}^2}{r_{\mathrm{si}}^2} + \frac{1-\mu_{\mathrm{r,M}}}{1+\mu_{\mathrm{r,M}}} \cdot \left(\frac{r_{\mathrm{mo}}^2}{r_{\mathrm{si}}^2} - \frac{r_{\mathrm{ro}}^2}{r_{\mathrm{mo}}^2}\right)} \cdot \sin(\theta - \theta_1)
\end{aligned}
\tag{4.49}
$$

The same calculation is done to obtain the fundamental $\nu = 1$ of the levitation field with $p_2 = 2$ as (4.50).

$$\begin{aligned}
B_{\mathrm{r},3,2}(r,\theta) &= \mu_0 A_2 \cdot \cos(2\theta-\theta_2)\cdot \\
&\frac{\frac{1-\mu_{\mathrm{r,M}}}{1+\mu_{\mathrm{r,M}}}\cdot\left(\frac{r_{\mathrm{si}}^3 r}{r_{\mathrm{mo}}^4}+\frac{r_{\mathrm{mo}}^4 r_{\mathrm{si}}^3}{r_{\mathrm{ro}}^4 r^3}\right)-\left(\frac{r_{\mathrm{si}}^3 r}{r_{\mathrm{ro}}^4}+\frac{r_{\mathrm{si}}^3}{r^3}\right)}{\frac{1-\mu_{\mathrm{r,M}}}{1+\mu_{\mathrm{r,M}}}\cdot\left(\frac{r_{\mathrm{si}}^4}{r_{\mathrm{mo}}^4}-\frac{r_{\mathrm{mo}}^4}{r_{\mathrm{ro}}^4}\right)+\left(1-\frac{r_{\mathrm{si}}^4}{r_{\mathrm{ro}}^4}\right)} \\
B_{\theta,3,2}(r,\theta) &= \mu_0 A_2 \cdot \sin(2\theta-\theta_2)\cdot \\
&\frac{\frac{1-\mu_{\mathrm{r,M}}}{1+\mu_{\mathrm{r,M}}}\cdot\left(\frac{r_{\mathrm{si}}^3 r}{r_{\mathrm{mo}}^4}-\frac{r_{\mathrm{mo}}^4 r_{\mathrm{si}}^3}{r_{\mathrm{ro}}^4 r^3}\right)-\left(\frac{r_{\mathrm{si}}^3 r}{r_{\mathrm{ro}}^4}-\frac{r_{\mathrm{si}}^3}{r^3}\right)}{\frac{1-\mu_{\mathrm{r,M}}}{1+\mu_{\mathrm{r,M}}}\cdot\left(\frac{r_{\mathrm{si}}^4}{r_{\mathrm{mo}}^4}-\frac{r_{\mathrm{mo}}^4}{r_{\mathrm{ro}}^4}\right)+\left(1-\frac{r_{\mathrm{si}}^4}{r_{\mathrm{ro}}^4}\right)}
\end{aligned} \tag{4.50}$$

4.2.5. Magnetic field due to stator current with rotor eccentricity

In order to obtain the modulation of the drive and levitation fields of Section 4.2.4 with the varying air gap width $\delta(\varphi)$ due to rotor eccentricity ϵ such as explained in Section 4.2.2, the same procedure is repeated as for the rotor field modulation of 4.2.2. Only the stator boundary condition from (4.21) to (4.51) is changing at $\xi_{3,4}$ due to the current loading $A_1(\varphi)$.

$$H_{\varphi,3}(\xi,\varphi,\epsilon)+\frac{\epsilon}{\xi}\cdot\sin(\varphi-\gamma)\cdot H_{\xi,3}(\xi,\varphi,\epsilon)\bigg|_{\xi_{3,4}=r_{\mathrm{si}}-\epsilon\cdot\cos(\varphi-\gamma)} \approx A_1(\varphi) \tag{4.51}$$

Inserting now (4.24) and (4.23) in (4.51), the first order expression (4.51) of the stator boundary condition takes the form (4.52).

$$\begin{aligned}
\frac{\partial^2\psi_3(r_{\mathrm{si}},\varphi,0)}{\partial\varphi\partial\epsilon} &= -\sin(\varphi-\gamma)\cdot\frac{\partial\psi_3(r_{\mathrm{si}},\varphi,0)}{\partial\xi} \\
&\quad +\cos(\varphi-\gamma)\cdot\left(\frac{\partial^2\psi_3(r_{\mathrm{si}},\varphi,0)}{\partial\xi\partial\varphi}+A_1(\varphi)\right)
\end{aligned} \tag{4.52}$$

For the drive winding, a similar magnetic scalar potential to Section 4.2.2 is chosen to fulfil at $\epsilon > 0$ the boundary conditions with (4.53).

$$\frac{\partial \psi_3(\xi,\varphi,0)}{\partial \epsilon} = (c^1_{2,3}\cdot\xi^2 + d^1_{2,3}\cdot\xi^{-2})\cdot\cos(2\varphi-\gamma-\theta_1) \tag{4.53}$$

The solution for the coefficients $c^1_{2,3}$ and $d^1_{2,3}$ are given by (4.54). From the two-pole drive field ($p_1 = 1$) and its MMF, characterised by the coefficients $c^0_{1,3}$ and $d^0_{1,3}$, modulated by the varying air gap width $\delta(\varphi)$, it results due to $\epsilon > 0$ a parasitic four pole eccentricity field ($p_1^+ = 2$) whose amplitude is proportional to the eccentricity ϵ.

$$\begin{aligned} c^1_{2,3} &= \frac{3d^0_{1,3} - c^0_{1,3} r^2_{\mathrm{si}}}{4r^4_{\mathrm{si}} r^4_{\mathrm{mo}}} \cdot \frac{(1+\mu_{\mathrm{r,M}})\cdot r^4_{\mathrm{mo}} - (1-\mu_{\mathrm{r,M}})\cdot r^4_{\mathrm{ro}}}{(1+\mu_{\mathrm{r,M}})\cdot\left(1-\frac{r^4_{\mathrm{ro}}}{r^4_{\mathrm{si}}}\right) + (1-\mu_{\mathrm{r,M}})\cdot\left(\frac{r^4_{\mathrm{mo}}}{r^4_{\mathrm{si}}} - \frac{r^4_{\mathrm{ro}}}{r^4_{\mathrm{mo}}}\right)} \\ d^1_{2,3} &= \frac{3d^0_{1,3} - c^0_{1,3} r^2_{\mathrm{si}}}{4r^4_{\mathrm{si}}} \cdot \frac{(1-\mu_{\mathrm{r,M}})\cdot r^4_{\mathrm{mo}} - (1+\mu_{\mathrm{r,M}})\cdot r^4_{\mathrm{ro}}}{(1+\mu_{\mathrm{r,M}})\cdot\left(1-\frac{r^4_{\mathrm{ro}}}{r^4_{\mathrm{si}}}\right) + (1-\mu_{\mathrm{r,M}})\cdot\left(\frac{r^4_{\mathrm{mo}}}{r^4_{\mathrm{si}}} - \frac{r^4_{\mathrm{ro}}}{r^4_{\mathrm{mo}}}\right)} \end{aligned} \tag{4.54}$$

In contrast, the levitation winding is a four-pole field ($p_2 = 2$) so that its MMF modulation with the varying air gap width $\delta(\varphi)$ gives rise to a parasitic two-pole eccentricity field ($p_2^- = 1$) and a parasitic six-pole eccentricity field ($p_2^+ = 3$). The first order approximation of the magnetic scalar potential ψ for the field of the levitation winding is therefore a superposition of two expressions with $n = 1$ and $n = 3$, and takes the form (4.55).

$$\begin{aligned} \frac{\partial \psi_3(\xi,\varphi,0)}{\partial \epsilon} =& (c^1_{1,3}\cdot\xi + d^1_{1,3}\cdot\xi^{-1})\cdot\cos(\varphi+\gamma-\theta_2) \\ &+ (c^1_{3,3}\cdot\xi^3 + d^1_{3,3}\cdot\xi^{-3})\cdot\cos(3\varphi-\gamma-\theta_2) \end{aligned} \tag{4.55}$$

The calculation of the four amplitude parameters of (4.55) results in the following solutions (4.56).

Table 4.1.: Fundamental rotor and stator fields: Pole counts and their modulated field components resulting from rotor eccentricity in region 3

Field	**Rotor magnet**	**Drive winding**	**Levitation winding**	
Pole pair number at $\epsilon = 0$	p_0	p_1	p_2	
Field parameters in reg. 3	$a^0_{1,3}$, $b^0_{1,3}$	$c^0_{1,3}$, $d^0_{1,3}$	$c^0_{2,3}$, $d^0_{2,3}$	
Pole pair number at $\epsilon > 0$	p_0^+	p_1^+	p_2^+	p_2^-
Field parameters in reg. 3	$a^1_{2,3}$, $b^1_{2,3}$	$c^1_{2,3}$, $d^1_{2,3}$	$c^1_{3,3}$, $d^1_{3,3}$	$c^1_{1,3}$, $d^1_{1,3}$

$$\begin{aligned}
c^1_{1,3} &= \frac{r_{\mathrm{si}}^4 c^0_{2,3} - 3d^0_{2,3}}{2r_{\mathrm{si}}^4 r_{\mathrm{mo}}^2} \cdot \frac{(1+\mu_{\mathrm{r,M}}) \cdot r_{\mathrm{mo}}^2 - (1-\mu_{\mathrm{r,M}}) \cdot r_{\mathrm{ro}}^2}{(1+\mu_{\mathrm{r,M}}) \cdot \left(1 - \frac{r_{\mathrm{ro}}^2}{r_{\mathrm{si}}^2}\right) + (1-\mu_{\mathrm{r,M}}) \cdot \left(\frac{r_{\mathrm{mo}}^2}{r_{\mathrm{si}}^2} - \frac{r_{\mathrm{ro}}^2}{r_{\mathrm{mo}}^2}\right)} \\
d^1_{1,3} &= \frac{r_{\mathrm{si}}^4 c^0_{2,3} - 3d^0_{2,3}}{2r_{\mathrm{si}}^4} \cdot \frac{(1-\mu_{\mathrm{r,M}}) \cdot r_{\mathrm{mo}}^2 - (1+\mu_{\mathrm{r,M}}) \cdot r_{\mathrm{ro}}^2}{(1+\mu_{\mathrm{r,M}}) \cdot \left(1 - \frac{r_{\mathrm{ro}}^2}{r_{\mathrm{si}}^2}\right) + (1-\mu_{\mathrm{r,M}}) \cdot \left(\frac{r_{\mathrm{mo}}^2}{r_{\mathrm{si}}^2} - \frac{r_{\mathrm{ro}}^2}{r_{\mathrm{mo}}^2}\right)} \\
c^1_{3,3} &= \frac{5r_{\mathrm{si}}^4 c^0_{2,3} - 7d^0_{2,3}}{6r_{\mathrm{si}}^6 r_{\mathrm{mo}}^6} \cdot \frac{(1+\mu_{\mathrm{r,M}}) \cdot r_{\mathrm{mo}}^6 - (1-\mu_{\mathrm{r,M}}) \cdot r_{\mathrm{ro}}^6}{(1+\mu_{\mathrm{r,M}}) \cdot \left(1 - \frac{r_{\mathrm{ro}}^6}{r_{\mathrm{si}}^6}\right) + (1-\mu_{\mathrm{r,M}}) \cdot \left(\frac{r_{\mathrm{mo}}^6}{r_{\mathrm{si}}^6} - \frac{r_{\mathrm{ro}}^6}{r_{\mathrm{mo}}^6}\right)} \\
d^1_{3,3} &= \frac{5r_{\mathrm{si}}^4 c^0_{2,3} - 7d^0_{2,3}}{6r_{\mathrm{si}}^6} \cdot \frac{(1-\mu_{\mathrm{r,M}}) \cdot r_{\mathrm{mo}}^6 - (1+\mu_{\mathrm{r,M}}) \cdot r_{\mathrm{ro}}^6}{(1+\mu_{\mathrm{r,M}}) \cdot \left(1 - \frac{r_{\mathrm{ro}}^6}{r_{\mathrm{si}}^6}\right) + (1-\mu_{\mathrm{r,M}}) \cdot \left(\frac{r_{\mathrm{mo}}^6}{r_{\mathrm{si}}^6} - \frac{r_{\mathrm{ro}}^6}{r_{\mathrm{mo}}^6}\right)}
\end{aligned} \tag{4.56}$$

An overview of all the calculated distribution parameters for each field (field sources are rotor magnet, drive winding and levitation winding) in the air gap (region 3 in Figure 4.3) at concentric rotor position ($\epsilon = 0$) and eccentric rotor position ($\epsilon \neq 0$) is given in Table 4.1.

4.2.6. Slot harmonics

The slot opening s_Q were replaced in Section 4.2.4 and Section 4.2.5 by infinitely small openings as dots or points. The real slot openings s_Q must be considered now and have different effects on the distribution of the rotor field and of the stator fields. The openings reduce the fundamental of the permanent magnet rotor field and add additional rotor harmonic field components, since the permanent magnet field is modulated with the non-constant air gap width as an air gap permeance slot ripple, caused by the slot openings. A method is presented in [23] which uses conformal mapping to transform the slotted configuration into a slotless plate-plate configuration between stator and rotor surface. Unfortunately the introduced relative (or normalised) air gap permeance $\lambda(r, \theta)$ has no explicit analytical solution elsewhere than at the rotor outer-radius r_ro where the field is devoid of interest. This problem is recurrent when using conformal mapping since the tranformations give the coordinates as function of the fields, but not the fields as function of the coordinates. The expressions can be inverted analytically only in a few cases such as for example for the determination of *Carter*'s coefficient (4.2) [15], [24] for increasing the air gap virtually by the average of the above noted permeance slot ripple. The modulation effect of the moving rotor magnet field with the stator slot opening permeance ripple is in our case due to a big magnetic equivalent air gap small and may be neglected. The slot effects on the stator fields are easier to be considered, as the permeance slot ripple is not moving relative to the stator. For that, the magneto-motive force is replaced by an equivalent constant current loading in the slot opening s_Q at $r = r_\mathrm{si}$ instead of concentrating the current loading at point-like idealised slots, leading to a reduction of $A_\nu(\theta)$ by (4.57). The reduction of the fundamental field waves of the drive and levitation winding due to an increased equivalent air gap are taken into consideration with (4.2), which for rotors with surface mounted magnets and $\mu_\mathrm{r,M} \approx 1$ is negligible ($\delta'_\mathrm{eq} \approx \delta_\mathrm{eq}$). The stator field harmonics of higher order are added therefore wimply with (4.48). For the higher order stator field harmonics however, the slot opening effect, given by (4.57), is not negligible any more

[25] and should be multiplied to the expression (4.48).

$$k_{\mathrm{so},\nu} = \frac{\sin\left(\nu \cdot s_{\mathrm{Q}}/(2r_{\mathrm{si}})\right)}{\nu \cdot s_{\mathrm{Q}}/(2r_{\mathrm{si}})}, \text{ where } k_{\mathrm{so},\nu=1} \approx 1 \text{ due to } \frac{s_{\mathrm{Q}}}{2r_{\mathrm{si}}} \ll 1 \qquad (4.57)$$

4.2.7. Torque and radial forces at concentric position

With the expression of the stator and rotor magnetic flux densities, the expression of the electromagnetic torque M_{e} as well as the expression of the electromagnetic single-sided forces F_{x} and F_{y} can be derived. First the force density vector in cylindrical coordinate $\boldsymbol{f}$ in the air gap linear region is calculated via *Maxwell* stress components $f_{\mathrm{r}}, f_{\theta}, f_{\mathrm{z}}$ with (4.58) where B_{r} (resp. B_{θ}) is the sum of all the stator and rotor radial (resp. tangential) magnetic flux density components, calculated in the previous sections 4.2.1-4.2.5.

$$\boldsymbol{f} = (f_{\mathrm{r}}, f_{\theta}, f_{\mathrm{z}})^{\mathsf{T}} = \left(\frac{B_{\mathrm{r}}^2 - B_{\theta}^2}{2\mu_0}, \frac{B_{\mathrm{r}} \cdot B_{\theta}}{\mu_0}, 0\right)^{\mathsf{T}} \qquad (4.58)$$

In order to obtain the torque M_{e}, the tangential *Maxwell* stress component f_{θ} is integrated over a closed surface S surrounding the rotor in the air gap region (4.59). The boundary effects, in axial direction, on both side of the rotor, are neglected. The obtained expression (4.59) is very simple and independent from the surface of integration S, since no current density and no variation of permeability is present in the air gap region 3 (Fig. 4.3). The coefficients $a_{1,3}^0$, $b_{1,3}^0$, $c_{1,3}^0$, $d_{1,3}^0$ and $c_{2,3}^0$ are valid for $\epsilon \approx 0$, which is denoted by the superscript 0.

$$M_{\mathrm{e}} = \int_0^{l_{\mathrm{Fe}}} \int_0^{2\pi} r \cdot f_{\theta}(r, \theta) \cdot \mathrm{d}\theta \cdot \mathrm{d}z = 2\pi\mu_0 l_{\mathrm{Fe}} \cdot (a_{1,3}^0 \cdot d_{1,3}^0 - b_{1,3}^0 \cdot c_{1,3}^0) \cdot \sin(\theta_1 - \theta_0) \qquad (4.59)$$

The torque expression (4.59) considers a magnet relative recoil permeability $\mu_{\mathrm{r,M}}$ different from 1. In [14] and [25], the torque calculation is derived considering $\mu_{\mathrm{r,M}} \neq 1$ for the permanent magnet field calculation, but with $\mu_{\mathrm{r,M}} = 1$ for the stator field calculation. Doing so, the calculated torque is still mathematically exact as long as it is integrated at the stator inner radius

$r = r_{\mathrm{si}}$. This is because the stator drive magnetic flux density $B_{\theta,3,\nu=1}(r,\theta)$ is independent from $\mu_{\mathrm{r,M}}$ at $r = r_{\mathrm{si}}$. In order to demonstrate this result, it is sufficient to insert r_{si} in the expression of $B_{\theta,3,\nu=1}(r,\theta)$ in (4.49).

For determination of the unbalanced radial magnetic forces F_{x} and F_{y} in the stator coordinate system, the magnetic force density components are integrated over a closed surface S surrounding the rotor in the air gap region 3. The force expressions into the direction x and y in the stator coordinate system are given by (4.60). Again the expressions are independent from the surface of integration S, in the air gap region 3, since no current density and no variation of permeability is present in the air gap.

$$\begin{aligned} F_{\mathrm{x}} &= \int_0^{l_{\mathrm{Fe}}} \int_0^{2\pi} (\cos\theta \cdot f_{\mathrm{r}}(r,\theta) - \sin\theta \cdot f_{\theta}(r,\theta)) \cdot \mathrm{d}\theta \cdot \mathrm{d}z \\ &= -4\pi\mu_0 l_{\mathrm{Fe}} c_{2,3}^0 \cdot (b_{1,3}^0 \cdot \cos(\theta_2 - \theta_0) + d_{1,3}^0 \cdot \cos(\theta_2 - \theta_1)) \\ F_{\mathrm{y}} &= \int_0^{l_{\mathrm{Fe}}} \int_0^{2\pi} (\sin\theta \cdot f_{\mathrm{r}}(r,\theta) + \cos\theta \cdot f_{\theta}(r,\theta)) \cdot \mathrm{d}\theta \cdot \mathrm{d}z \\ &= -4\pi\mu_0 l_{\mathrm{Fe}} c_{2,3}^0 \cdot (b_{1,3}^0 \cdot \sin(\theta_2 - \theta_0) + d_{1,3}^0 \cdot \sin(\theta_2 - \theta_1)) \end{aligned} \tag{4.60}$$

In (4.60) θ_0 is the direction of the rotor magnetisation and θ_1 and θ_2 are the phase angles of the current loading waves of (4.45). Both F_{x} and F_{y} contain a component of interaction of rotor magnet field with the levitation field ($\sim \cos(\theta_2 - \theta_0), \sim \sin(\theta_2 - \theta_0)$), as wanted, but also a unwanted component of interaction of rotor and drive field ($\sim \cos(\theta_2 - \theta_1), \sim \sin(\theta_2 - \theta_1)$). This yields two forces $F(p_0, p_2) = \sqrt{F_{\mathrm{x}}^2(\theta_2 - \theta_0) + F_{\mathrm{y}}^2(\theta_2 - \theta_0)}$ and $F(p_1, p_2) = \sqrt{F_{\mathrm{x}}^2(\theta_2 - \theta_1) + F_{\mathrm{y}}^2(\theta_2 - \theta_1)}$, where the latter is parasitic and unwanted. Thus it can be noticed that the drive field component $d_{1,3}^0$, together with the levitation field component $c_{2,3}^0$, generates a disturbing force $F(p_1, p_2) = \sqrt{F_{\mathrm{x}}^2 + F_{\mathrm{y}}^2}$. This results from the fact that the stator levitation field (with $p_2 = 2$) interacts with every two-pole field, and so not only with the rotor two-pole field, as wanted for magnetic levitation, but also with the stator drive field ($p_1 = 1$). In order to maximise the torque M_e in (4.59), the drive field phase angle θ_1 must fulfil the condition $\theta_1 = \theta_0 \pm \pi/2$, corresponding to the so called q-current operation. This condition implies due to $\theta_1 - \theta_0 = \pm\pi/2$, $\theta_2 - \theta_1 = \theta_2 - \theta_0 \mp \pi/2$, that the disturbing force component $F(p_1, p_2) \propto d^0_{1,3} \cdot c^0_{2,3}$ ($\sim (\theta_2 - \theta_1)$) in (4.60) is orthogonal to the desired levitation force $F(p_0, p_2) \propto b^0_{1,3} \cdot c^0_{2,3}$ ($\sim (\theta_2 - \theta_0)$) under q-current operation. Moreover, the field weakening with $\theta_1 = \theta_0 + \pi$ generates due $\theta_2 - \theta_0 = \theta_2 - \theta_1 + \pi$ with respect to $\theta_2 - \theta_1$ a disturbing force $F(p_1, p_2)$, opposing the levitation force $F(p_0, p_2)$. This result is intuitive since during the driving field weakening operation the rotor air gap field is reduced by the stator driving field, with which the levitation field interacts. This force disturbance $F(p_1, p_2)$ is proportional to the product of drive current and levitation current $i_1 \cdot i_2$ where the disturbance coefficient k_dist is given analytically in (4.64). It can be compensated via the control with for example a feed-forward of opposite expression, or it can be used to estimate the maximum model variations in a robust control design.

4.2.8. Torque and radial force disturbances due to rotor eccentricity

When the rotor is not at its concentric position, hence showing $\epsilon > 0$, the drive and levitation fields are modulated by the varying air gap width $\delta(\varphi)$, leading via the parasitic air gap eccentricity fields to additional torques and lateral forces. The analytical derivation of these disturbances is developed in this section. The electromagnetic torque M_e under rotor eccentricity ϵ at an angle γ (Fig. 4.4) is calculated with the superposition of the stator and rotor fields, derived in the previous sections 4.2.1 ÷ 4.2.5 (4.61). The calculation leads to four torque disturbances, listed in Table 4.2. The two disturbances $M(p_1^+, p_2)$ and $M(p_1, p_2^-)$ are negligibly small. The components $M(p_0, p_2^-)$ and $M(p_0^+, p_2)$ can be significant during rotor lift-up or after a strong radial disturbance where the eccentricity ϵ and the levitation current system i_2 are big. It should be noted that under static eccentricity $\epsilon = \text{const}$, $\gamma = \text{const}$, the disturbance torques are constant. Indeed, being stationary the levitation

Table 4.2.: Calculated torque and force components due to rotor eccentricity $\epsilon > 0$ and involved magnetic fields. Given the magnetic flux density B with p pole pairs at concentric rotor position $\epsilon = 0$, the modulated field pole counts are $p^+ = p + 1$ and $p^- = p - 1$. The subscripts 0, 1 and 2 indicate the rotor field, stator drive field and stator levitation field, respectively

Interaction	**Symbol**	**Expression**
Air gap torque	$M_\mathrm{e}(p_0,\, p_1)$	$2\pi\mu_0 l_\mathrm{Fe} \cdot (a^0_{1,3}d^0_{1,3} - b^0_{1,3}c^0_{1,3})$
Torque disturbance	$M(p_0,\, p_2^-)$	$2\epsilon\pi\mu_0 l_\mathrm{Fe} \cdot (a^0_{1,3}d^1_{1,3} - b^0_{1,3}c^1_{1,3})$
Torque disturbance	$M(p_0^+,\, p_2)$	$8\epsilon\pi\mu_0 l_\mathrm{Fe} \cdot (a^1_{2,3}d^0_{2,3} - b^1_{2,3}c^0_{2,3})$
Torque disturbance	$M(p_1,\, p_2^-)$	$2\epsilon\pi\mu_0 l_\mathrm{Fe} \cdot (c^0_{1,3}d^1_{1,3} - d^0_{1,3}c^1_{1,3})$
Torque disturbance	$M(p_1^+,\, p_2)$	$8\epsilon\pi\mu_0 l_\mathrm{Fe} \cdot (c^1_{2,3}d^0_{2,3} - d^1_{2,3}c^0_{2,3})$
Lateral force	$F_\mathrm{ir}(p_0,\, p_2)$	$4\pi\mu_0 l_\mathrm{Fe} c^0_{2,3} b^0_{1,3}$
Force disturbance	$F_\mathrm{dist}(p_1,\, p_2)$	$4\pi\mu_0 l_\mathrm{Fe} c^0_{2,3} d^0_{1,3}$
Negative stiffness	$F_\mathrm{sr}(p_0,\, p_0^+)$	$4\epsilon\pi\mu_0 l_\mathrm{Fe} a^1_{2,3} b^0_{1,3}$
Stiffness disturbance	$F(p_1,\, p_1^+)$	$4\epsilon\pi\mu_0 l_\mathrm{Fe} c^1_{2,3} d^0_{1,3}$
Stiffness disturbance	$F(p_2,\, p_2^-)$	$4\epsilon\pi\mu_0 l_\mathrm{Fe} d^1_{1,3} c^0_{2,3}$
Stiffness disturbance	$F(p_2,\, p_2^+)$	$12\epsilon\pi\mu_0 l_\mathrm{Fe} c^1_{3,3} d^0_{2,3}$
Force disturbance	$F(p_0,\, p_1^+)$	$4\epsilon\pi\mu_0 l_\mathrm{Fe} c^1_{2,3} b^0_{1,3}$
Force disturbance	$F(p_0^+,\, p_1)$	$4\epsilon\pi\mu_0 l_\mathrm{Fe} a^1_{2,3} d^0_{1,3}$

winding contributes to the power conversion, as it is induced by the rotor field according to (4.41). As the commonly encountered eccentricities ϵ in practice are due to rotor unbalance and are therefore rotating with rotor speed according to $\gamma(t) = 2\pi n t + \gamma_0$, the torque disturbances are depending on $\gamma(t)$ and are pulsating torque components with average value zero.

$$\begin{aligned} M_\mathrm{e}(\epsilon) &= 2\pi\mu_0 l_\mathrm{Fe} \cdot (a^0_{1,3}d^0_{1,3} - b^0_{1,3}c^0_{1,3}) \cdot \sin(\theta_1 - \theta_0) \\ &+ 2\epsilon\pi\mu_0 l_\mathrm{Fe} \cdot (a^0_{1,3}d^1_{1,3} - b_{1,3}c^1_{1,3} + 4 \cdot (a^1_{2,3}d^0_{2,3} - b^1_{2,3}c^0_{2,3})) \cdot \sin(\theta_2 - \theta_0 - \gamma) \\ &+ 2\epsilon\pi\mu_0 l_\mathrm{Fe} \cdot (c^0_{1,3}d^1_{1,3} - d_{1,3}c^1_{1,3} + 4 \cdot (c^1_{2,3}d^0_{2,3} - d^1_{2,3}c^0_{2,3})) \cdot \sin(\theta_2 - \theta_1 - \gamma) \end{aligned} \tag{4.61}$$

In the same manner, the electromagnetic lateral force F_{x} is calculated with the principle of field superposition in (4.62).

$$\begin{aligned} F_{\mathrm{x}}(\epsilon) = & -4\pi\mu_0 l_{\mathrm{Fe}} c^0_{2,3} \cdot (b^0_{1,3} \cdot \cos(\theta_2 - \theta_0) + d^0_{1,3} \cdot \cos(\theta_2 - \theta_1)) \\ & - 4\epsilon\pi\mu_0 l_{\mathrm{Fe}} \cdot (a^1_{2,3} b^0_{1,3} + c^1_{2,3} d^0_{1,3} + d^1_{1,3} c^0_{2,3} + 3c^1_{3,3} d^0_{2,3}) \cdot \cos\gamma \\ & - 4\epsilon\pi\mu_0 l_{\mathrm{Fe}} c^1_{2,3} b^0_{1,3} \cdot \cos(\theta_1 - \theta_0 + \gamma) \\ & - 4\epsilon\pi\mu_0 l_{\mathrm{Fe}} a^1_{2,3} d^0_{1,3} \cdot \cos(\theta_1 - \theta_0 - \gamma) \end{aligned} \tag{4.62}$$

The disturbance forces are listed in Table 4.2. The already calculated negative stiffness corresponds to the force component $F(p_0, p_0^+)$. Since $p_0 = 1$, the second component of the negative stiffness $F(p_0, p_0^-)$ is zero as there cannot be any homo-polar field in the considered geometry. As displayed in (4.62), the levitation field as well as the drive field contribute to an increased negative stiffness with the components $F(p_1, p_1^+)$, $F(p_2, p_2^+)$ and $F(p_2, p_2^-)$. As the force amplitudes are proportional to the square of the flux density amplitudes, the increase of stiffness is negligible as long as the rotor field amplitude is higher than the one of the stator fields. With increasing electromagnetic utilisation however, the resulting negative stiffness increases. There are two additional disturbances $F(p_0, p_1^+)$ and $F(p_0^+, p_1)$ that do not belong to the negative stiffness, since the forces are not orientated in the direction of the eccentricity angle γ. Even if these components are not negligible, they are playing a minor role as long as the eccentricity ϵ is small. Again these expressions can be used to characterise the model variation.

Table 4.2 gives an overview of all interactions between the three fundamental fields and and the parasitic eccentricity fields and the related disturbing torques and lateral forces. Since all the lateral force disturbances result from products of field amplitudes, the amplitude of the stator drive field and stator levitation field must be, by design, kept small compared to the one of the rotor field. Under these conditions, most of the disturbance components in Table 4.2 are negligibly small or compensated by a moderate control stiffness k_{P}. The motor behaviour is then linear and simple to control. This is one reason why the specific lateral force density and the electromagnetic utilization, commonly encountered in self-bearing motors, are inherently low compared to drives with magnetic bearings. For the same reason, the overload capability as well as the field weakening capability, commonly substantial in permanent magnet based motors, is a source of tendency towards instability of the magnetic levitation in active self-bearing drives.

4.3. Electromagnetic model of the active self-bearing machine

From the previous equations of Section 4.2.7 and 4.2.8, a simplified model of the self-bearing machine is derived. To simplify the representation, only the forces and torque at the concentric position ($\epsilon = 0$) are considered, together with the negative stiffness k_{sr} at $\epsilon \neq 0$ (4.36) in the x-y-coordinate frame due to the rotor field. The lateral force and the torque expressions (4.62) and (4.61) can be factorised in the form (4.63), where the coefficients k_{ir}, k_{dist}, k_{sr} and k_{M} are given by (4.64) for $\mu_{\mathrm{r,M}} \approx 1$ and $\mu_{\mathrm{Fe}} \to \infty$.

$$\begin{aligned} F_{\mathrm{x}} &= k_{\mathrm{ir}} \cdot i_{2,\mathrm{d}} + k_{\mathrm{dist}} \cdot (i_{2,\mathrm{d}} \cdot i_{1,\mathrm{d}} - i_{2,\mathrm{q}} \cdot i_{1,\mathrm{q}}) - k_{\mathrm{sr}} \cdot x \\ F_{\mathrm{y}} &= k_{\mathrm{ir}} \cdot i_{2,\mathrm{q}} + k_{\mathrm{dist}} \cdot (i_{2,\mathrm{q}} \cdot i_{1,\mathrm{d}} + i_{2,\mathrm{d}} \cdot i_{1,\mathrm{q}}) - k_{\mathrm{sr}} \cdot y \\ M &= k_{\mathrm{M}} \cdot i_{1,\mathrm{q}} \end{aligned} \tag{4.63}$$

$$\begin{aligned} k_{\mathrm{sr}} &\approx -\frac{\pi l_{\mathrm{Fe}}}{\mu_0} \cdot \frac{r_{\mathrm{si}}^4 \cdot \left(r_{\mathrm{mo}}^2 - r_{\mathrm{ro}}^2\right)^2}{\left(r_{\mathrm{si}}^2 - r_{\mathrm{ro}}^2\right)^3 \cdot \left(r_{\mathrm{si}}^2 + r_{\mathrm{ro}}^2\right)} \cdot B_{\mathrm{rem}}^2 \\ k_{\mathrm{ir}} &\approx 3 N_{\mathrm{s},2} k_{\mathrm{w},2} l_{\mathrm{Fe}} \cdot \frac{r_{\mathrm{si}}^4 \cdot \left(r_{\mathrm{mo}}^2 - r_{\mathrm{ro}}^2\right)}{\left(r_{\mathrm{si}}^2 - r_{\mathrm{ro}}^2\right)^2 \cdot \left(r_{\mathrm{si}}^2 + r_{\mathrm{ro}}^2\right)} \cdot B_{\mathrm{rem}} \\ k_{\mathrm{dist}} &\approx \frac{2\mu_0 3^2 N_{\mathrm{s},1} k_{\mathrm{w},1} N_{\mathrm{s},2} k_{\mathrm{w},2} l_{\mathrm{Fe}}}{\pi} \cdot \frac{r_{\mathrm{si}}^3 \cdot r_{\mathrm{ro}}^2}{\left(r_{\mathrm{si}}^2 - r_{\mathrm{ro}}^2\right)^2 \cdot \left(r_{\mathrm{si}}^2 + r_{\mathrm{ro}}^2\right)} \\ k_{\mathrm{M}} &\approx \frac{\pi N_{\mathrm{s},1} k_{\mathrm{w},1} l_{\mathrm{Fe}}}{\mu_0} \frac{r_{\mathrm{si}}^4 \cdot \left(r_{\mathrm{mo}}^2 - r_{\mathrm{ro}}^2\right)^2}{\left(r_{\mathrm{si}}^2 - r_{\mathrm{ro}}^2\right)^3 \cdot \left(r_{\mathrm{si}}^2 + r_{\mathrm{ro}}^2\right)} \cdot B_{\mathrm{rem}} \end{aligned} \tag{4.64}$$

An equivalent model of radial lateral forces is derived in Figure 4.5.

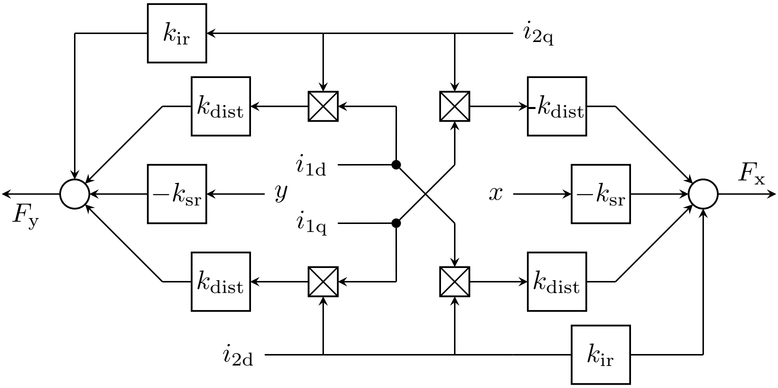

Figure 4.5.: Simplified current-force model of the self-bearing motor at the concentric rotor position $\epsilon = 0$ and lateral movements x, y

4.4. Recommendations for motor parameter calculation

The field expressions for any rotor magnetisation pattern or stator current loading can be found in the literature or may be calculated by hand without too much difficulty. It can be done with the scalar potential ψ or the vector potential A that has only one axial component in 2D. If the magnetic flux density should be evaluated in infinitely permeable parts (e.g. rotor), the vector potential A should be preferred. When the order n (as pole count) of the calculated harmonic field is big, care should be taken during numerical evaluation. In order to prevent numerical conditioning issues, the field coefficients a_{n}, b_{n}, c_{n} and d_{n} should be normalised for instance by the stator inner radius r_{si}. In this case, the normalised coefficients are $a_{\mathrm{n}}^* = a_{\mathrm{n}} \cdot r_{\mathrm{si}}^n$ and $b_{\mathrm{n}}^* = b_{\mathrm{n}}/r_{\mathrm{si}}^n$.

The field calculation at rotor eccentricity ϵ should be done preferably in the rotor coordinate system, since the system of equation is identical to that one at rotor concentric position $\epsilon = 0$. Only the boundary conditions at the stator inner radius r_{si} must be determined, as shown in (4.21). For each field harmonic of order $n > 1$, two systems of order $n-1$ and $n+1$ need to be solved due to the field modulation by the non-constant air gap $\delta(\varphi)$.

The calculation becomes troublesome when the torque and lateral forces are integrated, in particular at rotor eccentricity $\epsilon > 0$. The size of the expressions is quickly getting difficult to manage, so that analytic solvers such as *Mathematica* or *Matlab* (in *syms* environment) are not able to simplify the solution of the torque and forces even in problems as simple as the one presented in this chapter. Fortunately, being aware of some remarkable properties of the equations facilitates the calculation significantly, as it will be discussed in short.

The superposition of the different field distributions in the cylindrical coordinate system can always be factorised in the form with separated variables (4.65) where all the coefficients $k_{\mathrm{i,j}}$ can be a function of any parameter (geometry, stator current loading, eccentricity etc...).

$$\begin{aligned} B_{\mathrm{r}}(r,\theta) &= \sum_{n=1}^{\infty}(k_{1,n}\cdot r^{n-1}+k_{2,n}\cdot r^{-n-1})\cdot\cos(n\cdot\theta-\theta_{\mathrm{n}}) \\ B_{\theta}(r,\theta) &= \sum_{n=1}^{\infty}(k_{3,n}\cdot r^{n-1}+k_{4,n}\cdot r^{-n-1})\cdot\cos(n\cdot\theta-\theta_{\mathrm{n}}) \end{aligned} \tag{4.65}$$

Since the torque solution is a scalar, the integration of the magnetic *Maxwell* force densities f_{θ} in (4.59) must be independent from the surface of integration S, closing in the air gap region arround the rotor. Using an elementary surface element $\mathrm{d}S(r) = l_{\mathrm{Fe}}\cdot r\cdot\mathrm{d}\theta$, centred with respect to the coordinate system (r,θ), the integration becomes (4.66).

$$M_{\mathrm{e}} = l_{\mathrm{Fe}}\cdot\int_{\theta=0}^{2\pi} r^2\cdot f_{\theta}(r,\theta)\cdot\mathrm{d}\theta \tag{4.66}$$

Since the integration is independent from r within the air gap, only the elements of the magnetic force densities f_{θ} that have a radial dependency with r^{-2} can generate torque. Doing the product of B_{r} and B_{θ} from (4.65) to calculate f_{θ}, it results that only the products $k_{1,n}\cdot k_{4,n}$ and $k_{2,n}\cdot k_{3,n}$ lead to a non-vanishing torque. All the other products $k_{1,i}\cdot k_{4,j}$ and $k_{2,i}\cdot k_{3,j}$

with $i \neq j$ as well as all the products $k_{1,i} \cdot k_{3,j}$ and $k_{2,i} \cdot k_{4,j}$ do not need to be evaluated since they cannot contribute to torque. It proved also that two fields can generate torque, if and only if they have the same number of pole pairs p.

The same procedure is repeated for the integration to determine the lateral forces (4.60). This time, only the elements of the magnetic force densities f_{r} and f_{θ} that have a radial dependency with r^{-1} contribute to the resulting lateral forces F_{x}, F_{y}. It results that only the double product terms $k_{1,n+1} \cdot k_{2,n}$ and $k_{3,n+1} \cdot k_{4,n}$ lead to such a force. This proves also that two fields can generate force if and only if they have a pole pair number p differing by one.

5. Conical self-bearing motor

5.1. Motor description

Conventional self-bearing motors are designed with cylindrical rotors and produce only radial lateral forces for magnetic levitation. The axial displacement is passively stable since the magnetised rotor aligns with the stator iron stack axially. However, it cannot be controlled actively and leads to weakly damped position oscillations. In order to generate controllable axial forces without the use of an additional thrust magnetic bearing, some axial asymmetry must be provided. For example, the self-bearing motor can be designed with a conical rotor shape or with a skewed stator winding. The first approach is used in [26] while the second is used in [27]. The prototype in Figure 7.1 is composed of two half-motors each rated for 500 W and 18 000 rpm. Each half motor "a" (at DE) and "b" (at NDE) is composed of a three-phase two-pole stator driving winding and a three-phase four-pole stator levitation winding. The driving winding, excited with the current system $(i_{1\mathrm{Ua}}, i_{1\mathrm{Va}}, i_{1\mathrm{Wa}})$ (resp. $(i_{1\mathrm{Ub}}, i_{1\mathrm{Vb}}, i_{1\mathrm{Wb}})$), generates with the magnetised rotor a torque and an axial force. The levitation winding, excited with the current system $(i_{2\mathrm{Ua}}, i_{2\mathrm{Va}}, i_{2\mathrm{Wa}})$ (resp. $(i_{2\mathrm{Ub}}, i_{2\mathrm{Vb}}, i_{2\mathrm{Wb}})$), generates lateral forces. The rotor is composed of two opposed two-pole surface-mounted NdFeB permanent magnets. In order to obtain a pure fundamental field, the magnets are diametrically magnetised. Since the motor is small, the two ring magnets are not segmented. Each magnet is fixed by a carbon bandage. Since the rotor magnets have a conical shape (at inner and outer surface), two axial forces are concurring in the air gaps.

The self-centring axial force keeps the rotor position aligned with the stator as for conventional cylindrical self-bearing motors. The rotor magnetic field in the air gap penetrates the stator iron orthogonally. Since the stator inner surface is a cone, the magnetic field pulls the rotor axially towards the stator. Depending on the cone angle α (Fig. 5.1), the destabilising force can overcome the stabilising self-alignment.

5.2. Magnetic fields

The air gap field has now an axial dependency due to the conical air gap shape. The torque and force equations obtained in Chapter 4 are not valid for this motor geometry. Additionally, the axial magnetic stiffness, which is necessary to obtain a model of the suspension in axial direction, requires the calculation of the axial magnetic field. Two effects are involved in the expression of the axial magnetic stiffness. First, the misalignment in axial direction of the rotor and stator lengthen the path of the magnetic field in the air gap, leading to a counteracting magnetic pull to align rotor and stator axially. This stabilising component is well-known and was already determined analytically for cylindrical rotors in [28]. Second, the conical shape of the air gap leads to an axial field component that pulls the rotor out of the aligned position. This second component is destabilising. In order to obtain the exact expression of the resulting axial magnetic stiffness, the boundary conditions at the edges of the iron stack must be considered. The conformal mapping method is well suited for this kind of problem. While this method is used successfully for the determination of the axial magnetic pull of cylindrical machines in [28], it does not lead to the analytical expression of the axial force for the conical rotor form. The reason is that the *Schwarz-Christoffel* mapping to transform a polygonal boundary with more than two vertices, that are not multiples of $\pi/2$, leads to a differential equation whose integral has no analytical solution [29]. Since the boundary of the prototype has four angles that are not right-angled, no analytical solution can be found. In order to avoid this difficulty, the calculation derived

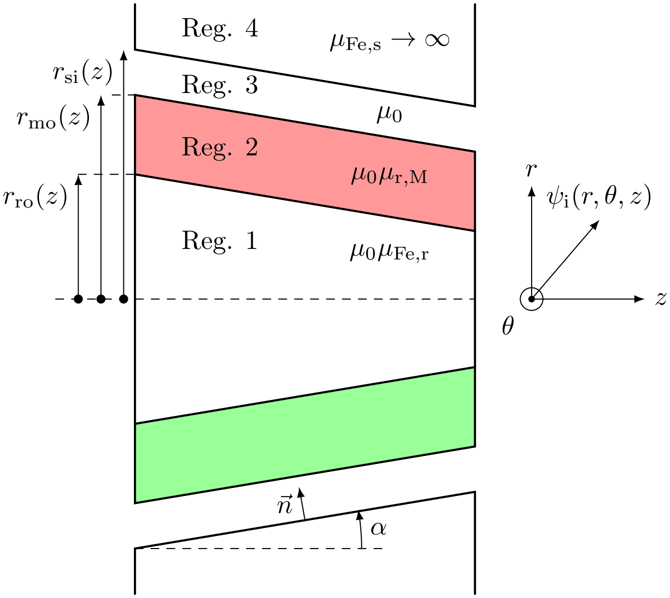

Figure 5.1.: Definition of the geometry with relevant machine parameters for the calculation of the axial magnetic field.

here disregards the border effects and consequently gives an overestimation of the resulting magnetic stiffness.

5.2.1. Magnetic fields at no-load and without rotor eccentricity

The analytical expression for the magnetic field of this motor prototype (Fig. 5.1) is different from the one calculated in Chapter 4 since the conical air gap is not of cylindrical symmetry. In order to obtain the magnetic radial stiffness, the analytical calculation in Chapter 4 is performed in the three dimension problem, considering the conical air gap. A cut view of the model in the axial direction is given in Figure 5.1 with the dimensions. The surface mounted two-pole permanent magnet is diametrically magnetised. *Laplace*'s equation and *Poisson*'s equation, that govern the scalar potential

ψ in the three-dimension cylindrical problem, are given in (5.1) and (5.2).

$$\frac{\partial^2\psi_i}{\partial r^2}+\frac{1}{r}\frac{\partial\psi_i}{\partial r}+\frac{1}{r^2}\frac{\partial^2\psi_i}{\partial\theta^2}+\frac{\partial^2\psi_i}{\partial z^2}=0,\ \text{with } i\in\{1,3\} \tag{5.1}$$

$$\frac{\partial^2\psi_2}{\partial r^2}+\frac{1}{r}\frac{\partial\psi_2}{\partial r}+\frac{1}{r^2}\frac{\partial^2\psi_2}{\partial\theta^2}+\frac{\partial^2\psi_2}{\partial z^2}=\frac{1}{\mu_{\mathrm{r,M}}}\cdot\left(\frac{M_{\mathrm{r}}}{r}+\frac{\partial M_{\mathrm{r}}}{\partial r}+\frac{1}{r}\frac{\partial M_{\theta}}{\partial\theta}+\frac{\partial M_{\mathrm{z}}}{\partial z}\right) \tag{5.2}$$

In order to obtain the basis functions that are solution of these equations, the method of the separation of variables [18] is used. The magnetic scalar potential $\psi(r,\theta,z)$ is written in the form (5.3) as a product of functions of separated variables.

$$\psi(r,\theta,z)=f(r)\cdot g(\theta)\cdot h(z) \tag{5.3}$$

The expression (5.3) is inserted in (5.1) to obtain (5.4).

$$\frac{1}{rf(r)}\frac{\partial f(r)}{\partial r}+\frac{1}{f(r)}\frac{\partial^2 f(r)}{\partial r^2}+\frac{1}{r^2g(\theta)}\frac{\partial^2 g(\theta)}{\partial\theta^2}+\frac{1}{h(z)}\frac{\partial^2 h(z)}{\partial z^2}=0 \tag{5.4}$$

As r, θ and z may vary independently, the expressions with r, resp. with θ and z must be each constant, e.g. the expression depending on z is equal k, so that (5.4) is fulfilled. It follows that the function $h(z)$ fulfils the second order differential equation (5.5).

$$\frac{\mathrm{d}^2h(z)}{\mathrm{d}z^2}=k\cdot h(z),\ \text{with } k\in\mathbb{R} \tag{5.5}$$

The general solution of (5.5) for $k\neq 0$, as well as the particular solution for $k=0$, is given in (5.6). The value of β depends on the boundary conditions.

$$\begin{aligned} h(z)&=A\cdot\exp(\beta z)+B\cdot\exp(-\beta z), &&\text{with } \beta^2=k\neq 0\\ h(z)&=A\cdot z+B, &&\text{for } k=0\end{aligned} \tag{5.6}$$

The function $g(\theta)$ fulfils the same equation (5.7) as for the calculation, performed for the cylindrical rotor in Chapter 4. Indeed, the conical shape of the rotor does not alter the periodicity of the field along the rotor circumference so that the magnetic field, resulting from the diametrically magnetised two-pole rotor magnets, is a pure fundamental field.

$$\frac{\mathrm{d}^2 g(\theta)}{\mathrm{d}\theta^2} = p^2 \cdot g(\theta), \text{ with } p = \text{rotor field pole pair number} \tag{5.7}$$

In contrast, the function $f(r)$ now fulfils the equation (5.8) whose solutions are given by the *Bessel* functions of first kind.

$$r^2 \cdot \frac{\partial^2 f(r)}{\partial r^2} + r \cdot \frac{\partial f(r)}{\partial r} + (\beta^2 r^2 - p^2) \cdot f(r) = 0 \tag{5.8}$$

$$\begin{aligned} \forall i \in \{1,2,3\}, (\boldsymbol{B_{i+1}}(r,\theta,z) - \boldsymbol{B_i}(r,\theta,z)) \cdot \boldsymbol{n_{i,i+1}}(r,z)\Big|_{(r,z)\in r_{i,i+1}} &= 0 \\ \forall i \in \{1,2\}, (\boldsymbol{H_{i+1}}(r,\theta,z) - \boldsymbol{H_i}(r,\theta,z)) \times \boldsymbol{n_{i,i+1}}(r,z)\Big|_{(r,z)\in r_{i,i+1}} &= 0 \\ -\boldsymbol{H_3}(r,\theta,z) \times \boldsymbol{n_{3,4}}(r,z)\Big|_{(r,z)\in r_{\mathrm{si}}} &= \boldsymbol{j_\mathrm{s}} \end{aligned} \tag{5.9}$$

$$\boldsymbol{n_{i,i+1}}(r,\theta,z) \approx (\cos\alpha,\ 0,\ -\sin\alpha)^{\mathsf{T}} \tag{5.10}$$

At the stator inner radius r_{si}, the boundary conditions are (5.9) where $\boldsymbol{j_\mathrm{s}}$ is the current loading vector at stator inner radius and $\boldsymbol{n}$ is a unity vector, which is orthogonal to the stator inner surface. They lead to the relations (5.11). The axial field at the stator inner radius is always proportional to the radial field with the proportionality coefficient -$\tan\alpha$. Therefore, the radial and axial magnetic pull are interlinked.

$$\begin{aligned} \forall\theta \in [0, 2\pi], H_{\mathrm{z},3}(r,\theta,z) &= -\tan\alpha \cdot H_{\mathrm{r},3}(r,\theta,z) \\ j_{\mathrm{r}}(r,\theta,z) &= \tan\alpha \cdot j_{\mathrm{z}}(r,\theta,z) \end{aligned} \tag{5.11}$$

The boundary conditions (5.9) can only be fulfilled by an infinite number of *Bessel* functions of first kind due to the discontinuities at both rotor ends. Therefore, the exact analytical solution can not be derived in the geometry from Figure 5.1. In order to overcome the problem, an approximation is proposed here. The intersection of the geometry from Figure 5.1 and a cone of equation $z = r_{\mathrm{ro}} + \tan\alpha \cdot r$, orthogonal to the region boundaries, is a very flat cut cone with the outer radius r_{si} and inner radius r_{ro} and the height $(r_{\mathrm{si}} - r_{\mathrm{ro}}) \cdot \tan \alpha$. The solution of the field calculation in cylindrical coordinates in Chapter 4 is applied as an approximation to this surface. As long as the cone angle α is small, the obtained approximative expression is acceptable.

In order to validate this approach, the radial and axial field fundamental components are evaluated at the inner stator radius r_{si} for the prototype [26] both with the presented analytical method and with a 3D FEM simulation (with the program *JMAG*) along the axial length $l_{\mathrm{Fe}} = 40$ mm at zero stator current. The $B(H)$ characteristic of M270-35A was used for the stator iron stack, and the non-laminated was assumed to have $\mu_{\mathrm{Fe}} = 4\ 000$. The air gap mesh has three layers in the carbon fibre bandage layer and three additional layers inside the mechanical air gap. The model has a 6 mm air layer on each side of the iron stack, to tack into account the axial flux fringing. The mesh model was taken from [14], so no further mesh refinement calculations were done to investigate the mesh size influence in the numerical results. More details on the FEM model are given in [14]. The evaluation is shown in Figure 5.3. The analytical approximation gives good results in the axial middle of the air gap, while the end effects lead to substantial discrepancies at both axial ends. The influence of the end effects is different on the radial and axial field components. The radial field components are analytically overestimated slightly on the side, so that the analytically obtained radial force displacement coefficient is too high. The axial field component however is increasing significantly at both axial ends, so that the obtained axial force displacement coefficient does not fit with the coefficient obtained in 3D FEM at all. Since the magnetic pull forces depend on the square of the magnetic flux density, the axial magnetic pull is dominated by the axial border effects. Additionally, the axial magnetic pull is compensated by the self-centering effect of the rotor with the stator which is not considered analytically. This effect is so dominant that the resulting axial force displacement is almost negligible, compared to the one obtained analytically. This was also observed during experimental identification of the prototype parameters [52].

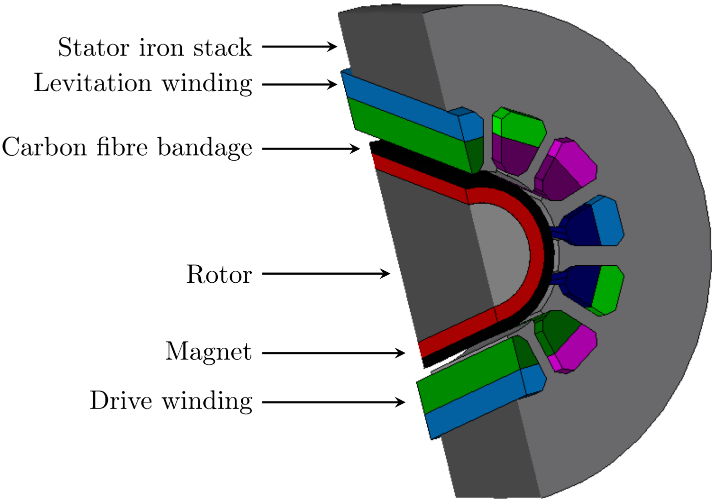

Figure 5.2.: Cut-view of the 3D model implemented in *JMAG* to validate the calculation of the field amplitudes along the axial length.

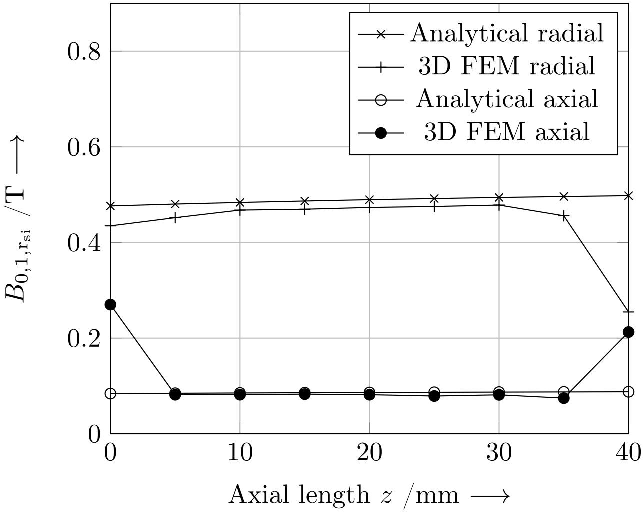

Figure 5.3.: Calculated radial and axial amplitude of the magnetic flux density fundamental $B_{0,1}$ at the stator inner radius r_{si} along the axial length z at no-load (currents are zero).

5.2.2. Magnetic fields at no-load under eccentricity and axial displacement

In the case of the conical rotor, the rotor can be displaced in two dimensions. It has a radial eccentricity ϵ and an axial displacement Δz. The calculation under radial eccentricity ϵ follows the same approach as in Chapter 4 with the approximation, proposed in Section 5.2.1. The axial displacement changes the stator boundary of both half motors DE and NDE according to (5.12).

$$\begin{aligned} r_{\mathrm{si,DE}}(\Delta z) &= r_{\mathrm{si}} - \tan\alpha \cdot \Delta z \\ r_{\mathrm{si,NDE}}(\Delta z) &= r_{\mathrm{si}} + \tan\alpha \cdot \Delta z \end{aligned} \tag{5.12}$$

Since the radial displacement Δz is limited to ±150...200 µm and since the cone angle $\alpha = 10°$ is small, the actual change of magnetic air gap length is very small (below 0.5%). The variation of the flux amplitude lies well below the inaccuracy, resulting from the approximation method, and is therefore neglected.

5.3. Forces and torque

5.3.1. Radial force-current coefficient

As for cylindrical machines, the conical self-bearing prototype has a radial stiffness k_{sr} and a radial force-current coefficient k_{ir} that can be calculated by integration of the *Maxwell* stress tensor as in Chapter 4. Since the field calculation approximation, presented in Section 5.2.1, gives a local field at the stator inner radius $r_{\mathrm{si}}(z)$, it must be integrated numerically along the axial length l_{Fe} at $r_{\mathrm{si}}(z)$. For simplicity, the axial length is cut in eight "cylindrical" sections where the radial and axial magnetic flux densities, given in Figure 5.3, are assumed constant in each section. The force-current coefficient is obtained by summation of the forces (4.60) on each section resulting from the levitation current system i_2. It should be noticed that the current loading $A_2(r = r_{\mathrm{si}}, \theta)$ (4.45), as well as the radial component of the rotor magnetic flux density $B_{\mathrm{PM,r}}(r = r_{\mathrm{si}}, \theta)$ (4.15), is changing in each section since the stator inner radius r_{si} depends on z. The numerical integration gives a radial force-current coefficient k_{ir} = 2.21 N/A, which is higher than the one obtained with the 3D finite element method (2.12 N/A) [14] and the one obtained experimentally (2.05 N/A) [14].

5.3.2. Radial stiffness

The numerical integration of the radial stiffness k_{sr} follows with the summation of the stiffness given by each "cylindrical" section with (4.36). As for the cylindrical rotor under radial eccentricity $\epsilon > 0$, the two-pole fundamental flux density amplitude $B_{0,1,\mathrm{r_{si}}}$ is unchanged at $\epsilon > 0$. However, a four-pole field results from the modulation of the rotor field with the varying air gap $\delta(\varphi)$. The resulting negative radial stiffness is obtained numerically by summation of each stiffness value per axial section with again eight axial cylindrical sections and gives k_{sr} = -31.4 N/mm. It is measured during the experiments, described in Chapter 8 and equals -26 N/mm.

5.3.3. Axial force-current coefficient

The axial force-current coefficient k_{iz} is obtained via numerical FEM simulation in [14] and is equal 2.26 N/A. It is also validated in measurement in [26] with 2.4 N/A. However, as described in 5.2.2, as the axial end field is determined only numerically with sufficient accuracy, it can not be calculated analytically.

5.3.4. Axial stiffness

For the same reason as explained in 5.3.3, since the analytically calculated axial magnetic flux density is considerably deviating from the one calculated with FEM, the single-sided axial stiffness is calculated by evaluation of the axial magnetic pull F_z via FEM at the DE and NDE for several different values of axial displacement $\Delta z =$ -150...-100...150 µm. By that, the axial pull difference (5.13) is derived approximately as a function of the displacement Δz. The axial stiffness coefficient k_sz is obtained with a linear regression of the calculated curve $F_\mathrm{z}(\Delta z)$ via (5.13).

$$F_{\mathrm{z,DE}}(\Delta z) - F_{\mathrm{z,NDE}}(-\Delta z) \approx -k_{\mathrm{sz}} \cdot \Delta z \tag{5.13}$$

For this particular prototype [26], the axial pull difference (5.13) is for values $\Delta z <$ 150 µm below 0.1 N and may be regarded in comparison to the other radial lateral force values as nearly zero. During the experiments, the axial position of this particular conical motor prototype is unstable, but the axial stiffness is too small to be measurable (i.e. for Δz in ±150 µm, the dependency $i_{1\mathrm{d}} = f(\Delta z)$ is nearly zero, resulting in a flat curve $i_{1\mathrm{d}} = f(\Delta z)$) for -150 µm $< \Delta z <$ 150 µm.

5.3.5. Interference forces

In Chapter 4.3, the force interferences due to the interaction of the drive field and the levitation field were presented. In this section, the force interference due to the driving field at rotor centre position $\Delta z = 0$, $\Delta\epsilon = 0$, is calculated and compared to measurements on the prototype. With equation (4.64) evaluated for the center cross-section $z =$ 20 mm of the prototype, the force interference coefficient is calculated to be $k_\mathrm{dist} =$ 0.021 N/A^2. When the prototype is operated at nominal radial levitation force $F_\mathrm{r,N} =$ 17.4 N and nominal torque $M_\mathrm{N} =$ 0.16 Nm, the interference force, which is orthogonal to the direction of the levitation force $F_\mathrm{r,N}$, is equal $k_\mathrm{dist} \cdot \sqrt{2} \cdot I_{1,\mathrm{N}} \sqrt{2} I_{2,\mathrm{N}}$ = 1.73 N. Divided by the radial force $F_\mathrm{r,N}$, this interference corresponds to a small shifting of the levitation force direction of F_r of 5.7° and leads to an increase of 0.5% of its amplitude F_r. As displayed in Figure 7.9, this misalignment of the levitation force direction has only little influence on the control stability, as demonstrated in section 7.3.4.

6. Self-bearing motor with combined torque and force winding

6.1. Stator winding description

One disadvantage, encountered during the design of the self-bearing motor, is that the stator slot cross section A_{slot} must be split in two areas to insert the drive and levitation winding separately. The bigger winding phase resistance, resulting from the smaller copper cross section, due to the limited slot space for the windings, leads to higher ohmic losses. An alternative is given when both the drive field and the levitation field are generated with the same winding. As explained previously, the levitation field must have a pole pair number that differs from the drive field by one. Furthermore, the current system for production of the lateral force and the current system for the torque must be separately controllable. Unfortunately, a conventional distributed winding does not have any consecutive harmonics with ordinal number difference of ± 1, since the even harmonics are missing due to the symmetry of north and south pole field distribution. Therefore, to that end, fractional winding can be used. In that case, a careful design is necessary not to produce sub-harmonic combinations that produce unwanted lateral forces or a lot of field harmonics with higher order that would cause increased iron losses at high-speed. In order to obtain two consecutive harmonics of the order n and $n \pm 1$ with a distributed winding, a two-layer three-phase

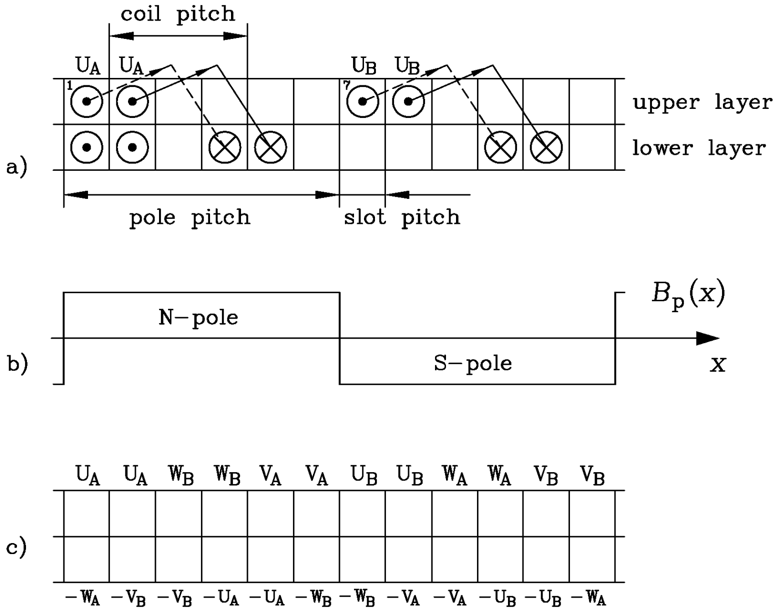

Figure 6.1.: Winding disposition of a dual (A and B) three-phase bearingless motor with two windings A and B: a) Half-pitched distributed stator winding of phase U, b) two pole PM rotor field, c) phase belt of winding A and B with each three phases U, V, W.

distributed winding is split into two three-phase antisymmetric three-phase windings. Figure 6.1 illustrates the split of a four-pole two-layer distributed winding, where the two opposing coils of phase U, named U_A and U_B, that are originally connected in series, are split into two separate branches A and B. The coils U_A, V_A and W_A are star-connected to form one three-phase winding named A. The same is done for the coils U_B, V_B and W_B to form the winding B. The windings A and B are spatially distanced by one pole pitch. The harmonic content of the field distribution of each winding A and B is now different to the conventional six-zone windings, because A and B are three-zone windings. At six zones the phase belt is U, -W, V, -U, W, -V, and at three zones it is U, V, W, so that north and south poles are not any longer symmetrical. Therefore the harmonics of the *Fourier* series of the radial field distribution contains also even ordinal numbers, i.e. it contains the ordinal numbers $\nu = 1 + mg$ with the number of phases $m = 3$ and $g \in \mathbb{Z}$. In order to produce torque and lateral radial forces with the winding A or B with the pole pair number p, two ordinal numbers ν_1 and ν_2 of the resulting air gap radial field distribution, described as *Fourier* series, should fulfil the relation $p \cdot |\nu_1| = p \cdot |\nu_2| \pm 1$. This equation, with the unknowns p, ν_1 and ν_2, can be set in four equations without modulus. However, only one of the four equations has solutions in $\mathbb{Z}^2$ and the solution is given by $p = 1$ and $\nu_1 = -\nu_2 - 1$. Therefore, the winding combination of A and B produces torque and lateral forces only for the case of a two-pole or four-pole winding. In case of a two-pole rotor field $p_1 = p = 1$, the driving field has one pole pair $p_1 = p \cdot |\nu_1| = 1$ and the levitation field has two pole pairs $p_2 = p \cdot |\nu_2| = 2$. Since $\nu_2 = -2$, the levitation field rotates opposite to the driving field direction $\nu_1 = 1 > 0$. In case of a four-pole rotor field $p_1 = p = 2$, $\nu_1 = 2$ and $\nu_2 = -1$, yielding $p_2 = |\nu_2| = 1$. However, it can be shown analytically [8] that the pole pair number of the levitation winding p_2 should not be chosen lower than the one of the drive winding p_1 for two reasons:

- First, the two levitation force components that result from the stator radial magnetic flux density $B_{\mathrm{r},2}$ and the stator tangential magnetic flux density $B_{\theta,2}$ are opposing each other when $p_2 > p_1$. Consequently a higher levitation current is required to get the same radial force which increases the ohmic losses in the winding. This effect is particularly important for high-speed machines due to their big air gap [8].
- Additionally, the inductance of the levitation winding of the configuration $p_2 = p_1 - 1$ is significantly higher compared to the one for $p_2 = p_1 + 1$ so that the reactive power requirement for the inverter, feeding the levitation winding, is increased.

This means that this phase-split winding is restricted to two-pole high-speed self-bearing motors. In contrast to conventional self-bearing motors, the two windings are fed with two identical inverters with approximately half the rating power required to drive the motor. The phase split halves the induced voltage per phase so that in many cases MOSFET inverters with lower voltage ratings and much lower switching losses are used instead of IGBT inverters, leading also to reduced inverter losses. This is particularly advantageous compared to conventional self-bearing motors with separated levitation and drive winding in low power applications where the drive and levitation windings are fed with inverters of similar ratings. For higher power applications, the drive side inverter is equipped with IGBTs, while the levitation side inverter, with its low voltage rating, is still MOSFET based. So for higher power ratings, the phase-split winding A and B is in this case inconvenient as only IGBT-inverters will have to be used above a certain voltage level of approximately 150 V. Other limitations restrict this winding to higher power ratings such as the reduced number of optimisation parameters to minimise the field harmonic amplitudes, which cause additional eddy-current losses in the stator and the rotor.

It should be noted that the active and independent control of torque and radial lateral forces is not possible with a single three-phase winding and a cylindrical rotor configuration. Mathematically, there are not enough degrees of freedom (which at maximum is three with fully isolated phases) to independently control two fields, which requires four degrees of freedom. Several publications claim to operate a novel bearingless motor with a single three-phase winding. In fact they refer to self-bearing motors which are radially passively suspended such as in [30], [31], where there the axial active position control is possible with the zero-sequence current component of the inverter output. The same observation is made with axial flux self-bearing prototypes such as in [32].

6.2. Designed prototype

A prototype was designed for a split stator winding A and B, based on this working principle, described in section 6.1. The ratings and dimensions are given in Table 6.1. They are based on the dimensions of a previously designed self-bearing motor [8] with a conventional winding system of separated levitation and drive three-phase winding. Since the air gap magnetic flux density is low (≈ 0.45 T) and the stator is cooled with natural air convection without any fan, the rated torque $M_\mathrm{N} = 0.105$ Nm is rather low. So the motor has to be regarded as a simple demonstrator which at forced cooling and elevated flux-densities would allow at the same volume a much higher power output.

6.3. Magnetic equations

6.3.1. Phase currents and current system definitions

Two sets of currents are fed to the two three-phase windings, so in Table 6.1 the complete winding is noted as $m = 6$-phase winding. The drive current system $\boldsymbol{i_1} = (i_{1,\mathrm{U}}\ i_{1,\mathrm{V}}\ i_{1,\mathrm{W}})^\intercal$ generates the fundamental field $\nu = 1$, and further (unwanted) harmonics, whereas the levitation current system $\boldsymbol{i_{-2}} = (i_{-2,\mathrm{U}}\ i_{-2,\mathrm{V}}\ i_{-2,\mathrm{W}})^\intercal$ generates the levitation field $\nu = -2$, and further (unwanted) harmonics. Since the levitation field is the harmonic $\nu = -2$, it rotates in opposition to the fundamental $\nu = 1$. In order to obtain a constant lateral force in the stator coordinate system, the levitation field B_{-2} must rotate with the same electrical frequency ω_e and in the same direction as the rotor field $\nu = 1$. Hence the current system $\boldsymbol{i_{-2}}$ should be a negative sequence system in opposition to the fundamental positive sequence system of the current system $\boldsymbol{i_1}$. Therefore, it has to be a negative sequence current that rotates at $-\omega_\mathrm{e}$. Figure 6.1 c shows for winding A and B each a three-zone winding with zones $\mathrm{U_A}$, $\mathrm{V_A}$, $\mathrm{W_A}$ and $\mathrm{U_B}$, $\mathrm{V_B}$, $\mathrm{W_B}$ as phase belt, where $\mathrm{U_A}$ and $\mathrm{U_B}$, $\mathrm{V_A}$ and $\mathrm{V_B}$, and $\mathrm{W_A}$ and $\mathrm{W_B}$ are shifted

Table 6.1.: Self-bearing motor parameter

Parameter	**Symbol**	**Value**	**Unit**
Rated speed	n_N	60 000	min^{-1}
Rated torque	M_N	105	mN m
Rated lateral force	F_N	8.2	N
Number of phases	m	6	-
Rated voltage	$U_\mathrm{s,N}$	48	V
Rated torque current	$I_\mathrm{s,1,N}$	3.18	A
Rated levitation current	$I_\mathrm{s,-2,N}$	2.26	A
Stator inner diameter	d_si	35	mm
Rotor axial length	l_Fe	40	mm
Mechanical air gap	δ_m	1.0	mm
Bandage thickness	h_B	1.5	mm
Magnet height	h_m	2.75	mm
Magnet length	l_m	48	mm
Permanent magnet type	-	SmCo_5	-
Magnet ring magnetization	-	Parallel	-
Permanent magnet remanence (100°C)	B_rem	0.96	T
Permanent magnet recoil permeability	$\mu_\mathrm{r,M}$	1.1	p.u.
Number of pole pairs (drive/levitation)	p_1/p_2	1/2	-
Number of layers	-	2	-
Coil pitch (for fundamental field $p_1 = 1$)	W/τ_p	0.5	-
Number of turns per coil	N_c	11	-
Slot fill factor	-	0.4	-

by a pole pitch τ_p or, correspondingly to $2\tau_\mathrm{p} \Leftrightarrow 2\pi$ at $\nu_1 = 1$, shifted by π. As a special case, the winding has $q = 2$ coils per pole and phase to reduce the amplitude of unwanted harmonics, but other values (e.g. $q = 4$) are also possible. We feed $\mathrm{U_A}$, $\mathrm{V_A}$, $\mathrm{W_A}$ and $\mathrm{U_B}$, $\mathrm{V_B}$, $\mathrm{W_B}$ by an identical, but by π shifted positive sequence current system. So we get for the system A $i_{1,\mathrm{U}}(t) = \hat{I}_1 \cdot \cos(\omega_\mathrm{e} t + \theta_1)$, $i_{1,\mathrm{V}}(t) = \hat{I}_1 \cdot \cos(\omega_\mathrm{e} t + \theta_1 - 2\pi/3)$, $i_{1,\mathrm{W}}(t) = \hat{I}_1 \cdot \cos(\omega_\mathrm{e} t + \theta_1 - 4\pi/3)$ or with the space vector formulation $\underline{i}(t) = 2/3 \cdot (i_\mathrm{U}(t) + \underline{a} \cdot i_\mathrm{V}(t) + \underline{a}^2 \cdot i_\mathrm{W}(t))$ with $\underline{a} = \exp(\mathrm{j}2\pi/3)$, the clockwise rotating feeding space vector $\underline{i}_{\mathrm{A,cw}}(t) = \hat{I}_1 \cdot \exp(\mathrm{j}(\omega_\mathrm{e} t + \theta_1))$ and for the winding system B: $\underline{i}_{\mathrm{B,cw}}(t) = \hat{I}_1 \cdot \exp(\mathrm{j}(\omega_\mathrm{e} t + \theta_1 + \pi))$. Hence, the field waves of A and B of odd order $\nu = 1, -5, 7, -11, 13, \ldots$ ($\nu = 1 + 6g$, $g \in \mathbb{Z}$) add up to double amplitude, whereas the field waves of even order $\nu = -2, 4, -8, 10, -14, \ldots$ cancel. Feeding in addition system A with a negative current system $i_{-2,\mathrm{U}}(t) = \hat{I}_{-2} \cdot \cos(\omega_\mathrm{e} t - \theta_{-2})$, $i_{-2,\mathrm{V}}(t) = \hat{I}_{-2} \cdot \cos(\omega_\mathrm{e} t - \theta_{-2} - 4\pi/3)$, $i_{-2,\mathrm{W}}(t) = \hat{I}_{-2} \cdot \cos(\omega_\mathrm{e} t - \theta_{-2} - 2\pi/3)$ or a counter-clockwise rotating space vector $\underline{i}_{\mathrm{A,ccw}}(t) = \hat{I}_{-2} \cdot \exp(-\mathrm{j}(\omega_\mathrm{e} t - \theta_{-2}))$ and system B with an identical space vector $\underline{i}_{\mathrm{B,ccw}}(t) = \underline{i}_{\mathrm{A,ccw}}(t)$ reverses the rotation of all harmonic field waves, which are exited by them. As $\underline{i}_{\mathrm{A,ccw}}$ and $\underline{i}_{\mathrm{B,ccw}}$ are in phase, all odd field harmonics ($\nu = 1, -5, 7, -11, 13, \ldots$) cancel, whereas all even field harmonics add up to double amplitude ($\nu = -2, 4, -8, 10, -14, \ldots$). So the dominating field waves $\nu = 1$ and $\nu = -2$ rotate in the same directions. The sum of $\underline{i}_{\mathrm{A,cw}}(t) + \underline{i}_{\mathrm{A,ccw}}(t) = \underline{i}_\mathrm{A}(t)$ is fed by inverter A to winding system A, and $\underline{i}_{\mathrm{B,cw}}(t) + \underline{i}_{\mathrm{B,ccw}}(t) = \underline{i}_\mathrm{B}(t)$ is fed by inverter B to winding system B, according to (6.1). The two space vectors $\hat{I}_1 \cdot \exp(\mathrm{j}(\omega_\mathrm{e} t + \theta_1))$ (and also $\hat{I}_1 \cdot \exp(\mathrm{j}(\omega_\mathrm{e} t + \theta_1 + \pi)))$ and $\hat{I}_{-2} \cdot \exp(-\mathrm{j}(\omega_\mathrm{e} t - \theta_{-2}))$ rotate in the cross-section plane of the electrical machine (with a complex coordinate system) as circular orbits with angular frequency ω_e, in opposite directions, at the radius $\hat{I}_1$ and $\hat{I}_{-2}$, respectively. The superposition of the circular orbits of opposite directions of rotation and of different radius lead to a resulting elliptical orbit of the resulting space vector $\underline{i}_\mathrm{A}(t)$, resp. $\underline{i}_\mathrm{B}(t)$.

$$\begin{aligned}\underline{i}_\mathrm{A}(t) &= \hat{I}_1 \cdot \exp(\mathrm{j}\,(\omega_\mathrm{e} t + \theta_1)) + \hat{I}_{-2} \cdot \exp(\mathrm{j}\,(-\omega_\mathrm{e} t + \theta_{-2})) \\ \underline{i}_\mathrm{B}(t) &= \hat{I}_1 \cdot \exp(\mathrm{j}\,(\omega_\mathrm{e} t + \theta_1 + \pi)) + \hat{I}_{-2} \cdot \exp(\mathrm{j}\,(-\omega_\mathrm{e} t + \theta_{-2}))\end{aligned} \tag{6.1}$$

The two current amplitudes $\hat{I}_\mathrm{a} = \hat{I}_1 + \hat{I}_{-2}$ and $\hat{I}_\mathrm{b} = \hat{I}_1 - \hat{I}_{-2}$ are defined. By splitting (6.1) in their real and imaginary parts as (6.2), the parametric equations of two orthogonal ellipses can be recognised, each one for space vector $\underline{i}_\mathrm{A}(t)$ and $\underline{i}_\mathrm{B}(t)$, respectively.

$$
\begin{aligned}
\mathrm{Re}(\underline{i}_\mathrm{A})(t) =& \hat{I}_\mathrm{a} \cdot \cos(\frac{\theta_1 + \theta_2}{2}) \cdot \cos(\omega_\mathrm{e} t + \frac{\theta_1 - \theta_2}{2}) \\
& - \hat{I}_\mathrm{b} \cdot \sin(\frac{\theta_1 + \theta_2}{2}) \cdot \sin(\omega_\mathrm{e} t + \frac{\theta_1 - \theta_2}{2}) \\
\mathrm{Im}(\underline{i}_\mathrm{A})(t) =& \hat{I}_\mathrm{a} \cdot \sin(\frac{\theta_1 + \theta_2}{2}) \cdot \cos(\omega_\mathrm{e} t + \frac{\theta_1 - \theta_2}{2}) \\
& + \hat{I}_\mathrm{b} \cdot \cos(\frac{\theta_1 + \theta_2}{2}) \cdot \sin(\omega_\mathrm{e} t + \frac{\theta_1 - \theta_2}{2}) \\
\mathrm{Re}(\underline{i}_\mathrm{B})(t) =& \hat{I}_\mathrm{a} \cdot \cos(\frac{\theta_1 + \theta_2 + \pi}{2}) \cdot \cos(\omega_\mathrm{e} t + \frac{\theta_1 - \theta_2 + \pi}{2}) \\
& - \hat{I}_\mathrm{b} \cdot \sin(\frac{\theta_1 + \theta_2 + \pi}{2}) \cdot \sin(\omega_\mathrm{e} t + \frac{\theta_1 - \theta_2 + \pi}{2}) \\
\mathrm{Im}(\underline{i}_\mathrm{B})(t) =& \hat{I}_\mathrm{a} \cdot \sin(\frac{\theta_1 + \theta_2 + \pi}{2}) \cdot \cos(\omega_\mathrm{e} t + \frac{\theta_1 - \theta_2 + \pi}{2}) \\
& + \hat{I}_\mathrm{b} \cdot \cos(\frac{\theta_1 + \theta_2 + \pi}{2}) \cdot \sin(\omega_\mathrm{e} t + \frac{\theta_1 - \theta_2 + \pi}{2})
\end{aligned}
\tag{6.2}
$$

The major axis length is $\hat{I}_\mathrm{a}$ and the minor axis length is $\hat{I}_\mathrm{b}$. Hence the two ellipses are phase shifted by $\pi/2$ so that the two major axes are orthogonal to one another. Figure 6.2 gives the elliptic current trajectories in the complex plane for the two space vector systems $\underline{i}_\mathrm{A}$ and $\underline{i}_\mathrm{B}$ with a drive current $\hat{I}_1$ = 7.5 A (resp. a levitation current $\hat{I}_{-2}$ = 2.5 A) and a phase $\theta_1 = 0$ (resp. $\theta_{-2} = \pi/2$). The drive current component (dotted arrow), levitation current component (dashed arrow) and resulting current (continuous arrow) are given for both systems at the time instant $\omega_\mathrm{e} t = \pi/8$. If one phase axis is aligned with the major axis of one of the two ellipses, the phase current at this phase is maximum and equals $\hat{I}_\mathrm{a} = \hat{I}_1 + \hat{I}_{-2}$. This high phase current leads to a local temperature increase and must be limited by design. Therefore it can be deduced that the split-winding is not well-suited for designs where the two current amplitudes $\hat{I}_1$ and $\hat{I}_{-2}$ are equal, because then $\hat{I}_\mathrm{a} = 2\hat{I}_1$, leading to a local ohmic loss increase by factor 4. Their orthogonal axis are rotated by the angle $(\theta_1 + \theta_2)/2$, respectively by $(\theta_1 + \theta_2 + \pi)/2$, from an original $x - y-$reference frame.

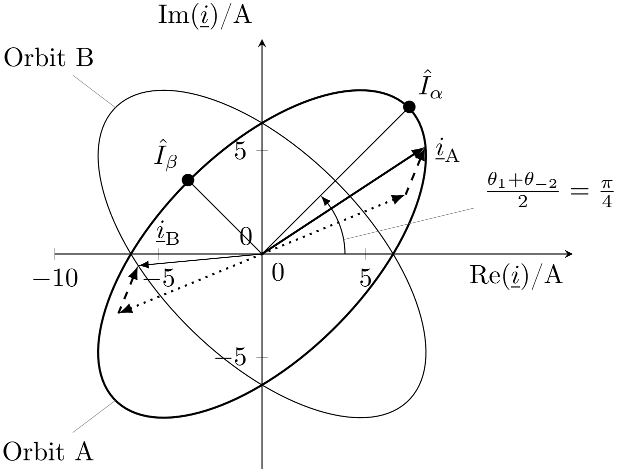

Figure 6.2.: Current space vector representation in the motor cross-section plane with complex coordinate system: $\hat{I}_\alpha = 10$ A, $\hat{I}_\beta = 5$ A, $\theta_1 = 0$, $\theta_{-2} = \pi/2$. Drive current space vector component (dotted arrow, amplitude $\hat{I}_1 = 7.5$ A), levitation current space vector component (dashed arrow, amplitude $\hat{I}_{-2} = 2.5$ A) and resulting current space vector at steady-state operation (constant frequency ω_e and constant period angles θ_1, θ_{-2}) and at the instant $\omega_\mathrm{e} t = \pi/8$. The current space vector orbits in the two windings A and B form two orthogonal ellipses.

6.3.2. Air gap fields

6.3.2.1. Rotor field

The rotor field, excited by the diametrically magnetised two-pole magnet, is calculated with equation (4.15). The calculated fundamental magnetic field amplitude $\nu = 1$ at stator inner radius r_si is compared to the 2D FEM evaluation in Table 6.2. A 2D FEM evaluation is performed first with a slotless stator, where the stator radius is increased with the *Carter*'s coefficient k_C (4.2) according to [23] and the iron relative permeability $\mu_\mathrm{r,Fe}$ is set constant at 4 000. The analytical and numerical evaluation match exactly. However the field amplitude in the 2D FEM model with slots displays a slightly higher amplitude compared to the slotless model. This is because the correction with *Carter*'s coefficient k_C is exact solely when the magnet is infinitely thin which is never the case. In the numerically evaluated air gap magnetic flux density at the air gap middle in Figure 6.3, the slot harmonics with ordinal numbers -11 and 13 are clearly visible. It is due to the 12 slot openings per pole pair that modulate the air gap field. Since the slot opening width $s_\mathrm{Q} = 2.5$ mm of the semi-closed slots is small compared to the magnetically equivalent air gap $\delta_\mathrm{e} = 5.25$ mm, the amplitude of the fundamental field is almost not reduced by the slot openings. Indeed, the *Carter*'s coefficient k_C (4.2) is only 1.004, so nearly unity. However, the rotor magnet, mounted on the built rotor, is 20% longer than the iron stack ($l_\mathrm{M} = 1.2\ l_\mathrm{Fe}$), so that the axial flux fringing has to be taken into account to obtain the actual magnetic field amplitude. Additionally, the rotor magnet is not axially symmetrical to the stator, leading to a different axial flux fringing on both ends of the rotor, as qualitatively represented in Figure 6.4. Therefore a 3D finite element calculation was performed with the actual magnet dimensions in order to evaluate the actual rotor flux and again with a iron relative permeability $\mu_\mathrm{r,Fe} = 4\ 000$. The reason for $l_\mathrm{M} > l_\mathrm{Fe}$ is that the rotor position is obtained with *Hall*-effect sensors, that are placed in the winding overhang instead of in the tight stator slot openings s_Q. The rotor position signal is less influenced by the stator field at that location. Unfortunately, the axial fringing field is responsible for some additional iron losses on both axial surfaces of the stator iron stack, since the induced eddy-currents can form along the stator lamination. As the motor rating is low, these additional eddy-current losses are small and were not considered. In contrast to the 2D model with the axial length l_Fe, the magnetic flux density $B_0(r_\mathrm{si}, \theta_0)$ is not constant in 3D along the axial direction. In order to obtain an equivalent value for the 2D calculation, the magnetic flux Φ_0 is numerically integrated over a cylindrical surface of length l_M and radius r_si to account for axial flux fringing. It is then divided by the stator pole surface area $l_\mathrm{Fe} \cdot \tau_\mathrm{p}$. The analytically obtained flux amplitude as well as the one obtained in 2D and 3D simulation are given in Table 6.2 for a magnet temperature of 100°C ($B_\mathrm{rem} = 0.96$ T). Since the saturation of the iron parts is low, the analytical calculation with $\mu_\mathrm{Fe} \to \infty$ and with consid-

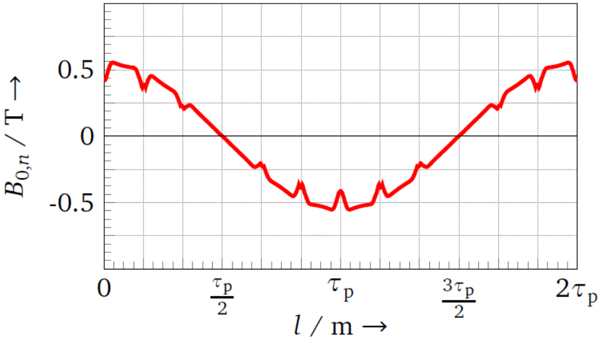

Figure 6.3.: Numerically 2D calculated radial magnetic flux density $B_{0,n}$ along the middle of the mechanical air gap. The slot openings are responsible for the dips in the distribution of the radial magnetic flux density (FEM program JMAG).

Table 6.2.: Two-pole self-bearing motor: Magnetic flux amplitudes at 100°C

Parameter	**Analytical**	**Slotless 2D FEM**	**2D FEM**	**3D FEM**
$B(r_{si}, \theta_0)$	0.440 T	0.440 T	0.447 T	0.48 T
Φ_0	616 µWb	616 µWb	627 µWb	660 µWb

eration of the *Carter*'s coefficient k_C (4.2) (which also assumes $\mu_{Fe} \to \infty$) fits well with the 2D FEM result. The axial flux fringing in the 3D FEM is responsible for a by 10% higher rotor magnetic flux. The finite element calculations for the slotless 2D model are done with the program *FEMM*. The slotted 2D and 3D models were done with the program *JMAG* in [53].

6.3.2.2. Stator field

Since the three-phase stator winding in Figure 6.1 generates two pronounced field waves with the pole pair numbers p_1 and p_2, and the flux densities are low, leading to low iron saturation, the superposition theorem is used in order to calculate the two fields with the magnetic equations (4.49) and (4.50). When the two windings A and B are fed with the current system $\boldsymbol{i}_1$,

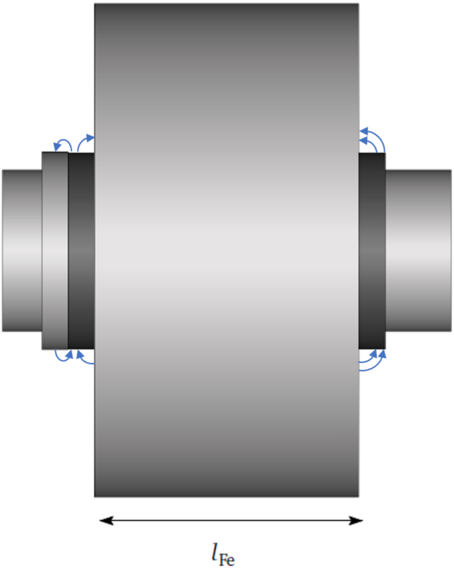

Figure 6.4.: Asymmetrical rotor with different flux fringing axially on both sides of the stator iron stack. The field lines, in blue, are not symmetrical on both sides of the stator. Since the stator is not laminated in radial direction, the axial flux fringing induces some additional eddy-current losses at both stator ends, when the magnet rotates.

the stator winding is equivalent to a two-pole ($p_1 = 1$) double-layer winding with a short-pitching of $W_1 = 0.5 \cdot \tau_{\mathrm{p}}$ and a number of slots per pole and phase $q_1 = Q/(6p_1)$, where Q is the number of stator slots. If they are fed with the current system $\boldsymbol{i_{-2}}$, the stator winding is equivalent to a four-pole ($p_{-2} = 2$) double-layer winding full-pitched $W_{-2} = \tau_{\mathrm{p}}$ and a number of slots per pole and phase $q_{-2} = Q/(3p_{-2})$. Therefore the magneto-motive force, given by the two windings, can be expressed with the usual expression (4.45), where the winding factors are given by (6.3).

Table 6.3.: Self-bearing motor parameters: The coefficients are evaluated for peak current values, since control models operate with instantaneous peak values. k_{ir} and k_{M} must be multiplied by $\sqrt{2}$ (and k_{dist} by 2), when the calculation is done with RMS currents, for example during motor design

Parameter	**Analytical**	**2D FEM**	**Unit**
Negative stiffness coefficient k_{sr}	-26070	-25300	N/m
Current-force coefficient k_{ir}	2.75	2.63	N/A
Current-torque coefficient k_{M}	28.9	28.0	mNm/A
Force interference coefficient k_{dist}	2.62	2.56	mN/A^2

$$k_{\mathrm{w},\nu} = k_{\mathrm{q},\nu} \cdot k_{\mathrm{p},\nu} = \begin{cases} 0 \text{ for } \nu \in 4\mathbb{Z} \\ k_{\mathrm{q},\nu} \text{ for } \nu \in 2 + 12\mathbb{Z} \\ \dfrac{k_{\mathrm{q},\nu}}{\sqrt{2}} \text{ for } \nu \in 1 + 6\mathbb{Z} \end{cases} \tag{6.3}$$

$$k_{\mathrm{q},\nu} = \frac{\sin(\frac{\nu\pi}{2m})}{q \cdot \sin(\frac{\nu\pi}{2mq})}, \quad k_{\mathrm{p},\nu} = \sin(\frac{W}{\tau_{\mathrm{p}}}\nu\frac{\pi}{2}) = \sin(\nu\frac{\pi}{4})$$

The minimum number of stator slots Q for such a motor is 12. For the winding disposition in Figure 6.1, the winding factors for the drive field ($\nu = 1$) and levitation field $\nu = -2$ are $k_{\mathrm{w},1} = 0.683$ and $k_{\mathrm{w},-2} = 0.866$, respectively. The winding factor of the fundamental $\nu = 1$ is low due to the short-pitching ($W_1/\tau_{\mathrm{p}} = 1/2$). A conventional self-bearing stator winding with a single layer drive winding and a single layer levitation winding would lead to $k^*_{\mathrm{w},1} = 0.966$ and $k^*_{\mathrm{w},2} = 1$. Since the rotor field and the mechanical dimensions are already given, the amplitudes of the stator fields depend on the required lateral forces and the torque. Before calculating the stator fields, the characteristic parameters (4.64) are determined. With the dimensions from Table 6.1, the parameters are obtained in Table 6.3. With the lateral force and torque ratings as well as with the characteristic parameters (4.64), it is now simple to evaluate the stator fields as well as the stator current. In practice, the number of turns per pole and phase N_c is not known so that the same procedure should be applied with $N_\mathrm{c} = 1$. The selection of N_c is governed by the voltage and current ratings of the inverter. The rated drive and levitation RMS currents are respectively 3.18 A and 2.26 A. The drive and levitation magnetic flux densities at the stator inner radius r_si are 29 mT and 14 mT, respectively.

6.3.3. Voltage complex representation in stationary conditions

Now that the field calculation is done, the phase voltages can be determined. In order to get compact expressions, the complex space vector representation (6.4) is adopted, where the complex space vector of voltage $\underline{u}_\mathrm{s}(t)$ is a function of the instantaneous phase voltages $u_\mathrm{U}(t)$, $u_\mathrm{V}(t)$ and $u_\mathrm{W}(t)$. This complex space vector representation (6.4) applies only to currents and voltages and is not a space vector representation of the magnetic field. Indeed, the representation of the main flux linkage Ψ in space vector results from the integration of the magnetic flux density over a particular pole-pitch τ_p. Since several flux linkages of different ordinal numbers (field waves $\nu = 1$ and $\nu = 2$) with different pole-pitches are present in this part, the definition of space vector according to *Kovacs* is not applicable for fluxes and flux linkages here.

$$\underline{u}_\mathrm{s}(t) = \frac{2}{3} \cdot \left(u_\mathrm{U}(t) + \underline{a} \cdot u_\mathrm{V}(t) + \underline{a}^2 \cdot u_\mathrm{W}(t)\right) \tag{6.4}$$

The permanent magnet flux linkage Ψ_0, rotating at ω_e, induces a voltage $\underline{U}_\mathrm{i}$ in each motor phase winding. The driving current system $\underline{I}_1$ generates two voltage components:

- The voltage drop $R_\mathrm{s} \cdot \underline{I}_1$ due to the phase resistance R_s
- The voltage drop $\mathrm{j}\omega_\mathrm{e} \cdot L_{\mathrm{s},1} \cdot \underline{I}_1$ due to the equivalent self inductance $L_{\mathrm{s},1}$

In the same manner, the levitation current system $\underline{I}_{-2}$ generates two additional voltage components $R_\mathrm{s} \cdot \underline{I}_{-2}$ and $\mathrm{j}\omega_\mathrm{e} \cdot L_{\mathrm{s},-2} \cdot \underline{I}_{-2}$. The determination of the equivalent inductances $L_{\mathrm{s},1}$ and $L_{\mathrm{s},-2}$ is detailed later in section 6.3.4. It leads to the voltage equations (6.5) in the stator reference coordinate system, where θ_0, θ_1 and θ_{-2} are the phase angles of the rotor flux linkage Ψ_0, of the stator driving flux linkage Ψ_1 and of the levitation flux linkage Ψ_{-2} respectively, related to the winding axis of phase winding $\mathrm{U_A}$. It should be noted that the voltage induction due to the rotor radial motion as well as due to a radial eccentricity is neglected for simplicity. Its amplitude is negligible, since the rotor orbits due to an eccentricity are small (< 20 µm).

$$\begin{aligned}
\underline{u}_\mathrm{A}(t) = \mathrm{j}\hat{U}_\mathrm{i} \cdot \exp(\mathrm{j}\,(\omega_\mathrm{e} t + \theta_0)) &+ (R_\mathrm{s} + \mathrm{j}\omega_\mathrm{e} L_{\mathrm{s},1}) \cdot \hat{I}_1 \cdot \exp(\mathrm{j}\,(\omega_\mathrm{e} t + \theta_1)) \\
&+ (R_\mathrm{s} - \mathrm{j}\omega_\mathrm{e} L_{\mathrm{s},-2}) \cdot \hat{I}_{-2} \cdot \exp(\mathrm{j}\,(-\omega_\mathrm{e} t + \theta_{-2})) \\
\underline{u}_\mathrm{B}(t) = -\mathrm{j}\hat{U}_\mathrm{i} \cdot \exp(\mathrm{j}\,(\omega_\mathrm{e} t + \theta_0)) &- (R_\mathrm{s} + \mathrm{j}\omega_\mathrm{e} L_{\mathrm{s},1}) \cdot \hat{I}_1 \cdot \exp(\mathrm{j}\,(\omega_\mathrm{e} t + \theta_1)) \\
&+ (R_\mathrm{s} - \mathrm{j}\omega_\mathrm{e} L_{\mathrm{s},-2}) \cdot \hat{I}_{-2} \cdot \exp(\mathrm{j}\,(-\omega_\mathrm{e} t + \theta_{-2}))
\end{aligned} \tag{6.5}$$

Since the two windings A and B are spatially shifted by one pole pitch τ_p (Figure 6.1), the voltage components related to the fundamental field wave ($\nu = 1$) are in phase opposition. In contrast, the voltage components related to the second harmonic ($\nu = -2$) are in phase, but rotate in opposite direction.

6.3.4. Inductance calculation

In order to calculate all the inductances related to each field component ($\nu = 1$ and $\nu = -2$), the same technique is used as for the air gap field determination. First, a pure fundamental current I_1 is assumed ($I_{-2} = 0$). Then a pure second harmonic current I_{-2} is assumed ($I_1 = 0$). The considered inductances are the following:

- The magnetising inductance L_h

- The air gap leakage inductance L_{σ}, that comprises the part of the stator fundamental field that closes in the air gap without reaching the rotor and the harmonic field components of $|\nu| > 2$
- The slot leakage inductance $L_{\sigma,\mathrm{Q}}$, that characterises the flux lines, closing tangentially in the stator slots
- The overhang leakage inductance $L_{\sigma,\mathrm{ov}}$, that characterises the flux lines, closing at both axial ends and that do not link to the rotor

The magnetising inductance L_{h} is calculated by dividing the magnetic flux linkage, excited by the stator current I_{s} and integrated as flux over one pole pitch τ_{p} for $\nu = 1$, or $\tau_{\mathrm{p}}/2$ for $|\nu| = 2$ on the rotor surface, by the stator current I_{s} itself. The leakage inductances are calculated by integration of the magnetic energy W in the respective volumes V as proposed in [33]. Since the air regions, where W is integrated, are magnetically linear, equation (6.6) is used, where B is the *Euclidean* norm of the magnetic flux density vector $\boldsymbol{B}$. The analytical calculation of the overhang leakage inductance is more complicated, since the actual 3D field distribution in the winding overhang region is not known. Fortunately, it represents only a small part of the total leakage inductance, and some approximations are given in the literature [34].

$$W = \frac{m \cdot L_{\sigma} \cdot \hat{I}_{\mathrm{s}}^{2}}{2} = \int_{\mathrm{V}} \frac{B^{2}}{2\mu_{0}} \cdot \mathrm{d}V \tag{6.6}$$

Since high speed motors with surface mounted magnets have a significantly large air gap, the total leakage inductance $L_{\sigma,\mathrm{t}} = L_{\sigma} + L_{\sigma,\mathrm{Q}} + L_{\sigma,\mathrm{ov}}$ is significant and can be bigger than the magnetising inductance L_{h}. While a high leakage inductance $L_{\sigma,\mathrm{t}}$ is usually avoided in conventional machines, it is advantageous for this prototype for two reasons:

- It reduces the required minimum switching frequency of the two inverters to a manageable level, as $L_{\sigma,\mathrm{t}}$ smooths the current ripple. The prototype in Figure 6.10 was fed at a switching frequency of 31 kHz.

- Since the ratio of the two linkage inductances $L_{\mathrm{h},1}/L_{\mathrm{h},-2}$ is much higher than the ratio of leakage inductances $L_{\sigma,\mathrm{t},1}/L_{\sigma,\mathrm{t},-2}$, a high leakage inductance $L_{\sigma,\mathrm{t}}$ leads to a ratio of electrical time constants $\tau_2/\tau_1 = (L_{\mathrm{h},-2} + L_{\sigma,\mathrm{t},-2})/(L_{\mathrm{h},1} + L_{\sigma,\mathrm{t},1})$ closer to unity [50]. Therefore, the two current control gain settings (k_{P} and k_{D}) for each current system $\nu = 1$ and $\nu = -2$ are closer to one another. Consequently, the current control is less sensitive to an inaccuracy in current transformations, since it is properly set for both current components.

The calculation of the inductances for this prototype is described in detail in [53]. The obtained inductances are given in Table 6.4. The analytically obtained values are both 50% higher than the ones obtained with the 2D FEM program *JMAG*. Since the short-circuit current is very high and the rotor can not levitate at stator short-circuit, the measurement of the phase inductances is done at nominal speed n_{N}, where the voltage drop due to the phase resistance R_{s} is negligible, compared to the voltage drops due to the two inductances. The measured fundamental field inductance $L_{\mathrm{s},1}$ and the second field inductance $L_{\mathrm{s},-2}$ are obtained with (6.7), where the voltage and current variables are recorded from the inverter and are averaged over 30 electrical periods. The additional inductance due to the cable is neglected (at a used cable length 3.2 m). The measured value are also given in Table 6.4.

$$L_{\mathrm{s},1} \approx -\frac{U_{1,\mathrm{d}}}{\omega_{\mathrm{e}} \cdot I_{1,\mathrm{q}}}, \quad L_{\mathrm{s},-2} \approx \frac{\sqrt{U_{-2,\mathrm{d}}^2 + U_{-2,\mathrm{q}}^2}}{\omega_{\mathrm{e}} \cdot \sqrt{I_{-2,\mathrm{d}}^2 + I_{-2,\mathrm{q}}^2}} \tag{6.7}$$

The analytically calculated inductances are closer to the measured inductances than the ones obtained with the program *JMAG*, but this might be accidentally.

Table 6.4.: Self-bearing motor phase inductances in µH

Parameter	**Analytical**	**2D FEM** [53]	**Measured**
Drive inductance $L_{\mathrm{s},1}$ for $\nu = 1$	234	181	259
Levitation inductance $L_{\mathrm{s},-2}$ for $\nu = 2$	177	121	178

6.3.5. Phase resistance and ohmic losses

The ohmic losses are obtained by calculating first the phase resistance R_s. The phase resistance R_s for a double layer winding with series connection of all coils per phase, where only half the slots are wound (Figure 6.1 c, hence $N_\mathrm{s} = p \cdot q \cdot N_\mathrm{c}/4$), is given by (6.8) where ρ is the copper resistivity at 20°C, q (here: $q = 2$) is the number of slots per pole (here: pole pair count $p = 1$) and phase (here: phase count $m = 6$), N_c is the number of turns per coil, l_Fe is the iron stack length, k_slot is the slot fill factor and A_slot is the slot cross section. In (6.8), it is assumed that the average length of a turn is $2 \cdot (l_\mathrm{Fe} + 1.5W)$, where W is the width of a turn, which in this particular winding is $W = \tau_\mathrm{p}/2$, where τ_p is the pole pitch.

$$R_\mathrm{s} = \frac{2\rho \cdot q \cdot N_\mathrm{c}^2 \cdot (l_\mathrm{Fe} + 1.5W)}{k_\mathrm{slot} \cdot A_\mathrm{slot}} \tag{6.8}$$

In stationary operation, the phase currents are define from (6.1) via $\underline{i}_{\mathrm{U,A}}(t) = \mathrm{Re}(\underline{i}_\mathrm{A}(t))$, $\underline{i}_{\mathrm{V,A}}(t) = \mathrm{Re}(\underline{a}^2 \underline{i}_\mathrm{A}(t))$, $\underline{i}_{\mathrm{W,A}}(t) = \mathrm{Re}(\underline{a} \cdot \underline{i}_\mathrm{A}(t))$ and in the same way for $\underline{i}_{\mathrm{U,B}}(t) = \mathrm{Re}(\underline{i}_\mathrm{B}(t))$, … . The instantaneous ohmic losses $P_{\mathrm{Cu,A}}(t)$ and $P_{\mathrm{Cu,B}}(t)$ are given by (6.9).

$$\begin{aligned} P_{\mathrm{Cu,A}}(t) &= \frac{3R_\mathrm{s}}{2} \cdot (\hat{I}_1^2 + \hat{I}_{-2}^2 + 2\hat{I}_1 \cdot \hat{I}_{-2} \cdot \cos(2\omega_\mathrm{e} t + \theta_1 - \theta_{-2})) \\ P_{\mathrm{Cu,B}}(t) &= \frac{3R_\mathrm{s}}{2} \cdot (\hat{I}_1^2 + \hat{I}_{-2}^2 - 2\hat{I}_1 \cdot \hat{I}_{-2} \cdot \cos(2\omega_\mathrm{e} t + \theta_1 - \theta_{-2})) \\ P_\mathrm{Cu}(t) &= P_{\mathrm{Cu,A}}(t) + P_{\mathrm{Cu,B}}(t) = 3R_\mathrm{s} \cdot (\hat{I}_1^2 + \hat{I}_{-2}^2) \end{aligned} \tag{6.9}$$

The ohmic losses in both windings A and B have a variable part, pulsating with the double frequency $2\omega_\mathrm{e}$. The average ohmic losses, integrated over a half electrical period $T_\mathrm{e}/2 = 1/(2f_\mathrm{e})$, are equal in both windings. Finally the sum of the instantaneous losses $P_\mathrm{Cu}(t)$ of both windings A and B is constant and is given by the last formula in (6.9). It should be noticed that in steady state, the ohmic losses due to the driving current $\hat{I}_1$ and due to the levitation current $\hat{I}_{-2}$ are independent, as it is also the case for a conventional self-bearing motor with separated drive and levitation windings.

Due to the short-pitching $W/\tau_\mathrm{p} = 0.5$, the winding factor $k_{\mathrm{w},1}$ of the fundamental of the split winding with $q = 2$ is $k_{\mathrm{w},1} = 0.683$ so rather low. Still, the resulting ohmic losses are lower in this split winding of Figure 6.1 compared to the conventional self-bearing motor with two separated windings for two reasons:

- The utilised slot cross section area is 100% for both the drive current and for the levitation current.
- The winding overhang length is halved, halving the associated portion of the phase resistance R_s, which is calculated with (6.8).

A comparison is derived thoroughly in [47], where an existing prototype with separated drive and levitation windings [8] is compared with its equivalent split winding according to Figure 6.1 [49]. It is shown that the ohmic losses in the split winding are lower than in the conventional winding for all operating points of the motor by typically 45% [47]. Additionally, the motor with split winding displays at identical ohmic losses higher torque and lateral force capability since the current feeding can focus exclusively either on production of torque M_e or lateral force F_r. Indeed, the two inverters A and B, feeding the split winding parts A and B, are rated for a current $I_\mathrm{N} = \sqrt{I_{1,\mathrm{N}}^2 + I_{-2,\mathrm{N}}^2}$. In case a radial force disturbances F_dist occurs, which exceeds the rated force $F_{\mathrm{r,N}}$, the drive current I_1 may be reduced, so that the levitation control current limit can be increased, from $I_{-2,\mathrm{N}}$ to I_N. In the same manner, the drive current I_1 can be increased when the

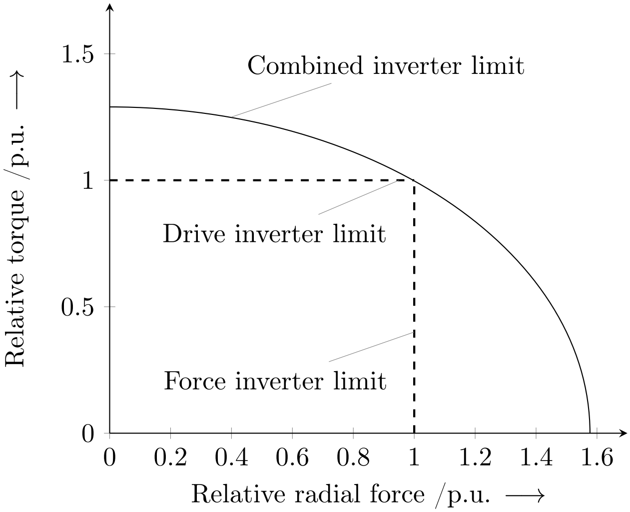

Figure 6.5.: Maximum relative torque and radial force at an inverter current limit for: separated levitation and drive windings in dashed line, split winding according to Figure 6.1 in solid line [47]. The torque and levitation force are related to nominal torque 80 mNm and nominal lateral force 10 N.

lateral force is less than its nominal value. The resulting "torque vs. radial force" characteristic for a normalised current limit of 1 p.u. is displayed in Figure 6.5.

The phase resistance R_s of the prototype (Table 6.1) is equal 80 mΩ at 20°C and stays below 100 mΩ at the temperature encountered during nominal operation ($T <$ 80°C). The ohmic losses represent a very small part of the total losses (under 5% of total losses at nominal operation whereas the iron losses and the air friction losses account for 28% and 25% respectively).

6.4. Control scheme

6.4.1. Position control

The electromagnetic model for this prototype (Table 6.1) is the same as the one in Figure 4.5, and the model parameters where already calculated in Table 6.3. The position controller for radial rotor position at levitation is a simple proportional-integral-differential controller with second-order low-pass filter on the differential action. The natural stiffness gain for this prototype is given by $-2k_{\mathrm{sr}}/k_{\mathrm{ir}} = 19$ kA/m. A slightly higher proportional gain of $k_{\mathrm{P}} = 25$ kA/m was selected to compensate the decreasing k_{ir} with increasing rotational speed (see Section 7.3.6).

The 800 g mass of the shaft is not equally shared between the active magnetic bearing and the self-bearing motor, thus changes significantly when the propeller is added at the drive end of the shaft. With an estimation of 60% of rotor gravity force borne by the self-bearing motor, the natural damping [4] is obtained with a differential gain of $k_{\mathrm{D}} = 20$ As/m. In practice this gain was tuned slightly higher at 26.5 As/m because of the increased k_{P}. The noisy position signal derivative is filtered with a second-order low-pass filter with a cut-off frequency of $f_{\mathrm{c}} = 500$ Hz and a damping ratio of $\zeta = 0.7$. In order not to reduce the phase margin, brought by the differential action k_{D}, the integral action is set arbitrarily low at $k_{\mathrm{I}} = 15.7$ kA/(sm). A setting with twice the stiffness $2k_{\mathrm{P}}$ was also tested to verify the position control redundancy. Indeed, both inverters A and B contribute to the levitation force. When one inverter is switched off, the position control stays stable, if half of the control stiffness is still sufficient to levitate the rotor (i.e. $0.5 \times 2k_{\mathrm{P}} > |k_{\mathrm{sr}}/k_{\mathrm{ir}}|$). While the rotor successfully levitates in both configurations, this redundancy function was tested only at stand-still, since the inverters from the company *LTI motion GmbH* (Lahnau Germany) actively short-circuit those phases which are switched off, preventing the motor from running.

6.4.2. Current control

In order to control independently the torque and the lateral force of the self-bearing motor with split winding A and B, the drive current space vector $\underline{i}_1(t)$ and the levitation current space vector $\underline{i}_{-2}(t)$ must be isolated from the six measured phase currents $i_{\mathrm{U,A}}(t) \dots i_{\mathrm{W,B}}(t)$. Since each winding A (resp. B) is star-connected, the sum of the three phase currents U, V, W is zero. Therefore, only four phase currents need to be measured (e.g. $i_{\mathrm{U,A}}(t)$, $i_{\mathrm{V,A}}(t)$, $i_{\mathrm{U,B}}(t)$ and $i_{\mathrm{V,B}}(t)$) to obtain all the six phase currents. Moreover, the simplified *Clarke* transform (6.10) with only two phase components can be used to transform the two phase currents (here i_{U} and i_{V}) into two orthogonal components i_α and i_β in a stator fixed coordinate system (α/β).

$$\begin{pmatrix} i_\alpha \\ i_\beta \end{pmatrix} = \boldsymbol{T}_{\mathrm{U,V}} \begin{pmatrix} i_{\mathrm{U}} \\ i_{\mathrm{V}} \end{pmatrix} = \frac{1}{\sqrt{3}} \cdot \begin{pmatrix} \sqrt{3} & 0 \\ 1 & 2 \end{pmatrix} \begin{pmatrix} i_{\mathrm{U}} \\ i_{\mathrm{V}} \end{pmatrix} \tag{6.10}$$

Since there are two fields to be controlled, namely the driving field (two-pole fundamental field in the presented machine Table 6.1), and the levitation field (four-pole field), there are two different stator coordinate systems, namely (α_1/β_1) for the fundamental field and (α_{-2}/β_{-2}) for the harmonic field of ordinal number $\nu = -2$. By adding the two stator current space vectors $\underline{i}_{\mathrm{A}}(t)$ and $\underline{i}_{\mathrm{B}}(t)$ of (6.1), the drive current component $\underline{i}_1(t)$ vanishes and the double of the levitation current component $2\,\underline{i}_{-2}(t)$ is obtained. Additionally, by subtracting $\underline{i}_{\mathrm{B}}(t)$ from $\underline{i}_{\mathrm{A}}(t)$, the double of the drive current component $2\,\underline{i}_1(t)$ is obtained and $\underline{i}_{-2}(t)$ vanishes. Therefore, it is possible to extend the *Clarke* transform (6.10) to (6.11) so that the four phase currents $i_{\mathrm{U,A}}$, $i_{\mathrm{V,A}}$, $i_{\mathrm{U,B}}$ and $i_{\mathrm{V,B}}$ are transformed into two independent stator current space vectors, namely $\underline{i}_1 = i_{\alpha,1} + \mathrm{j} \cdot i_{\beta,1}$ in the fundamental stator fixed coordinate system (α_1/β_1) and $\underline{i}_{-2} = i_{\alpha,-2} + \mathrm{j} \cdot i_{\beta,-2}$ in the stator fixed coordinate system (α_{-2}/β_{-2}) of the harmonic $\nu = -2$.

$$\begin{pmatrix} i_{\alpha,1} \\ i_{\beta,1} \\ i_{\alpha,-2} \\ i_{\beta,-2} \end{pmatrix} = \frac{1}{2} \cdot \begin{pmatrix} \boldsymbol{T}_{\mathrm{U,V}} & -\boldsymbol{T}_{\mathrm{U,V}} \\ \boldsymbol{T}_{\mathrm{U,V}} & \boldsymbol{T}_{\mathrm{U,V}} \end{pmatrix} \begin{pmatrix} i_{\mathrm{U,A}} \\ i_{\mathrm{V,A}} \\ i_{\mathrm{U,B}} \\ i_{\mathrm{V,B}} \end{pmatrix} \tag{6.11}$$

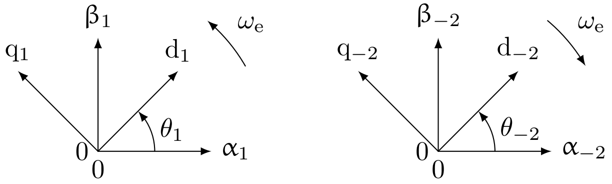

Figure 6.6.: Definition of the two stator coordinates systems (α_1/β_1) for the fundamental field $\nu = 1$ and (α_{-2}/β_{-2}) for the harmonic field $\nu = -2$. The synchronous coordinate system (d_1/q_1) rotates with ω_e in positive direction, while the coordinate system (d_{-2}/q_{-2}) rotates with ω_e in the negative direction.

As for a conventional three-phase synchronous motor, the fundamental stator current components $i_{\alpha,1}$ and $i_{\beta,1}$ are rotated in the synchronous coordinate system (d_1/q_1) (Figure 6.6 left), which is rotor fixed, rotating with ω_e, and oriented so that the d-axis corresponds to the rotor field orientation, to enable independent control of field weakening and torque, respectively. The second harmonic stator current components $i_{\alpha,-2}$ and $i_{\beta,-2}$ are rotated in a coordinate system (d_{-2}/q_{-2}) (Figure 6.6 right), rotating at $-\omega_e$ and orientated so that the d-current component $i_{d,-2}$ generates a horizontal force and the q-current component $i_{q,-2}$ generates a vertical force in the stator fixed coordinate system (α_{-2}/β_{-2}). In the synchronous coordinate system (d_1/q_1), the split winding motor is equivalent to a conventional PMSM with its phase resistance R_s, inductance $L_{s,1}$ and induced voltage (back EMF) in the stator winding per phase $\omega_e \Psi_0$. The stator winding inductance $L_{s,1}$ is the sum of the magnetising inductance of the fundamental field $L_{h,1}$ and of the total leakage inductance $L_{\sigma,1}$, described in Section 6.3.4, that results when $\underline{i}_A = -\underline{i}_B$. In the coordinate system (d_{-2}/q_{-2}), the split winding motor is equivalent to a simple $R-L$-load with its phase resistance R_s and inductance $L_{s,-2}$ as no back EMF occurs at $\epsilon = 0$. While the phase resistance R_s is the same as in the coordinate system (d_1/q_1), the inductance $L_{s,-2}$ is different from the inductance $L_{s,1}$, as both the magnetising inductances are different (different air gap field waves) and the leakage inductances are different (different current flow orientation in the stator slots).

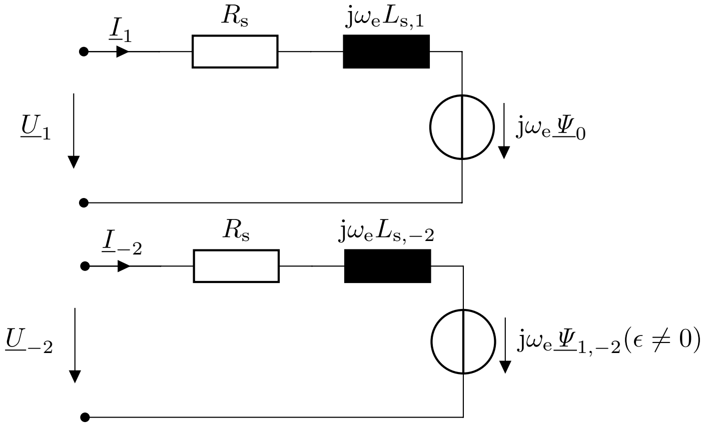

Figure 6.7.: Equivalent circuit of the fundamental wave (subscript 1) and second harmonic wave (subscript -2). The phase resistance R_s is the same for both circuits whereas the main inductances L_1 and L_{-2} are different. The induced voltage per phase (back EMF) in the stator winding $\underline{U}_\mathrm{i} = \mathrm{j}\omega_\mathrm{e}\mathit{\Psi}_0$ is present in the fundamental voltage $\underline{U}_1$. A small back EMF may occur in $\underline{U}_{-2}$, if the rotor is not concentric to the stator (4.41), hence $\epsilon \neq 0$.

Indeed, the induced voltage $\underline{u}_{\mathrm{i,A}}$ in winding A in (6.5) is in phase opposition with the induced voltage $\underline{u}_{\mathrm{i,B}}$ in winding B, so that both cancel after addition of the two with the extended *Clarke* transform (6.11). A small induced voltage per stator phase remains however, when the rotor is not concentric to the stator ($\epsilon \neq 0$), because the two induced voltages $\underline{u}_{\mathrm{i,A}}$ and $\underline{u}_{\mathrm{i,B}}$ do not cancel each other completely. This voltage disturbance is accommodated by the current controller. The equivalent circuits of the two voltage systems for $\nu = 1$ and for $\nu = -2$ are obtained by transformation of the voltage equations (6.5) in the two reference frames. They are illustrated in Figure 6.7. The rotor permanent magnet flux linkage with the stator winding $\mathit{\Psi}_0$ induces a stator voltage primarily in the fundamental system $\nu = 1$, but a small induced voltage is present in the second harmonic system ν = -2 in case of rotor eccentricity $\epsilon \neq 0$. Since the two equivalent circuits are simple $R - L$-models, they can be controlled with simple proportional-integral or dead-beat controllers. The four voltage references $(u_{\mathrm{d},1}, u_{\mathrm{q},1}, u_{\mathrm{d},-2}, u_{\mathrm{q},-2})^\mathsf{T}$, that are calculated by the four current controllers, are then transformed back into the stator coordinate systems A and B according to (6.12). The calculation of the two voltage pulse patterns A and B is the same as for a conventional space vector modulation for three-phase windings.

$$\begin{pmatrix} u_{\alpha,\mathrm{A}} \\ u_{\beta,\mathrm{A}} \\ u_{\alpha,\mathrm{B}} \\ u_{\beta,\mathrm{B}} \end{pmatrix} = \frac{1}{2} \cdot \begin{pmatrix} \cos\theta_1 & -\sin\theta_1 & \cos\theta_2 & -\sin\theta_2 \\ \sin\theta_1 & \cos\theta_1 & \sin\theta_2 & \cos\theta_2 \\ -\cos\theta_1 & \sin\theta_1 & \cos\theta_2 & -\sin\theta_2 \\ \sin\theta_1 & -\cos\theta_1 & \sin\theta_2 & \cos\theta_2 \end{pmatrix} \cdot \begin{pmatrix} u_{\mathrm{d},1} \\ u_{\mathrm{q},1} \\ u_{\mathrm{d},-2} \\ u_{\mathrm{q},-2} \end{pmatrix} \tag{6.12}$$

6.4.3. Complete control scheme

The control structure, which is implemented in the two three-phase inverters A and B to test the prototype motor of Table 6.1, is illustrated in Figure 6.8. The inner current loop and the outer rotor lateral position loop can be recognised. The lower part to control the combined magnetic bearing (CMB) is implemented in one separate inverter with three independent H-bridges, while the self-bearing control is implemented in the second six-phase inverter, where three phases are used for inverter A and three phases for inverter B.

6.5. Motor construction

The prototype was realised with the support of the company *LTI Motion GmbH*. Two special six-phase inverters, the complete combined axial-radial magnetic bearing with permanent magnet excitation for the second bearing force at NDE, the axial and radial position sensors, the laminated stator iron packet, the rotor-magnet and the bandage were produced or purchased by the company, while the other parts were made in the university workshop. The prototype is very similar to the prototype in [8]. The completed rotor is shown in Figure 6.9 and the assembled prototype motor in Figure 6.10. The prototype motor is however more compact than the previous

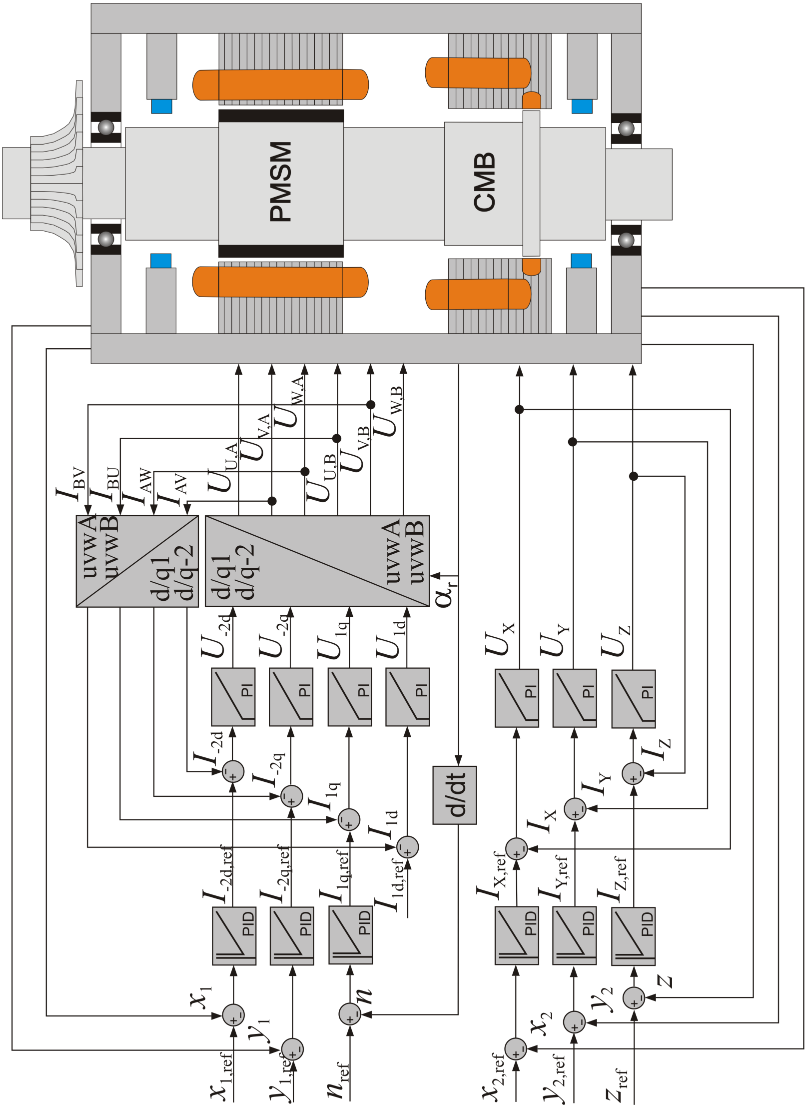

Figure 6.8.: Control scheme with position control as outer loop and current control as inner loop.

prototype [8], with two separated drive and levitation windings, mainly due to the short winding overhang, as can be seen in Figure 6.11. It is able

Figure 6.9.: Assembled rotor with combined axial-radial magnetic bearing on the left and the self-bearing motor rotor on the right: The combined axial-radial magnetic bearing is composed of an axial disk to generate axial thrust and an iron stack part to generate radial forces on the non-drive end. The permanent magnet is two-pole diametrically magnetised and supported by a carbon bandage (in black) in order to withstand the high centrifugal forces at 60 000 /min.

Figure 6.10.: Assembled motor prototype: The stator is naturally air-cooled with the help of small cooling fins of the aluminium housing. The rotor is loaded with a propeller, which was originally designed for car turbochargers.

to provide continuously much more power as well. Unfortunately, the two motor active parts of the prototype motor (Table 6.1) and the former prototype [8] are significantly different in terms of selected material parameters and dimensions, so that a fair performance comparison is not possible. Indeed, the stator iron sheets of the prototype (Table 6.1) are of the type

Figure 6.11.: Stator iron stack with 12 unskewed slots and split winding with winding part A and B: The winding A and B is a two-pole distributed winding (Figure 6.1), therefore, the winding overhang looks like the one of a four-pole winding. Since the stator yoke is large (for the higher flux of a two-pole motor), it was possible to tighten the winding overhang very close to the stator packet, leading to a significant reduction of the prototype axial length. Two temperature sensors KTY 84-130 are glued in the winding overhang (not visible in the picture).

M330-35A and are not well suited for high-frequency, so that the no-load losses are high due to high iron losses. The rotor positioning uses the same differential eddy-current sensors as the one presented in [14]. The working principle is detailed in Section 3.3.1. The MOSFET-power inverters are rated at 150 V DC supply, 1.2 kW input power and 8 A phase current. The complete test-bench is shown in Figure 6.12.

6.6. Measurements on the prototype

The prototype motor (Table 6.1) was measured at no-load and at load to validate the motor design. Whereas the no-load measurement in motor operation is simple, the load measurement could not be performed with a load machine in a back-to-back configuration since there was no prototype

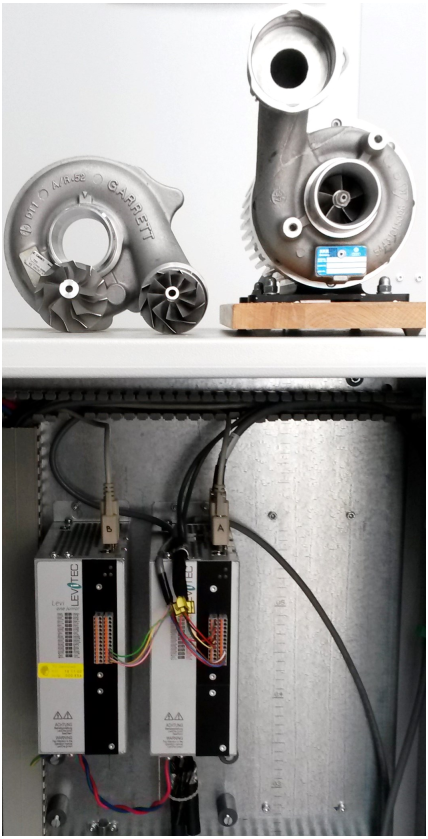

Figure 6.12.: Motor test-bench: The prototype motor (Table 6.1) on the top right is loaded with three different turbocharger propellers to set different values of the load torque. The two inverters that drive the combined magnetic bearing and the prototype are in the cabinet below. The power cables for the feeding of the windings are coming from the bottom of the inverters, whereas the shielded sensor cables are coming from the top of the inverters.

able to give sufficient shaft torque at $n_{\mathrm{N}} = 60\,000$ rpm. Instead, the motor was loaded with different propellers that are originally designed for car turbochargers. For this reason, the motor losses are measured indirectly. The measurement of the electrical quantities is done with a *NORMA 5000* power analyser that can simultaneously measure the power input of six phases. The DC voltage 150 V and DC current from the battery supply are measured with a voltmeter and ammeter.

In order to prevent the air flow from the propeller to actively cool the motor housing, the air inlet and outlet are deflected with shields from the motor housing. Still two unwanted cooling effects are taking place. First the air flow must pass close to the motor front, where the propeller is located, cooling a front portion of the stator at that location. Secondly, the air flow between stator and rotor at nominal speed is very turbulent (the *Reynolds* number Re reaches at nominal speed n_N values over 70 000 in the air gap). Therefore calculations show that some heat power is also flowing by convection from the stator to the rotor through the air gap and is then flowing axially via the shaft to the intensively air-cooled propeller. This two effects are so dominant that the motor is much cooler (by 40 K) under propeller load than at (motor) no-load. Due to this cooling improvement, the motor is able to deliver continuously more than 150% of the power it was originally dimensioned for. Although the winding end-temperature rise $\theta_{1.5\mathrm{P_N}} = 51$ K at 1.5 P_N is well below the maximum 90 K allowed by the Thermal Class B (IEC 60034-1) of the winding insulation, the maximum continuous power output (estimated at 1.5 kW) could not be reached, as the inverter input current limit was too low, leading to a tripping of the inverter input current protection. Another encountered problem was that the cooling fins of the aluminium housing gave a cooling surface $A_\mathrm{hs} = 0.155\ \mathrm{m}^2$, which was realised on the Lathe in the workshop. This gave a housing-to-ambient air equivalent thermal resistance $R_\mathrm{th,hs} = 0.43$ K/W, which is too high to dissipate the motor no-load losses of 175 W. It should be noted that most high-speed machines are intensively air-cooled or water-cooled, because they have to cope with high loss densities. The choice for natural-air cooling was made for the sake of simplicity, though it is not appropriate for this kind of high-speed motors.

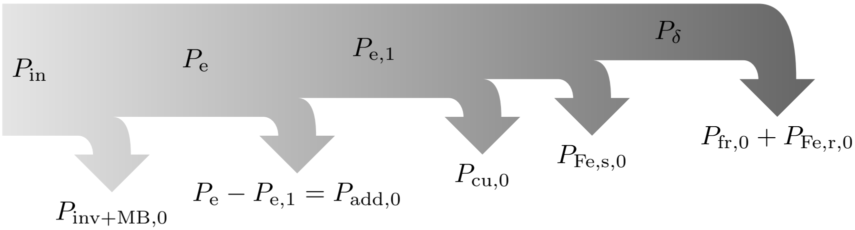

Figure 6.13.: Illustration of the power flow of the prototype motor (Table 6.1) at nominal speed and no-load operation.

6.6.1. No-load measurements

The no-load losses (Table 6.5, Figure 6.13) are composed of:

- No-load ohmic losses $P_{\text{cu},0}$ mainly due to the levitation current I_{-2}
- No-load inverter and magnetic bearing losses $P_{\text{inv+MB},0}$ of the axial-radial combined magnetic bearing
- Additional no-load losses $P_{\text{add},0}$, such as eddy current losses in rotor magnets due to field harmonics
- The sum of the air-friction losses and no-load iron losses in the stator and rotor $P_{\text{Fe+fr},0}$

$P_{\text{inv+MB},0}$ is obtained by subtraction of the motor input power P_{e} from the electrical input power at the DC-link P_{in}. The no-load ohmic losses $P_{\text{cu},0}$ are calculated indirectly from the RMS currents and the corrected phase resistance $R_{\text{s}}(\theta)$ according to (6.13). For that, the winding temperature θ is considered equal in all the phases, even though the phase currents of the unbalanced current systems A and B are quite different for some operation points (see Figure 6.15). The additional no-load losses $P_{\text{add},0}$ equal the motor input power P_{e} minus the measured fundamental component of the electrical power $P_{\text{e},1}$. The air-friction plus iron losses $P_{\text{Fe+fr},0}$ are equal to the electrical fundamental power $P_{\text{e},1}$ minus $P_{\text{cu},0}$.

Table 6.5.: Measured and calculated no-load losses

Parameter	**Symbol**	**Calculated**	**Measured**	**Unit**
Electrical input power	$P_{\mathrm{e},1,0}$	138^{a}	132	W
Ohmic losses	$P_{\mathrm{cu},0}$	1^{a}	0.64	W
Iron losses	$P_{\mathrm{Fe,s},0}$	68.7^{b}	131	W
Air friction losses	$P_{\mathrm{fr},0}$	65.0^{a} [35]		W
Rotor losses	$P_{\mathrm{Fe,r},0}$	3.4^{b}		W
Additional losses	$P_{\mathrm{add},0}$	-	43.2	W
Inverter and MB losses	$P_{\mathrm{inv+MB},0}$	-	54.1	W

---

[a] Values calculated analytically

[b] Values obtained in 3D FEM simulations using the program *JMAG*

$$P_{\mathrm{cu},0} = R_{\mathrm{s}}(\theta) \cdot \sum_{\substack{j=\mathrm{A,B} \\ k=\mathrm{U,V,W}}} I_{j,k,0}^{2} \tag{6.13}$$

6.6.2. Load measurements

The motor was measured at three operation points, which are listed in Table 6.6. The shaft torque values were set by the different propellers 1, 2 and 3 in Table 6.6, and could not be tuned precisely. The ohmic losses P_{cu}, additional losses at load P_{add} and the inverter plus magnetic bearing losses $P_{\mathrm{inv+MB}}$ at load are derived in the same way as at no-load, using the equations (6.14).

Table 6.6.: Measured operation points

Propeller Symbol	**Speed** n /min^{-1}	**Torque** M /N m	**Power input** P_e /W	**Power output** P_m /W
No-load 1	48 360	0	129	0
No-load 2	60 180	0	175	0
Propeller 1	48 000	0.200[a]	1168	1012
Propeller 2	60 000	0.090[a]	749	567
Propeller 3	60 060	0.160[a]	1164	979

---

[a] The torque is calculated via speed and the calculated output power P_m from the measured total losses P_d (Table 6.7) and the input power $P_\mathrm{in} = P_\mathrm{e} - P_\mathrm{d}$.

$$\begin{aligned} P_\mathrm{d} &= P_\mathrm{cu} + P_\mathrm{fr} + P_\mathrm{Fe} + P_\mathrm{add} \\ P_\mathrm{in} &= P_\mathrm{e} + P_\mathrm{inv+MB} \\ P_\mathrm{add} &= P_\mathrm{e} - P_\mathrm{e,1} \\ P_\mathrm{e,1} &= P_\mathrm{cu} + P_\mathrm{fr} + P_\mathrm{Fe} + P_\mathrm{m} \end{aligned} \tag{6.14}$$

In order to obtain the air friction losses and iron losses $P_\mathrm{Fe+fr}$, a motor no-load measurement is performed after each load measurement at approximately the same winding temperature and housing temperature. From this no-load post-measurement, the losses $P_\mathrm{Fe+fr,0}$ are determined as presented in Section 6.6.1. The air-friction losses are calculated analytically according to [35] and subtracted from $P_\mathrm{Fe+fr,0}$ to obtain an estimation of the measured iron losses $P_\mathrm{Fe,0}$. The iron losses P_Fe at load are different from the value at no-load due to the increased stator magnetic field. They are estimated with the correction equation (6.15), where U_0 is the average of the RMS phase voltages at no-load and U_N is the average of the RMS phase voltage at load. Since the voltage at load is almost equal to the one at no-load, the influence of this correction is not significant. The measured losses are compiled in Table 6.7.

Table 6.7.: Measured and calculated losses at load for the prototype motor of Table 6.1

Parameter	**Symbol**	**Prop. 2**	**Prop. 3**	**Prop. 1**
Speed	n /min^{-1}	60 000	60 060	48 000
Torque	M /N m	0.09	0.16	0.20
Fundamental electrical input power	$P_{\mathrm{e},1}$ /W	705	1123	1117
Ohmic losses	P_{cu} /W	5.8	12.9	18.5
Air friction	P_{fr} /W	65	65	34
Iron losses	P_{Fe} /W	74	80	73
Additional losses	P_{add} /W	44.9	40.7	50.3
Inverter + MB losses	$P_{\mathrm{inv+MB}}$ /W	72.5	96.1	101.2

$$P_{\mathrm{Fe}} = P_{\mathrm{Fe},0} \cdot \left(\frac{U_{\mathrm{N}}}{U_0} \right)^2 \tag{6.15}$$

It should be noticed that the ohmic losses represent a very small part of the total losses (Table 6.7: respectively 2.2%, 4.4% and 6.8% for propeller no. 2, no. 3 and no. 1) so that the motor is significantly under-loaded in the stator winding. The overall efficiency of the drive η and the motor efficiency η_{M}, are calculated with (6.16) and given in Table 6.8.

$$\eta_{\mathrm{M}} = \frac{P_{\mathrm{m}}}{P_{\mathrm{e}}}, \ \eta = \frac{P_{\mathrm{m}}}{P_{\mathrm{e}} + P_{\mathrm{inv+MB}}} = \frac{P_{\mathrm{m}}}{P_{\mathrm{in}}} \tag{6.16}$$

The efficiency values are low and increase with increasing load, since the no-load losses account for the biggest part of the total losses. A higher loading at 60 000 /min was not possible for the existing test rig, so the maximum efficiency could not be tested, due to the too low inverter limit.

Table 6.8.: Indirectly estimated drive efficiency

Parameter	**Symbol**	**Prop. 2**	**Prop. 3**	**Prop. 1**
Speed	n /min^{-1}	60 000	60 060	48 000
Torque	M /N m	0.09	0.16	0.20
Electrical input power	P_e /W	749	1164	1168
Fundamental electrical input power	$P_{\mathrm{e},1}$ /W	705	1123	1117
Output power	P_m /W	567	979	1012
Motor efficiency	η_M /%	0.757	0.841	0.866
Drive efficiency	η /%	0.69	0.777	0.797

6.6.3. Back EMF

The line-to-line back EMF was measured at motor no-load. Since both windings A and B must be fed to provide levitation force, a no-load measurement with open terminals is not possible with this prototype. Even if the levitation current at no-load is low (below 1.4 A in all phases) and mainly due to the levitation current $I_{-2,0}$, the high rotation frequency ω_e at 60 000 /min, $\omega_\mathrm{e} = 6283$ /s as well as the non-negligible inductance $L_{-2} = 178$ µH lead to relative differences between the different phase voltages (±2.5%) as the phase circuits are not symmetrical. In order to obtain a good approximation of the measured induced voltage U_i by measuring the terminal voltages, the fundamental voltage component $U_{1,0}$ of each phase is isolated out of the pulse width modulated voltage by the power analyser *NORMA 5000*. Then equation (6.17) is used to approximate U_i. This equation is obtained from (6.5) by neglecting the resistive voltage drop at no-load and gives a good approximation for this prototype, since the induced voltage U_i is much bigger than the two other voltage components of self-induction in (6.17).

$$\begin{aligned} U_\mathrm{i} &\approx \sqrt{U_\mathrm{i}^2 + \omega_\mathrm{e}^2 \cdot L_{\mathrm{s},1}^2 \cdot I_{1,0}^2 + \omega_\mathrm{e}^2 \cdot L_{\mathrm{s},-2}^2 \cdot I_{-2,0}^2} \\ &\approx \sqrt{\frac{1}{3} \cdot \left(U_{\mathrm{U},1,0}^2 + U_{\mathrm{V},1,0}^2 + U_{\mathrm{W},1,0}^2\right)} \end{aligned} \tag{6.17}$$

A RMS voltage of 43.75 V (resp. 43.63 V) is obtained in winding A (resp. winding B). The magnet temperature could not be measured. Since the winding temperatures are measured as 77°C and the rotor magnet is made of $\mathrm{SmCo_5}$ with a low reversible temperature coefficient of -0.04%/K, the rotor temperature is estimated also at 77°C, and the influence on the voltage measurement due to the unknown rotor temperature is low. The calculated no-load voltage at 100°C in 3D FEM is 44.1 V, so slightly higher than measured out. The voltage harmonics components are obtained by transforming the voltage signals in the complex representation $\underline{u}_\mathrm{A}(t)$ and $\underline{u}_\mathrm{B}(t)$ (6.5) and applying the discrete *Fourier* transformation, leading to the ordinal number k. A negative k is due to negative sequence voltage systems. They are numerically evaluated at operation with propeller 3 (Table 6.6) in Figure 6.14. It can be noticed that the positive sequence voltage (ordinal number $k = 1$) is much higher than the other components. The third harmonic components are present, because the inverter uses space vector modulation. They are not present in the actual motor phase voltages, which are induced from the rotor magnet field.

6.6.4. Phase currents

In each phase, a pulsating current with a different amplitude is flowing. As expressed mathematically in (6.1), the amplitude in each phase depends not only on the sum of the drive current I_1 and the levitation current I_{-2}, but also on their phase difference, manifested in each phase as a different time shift between the maxima of the two pulsating currents. This is illustrated in Figure 6.15, where the phase currents, recorded with the scope function of the inverter, are different in amplitude. The phase shift between

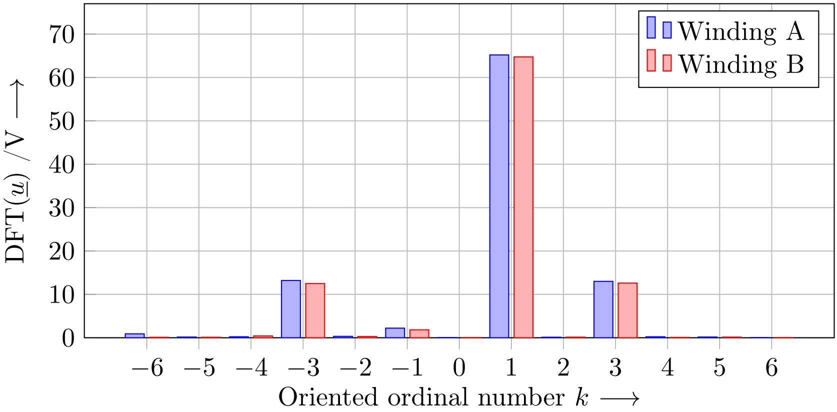

Figure 6.14.: Discrete *Fourier* transformation (DFT) of the two measured complex stator voltages $\underline{u}_\mathrm{A}$ and $\underline{u}_\mathrm{B}$ at speed 60 060 /min and torque 0.16 Nm (Table 6.6). The two positive sequence voltage amplitudes are approximately 65.5 V, whereas the negative sequence voltage amplitudes are 2.0 V. Two harmonic components at $|k| = 3$ are present with an amplitude of 12.7 V each. They are caused in the phase voltage by the inverters which use space vector modulation.

the current maxima is not $2\pi/3$. The power measurement system gives a single phase current amplitude and can not separate I_1 from I_{-2}. At no-load, the fundamental of the levitation current $I_{-2,0}$ is separated from the drive current $I_{1,0}$ with the following power consideration: At steady-state, the air-friction losses and the iron losses $P_{\mathrm{Fe+fr},0}$ must be covered by the no-load electrical input power $P_{\mathrm{e},1,0}$, which depends on the drive current $I_{1,0}$ according to (6.18). As U_i and $P_{\mathrm{Fe+fr},0}$ were already calculated before, the no-load drive current at nominal speed is obtained and equals 0.50 A at $n_\mathrm{N} = 60\ 000$ /min. The actual drive current signal $I_{\mathrm{q},1,\mathrm{act}}$, measured by the inverter, displays an average value equal to 0.47 A RMS. The calculated no-load drive current $I_{1,0}$ in FEM simulation to compensate the analytically calculated air-friction losses (expressed as a load torque) and the numerically (3D FEM) obtained iron losses, is equal 0.52 A [53]. Indeed, the slightly higher calculated losses $P_{\mathrm{Fe+fr},0}$ compensate the slightly higher calculated induced voltage U_i, so that the measured and calculated no-load

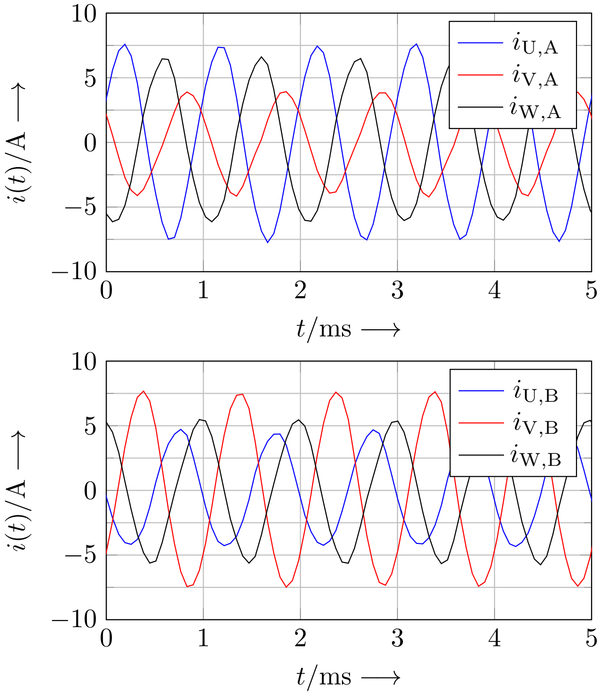

Figure 6.15.: Measured phase currents in the two three-phase windings A (top) and B (bottom), measured at $n = 60\ 060$ rpm, $F_\mathrm{r} = 5$ N, $M = 0.160$ Nm (Table 6.6).

drive current $I_{1,0}$ are agreeing. The levitation current component I_{-2} is then obtained, using the orthogonality property of the square of current components, previously derived in (6.9). For that, equation (6.19) is used, where $I_{j,k}$ is the RMS amplitude of the current fundamental in phase k of winding j.

$$\begin{aligned} P_{\mathrm{Fe+fr},0} =& P_{\mathrm{e},1,0} - P_{\mathrm{Cu},1,0} = 6\cdot U_\mathrm{i}\cdot I_{1,0} \\ \approx& \sqrt{3}\cdot\sum_{j=\mathrm{A,B}}\sqrt{\sum_{k=\mathrm{U,V,W}} U_{j,k,0}^2}\cdot I_{1,0} \end{aligned} \tag{6.18}$$

$$I_{-2} = \sqrt{\left[\frac{1}{6} \cdot \sum_{\substack{j=\mathrm{A,B} \\ k=\mathrm{U,V,W}}} I_{j,k}^2\right] - \left(\frac{P_{\mathrm{Fe+fr},0}}{6U_{\mathrm{i}}}\right)^2} \tag{6.19}$$

The obtained current $I_{-2,1}$ amplitude is equal 0.91 A RMS at no-load and is increased, when the propeller load is added, until 1.37 A RMS with the biggest propeller number 1. Taking the force-current factor k_{ir} from Table 6.3, it means that the self-bearing motor is bearing 360 g at no-load (45% of rotor mass) and 530 g at load (65% or rotor mass). The propeller mass is less than 40 g, but significantly shifts the center of mass of the shaft, so that the self-bearing motor must bear a higher proportion of the shaft weight at load. In the phase current, additional harmonic components are present due to imperfection of the control at rated operation. In order to estimate their amplitudes, the sampled phase currents in Figure 6.15 are transformed in complex stator currents $\underline{i}_{\mathrm{A}}[n]$ and $\underline{i}_{\mathrm{B}}[n]$ according to (6.20) where n is the sample number of the discrete current signal $i[n]$.

$$\begin{aligned} \underline{i}_{\mathrm{A}}[n] &= i_{\mathrm{U,A}}[n] - \mathrm{j} \cdot \frac{1}{\sqrt{3}} \cdot (i_{\mathrm{U,A}}[n] + 2 \cdot i_{\mathrm{W,A}}[n]) \\ \underline{i}_{\mathrm{B}}[n] &= i_{\mathrm{U,B}}[n] - \mathrm{j} \cdot \frac{1}{\sqrt{3}} \cdot (i_{\mathrm{U,B}}[n] + 2 \cdot i_{\mathrm{W,B}}[n]) \end{aligned} \tag{6.20}$$

Subsequently the harmonic components of the complex currents $\underline{i}_{\mathrm{A}}[n]$ and $\underline{i}_{\mathrm{B}}[n]$ are obtained, again using the discrete *Fourier* transformation, leading to harmonic ordinal numbers k. Negative values of k are for negative sequence systems. In order to obtain a sufficient resolution, a 30 ms record is taken with exactly 30 electrical periods. The amplitudes in the spectra of the two DFTs are given in Figure 6.16. The levitation component (ordinal number $k = -1$ in the phase current) has a RMS value of 1.4 A with the biggest propeller number 1 while calculated to be 1.37 A with (6.19). The drive component (ordinal number $k = 1$) equals 4.0 A and does not fit the calculated 4.29 A, since the drive current was not really constant during the 30 ms record. The higher harmonic current components are below 0.14 A RMS.

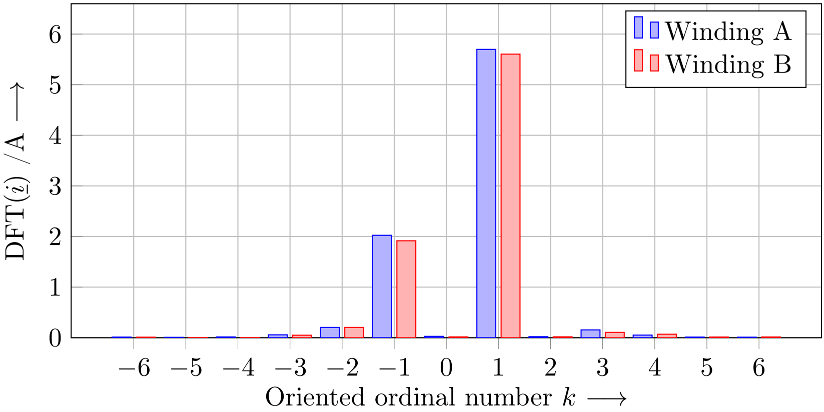

Figure 6.16.: Discrete Fourier transformation of the two measured complex stator currents $\underline{i}_{\mathrm{A}}$ and $\underline{i}_{\mathrm{B}}$ from Figure 6.15. The two drive current amplitudes are approximately 5.7 A whereas the levitation current amplitudes are 2.0 A. Some small additional harmonic components are visible in particular at the ordinal number -2 and 3.

7. Control scheme of self-bearing drives

In the previous chapters, two self-bearing motors were modelled, based on the electromagnetic model obtained in Chapter 4. This chapter deals with control strategies to stabilise self-bearing motors. Since this topic is already thoroughly detailed in the literature on drives with active magnetic bearings, a particular focus is given here on control aspects related to the self-bearing motor. For illustration purpose, the presented schemes are evaluated for the double conical motor prototype [26], presented in Chapter 5.

7.1. Plant description

7.1.1. Definitions and reference frames

In this section, the definitions of the positions, of the motor mechanical parameters and reference frames are given. A representation of the active self-bearing motor is given in Figure 7.1. The rotor has a mass m_r, a rotor polar moment of inertia J_z and two equal rotor transverse moments of inertia J_x and J_y. The presented model in Figure 4.1 is passively stable in the axial direction since the rotor aligns with the stator iron stack. However it is not able to generate any controllable axial force. To do so, the motor needs an additional axial magnetic bearing or an axial asymmetry as for example a conical air gap [14]. The second solution with two conical half-rotors is illustrated in Figure 7.1. The rotor positions are measured at the

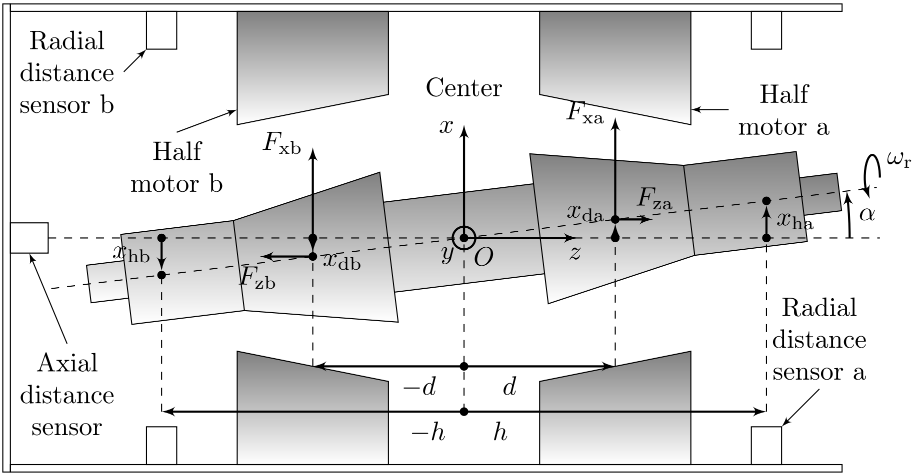

Figure 7.1.: Simplified mechanical model of the conical motor with the two half motors a and b and with definitions of variables for the x-z-plane tilted rotor. A similar cut-view for the y-z-plane delivers the corresponding variables: (x_{ha}, x_{hb}) $\rightarrow$ (y_{ha}, y_{hb}), (x_{da}, x_{db}) $\rightarrow$ (y_{da}, y_{db}), ($\alpha \rightarrow \beta$) and (F_{xa}, F_{xb}) $\rightarrow$ (F_{ya}, F_{yb}).

position sensor locations while the levitation forces are distributed along the air gaps. In order to simplify the model, the levitation forces are considered to be acting in the axial middle of each half-motor. Furthermore, the drive-end (DE) and the non-drive end (NDE) rotor parts are considered to be symmetrical. The measured positions are gathered in a position vector $\boldsymbol{q}_{\mathrm{h}}$ (7.3) where x_{ha}, y_{ha} (resp. x_{hb}, y_{hb}) are the displacements measured radially at the drive end (resp. non-drive end), θ is the rotational angle along the z-axis and z is the displacement along the z-axis. It is transformed into the state vector $\boldsymbol{q}$ (7.1) where α and β are the rotor tilting along the y- and x-axes respectively, and where x and y are the rotor parallel displacement along the x- and y-axes respectively. The position vector where the forces take place is $\boldsymbol{q}_{\mathrm{d}}$ (7.2). The state vector $\boldsymbol{q}$ is transformed to $\boldsymbol{q}_{\mathrm{d}}$ (resp. $\boldsymbol{q}_{\mathrm{h}}$) using the transformation matrix $\boldsymbol{B}_{\mathrm{d}}$ (resp. $\boldsymbol{B}_{\mathrm{h}}$) in (7.4).

$$\boldsymbol{q} = (\alpha, x, \beta, y, \theta, z)^{\mathsf{T}} \tag{7.1}$$

$$\boldsymbol{q_\mathrm{d}} = (x_\mathrm{da}, x_\mathrm{db}, y_\mathrm{da}, y_\mathrm{db}, \theta, z)^\mathsf{T} = \boldsymbol{B}_\mathrm{d}^\mathsf{T}\boldsymbol{q} \tag{7.2}$$

$$\boldsymbol{q_\mathrm{h}} = (x_\mathrm{ha}, x_\mathrm{hb}, y_\mathrm{ha}, y_\mathrm{hb}, \theta, z)^\mathsf{T} = \boldsymbol{B}_\mathrm{h}^\mathsf{T}\boldsymbol{q} \tag{7.3}$$

$$\boldsymbol{B}_\mathrm{d} = \begin{pmatrix} d & -d & 0 & 0 & 0 & 0 \\ 1 & 1 & 0 & 0 & 0 & 0 \\ 0 & 0 & d & -d & 0 & 0 \\ 0 & 0 & 1 & 1 & 0 & 0 \\ 0 & 0 & 0 & 0 & 1 & 0 \\ 0 & 0 & 0 & 0 & 0 & 1 \end{pmatrix} \quad \boldsymbol{B}_\mathrm{h} = \begin{pmatrix} h & -h & 0 & 0 & 0 & 0 \\ 1 & 1 & 0 & 0 & 0 & 0 \\ 0 & 0 & h & -h & 0 & 0 \\ 0 & 0 & 1 & 1 & 0 & 0 \\ 0 & 0 & 0 & 0 & 1 & 0 \\ 0 & 0 & 0 & 0 & 0 & 1 \end{pmatrix} \tag{7.4}$$

It should be noted that the axial displacement z is independent from the other displacements in (7.4) as the rotations α and β along the transversal axes are very small. Therefore, the axial control is independent from the radial control from the mechanical point of view. The same applies to the rotation θ along the z-axis.

7.1.2. Mechanical equations

In order to derive the rotor motion, the description of rigid rotor dynamic presented in [4] is followed. Since both presented prototypes are operating below the first bending frequency, rotor elasticity is not considered. As for AMB, the inertia matrix $\boldsymbol{M}$ is composed of the rotor mass m_r, and the three inertias $J_\mathrm{x}, J_\mathrm{y}, J_\mathrm{z}$ along the axes x, y and z respectively. The gyroscopic matrix $\boldsymbol{G}$ is composed only of the inertia component J_z. The force displacement matrix $\boldsymbol{K_\mathrm{st}}$ gathers the radial stiffness coefficient k_sr and the axial stiffness coefficient k_sz. The force vector $\boldsymbol{f}$ is the product of the force-current matrix $\boldsymbol{K_\mathrm{it}}$ with the current vector $\boldsymbol{i_\mathrm{t}}$. The matrices are given in (7.5). It should be noted that the term "force" designates both force and torque components. In contrast to AMB, the input current vector $\boldsymbol{i_\mathrm{t}} = (i_\mathrm{1da}, i_\mathrm{1qa}, i_\mathrm{1db}, i_\mathrm{1qb}, i_\mathrm{2da}, i_\mathrm{2qa}, i_\mathrm{2db}, i_\mathrm{2qb})^\mathsf{T}$ is composed of current components that are oriented in the synchronous coordinate system $(\mathrm{d/q})_1$ and in a fictive synchronous coordinate system $(\mathrm{d/q})_2$, that rotates at the same electrical frequency ω_e but is oriented so that the current component along d_2 (resp. q_2) generates a force in the radial direction x (resp. y). The axial force component $f_\mathrm{z} = k_\mathrm{iz} \cdot (i_\mathrm{1da} - i_\mathrm{1db})$ results from the opposite axial-pulls in each half-motor a and b, generated by the rotor field-weakening currents i_1da and i_1db. This expression is particular to this self-bearing motor configuration and is further detailed in Chapter 5. *Newton*'s law of motion is given by (7.6) where ω_r is the mechanical rotational speed. Due to the gyroscopic part $\omega_\mathrm{r}\boldsymbol{G}$, the system is not linear. However the rotational speed is changing very slowly compared to the rotor displacement dynamic so that a linearisation of the system at the rotational speed ω_r is legitimate.

$$\boldsymbol{M} = \mathrm{diag}(J_\mathrm{x}, m_\mathrm{r}, J_\mathrm{y}, m_\mathrm{r}, J_\mathrm{z}, m_\mathrm{r}) \quad \boldsymbol{K}_\mathbf{st} = \mathrm{diag}(k_\mathrm{sr}, k_\mathrm{sr}, k_\mathrm{sr}, k_\mathrm{sr}, 0, k_\mathrm{sz}) \tag{7.5}$$

$$\boldsymbol{G} = \begin{pmatrix} 0 & 0 & J_\mathrm{z} & 0 & 0 & 0 \\ 0 & 0 & 0 & 0 & 0 & 0 \\ -J_\mathrm{z} & 0 & 0 & 0 & 0 & 0 \\ 0 & 0 & 0 & 0 & 0 & 0 \\ 0 & 0 & 0 & 0 & 0 & 0 \\ 0 & 0 & 0 & 0 & 0 & 0 \end{pmatrix} \qquad \boldsymbol{f} = \begin{pmatrix} k_\mathrm{ir} i_\mathrm{2da} \\ k_\mathrm{ir} i_\mathrm{2db} \\ k_\mathrm{ir} i_\mathrm{2qa} \\ k_\mathrm{ir} i_\mathrm{2qb} \\ k_\mathrm{iM}(i_\mathrm{1qa} + i_\mathrm{1qb}) \\ k_\mathrm{iz}(i_\mathrm{1da} - i_\mathrm{1db}) \end{pmatrix} = \boldsymbol{K}_\mathbf{it} \boldsymbol{i}_\mathbf{t}$$

$$\boldsymbol{M}\ddot{\boldsymbol{q}} + \omega_\mathrm{r}\boldsymbol{G}\dot{\boldsymbol{q}} + \boldsymbol{B}_\mathbf{d}\boldsymbol{K}_\mathbf{st}\boldsymbol{B}_\mathbf{d}^\intercal \boldsymbol{q} = \boldsymbol{B}_\mathbf{d}\boldsymbol{K}_\mathbf{it} \cdot \boldsymbol{i}_\mathbf{t} \tag{7.6}$$

In order to obtain the system poles, the equation is transformed in state space representation with respectively the state, input, output and feed-through matrix $\boldsymbol{A}$, $\boldsymbol{B}$, $\boldsymbol{C}$, $\boldsymbol{D}$ in (7.7). For the particular case $\omega_\mathrm{r} = 0$, the open-loop poles can be obtained analytically and are given by (7.8). The four poles $p_{0,i}^\mathrm{p}$ correspond to the parallel displacements of the rotor along the x- and y-direction (superscript p). The four poles $p_{0,i}^\mathrm{c}$ correspond to the rotor tilting with α and β (superscript c). The two poles $p_{0,j}^\mathrm{z}$ correspond to the axial rotor displacement z (superscript z). In absence of friction forces, the two poles $p_{0,j}^\theta$, that characterise the rotation θ, equal zero.

$$\boldsymbol{A} = \begin{pmatrix} \mathbf{0} & \boldsymbol{I}_\mathbf{6} \\ -\boldsymbol{M}^{-1}\boldsymbol{B}_\mathbf{d}\boldsymbol{K}_\mathbf{st}\boldsymbol{B}_\mathbf{d}^\intercal & -\omega_\mathrm{r}\boldsymbol{M}^{-1}\boldsymbol{G} \end{pmatrix}, \quad \boldsymbol{B} = \begin{pmatrix} \mathbf{0} \\ \boldsymbol{M}^{-1}\boldsymbol{B}_\mathbf{d}\boldsymbol{K}_\mathbf{it} \end{pmatrix} \tag{7.7}$$
$$\boldsymbol{C} = \begin{pmatrix} \boldsymbol{B}_\mathbf{h}^\intercal & \mathbf{0} \end{pmatrix}, \qquad \boldsymbol{D} = \begin{pmatrix} \mathbf{0} \end{pmatrix}$$

$$
\begin{aligned}
p^{\mathrm{p}}_{0,i} &= (-1)^i \cdot \sqrt{\frac{2|k_{\mathrm{sr}}|}{m_{\mathrm{r}}}},\; p^{\mathrm{c}}_{0,i} = (-1)^i \cdot \sqrt{\frac{2|k_{\mathrm{sr}}|d^2}{J_{\mathrm{x}}}}, \\
p^{\mathrm{z}}_{0,j} &= (-1)^j \cdot \sqrt{\frac{2|k_{\mathrm{sz}}|}{m_{\mathrm{r}}}},\; p^{\theta}_{0,j} = 0,\; \text{with } i \in \{1,2,3,4\}, j \in \{1,2\}
\end{aligned}
\tag{7.8}
$$

Five poles in (7.8) are strictly positive so that the system is inherently unstable. It must be stabilised by the position controller. Since the rotors DE (a) and NDE (b) are considered symmetrical and the rotor is considered rigid, the system can be split into radial parallel modes, radial tilting modes and axial and rotational mode along the rotor axis. As the rotational speed ω_{r} increases, the two sets of conjugate pole pairs of the tilting motions $p^{\mathrm{c}}_{0,\mathrm{i}}$ are split in two, leading to four different Eigenvalues. The poles of the other motions are speed independent.

7.2. Control strategies

To simplify the presented position control strategies, the inner current control 2.1, identical to the one of PMSM, is assumed to be infinitely fast. It will be proven that this assumption is valid since the current control dynamic is much faster than the achievable position control dynamic.

7.2.1. Control scheme with decentralised PID controller

The popular PID controller is an old-fashioned and well suited controller to stabilise self-bearing motors. The proportional coefficient k_{P} of the controller is mandatory to overcome the inherent negative stiffness k_{sr} of the plant. The differential coefficient k_{D} is required to provide closed-loop damping. The optional integral coefficient k_{I} is added to get steady-state accuracy. Since it lowers the controller phase, it has a destabilising effect on the control loop. Therefore, it is often tuned low to ensure better damping at the cost of a slower convergence of the position error. In contrast to current control, the position control has a constant reference signal (generally rotor centre position) so that step response is of little relevance. In magnetically levitated drives, each position signal (e.g. DE) is commonly used as position error for the position controller that operates the actuator at the corresponding position (e.g. DE). This is called a decentralised Single-Input-Single-Output (SISO) control. In self-bearing drives, the positions where the displacements are measured differ significantly from the positions where the levitation forces take place. This inherent problem of the self-bearing motor is due to the relatively long motor active part and winding overhang that impose a long distance between net force position and sensor position. In the model illustrated in Figure 7.1, the radial positions, measured at $\pm h$ do not correspond to the net levitation force positions $\pm d$. Since only the tilting motion is affected by the location of the sensors, significant performance degradation can be observed when the control structure accommodates solely with SISO feedback. Since there are two underlying motions in each position signal, the decentralised controller can be tuned either for the parallel or tilting motion. For the parallel motion, the controller proportional part $k_{\mathrm{P}}^{\mathrm{p}}$ and differential part $k_{\mathrm{D}}^{\mathrm{p}}$ are tuned at "natural stiffness" with a damping ratio $\zeta \leq 1$ with (7.9). The critical damping ratio $\zeta = 1$ makes the closed-loop robust to disturbances. However lower values such as $\zeta = \sqrt{3}/2$ are commonly found in the literature [4].

$$G_{\mathrm{w}}^{\mathrm{p}}(s) = k_{\mathrm{P}}^{\mathrm{p}} + s \cdot k_{\mathrm{D}}^{\mathrm{p}}, k_{\mathrm{P}}^{\mathrm{p}} = 2 \cdot |k_{\mathrm{sr}}|/k_{\mathrm{ir}}, k_{\mathrm{D}}^{\mathrm{p}} = \zeta \cdot \sqrt{2m_{\mathrm{r}}|k_{\mathrm{sr}}|}/k_{\mathrm{ir}} \tag{7.9}$$

This controller tuning shifts the unstable parallel mode poles $p_{0,2}^{\mathrm{p}}$ and $p_{0,4}^{\mathrm{p}}$ to the desired position $p_{0,1}^{\mathrm{p}}$ (equal to $p_{0,3}^{\mathrm{p}}$) on the left half-plane. However it does not place the tilting mode poles $p_{0,2}^{\mathrm{c}}$ and $p_{0,4}^{\mathrm{c}}$ at $p_{0,1}^{\mathrm{c}}$. To do so, the controller tuning should fulfil (7.10).

$$G_{\mathrm{w}}^{\mathrm{c}}(s) = k_{\mathrm{P}}^{\mathrm{c}} + s \cdot k_{\mathrm{D}}^{\mathrm{c}}, k_{\mathrm{P}}^{\mathrm{c}} = 2d|k_{\mathrm{sr}}|/(h \cdot k_{\mathrm{ir}}), k_{\mathrm{D}}^{\mathrm{c}} = \zeta\sqrt{2J_{\mathrm{x}}|k_{\mathrm{sr}}|}/(h \cdot k_{\mathrm{ir}}) \tag{7.10}$$

Since $h \neq d$, $k_{\mathrm{P}}^{\mathrm{p}}$ and $k_{\mathrm{P}}^{\mathrm{c}}$ can not be equal. Furthermore, the motor parameters are generally not fulfilling the equation $J_{\mathrm{x}} = m_{\mathrm{r}}h^2$ so that $k_{\mathrm{D}}^{\mathrm{p}}$ and $k_{\mathrm{D}}^{\mathrm{c}}$ are not equal either. Depending on the motor parameters J_{x}, m_{r}, h and d, the local feedback can lead to either great or poor performances.

7.2.2. Illustration of decentralised controller deficiency due to local feedback

To illustrate the problem with the SISO approach, the control plant with motor parameters of the double conical prototype [26] listed in Table 7.1 is considered. To simplify the analysis, a simple PD controller with local feedback is considered. The sensors on the NDE (resp. DE) are used as position feedback for the control of the levitation forces of the NDE (resp. DE). The rotor is considered perfectly symmetrical as in Figure 7.1. The ratio of parallel to tilting Eigenfrequencies $r_\lambda = 0.5{\cdot}\sqrt{m_\mathrm{r} d^2 / J_\mathrm{x}} = 0.7$ is relatively close to one so that the control settings for the two motions should be very similar if $h/d \approx 1$. In this particular motor geometry however, this ratio is $h/d{=}\ 2.8$. This ratio affects the tilting motion only and is equivalent to a virtual gain of the position signal. Taking the motor parameters of the prototype [26] in Table 7.1, and using the equations (7.9) and (7.10) for a damping ratio $\zeta = \sqrt{3}/2$, the control parameters are calculated as (7.11).

$$\begin{aligned} k_\mathrm{P}^\mathrm{p} &= 29.0\ \mathrm{kA/m}, k_\mathrm{D}^\mathrm{p} = 130\ \mathrm{As/m} \\ k_\mathrm{P}^\mathrm{c} &= 10.3\ \mathrm{kA/m}, k_\mathrm{D}^\mathrm{c} = 66.3\ \mathrm{As/m} \end{aligned} \tag{7.11}$$

If only one position signal (e.g. x_ha) is used per position controller (e.g. acting at x_da), the signal x_ha contains both a parallel displacement x and a tilting displacement α so that the control must be tuned to stabilise both the rotor parallel and tilting motion. Since the proportional part of the tilting motion k_P^c is less than the minimum gain to ensure the parallel motion stability of 14.5 kA/m, the highest controller gain $k_\mathrm{P} = k_\mathrm{P}^\mathrm{p}$ must be chosen, leading in this example to a very stiff tilting motion setting (463% natural stiffness). The stiffness increase is bigger than the virtual gain 2.8 due to the overcompensation of the negative stiffness. The root-locus for a rotational speed variation from zero to rated speed ω_N is given in Figure 7.2. Due to the virtual gain h/d affecting the tilting motion, the placement of the tilting poles "+" is not at the expected position "o" in Figure 7.2. As explained before, this problem is inherent to self-bearing machines due to

Table 7.1.: Motor parameters of the double conical prototype [26]. The force current coefficients k_{ir} and k_{iz} are scaled by $1/\sqrt{2}$ because the control considers peak currents and not RMS currents

Parameter	**Symbol**	**Value**	**Unit**
Rotor mass	m_{r}	1.12	kg
Radial force displacement coefficient	k_{sr}	-21	N/mm
Axial force displacement coefficient	k_{sz}	-2.5	N/mm
Radial force current coefficient	k_{ir}	1.45	N/A
Axial force current coefficient	k_{iz}	1.7	N/A
Rotor transverse moment of inertia	J_{x}, J_{y}	4657	kg/mm^2
Rotor polar moment of inertia	J_{z}	141.2	kg/mm^2
Distance of net force from rotor centre	d	45	mm
Distance of sensors from rotor centre	h	126	mm
Rated speed	ω_{N}	1885	rad/s

the difference between net force position d and sensor position h. At first glance, this issue seems very easy to solve with a linear transformation of the position signals. In practice, the task is more complicated because in micro-metre range, the rotor is always slightly bent (e.g. static bending due to rotor imperfection or dynamic bending due to unbalanced forces acting at high speed). Therefore, the transformed positions x_{d}, obtained from the measured positions x_{h}, are modulated with the rotation angle θ with a characteristic that is itself rotor speed dependant.

This simple illustration shows why the system should be considered mechanically as a MIMO system and each motion should be controlled separately. It has to be noted that this approach considers only the rigid body motions. It applies if the bending Eigenfrequencies of the shaft are much higher than the closed-loop poles, set by the controller. The consideration of rotor elasticity in the control design is a much more complicated task and depends on numerous parameters (exact geometry and material properties of the shaft, placement of position sensors and actuators with regards to the node

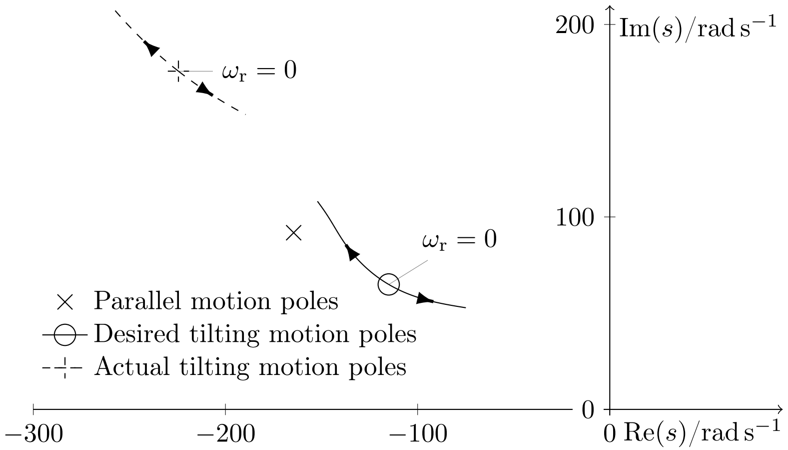

Figure 7.2.: Calculated root loci of the closed-loop control with PD controller with SISO feedback tuned according to natural stiffness. The actual poles of the tilting motion ("+") are not at the desired position ("o") to fulfil natural stiffness setting. This pole shift is due to the gain h/d that affects the tilting position only. As the rotational speed ω_r increases, the tilting motion pole are split.

of each bending mode, current and position control delay etc.) [4]. In practice, a computer-aided-design approach is recommended using a rotor-dynamic simulation program such as *Madyn 2000*, that is able to integrate the controller action [36]. This approach is compulsory if stiff control is desired.

7.2.3. PD Control with motion separation

In the mechanical equation (7.7), the state matrix $\boldsymbol{A}$ is sparse and has block matrices on its diagonals. Using the position transformation matrix $\boldsymbol{B}_\mathbf{d}$, it can be decomposed in two identical parallel mode sub-matrices $\boldsymbol{A}^\mathrm{p}$ (horizontal and vertical parallel modes), one tilting mode sub-matrix $\boldsymbol{A}^\mathrm{c}$, one axial mode sub-matrix $\boldsymbol{A}^\mathrm{z}$ and one rotation sub-matrix $\boldsymbol{A}^\theta$. The respective state vectors are $(x,\dot{x})^\intercal$, $(y,\dot{y})^\intercal$, $(\alpha,\beta,\dot{\alpha},\dot{\beta})^\intercal$, $(z,\dot{z})^\intercal$ and $(\theta,\dot{\theta})^\intercal$. The respective input vectors are $(i_\mathrm{2da}+i_\mathrm{2db})^\intercal$, $(i_\mathrm{2qa}+i_\mathrm{2qb})^\intercal$,

$(i_{2\mathrm{da}} - i_{2\mathrm{db}}, i_{2\mathrm{qa}} - i_{2\mathrm{qb}})^\intercal$, $(i_{1\mathrm{da}} - i_{1\mathrm{db}})^\intercal$ and $(i_{1\mathrm{qa}} + i_{1\mathrm{qb}})^\intercal$. The rotation sub-matrix $\boldsymbol{A}^\theta$ has two Eigenvalues at zero since no friction was considered in the model. In reality, air friction losses and rotor losses are generating some friction and damping so that the rotation motion does not need to be stabilised and is omitted here. Now that the motions are decoupled, the equations (7.9) and (7.10) are used to stabilise the unstable motions. The closed-loop system matrices with motion separation and PD control are given by (7.12).

$$\boldsymbol{A}_{\mathbf{w}}^{\mathbf{p}} = -\begin{pmatrix} 0 & -1 \\ \dfrac{2\cdot(k_\mathrm{P}^\mathrm{p} k_\mathrm{ir} + k_\mathrm{sr})}{m_\mathrm{r}} & \dfrac{2k_\mathrm{D}^\mathrm{p} k_\mathrm{ir}}{m_\mathrm{r}} \end{pmatrix}, \boldsymbol{A}_{\mathbf{w}}^{\mathbf{z}} = -\begin{pmatrix} 0 & -1 \\ \dfrac{2\cdot(k_\mathrm{P}^\mathrm{p} k_\mathrm{iz} + k_\mathrm{sz})}{m_\mathrm{r}} & \dfrac{k_\mathrm{D}^\mathrm{z} k_\mathrm{iz}}{m_\mathrm{r}} \end{pmatrix}$$

$$\boldsymbol{A}_{\mathbf{w}}^{\mathbf{c}} = -\begin{pmatrix} 0 & 0 & -1 & 0 \\ 0 & 0 & 0 & -1 \\ \dfrac{2d^2\cdot(k_\mathrm{P}^\mathrm{c} k_\mathrm{ir} + k_\mathrm{sr})}{J_\mathrm{x}} & 0 & \dfrac{2d^2 k_\mathrm{D}^\mathrm{c} k_\mathrm{ir}}{J_\mathrm{x}} & \dfrac{J_\mathrm{z}\omega_\mathrm{r}}{J_\mathrm{x}} \\ 0 & \dfrac{2d^2\cdot(k_\mathrm{P}^\mathrm{c} k_\mathrm{ir} + k_\mathrm{sr})}{J_\mathrm{x}} & -\dfrac{J_\mathrm{z}\omega_\mathrm{r}}{J_\mathrm{x}} & \dfrac{2d^2 k_\mathrm{D}^\mathrm{c} k_\mathrm{ir}}{J_\mathrm{x}} \end{pmatrix} \tag{7.12}$$

The parallel mode closed-loop $\boldsymbol{A}_{\mathbf{w}}^{\mathbf{p}}$ and the axial mode closed-loop $\boldsymbol{A}_{\mathbf{w}}^{\mathbf{z}}$ are speed independent. The tilting mode closed-loop $\boldsymbol{A}_{\mathbf{w}}^{\mathbf{c}}$ displays a skewed symmetrical part given by the gyroscopic effect. At $\omega_\mathrm{r} = 0$, the closed-loop poles p_w^p, p_w^c, p_w^z can be placed on the left half-plane with (7.13). Though, the poles can not be placed far on the left half-plane due to limitations that are detailed in 7.3. The case $\omega_\mathrm{r} \neq 0$ is also detailed in 7.3.3.

$$\begin{aligned} k_\mathrm{P}^\mathrm{p} &= \frac{|k_\mathrm{sr}|}{k_\mathrm{ir}} \cdot \left(1 + \frac{|p_\mathrm{w}^\mathrm{p}|^2}{|p_0^\mathrm{p}|^2}\right), & k_\mathrm{D}^\mathrm{p} &= -\frac{\mathrm{Re}(p_\mathrm{w}^\mathrm{p})}{|p_0^\mathrm{p}|} \cdot \frac{\sqrt{2m_\mathrm{r}|k_\mathrm{sr}|}}{k_\mathrm{ir}} \\ k_\mathrm{P}^\mathrm{c} &= \frac{|k_\mathrm{sr}|d}{k_\mathrm{ir}h} \cdot \left(1 + \frac{|p_\mathrm{w}^\mathrm{c}|^2}{|p_0^\mathrm{c}|^2}\right), & k_\mathrm{D}^\mathrm{c} &= -\frac{\mathrm{Re}(p_\mathrm{w}^\mathrm{c})}{|p_0^\mathrm{c}|} \cdot \frac{\sqrt{2J_\mathrm{x}|k_\mathrm{sr}|}}{hk_\mathrm{ir}} \\ k_\mathrm{P}^\mathrm{z} &= \frac{|k_\mathrm{sz}|}{k_\mathrm{iz}} \cdot \left(1 + \frac{|p_\mathrm{w}^\mathrm{z}|^2}{|p_0^\mathrm{z}|^2}\right), & k_\mathrm{D}^\mathrm{z} &= -\frac{\mathrm{Re}(p_\mathrm{w}^\mathrm{z})}{|p_0^\mathrm{z}|} \cdot \frac{\sqrt{2m_\mathrm{r}|k_\mathrm{sz}|}}{k_\mathrm{iz}} \end{aligned} \tag{7.13}$$

The controller integral action, not addressed until now, adds a new pole in the system. Therefore, the sub-systems are of order three and the placement of the closed-loop poles is done numerically. A control structure with full-state feedback and integral action is presented below.

7.2.4. Full-state feedback control scheme with integral action

In this section, the rotor speed ω_r is assumed constant so that the tilting mode is independent from the rotational speed. Since the different motions are decoupled, it is possible to design a state-feedback control for each motion. The parallel, the axial and the rotational motions are decoupled and speed independent so that a single feedback matrix for each mode is necessary. In the case of tilting motion, the state matrix $\boldsymbol{A}^\mathrm{c}$ is speed dependent so that the state feedback should adapt to speed changes. When the gyroscopic effect is too important, a coarse feedback gain scheduling is commonly used. Such a strategy is presented in 7.3.3.

For each motion, only the position is measured (e.g. x for the horizontal parallel motion). The numerical differentiation of the position x to get the speed $\dot{x}$ is not a good practice since the sensor noise, inherently present in real-life signals, is magnified with increasing frequency at a rate of 20 dB/decade. The state derivative $\dot{x}$ is obtained with a simple reduced observer such as the one in Figure 7.5 whereas the state integral x_I is obtained by integration. If additional filtering is required on the position signal x, a non-reduced observer is preferred. The closed-loop system performed better experimentally with reduced-order observer than with full-state observer [54]. The state matrix $\boldsymbol{A}^\mathrm{p}$ is extended with the integral state and becomes $\boldsymbol{A}^\mathrm{p}_\mathrm{ext}$ (7.14). The same procedure is repeated for all the other motions.

$$\boldsymbol{A}^\mathbf{p}_\mathbf{ext} = \begin{pmatrix} 0 & 1 & 0 \\ 0 & 0 & 1 \\ 0 & \dfrac{-2k_\mathrm{sr}}{m_\mathrm{r}} & 0 \end{pmatrix} \tag{7.14}$$

Since the model is not exact and the system inherently unstable, the pole placement must guarantee a certain control robustness. That is to say, the feedback gain $\boldsymbol{K}$ should be determined so that the closed loop poles are not sensitive to model variations and uncertainties. For that, there are two underlying conditions:

- The closed-loop poles should be placed reasonably.
- The numerical evaluation of the feedback gain $\boldsymbol{K}$ should use the additional degrees of freedom of the under-constrained pole placement problem to find a robust solution.

The first point will be discussed below. The latter is out of the scope of this thesis. It was however taken into account by using the algorithm of [37] implemented in *Matlab* (function *place*).

The pole placement is commonly restricted in a "preferred region" as illustrated in Figure 7.3. This region ensures a minimum dynamic, a good damping and a reasonable maximum dynamic. Poles that are placed left from the "preferred region" are likely to mismatch the actual closed-loop poles since they are influenced by current control dynamic, filters and actuator delay that were neglected. The stable open-loop poles of the considered motion are usually inside this region (natural stiffness principle [4]). Since the actual system is likely to vary from the nominal model (e.g. due to temperature change or gyroscopic effect), the actual poles are drifting during operation. In order to ensure control robustness, the poles should not drift too far from the preferred region. To that end, a second region is defined to delimit where the closed-loop poles are allowed to drift (solid line region in Figure 7.3). The actual shape and region borders depend on dynamic and robustness requirements.

The control structure for the parallel motion x is shown in Figure 7.4 and the corresponding reduced-order observer in Figure 7.5. The same is done for the tilting and axial motions. The dynamic and damping of the position controller is set by $\boldsymbol{K}$ whereas the dynamic of the observer is set by $\boldsymbol{L}$. According to the principle of separation, the two dynamics can be set

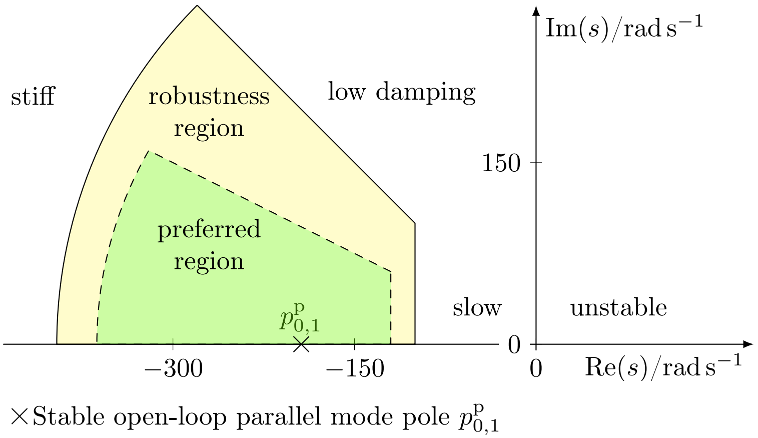

Figure 7.3.: Region for pole placement for parallel mode: The closed-loop poles of the nominal model are placed in the preferred region (dashed). The selected poles should not leave the robustness region (solid) under model variation. Poles that are placed left from the preferred region are likely to mismatch actual system poles. Poles that are close to the imaginary axis are too weakly damped. Poles that are close to the origin are too slow.

independently. This is an advantage compared to a PID control with low pass filter on the differential action where the filter poles are influencing the closed-loop directly. Since the observer is used for state feedback, the observer poles are selected so that the estimated states converge faster than the plant states. A realistic placement of the poles prevents estimator peaking and acts as a low-pass filter on $\dot{x}$. As illustrated in the previous part, the choice of the closed-loop poles should be guided by the intrinsic (open-loop) poles of the plant. Since the integral action inserts a third closed-loop pole, three poles have to be selected per motion. As the damping ratio ζ is only defined in the traditional sense for second order systems, the placement is done to obtain a two-dominant-pole system characteristic. That is to say, two complex conjugate poles $-p \cdot \exp(\pm \mathrm{j}\theta)$ are selected according to the "natural stiffness rule" (i.e. $p = |p_0|$) and define the slow "dominant poles". The third pole is placed farther on the left real axis so that it vanishes faster than the two dominant poles. Doing so, the damping ratio ζ and the sub-

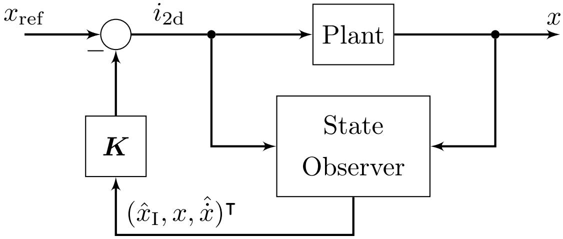

Figure 7.4.: Control structure of parallel motion x with full-state feedback. The plant is composed of the machine with the current-controlled voltage source converter. The state observer (Figure 7.5) estimates x_{I} and $\dot{x}$. The feedback matrix $\boldsymbol{K}$ sets the closed-loop dynamic.

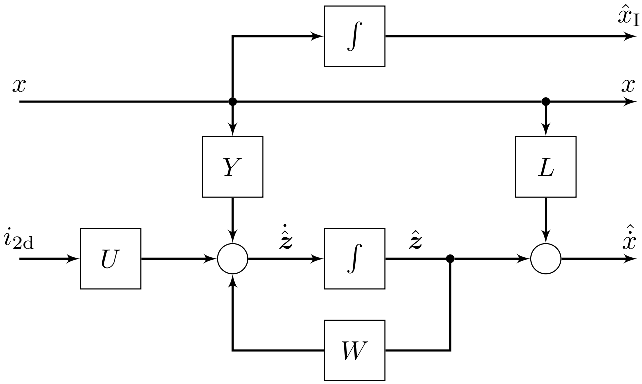

Figure 7.5.: Reduced-order state observer necessary to obtain the derivative of the position signal x. The input current $i_{2\mathrm{d}}$ is equal $i_{2\mathrm{da}} + i_{2\mathrm{db}}$. The gain L sets the dynamic of the observer. The elements are defined in (7.18).

sequence unit step response overshoot x_{m} are obtained with (7.15). Given the open-loop poles p_0 and $-p_0$, a good compromise is found by setting the dominant poles at $-|p_0| \cdot \exp(\pm\pi/6)$ and the third pole at $-2 \cdot |p_0|$. In such a case, the damping ratio ζ is approximately 0.87. No over-shoot is expected since the dominant poles are well damped. The settling time to 5% $T_{\mathrm{s},5\%}$ is slightly slower than its second order approximation due to the third pole.

For this particular placement, the settling time $T_{\mathrm{s},5\%}$ is given by (7.16).

$$\zeta \approx \cos\theta, \quad x_{\mathrm{m}} \approx \exp\left(\frac{-\zeta\pi}{\sqrt{1-\zeta^2}}\right) \tag{7.15}$$

$$T_{\mathrm{s},5\%} \approx 2/p_0 \tag{7.16}$$

For illustration, the open-loop poles of the prototype [26] are calculated with (7.8) in Table 7.2. The 17 closed-loop poles are then selected as explained above and are given in Table 7.2. Since the rotation motion has two poles at zero, the closed-loop poles must be selected differently. The inverse of the starting time constant $T_{\mathrm{J}} = 2\pi n_{\mathrm{N}} J_{\mathrm{z}}/M_{\mathrm{N}}$ can be taken as guiding value for the closed-loop poles $p^{\theta}_{\mathrm{c},i}$ but is a very conservative value since a speed step of n_{N} would lead to a torque reference step of only M_{N}. In practice, a faster pole can be chosen so that the maximum reference torque is set for a smaller speed step. Only two poles are necessary since only rotor speed steady-state accuracy is required.

For each motion, the observer feedback L is given by (7.17). The elements W, U and Y in Figure 7.5 are given by (7.18). In order to have an observer with constant feedback, the rotational speed ω_{r} is set to zero.

$$L^i = -p^i_{\mathrm{ob}}, i \in \{\mathrm{p}, \mathrm{c}, \mathrm{z}, \theta\} \tag{7.17}$$

$$\begin{aligned}
W^{\mathrm{p}} &= -L^{\mathrm{p}}, U^{\mathrm{p}} = 2k_{\mathrm{ir}}/m_{\mathrm{r}}, Y^{\mathrm{p}} = -(L^{\mathrm{p}})^2 - 2k_{\mathrm{sr}}/m_{\mathrm{r}} \\
W^{\mathrm{c}} &= -L^{\mathrm{c}}, U^{\mathrm{c}} = 2dk_{\mathrm{ir}}/J_{\mathrm{x}}, Y^{\mathrm{c}} = -(L^{\mathrm{c}})^2 - 2d^2k_{\mathrm{sr}}/J_{\mathrm{x}} \\
W^{\mathrm{z}} &= -L^{\mathrm{z}}, U^{\mathrm{z}} = 2k_{\mathrm{iz}}/m_{\mathrm{r}}, Y^{\mathrm{z}} = -(L^{\mathrm{z}})^2 - 2k_{\mathrm{sz}}/m_{\mathrm{r}} \\
W^{\theta} &= -L^{\theta}, U^{\theta} = 2k_{\mathrm{iM}}/J_{\mathrm{z}}, Y^{\theta} = -(L^{\theta})^2
\end{aligned} \tag{7.18}$$

As mentioned in the beginning of this chapter, the dynamic of the inner current control loop as well as the control delay is not considered. In order to get an accurate pole placement, the dominant poles of the current controller must be much farther on the left half-plane compared to the chosen position control poles. In the experimental part in Chapter 8, the current controllers are set with poles in the range of -40 000 rad/s which is much faster than

Table 7.2.: Open-loop poles and selected closed-loop poles for the position controller and observer. PM: parallel motions, TM: tilting motions

Parameter	**Symbol**	**Value** in $\mathrm{rad\,s^{-1}}$
Open-loop poles of PM x and y	$p^{\mathrm{p}}_{0,i}$	± 194
Open-loop poles of TM α and β	$p^{\mathrm{c}}_{0,i}$	± 135
Open-loop poles of axial motion z	$p^{\mathrm{z}}_{0,i}$	± 67
Open-loop poles of rotation motion θ	$p^{\theta}_{0,i}$	± 0
Closed-loop poles of PM x and y	$p^{\mathrm{p}}_{\mathrm{w},i}$	$-168 \pm \mathrm{j}97, -387$
Closed-loop poles of TM α and β	$p^{\mathrm{c}}_{\mathrm{w},i}$	$-117 \pm \mathrm{j}68, -270$
Closed-loop poles of axial motion z	$p^{\mathrm{z}}_{\mathrm{w},i}$	$-58 \pm \mathrm{j}34, -134$
Closed-loop poles of rotation motion θ	$p^{\theta}_{\mathrm{w},i}$	$-9 \pm \mathrm{j}2$
Observer poles for PM $\hat{x}$ and $\hat{y}$	$p^{\mathrm{p}}_{\mathrm{ob},i}$	-1548
Observer poles for TM $\hat{\alpha}$ and $\hat{\beta}$	$p^{\mathrm{c}}_{\mathrm{ob},i}$	-1080
Observer pole for axial motion $\hat{z}$	$p^{\mathrm{z}}_{\mathrm{ob}}$	-400
Observer pole for rotation motion $\hat{\theta}$	p^{θ}_{ob}	-1250

the poles selected for the position control in Table 7.2. Therefore, the assumption of infinitely fast inner current control loops is valid.

7.3. Model uncertainties and limitations

As previously mentioned, the closed-loop poles cannot be placed far on the left half-plane due to limitations of different nature:

- Model validity: The plant model at rotor bending frequency differs significantly from the rigid body model [36] so that the plant equation (7.6) does not apply at that frequency.
- Control limitation: The dynamic of the inner current control loop is finite (discrete time control) and can not be overcome.

- Sensor bandwidth: The position sensors have a finite bandwidth that also cannot be overcome.
- Actuator bandwidth: The self-bearing rotor is not laminated so that eddy-currents on the rotor reduce the force current coefficient k_{ir} at higher frequencies.

The current control dynamic and bending frequency limitations are similar to the ones in drives with magnetic bearings and are addressed in [38] and [36] respectively. The actuator bandwidth limitation is treated in Section 7.3.6.

7.3.1. Position sensor filter and current control bandwidth

The effect of a position filter or finite current control bandwidth on the closed-loop stability can be illustrated by adding a first order lag element $(1+T_{\mathrm{f}}\cdot s)^{-1}$ in the feedback loop of a PD-based control. Since the controller reference position is zero $x_{\mathrm{ref}}=0$, the filter directly affects the controller input so that the transfer function of the PD controller with filter becomes the lead-lag compensator (7.19).

$$G_{\mathrm{w,filt}}(s)=\frac{k_{\mathrm{P}}+k_{\mathrm{D}}\cdot s}{1+T_{\mathrm{f}}\cdot s}=k_{\mathrm{P}}\cdot\frac{1+T_{\mathrm{D}}\cdot s}{1+T_{\mathrm{f}}\cdot s} \tag{7.19}$$

Since the differential action is necessary to add phase margin at open-loop gain zero-crossing, the filter time constant T_{f} shall not be bigger than the controller time constant $T_{\mathrm{D}}=k_{\mathrm{D}}/k_{\mathrm{P}}$. Additionally, the gain k_{P} should be low enough so that the open-loop gain zero-crossing happens before the filter cut-off frequency T_{f}^{-1}. Thus T_{f} limits the maximum controller tuning. To get a quantitative illustration of the filter effect, the previous parallel mode state matrix $\boldsymbol{A}^{\mathsf{P}}$ is extended adding the first order lag element with a new element in the vector state $(x,\dot{x},x_{\mathrm{filt}})^{\mathsf{T}}$. The new closed-loop state matrix with PD controller $\boldsymbol{A}^{\mathbf{p}}_{\mathbf{w,filt}}$ becomes (7.20).

$$\boldsymbol{A}^{\mathbf{p}}_{\mathbf{w,filt}} = \begin{pmatrix} 0 & 1 & 0 \\ -\frac{2}{m_\mathrm{r}} \cdot (k_\mathrm{sr} + \frac{k_\mathrm{ir} k_\mathrm{D}^\mathrm{p}}{T_\mathrm{f}}) & 0 & -\frac{2k_\mathrm{ir}}{m_\mathrm{r}} \cdot (k_\mathrm{P}^\mathrm{p} - \frac{k_\mathrm{D}^\mathrm{p}}{T_\mathrm{f}}) \\ \frac{1}{T_\mathrm{f}} & 0 & -\frac{1}{T_\mathrm{f}} \end{pmatrix} \tag{7.20}$$

The filter time constant T_f is varied from 0 until $T_\mathrm{D}^\mathrm{p} = k_\mathrm{D}^\mathrm{p}/k_\mathrm{P}^\mathrm{p} = 4.5$ ms. The resulting poles are displayed in Figure 7.6. At $T_\mathrm{f} = 0$, the two original poles $p_{\mathrm{w},1}^\mathrm{p} = |p_0^\mathrm{p}| \cdot \exp(\mathrm{j}\pi/6)$ and $p_{\mathrm{w},2}^\mathrm{p} = |p_0^\mathrm{p}| \cdot \exp(-\mathrm{j}\pi/6)$ are present while the third pole (filter) is at $-\infty$. As the time constant T_f increases, the system damping is dropping since the two poles are moving toward the imaginary axis. At $T_\mathrm{f} = T_\mathrm{D}$, the controller and filter action cancels out in (7.19) so that $G_\mathrm{w,filt}$ is a simple gain. The two closed-loop poles are pure imaginary $p_{\mathrm{w},1}^\mathrm{p} = \mathrm{j}\,|p_0^\mathrm{p}|$ and $p_{\mathrm{w},2}^\mathrm{p} = -\mathrm{j}\,|p_0^\mathrm{p}|$. In Figure 7.7, the damping ratio ζ of the system poles is displayed as a function of the relative filter time constant $\tau_\mathrm{f} = T_\mathrm{f}/T_\mathrm{D}$. For $\tau > 0.3$, the damping ratio ζ is too low so that the closed-loop poles should be chosen at least three time slower than the slowest inherent system pole.

7.3.2. Model disturbances

A real active self-bearing motor is affected by disturbances of different nature. Some are of purely mechanical origin such as:

- Gyroscopic effect experienced as a speed dependent mechanical coupling between the two tilting modes.
- Static and dynamic rotor unbalance forces, whose amplitude increases with the square of the rotational speed ω_r.
- Modulation of the rotor displacement with rotor angle due to the rotor bending.

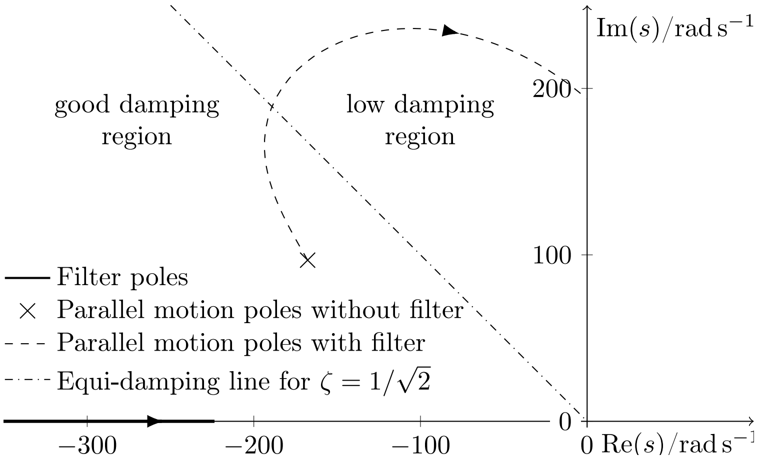

Figure 7.6.: Closed-loop poles change due to filter delay on the position feedback. The poles are moving from the selected closed-loop poles toward the imaginary axis as the filter time constant T_f increases from 0 until $T_\mathrm{D}^\mathrm{p} = k_\mathrm{D}^\mathrm{p}/k_\mathrm{P}^\mathrm{p}$.

- Additional position noise due to imperfection of the rotor measurement surface.

Some are of electromagnetic origin such as:

- A multitude of torque and force components resulting from superposition of fields in the air gap and rotor eccentricity. Though, it was shown in Chapter 4 that only one force interference is dominant.
- Harmonic force disturbances due to the superposition of the levitation and rotor fields in the magnetically non-linear stator teeth and yoke.
- Misalignment of the rotor magnetic axis and rotational axis, leading to disturbances similar to rotor static unbalance.
- Frequency and temperature dependent force current coefficient k_ir.

The influence of the listed disturbances on the levitation performance are highly dependent on the chosen control scheme, closed-loop poles, or on

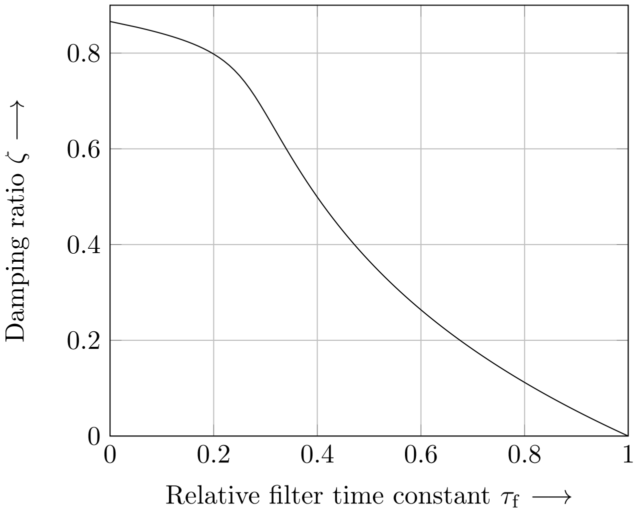

Figure 7.7.: Damping ratio ζ as function of the relative filter time constant $\tau_{\mathrm{f}} = T_{\mathrm{f}}/T_{\mathrm{D}}$. In accordance with Figure 7.6, the damping ratio ζ decreases with increasing filtering. The damping becomes low for $\tau_{\mathrm{f}} > 0.3$ so that the filter time constant T_{f} limits the maximum dynamic of the closed-loop system.

motor parameters such as the location of the position sensors relative to the force locations or the centre of mass. Therefore, it is difficult to evaluate and compare the influence of each disturbance. An overview of the prevailing disturbances encountered during the experimental part is presented below.

7.3.3. Gyroscopic effect

As the rotors of high-speed drives display a rotor polar moment of inertia J_{z} much smaller than the rotor transverse moment of inertia J_{x}, the high-speed drives are inherently insensitive to dynamic unbalance [4]. Still the gyroscopic effect is increasing with rotational speed, destabilising the levitated drive at some point. The alteration of the closed-loop system poles due to gyroscopic effect are evaluated numerically in Figure 7.2 for the double conical prototype [26] and a speed varying from standstill to nominal speed $n_\mathrm{N} = 18\ 000$ rpm. It can be seen that only the tilting motion is affected. While four tilting poles are moving farther to the left, the other four are getting closer to the imaginary axis. Still the poles are all sufficiently damped at nominal speed so that the gyroscopic effect does not compromise the control stability of the considered prototype [26]. If required, the compensation of gyroscopic coupling is similar to drives with magnetic bearings as for example in [39]. For illustration, the previous reduced state matrix $\boldsymbol{A}^\mathrm{c}$ at speed ω_r is considered. The function *place* from *Matlab* calculates numerically the feedback gain matrix $\boldsymbol{K}^\mathrm{c}$ so that $\boldsymbol{A}^\mathrm{c} - \boldsymbol{B}^\mathrm{c}\boldsymbol{K}^\mathrm{c}$ has the desired set of poles $\{p^\mathrm{c}_{\mathrm{w},i} \mid i \in \{1{,}2{,}3{,}4\}\}$. The result is equal to the numerical evaluation of (7.21). This means that the pole placement for the state matrix $\boldsymbol{A}^c$, using the function *place*, is equivalent to the PD-controller tuning of (7.13) with additionally a skewed symmetrical part to oppose the gyroscopic effect.

$$\boldsymbol{K}^\mathrm{c}(\omega_\mathrm{r}) = \begin{pmatrix} k^\mathrm{c}_\mathrm{P} & 0 & k^\mathrm{c}_\mathrm{D} & -\dfrac{J_\mathrm{z} \cdot \omega_\mathrm{r}}{2k_\mathrm{ir}d^2} \\ 0 & k^\mathrm{c}_\mathrm{P} & \dfrac{J_\mathrm{z} \cdot \omega_\mathrm{r}}{2k_\mathrm{ir}d^2} & k^\mathrm{c}_\mathrm{D} \end{pmatrix} \tag{7.21}$$

Thanks to symmetry properties of the state matrix $\boldsymbol{A}^c$, it is possible to analytically calculate the feedback required to compensate the gyroscopic effect. With increasing system order, the numerical approach is however preferred. Since the pole placement has a fixed feedback matrix $\boldsymbol{K}^\mathrm{c}$, it should be selected for the speed range of interest. In the experimental section 8, the feedback $\boldsymbol{K}^\mathrm{c}$ was chosen for $\omega_\mathrm{r} = 0$ since the prototype is able to rotate in both directions but a different tuning could be preferred if for example the drive is to be operated in a single direction (e.g. air compressor).

The closed-loop poles of $\boldsymbol{A}^\mathrm{c} - \boldsymbol{B}^\mathrm{c}\boldsymbol{K}^\mathrm{c}$ are numerically evaluated for $\boldsymbol{K}^\mathrm{c}(0)$, $\boldsymbol{K}^\mathrm{c}(0.5\ \omega_\mathrm{N})$ and $\boldsymbol{K}^\mathrm{c}(\omega_\mathrm{N})$ in the speed range $[0,\ \omega_\mathrm{N}]$ in Figure 7.8. In order to differentiate the overlapping curves, they are horizontally shifted by +20, 0 and -20 rad/s respectively. As expected, the setting $\boldsymbol{K}^\mathrm{c}(0)$ is best at low speed ($\omega < 0.25\ \omega_\mathrm{N}$) whereas $\boldsymbol{K}^\mathrm{c}(\omega_\mathrm{N})$ is best at nominal speed ($\omega > 0.75\ \omega_\mathrm{N}$). If the drive is operated only in positive direction, $\boldsymbol{K}^\mathrm{c}(0.5\ \omega_\mathrm{N})$

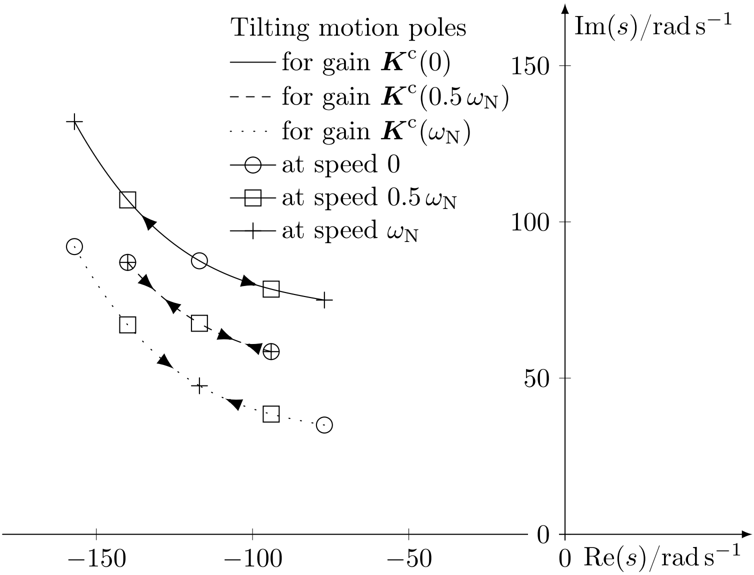

Figure 7.8.: Calculated tilting motion poles due to gyroscopic effect for three different feedback gains $\boldsymbol{K}^{c}$ and for a rotational speed in $[0,\ \omega_N]$: For readability, the three curves are artificially shifted vertically by +20, 0 and -20 rad/s respectively so that they do not overlap.

is preferred since the pole changes are minimum for this setting (see Figure 7.8). Obviously, the gains $\boldsymbol{K}^{c}(0.5\ \omega_N)$ and $\boldsymbol{K}^{c}(\omega_N)$ are not suited for negative rotation direction and should be reversed if $\omega_r < 0$. One simple gain scheduling to improve pole placement in the speed range $[0,\ \omega_N]$ is given by $\{\boldsymbol{K}^{c}(0),\ \boldsymbol{K}^{c}(0.5\ \omega_N),\ \boldsymbol{K}^{c}(\omega_N)\}$ where the gain transitions are done at respectively $0.25\ \omega_N$ and $0.75\ \omega_N$. Doing so, the tilting motion poles, originally varying from -77 ± j55 rad/s to -157 ± j112 rad/s, are now restricted between -105 ± j61 rad/s and -129 ± j76 rad/s. Since the damping variation is, in both cases, negligible, such a strategy was not implemented in the experimental part.

7.3.4. Self-bearing motor force interference

As presented in the previous chapter, the magnetic force interferences that take place in the air gap are given by superposition of the levitation field with the drive field. The interference forces result from products of drive and levitation currents and consequently are non-linear disturbances. When the interference forces are small enough, the control stability should be provided by sufficient control robustness. When the controller stiffness is set low (i.e. less than 25% of the system natural stiffness), the interference must be modelled and compensated. Since the poles of the axial motion and rotation motion are slower than the ones of radial motions, it is reasonable to consider that the drive current components i_{1da}, i_{1qa}, i_{1db}, i_{1qb} in (4.63) vary slowly compared to the levitation current components i_{2da}, i_{2qa}, i_{2db}, i_{2qb}. By linearisation of the model at a steady-state operation point, the dominant interference force is expressed in matrix form $\boldsymbol{K}_{\mathbf{dist}}$ as (7.22).

$$\boldsymbol{K}_{\mathbf{dist}} = k_{\mathrm{dist}} \cdot \begin{pmatrix} i_{\mathrm{1da}} & -i_{\mathrm{1qa}} & 0 & 0 & 0 & 0 \\ i_{\mathrm{1qa}} & i_{\mathrm{1da}} & 0 & 0 & 0 & 0 \\ 0 & 0 & i_{\mathrm{1db}} & -i_{\mathrm{1qb}} & 0 & 0 \\ 0 & 0 & i_{\mathrm{1qb}} & i_{\mathrm{1db}} & 0 & 0 \\ 0 & 0 & 0 & 0 & 0 & 0 \\ 0 & 0 & 0 & 0 & 0 & 0 \end{pmatrix} \tag{7.22}$$

The field weakening currents i_{1da} and i_{1db} are responsible for a reduction of the force-current coefficient k_{ir}. The torque currents i_{1qa} and i_{1qb} lead to force interferences that are, as for the gyroscopic effect, given by a skewed symmetrical matrix (7.22). This time, not only the tilting motion is affected but also the parallel motion. The axial control and rotation control are not subjected to these disturbances and may be omitted here. The parallel mode and tilting mode reduced systems in (7.23) are expressed with the disturbance components in (4.63).

$$\boldsymbol{A}_{\mathrm{w}}^{\mathrm{p}} = \begin{pmatrix} 0 & 0 & 1 & 0 \\ 0 & 0 & 0 & 1 \\ a & b & c & d \\ -b & a & -d & c \end{pmatrix} \qquad \begin{aligned} a &= -\frac{k_{\mathrm{P}}^{\mathrm{p}} \cdot (2k_{\mathrm{ir}} + k_{\mathrm{dist}} \cdot (i_{\mathrm{1da}} + i_{\mathrm{1db}})) + 2k_{\mathrm{sr}}}{m_{\mathrm{r}}} \\ b &= -\frac{k_{\mathrm{P}}^{\mathrm{p}} k_{\mathrm{dist}} \cdot (i_{\mathrm{1qa}} + i_{\mathrm{1qb}})}{m_{\mathrm{r}}} \\ c &= -\frac{k_{\mathrm{D}}^{\mathrm{p}} \cdot (2k_{\mathrm{ir}} + k_{\mathrm{dist}} \cdot (i_{\mathrm{1da}} + i_{\mathrm{1db}}))}{m_{\mathrm{r}}} \\ d &= -\frac{k_{\mathrm{D}}^{\mathrm{p}} k_{\mathrm{dist}} \cdot (i_{\mathrm{1qa}} + i_{\mathrm{1qb}})}{m_{\mathrm{r}}} \end{aligned} \tag{7.23}$$

$$\boldsymbol{A}_{\mathrm{w}}^{\mathrm{c}} = \begin{pmatrix} 0 & 0 & 1 & 0 \\ 0 & 0 & 0 & 1 \\ e & f & g & h \\ -f & e & -h & g \end{pmatrix} \qquad \begin{aligned} e &= -\frac{d^2 k_{\mathrm{P}}^{\mathrm{c}} \cdot (2k_{\mathrm{ir}} + k_{\mathrm{dist}} \cdot (i_{\mathrm{1da}} - i_{\mathrm{1db}})) + 2k_{\mathrm{sr}}}{m_{\mathrm{r}}} \\ f &= -\frac{d^2 k_{\mathrm{P}}^{\mathrm{c}} k_{\mathrm{dist}} \cdot (i_{\mathrm{1qa}} - i_{\mathrm{1qb}})}{m_{\mathrm{r}}} \\ g &= -\frac{2d^2 k_{\mathrm{D}}^{\mathrm{c}} k_{\mathrm{ir}}}{J_{\mathrm{x}}} \\ h &= -\frac{J_{\mathrm{z}} \omega_{\mathrm{r}}}{J_{\mathrm{x}}} - \frac{d^2 k_{\mathrm{D}}^{\mathrm{c}} k_{\mathrm{dist}} \cdot (i_{\mathrm{1qa}} - i_{\mathrm{1qb}})}{J_{\mathrm{x}}} \end{aligned} \tag{7.24}$$

Physically, the radial levitation force is deviated from its original orientation due to the driving field by an angle $\arctan(k_{\mathrm{dist}}\, i_{\mathrm{1q,N}}/k_{\mathrm{ir}}) = 5.7°$ at nominal torque M_{N}. As for the gyroscopic effect, the interference forces can be compensated with a skewed symmetrical matrix feedback that produces the opposite coupling (terms b, d, f and h in (7.23)) from the controller side. However, an adequate stiffness and damping can be sufficient to ensure stability of the closed-loop system. In order to illustrate the influence of the control settings on the system robustness against interference forces, the root loci of the parallel motion poles of the prototype [26] are evaluated numerically for different stiffness and damping ratios. The root loci are evaluated in Figure 7.9 for an air gap torque varying from zero to $7{\cdot}M_{\mathrm{N}}$ with various stiffness setting and with a fixed damping ratio $\zeta = 0.5$. The poles are evaluated numerically with the expressions (3.3). In Figure 7.9, the position of the parallel motion poles with the lowest damping at rated

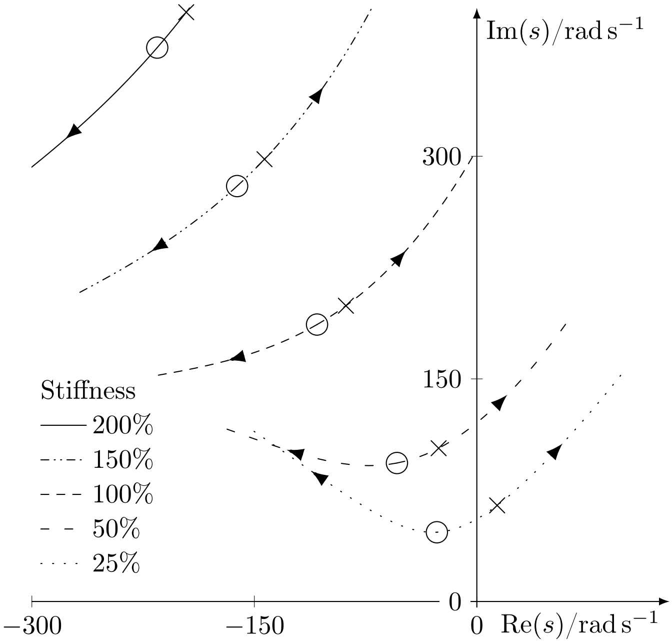

Figure 7.9.: Calculated root loci of the parallel motion poles with varying air gap torque for different control stiffnesses: The controllers are tuned with a low damping ratio $\zeta = 0.5$ and a stiffness varying from 25% to 200% "natural stiffness". The torque is varying from zero to $7 \cdot M_{\mathrm{N}}$. The poles at zero torque are marked with "o" while the least damped poles at nominal torque M_{N} are marked with "×". As the torque increases, two poles are migrating toward the right half-plane. The instability concerns in particular the closed-loop system with low stiffness.

torque M_{N} are marked with crosses "×". With increasing stiffness, the crosses are moving toward the left half-plane. Therefore, control robustness against force interference is given by increasing stiffness. The pole placement with natural stiffness (100% in Figure 7.9) is almost not affected by the interference whereas the one with 25% stiffness is unstable at rated torque M_{N}. The damping also significantly improves the robustness as illustrated in the root loci in Figure 7.10. Here the stiffness is fixed at 50% of natural stiffness and the damping ratio ζ is varied. Starting from the low-damped setting with $\zeta = 0.5$, the poles are migrating to the left half-plane as the

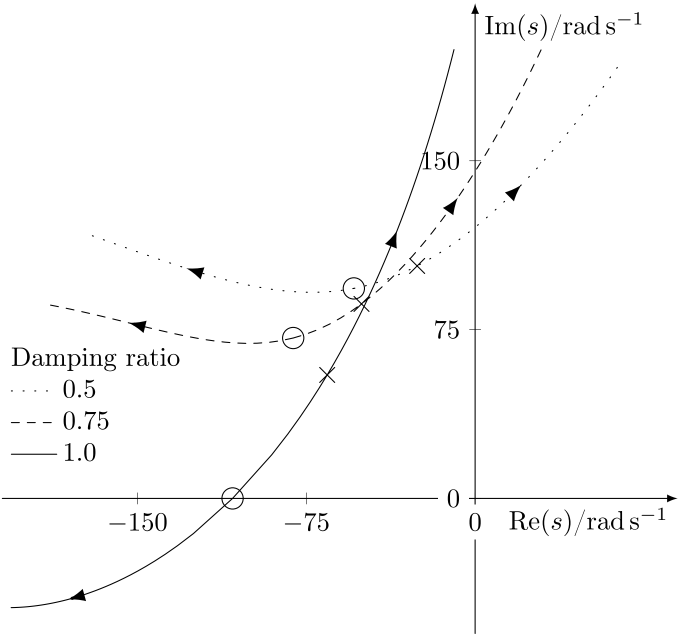

Figure 7.10.: Calculated root loci of the parallel motion poles with varying air gap torque for different control dampings: The controllers are tuned with low stiffness (50% of "natural stiffness") and a damping ratio varying from 50% to 100%. The torque is varying from zero to $7{\cdot}M_\mathrm{N}$. The poles at zero torque are marked with "o" while the least damped poles at nominal torque M_N are marked with "$\times$". As the torque increases, two poles are migrating toward the right half-plane. The instability concerns in particular the closed-loop system with low damping.

damping ratio reaches 1.

7.3.5. Unbalance forces

When the rotor geometric axis differs from the inertia axis due to the presence of some rotor unbalance, the rotor has the tendency to align with the inertia axis as the rotational speed ω_r increases. The control however seeks to maintain the rotor to rotate around the geometric axis for which it is calibrated. Consequently, quadratically increasing actuator forces are necessary with increasing rotational speed to keep the rotor at the geometric centre. Due to the limited force of the active self-bearing motor, the current limitation of the actuators is reached already at low rotational speed. If the rotor balancing is poor, a synchronous notch filter is necessary to perform imbalance force rejection [4]. Since this disturbance is related to a deficiency of the realised prototype [14], it is detailed in the experimental part in Chapter 8.

7.3.6. Variation of motor parameters

In drives with magnetic bearing, the force current coefficient k_{ir} is relatively constant over frequency owing to the thin rotor and stator laminations. In [40], the force current coefficient is determined experimentally and observed to be almost constant until 1.4 kHz. In self-bearing motors however, eddy-current effects are more important. Each of the two presented self-bearing machines has a non-laminated rotor and a non-segmented rotor magnet so that eddy-currents are induced in the rotor and in the magnet already at low frequencies. The rotor material 42CrMo4 has a good conductivity of 5.26 MS/m together with a good DC relative permeability μ_{r} over 600. The levitation field is repelled from the rotor centre at a few Hertz already. In [41], the threshold frequency f_{mgi} of a magnetic circuit with 42CrMo4 material is given to be 11 Hz. At this frequency, the effective permeability of steel is decreasing at 10 dB/dec so that it barely contributes to the levitation field magnetic path. Even at zero frequency, the stator levitation field is rotating asynchronously to the rotor so that the eddy-currents on the rotor squeeze the levitation field out of the rotor at very low speed already (e.g. 600 rpm). Fortunately, the levitation force amplitude is hardly influenced by this effect in the two presented prototypes as long as the levitation field amplitude is low. Magnetic steel is only required to get a high DC rotor magnetisation field. The levitation field closes almost exclusively at the rotor surface as illustrated in Figure 7.11.

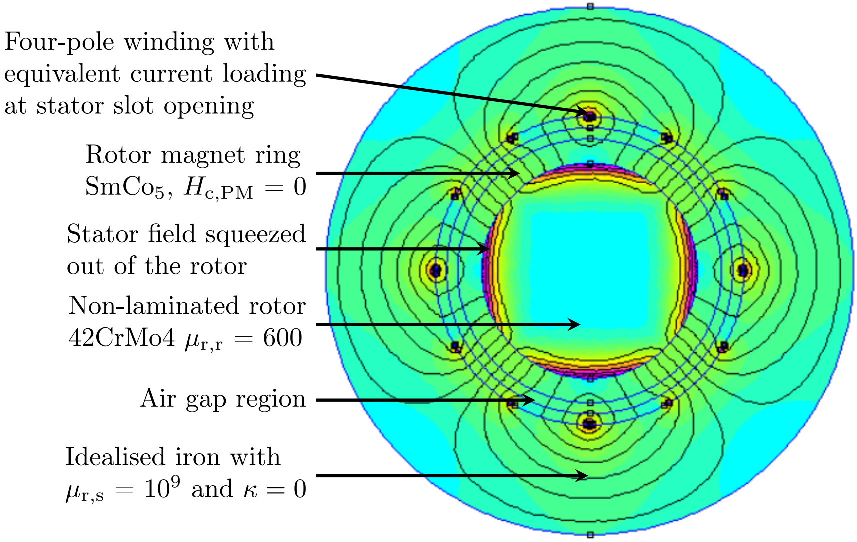

Four-pole winding with equivalent current loading at stator slot opening

Rotor magnet ring SmCo_5, $H_{\mathrm{c,PM}} = 0$

Stator field squeezed out of the rotor

Non-laminated rotor 42CrMo4 $\mu_{\mathrm{r,r}} = 600$

Air gap region

Idealised iron with $\mu_{\mathrm{r,s}} = 10^9$ and $\kappa = 0$

Figure 7.11.: Numerical calculation of the four-pole rotor levitation field pulsating at 10 Hz (program FEMM). Due to the high permeability and conductivity of the rotor material (simulation at $\mu_{\mathrm{r,r}} = 600$ and $\kappa = 5.6$ MS/m), the stator field is squeezed out of the rotor inner part. Since the stator magnetic field is low, the rotor part is not saturated so that the field lines in the magnet region are hardly influenced by rotor eddy-currents.

Therefore, the actuator bandwidth of self-bearing motors is limited by the magnet properties. Rare-earth magnets have permanent magnet recoil permeabilities close to one so that they differ essentially in terms of electrical conductivity κ. The conductivity of NdFeB is the lowest with values below 0.67 MS/m, leading to the highest actuator bandwidth. $\mathrm{Sm}_2\mathrm{Co}_{17}$ has also a moderate conductivity of 1.16 MS/m so gives a slightly lower bandwidth compared to NdFeB. SmCo_5 has a high conductivity of 20 MS/m and is therefore the least appropriate magnet for such an actuator. Unfortunately, a high magnet conductivity is preferred for high speed PMSM since it leads to lower rotor eddy-current losses induced by stator slot harmonics.

The double conical prototype [26] is composed of NdFeB magnets. The second cylindrical prototype (Table 6.1) has a SmCo_5 ring magnet. For illustration, the relative force current coefficient $k_{\mathrm{ir,r}}$ of the cylindrical prototype is calculated numerically with the program *FEMM* in Figure 7.12 for the original magnet material $\mathrm{SmCo_5}$ and for a NdFeB magnet material with a conductivity of 0.67 MS/m. In the case of $\mathrm{SmCo_5}$, the force current coefficient amplitude decreases at 200 Hz and more importantly, has a significant negative imaginary part. This imaginary part describes the phase delay between stator current and resulting levitation force caused by eddy-currents. The delay is maximal at 300 Hz, in the frequency range where control damping is necessary, that is where the control phase should be positive. With increasing frequency, the levitation field is squeezed out of the magnet so that the effective force current coefficient tends to half its value at DC. In the case of NdFeB, the coefficient $k_{\mathrm{ir,r}}$ stays relatively constant until 3 kHz. In both cases, the rotor is not moving $\omega_{\mathrm{r}} = 0$ and the stator is assumed to be of infinite permeability $\mu_{\mathrm{r}} = \infty$ and infinite resistivity $\rho = \infty$. The frequency characteristic of $k_{\mathrm{ir,r}}$ changes with the rotor speed ω_{r} as illustrated in Figure 7.12. It can be explained as follows: The three-phase levitation winding excites a pulsating air gap magnetic field at ω_2 with a fundamental wave $B_{\mathrm{s,2}}$ given by (7.25). This stator field can be split mathematically into two travelling waves $B_{\mathrm{s,2,fwd}}$ and $B_{\mathrm{s,2,bwd}}$, where $B_{\mathrm{s,2,fwd}}$ travels in the rotor rotation direction and $B_{\mathrm{s,2,bwd}}$ in the opposite direction. By transformation of (7.25) in the rotor coordinate system, rotating at ω_{r}, the two travelling waves become (7.26).

$$\begin{aligned} B_{\mathrm{s,2}}(\gamma,\omega_2,t) &= \hat{B}_{\mathrm{s,2}} \cdot \sin(p_2 \cdot \gamma)\cos(\omega_2 \cdot t) \\ B_{\mathrm{s,2,fwd}}(\gamma,\omega_2,t) &= 0.5 \cdot \hat{B}_{\mathrm{s,2}} \cdot \sin(p_2 \cdot \gamma - \omega_2 \cdot t) \\ B_{\mathrm{s,2,bwd}}(\gamma,\omega_2,t) &= 0.5 \cdot \hat{B}_{\mathrm{s,2}} \cdot \sin(p_2 \cdot \gamma + \omega_2 \cdot t) \end{aligned} \tag{7.25}$$

$$\begin{aligned} B_{\mathrm{s,2,fwd}}(x,\omega_2,t) &= 0.5 \cdot \hat{B}_{\mathrm{s,2}} \cdot \sin(p_2 \cdot x + (p_2 \cdot \omega_{\mathrm{r}} - \omega_2) \cdot t) \\ B_{\mathrm{s,2,bwd}}(x,\omega_2,t) &= 0.5 \cdot \hat{B}_{\mathrm{s,2}} \cdot \sin(p_2 \cdot x + (p_2 \cdot \omega_{\mathrm{r}} + \omega_2) \cdot t) \end{aligned} \tag{7.26}$$

At $p_2 \cdot \omega_{\mathrm{r}} = \omega_2$, the travelling wave $B_{\mathrm{s,2,fwd}}$ is synchronous to the rotor and does not induce rotor eddy-currents. At this speed, the second travelling wave $B_{\mathrm{s,2,bwd}}$ induces the rotor with a frequency $2 \cdot \omega_2$. Since the levitation

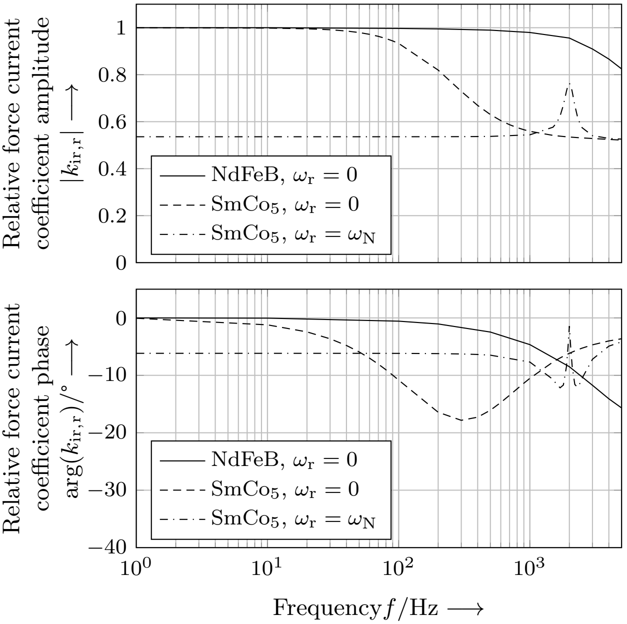

Figure 7.12.: Numerically calculated relative force current coefficient $k_{\mathrm{ir,r}}$ of the motor geometry in Table 6.1 for two magnet materials: NdFeB magnets (solid line) have a rather low conductivity so that the effective force current coefficient is constant until 2 kHz. SmCo$_5$ magnets (dashed line) have a high conductivity so that the effective force current coefficient k_{ir} decreases and leads to phase delay over 300 Hz at rotor standstill. At nominal speed ω_N, the rotor eddy-currents are induced by motion induction and reduce the effective force current coefficient by 47% over the full frequency range.

fields of the presented prototypes have two pole-pairs $p_2 = 2$, the travelling wave $B_{2,\mathrm{fwd}}$ is synchronous to the rotor when the rotor rotates at $0.5 \cdot \omega_2$. If the magnet material is assumed to be magnetically anisotropic, the superposition principle holds and the coefficient $k_{\mathrm{ir,r}}$ is composed of 50% of the effective coefficient $k_{\mathrm{ir,r}}$ at $|p_2 \cdot \omega_\mathrm{r} - \omega_2|$ and 50% of the one at $|p_2 \cdot \omega_\mathrm{r} + \omega_2|$. The resulting effective coefficient $k_{\mathrm{ir,r}}$ at nominal speed $\omega_\mathrm{N} = 2\pi \cdot\ 1\,000\ /\mathrm{s}$ is also displayed in Figure 7.12. It drops to 53% of its nominal value at $\omega_\mathrm{r} = 0$ due to eddy-currents. For this reason, the control setting must be set stiffer than the natural stiffness to ensure closed-loop stability at high speed.

Table 7.3.: Motor parameter variations for a magnet temperature rise of 80 K. The magnet temperature coefficient is set at -0.11%/K (NdFeB)

Parameter	**Symbol**	**Variation**
Radial force displacement coefficient	k_{sr}	-17%
Radial force current coefficient	k_{ir}	-8%
Force interference coefficient	k_{dist}	0%
Torque current coefficient	k_{M}	-8%

Due to their high resistivity, NdFeB magnets are less frequency dependent. However they have a higher temperature dependency than Samarium Cobalt magnets. The temperature coefficient of remanent magnetisation for NdFeB magnets is typically -0.11%/K. The variation of the motor parameters (4.64) is given as an illustration for a typical temperature increase of 80 K in Table 7.3. The motor stiffness as well as the control action (with k_{ir}) is reduced as the temperature increases. Sufficient robustness is necessary so that the temperature-independent interference forces and gyroscopic effect do not destabilise the closed-loop as the rotor temperature increases. Since the two components are, by design, small compared to the force due to the negative stiffness k_{sr}, the closed-loops are robust against temperature variation if the chosen closed-loop poles have a negative part equal or greater than their respective natural poles (7.8). This is the reason why the "natural stiffness" rule in [4] again gives a good hint where to place the closed-loop poles. It should also be noted that, since k_{sr} decreases faster than k_{ir} as the temperature increases, the minimum control gain that ensures levitation stability decreases with temperature. The $\mathrm{Sm}_2\mathrm{Co}_{17}$ magnet material is less sensitive to temperature change than NdFeB and has a high resistivity so that it is best suited for levitation control.

In order to improve control robustness against parameter variations, stiffer control settings can be aimed at if sufficient bandwidth is provided by the inner current-control loop, position sensors and the actuator. Since the *Bode*'s sensitivity integral sets limits to the shape of the closed-loop sensitivity function S_w according to (7.27), increasing the control stiffness inevitably worsens the sensitivity in the middle frequency region. This well-known "Waterbed" effect is of particular importance here since the system has right half-plane poles [42] and explains why, in contrast to the current control setting, the position control setting is kept low. To this extent, some recommendations are given in the international standard ISO 14839-2 [1] for the maximum of the sensitivity function S_w.

$$\int_0^\infty \ln\left|S_\mathrm{w}^k(\mathrm{j}\omega)\right| \cdot \mathrm{d}\omega = \pi \cdot p_{0,1}^k \text{ where } k \in \{p, c, z\} \tag{7.27}$$

8. Experimental investigation

In order to design and investigate different control structures, a flexible Linux-based real-time system was selected, which has the ability to process models built from *Matlab/Simulink*. This real-time system was developed in the work [43]. It consists of a dual-core mini-computer *Intel Atom* D510 where a control interrupt is able to operate in real-time until 20 kHz. A FPGA board is used to interconnect the computer (through a PCI connection) with the different hardware parts (parallel and SPI connections). The required peripherals and fast processing algorithms are implemented in VHDL in the *Spartan 3* FPGA, while the control is easily implemented in *Matlab/Simulink*. A second computer is used as an interface in order to give the reference values (positions, speed and torque) and to record and display all the control variables. It communicates remotely with the real-time computer through an Ethernet connection. While being able to drive both machine prototypes, the test-bench was designed to control the conical self-bearing motor [26]. All the presented results are derived for this particular prototype.

8.1. Hardware parts

In order to control a self-bearing motor, several hardware components are necessary. The rotor positions (rotation angle and displacements) and winding currents have to be processed. In order to feed the different windings, four three-phase inverters are necessary.

8.1.1. Rotor angle processing hardware

In order to obtain the rotor angular position, the field of a diametrically magnetised magnet mounted on the rotor is evaluated with a two-axis *Hall*-sensor MLX91204. The cosine and sine signals are digitalised with two analogue-to-digital converters ADCS7476. The two digital *Hall*-sensors SS360NT are required for high speed operation (see Chapter 3).

8.1.2. Rotor displacement processing hardware

The processing of the eddy-current sensors is realised with a dedicated processing board. The sensor excitation (u_{ex} in Figure 3.4b) is generated by a 16-bit digital-to-analogue converter DAC8580 that is dedicated to signal generator applications. It is amplified with an AD8397 operational amplifier. The measured differential displacement signals (u_{mea} in Figure 3.4b) are amplified and filtered with second-order multi-feedback band-pass differential filters. The band-pass filters are tuned to pass frequencies from 75 kHz to 500 kHz. It is followed with a low-pass differential to single-ended filter with a cut-off frequency $f_{\mathrm{c}} = 500$ kHz and is sampled by ADCS7476 analogue-to-digital converters. The schematic of one sensor channel is given in Figure 8.1. The actual frequency of the eddy-current is constant. The wide frequency bandwidth was chosen since the excitation frequency of the sensors from the company *LTI-Motion* was not known at this early stage. Later this choice revealed to be unsatisfying for inverter drive. Indeed, the switching transients of the inverter PWM voltage were very present in the filtered signals and could be eliminated only with synchronisation of the signal sampling with the PWM pulse pattern. Consequently the signal sampling frequency f_{samp} of the position signals was reduced from the initial 500 kHz to 125 kHz and was sampled at the middle of the pulse-width voltage patterns. Since the signal excitation frequency f_{ex} is 312.5 kHz, the position signals are undersampled and the base-band alias signals are mirrored at the center frequency $f_{\mathrm{dem}} = 62.5$ kHz.

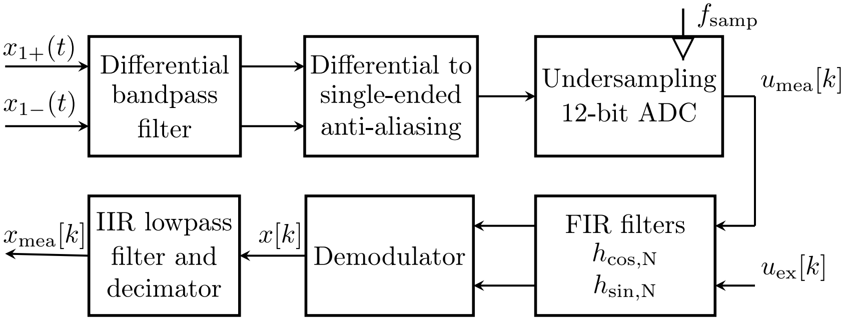

Figure 8.1.: Analogue signal processing (top) for one differential eddy-current position signal. The differential signal is filtered with a fully-differential multi-feedback band-pass filter and converted to single-end before being digitally converted by the analogue-to-digital converter. The digital processing (bottom) is detailed in section 3.3.3.

8.1.3. Current sensor processing

The motor phase currents are converted in voltage signals with the current sensor CASR 6-NP from the company *LEM*. In order to match the low impedance requirement of the 12-bit analogue-to-digital converter ADCS7476, the signals are strengthened by analogue followers. For each three-phase inverter, the phase current of phase U and W are measured.

8.1.4. Inverter

In order to feed the self-bearing prototypes, four three-phase inverters were built. Whereas their design is out of the scope of this work, there were realised for this particular test-bench since no three-phase inverter was available on the market that could operate at 160 V DC link, 10 A phase current and 62.5 kHz switching frequency with direct control of power switches. Since integrated circuit manufacturers propose very fast and powerful MOSFETs (such as the IRFB4127 chosen here), as well as fully integrated half-bridge bootstrap MOSFET drivers (such as the IR2183 chosen here), such low ratings were not difficult to realise.

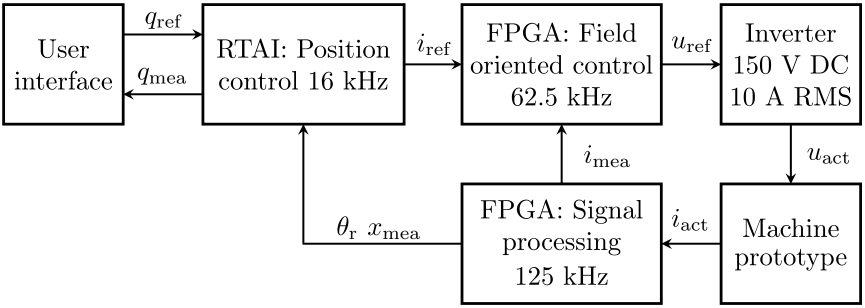

Figure 8.2.: Overview of the set-up: The position control operates on a real-time computer (RTAI) at 15.625 Hz and gives the current references i_{ref} to a FPGA. In the FPGA, four field-oriented controls are operating in pipeline, at 62.5 kHz, to control the current of the four three-phase systems. The switching patterns u_{ref} are sent to the four inverters which feed the prototype [26]. The FPGA processes the five eddy-current-based displacement sensors, the rotation sensor and the current sensors.

8.1.5. Overview of the set-up

The different parts are connected as displayed in Figure 8.2. The reference positions as well as the control settings are send from the computer user interface to the real-time computer where the position control and speed control operate. The Ethernet connection between the two computers is not real-time capable so that all the record and trigger functions are implemented in the real-time computer. The position controllers give a set of reference currents (eight reference currents) that is sent to the FPGA through a PCI port at 15.6 kHz. The processed position signals (five displacement signals and one rotor angle signal) are sent back from the FPGA to the real-time computer at the same rate. The current controllers are implemented in the FPGA and operate at 62.5 kHz. The reason for the split of position and current control as well as the choice of the control frequencies is explained later. The 24 trigger signals from the pulse-width modulators are sent to the four inverters. The eight phase currents (two per inverter), digitally converted in the inverters, are sent back to the FPGA at a 62.5 kHz rate. Additionally, the digitally converted position signals (five displacement signals plus the signal excitation and two rotor angle position signals) are sent to the FPGA at a rate of 125 kHz, 250 kHz or 500 kHz depending on the processing algorithm implemented in the FPGA. The serial data transfer between peripherals and the FPGA amounts to over 45 Mbps. The parallel transfer from the FPGA to the RT computer is however limited to about 4 Mbps to ensure sufficient calculation time for the position control. A lot of work was necessary to set and synchronise the communication as well as to optimise the fixed-point signal processing and current control in the FPGA. Indeed, the communication protocol goes through several software layers, implemented partially in *Matlab/Simulink* code, in TLC, in C (in the real-time computer Kernel and in the user-space) and in VHDL for the FPGA. Taking some perspective on this work, the set-up was too complicated. It would have been much more efficient and easier to implement the control with floating point micro-controllers dedicated for control applications such as the TMS320F28335 or with a *DSpace* system.

8.2. Experimental evaluation of motor parameters

8.2.1. Force-displacement parameter

With the operating set-up, the motor parameters are validated experimentally and the different controller tested. The radial stiffness is validated experimentally with an indirect method as follows: The horizontal rotor position x is changed within the emergency bearing clearance (±150 µm) and the levitation current amplitude $i_{2,\mathrm{d}}$, necessary to hold the rotor position, is measured. At stationary condition, the radial pull $k_{\mathrm{sr}} \cdot x$ due to the rotor displacement x must be equal and opposed to the levitation force $k_{\mathrm{ir}} \cdot i_{2,\mathrm{d}}$. With a regression of the curve $i_{2,\mathrm{d}} = f(x)$ in Figure 8.3, the coefficient $k_{\mathrm{sr}}/k_{\mathrm{ir}}$ is obtained. Since k_{ir} is known, the radial stiffness is obtained experimentally and gives -26 N/mm for both the DE and NDE motor.

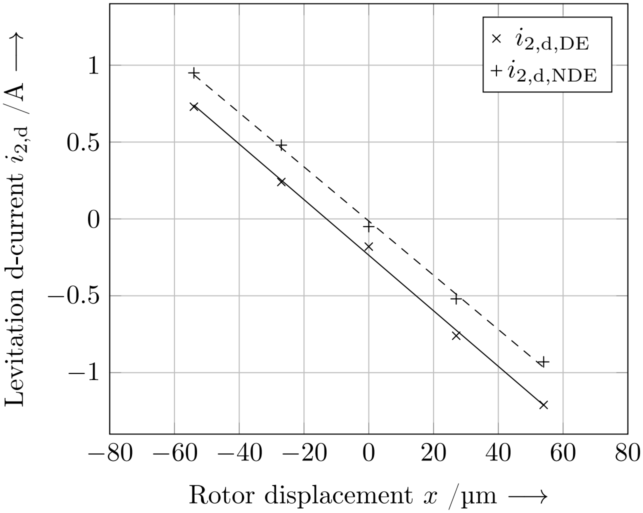

Figure 8.3.: Measurement of the force-displacement coefficient k_{sr}: The rotor is moved from –54 µm to 54 µm in horizontal direction x and the levitation current amplitude $i_{2,\mathrm{d}}$ is measured.

8.2.2. Force-interference coefficient

The measurement of k_{dist} is indirect and is done as the following: The motor is driven in steady-state condition at the concentric position $\epsilon = 0$. Since no external force acts on the rotor in the horizontal direction, the horizontal levitation disturbance force component due to the driving q-current $k_{\mathrm{dist}} i_{1,\mathrm{q}} i_{2,\mathrm{q}}$ is equal and opposite to the horizontal levitation force component $k_{\mathrm{ir}} i_{2,\mathrm{d}}$ for all values $i_{1,\mathrm{q}}$. In order to vary $i_{1,\mathrm{q}}$, one half-motor (DE) is loaded with the second half-motor (NDE). The levitation component $i_{2,\mathrm{d}}$ is measured as a function of $i_{1,\mathrm{q}}$ and displayed in Figure 8.4. With a linear regression of the curve, and using the current-force coefficient k_{ir}, the radial disturbance force-current coefficient of the conical self-bearing machine is measured to be $k_{\mathrm{dist}} = 0.018\ \mathrm{N/A^2}$.

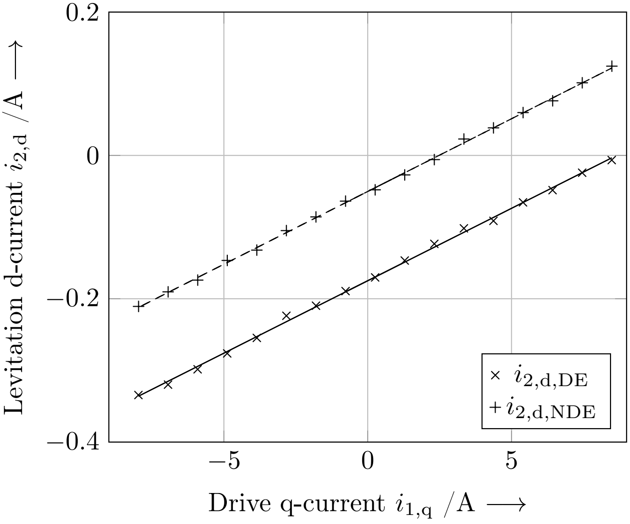

Figure 8.4.: Measurement of the disturbance force-current coefficient k_{dist}: The rotor is loaded with a drive current $i_{1,\mathrm{q}}$ and the levitation current amplitude $i_{2,\mathrm{d}}$ is measured.

8.3. Control implementation

8.3.1. Current control

The current control was first implemented in the real-time computer with proportional integral controllers according to amplitude optimum. At an early stage of the control implementation, it was observed that the computer could not process four field oriented controls and the position control at a sufficient rate. For this reason, the field oriented controls with current control and space vector modulation were transferred from the computer to the FPGA. This valuable work was part of the Master-Thesis [55]. In order to fit into the FPGA, a simple proportional integral controller was implemented with an integral freezing anti-windup. Up to four space vector modulations can operate in a finely granulated pipeline structure. This structure revealed to reach almost the performances of four parallel space vector modulations while using approximately one fourth of the logic blocks. In order to simplify the fixed point implementation of the vector modulator, the control frequency was set as such that the FPGA clock frequency (128 MHz) is a power of two of the control frequency (chosen at 62.5 kHz). The switching frequency was selected high for several reasons:

- The MOSFET inverters can handle high switching frequencies due to their inherent low switching losses.
- The current ripple due to the switched voltage and the very low phase inductances is kept to an acceptable value. The levitation winding inductivity of the prototype [26] is below 100 µH, leading to current rates as high as 1 A/µs. A high switching frequency reduces in particular the rotor losses of the non-laminated two pole rotor.
- The current controller, that operates at the same frequency, is able to set the actual current to its reference value within one position control period (64 µs). Its dynamic can be neglected during the design of the position control.

The step response for a current step of 4 A in the levitation winding of the prototype [26] is illustrated in Figure 8.5 [55]. The measured step response (in blue) is obtained with a *Tektronix* current probe TCP with 100 MHz bandwidth and a *Tektronix* oscilloscope TDS2014. The step reference (dotted line), added for illustration, does not consider the current control period delay. The current over-shoot is approximately 5%. The control delay plus the rising time to 95% account for 61 µs delay which is approximately one position control period of 64 µs. The step response in Figure 8.5 is realised with a 40 V DC link voltage only, so the measured current rate of 0.3 A/µs is only one fourth of the actual current rate during normal operation. This value is very high and is responsible for strong EMI in the position signals inside the motor housing. In order to mitigate the problem, the cables of each three-phase system were shielded inside the prototype as illustrated in Figure 8.6.

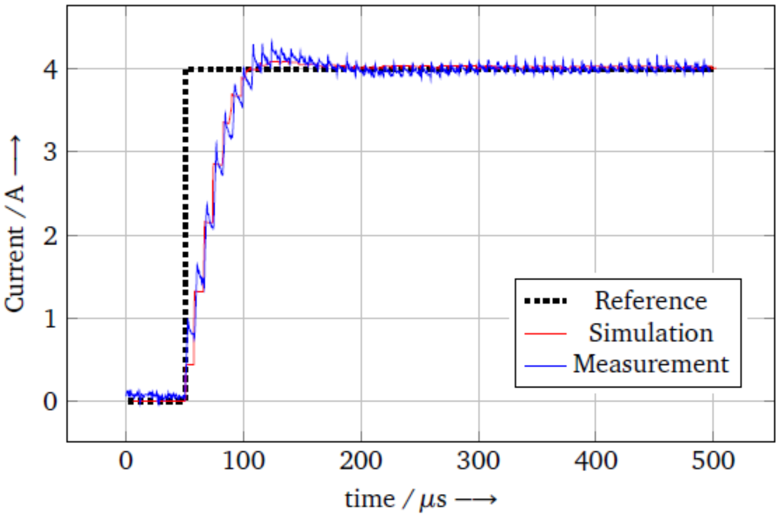

Figure 8.5.: Current step response of the proportional integral current controller tuned with amplitude optimum, feeding the levitation winding of the prototype [26]. The measured curve (in blue) is compared to the simulated step response (in red). The reference current is added for illustration [55].

8.3.2. Position control

At first, a simple control structure with local PID controllers was implemented to verify proper operation and to experimentally measure the motor parameters. The prototype [26] could not be operated over 10 000 rpm without reaching the current limit of the radial position controllers due to the increasing imbalance forces.

8.3.3. Imbalance force rejection

The rotor imbalance of the tested prototype is too big to be operated without imbalance rejection. In order to resolve the issue, three different synchronous notch filters were tested, two with feedback retro-action and one with feed-forward action, all already detailed in the literature [4],

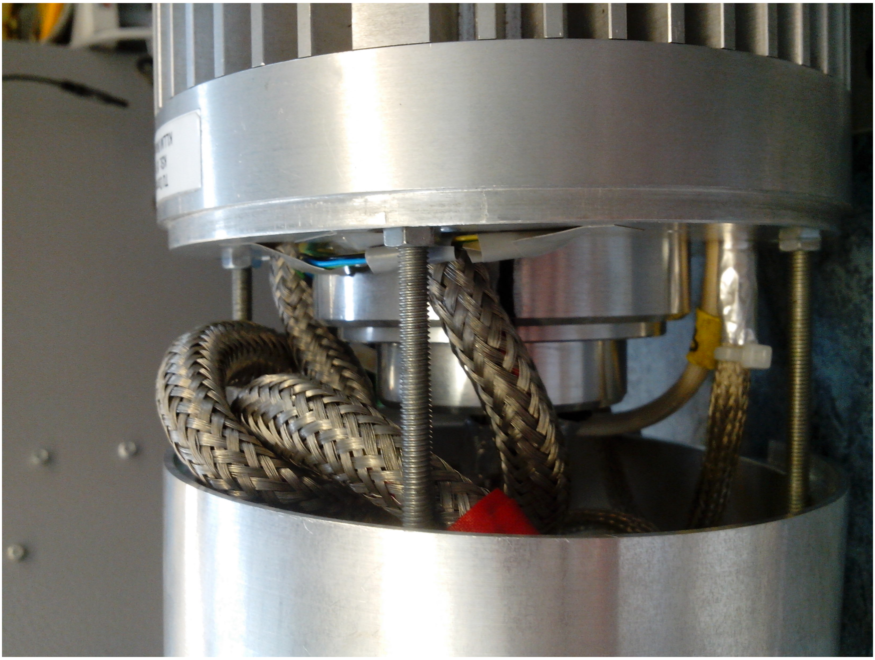

Figure 8.6.: Intern shielding of the power cables to reduce EMI in the position signals inside the motor housing. The cables are kept tight together inside the coarsely braided strands. These cable shields reduce the common-mode capacitive interference between power and sensor cables. Since there are connected at both ends, they reduce also the emitted magnetic field caused by high current rate by giving a current return path. The position signals on the right have a shield with finer braided strands.

[44]. The particularity of those notch-filters is that they adapt to the varying speed. The feedback notch filter presented in [44] gave the best results with a straightforward method to select the parameters of the retro-action. The filter structure is illustrated in Figure 8.7. The choice of the speed-dependent parameters T_R and T_J to maximise the notch filter damping is $T_\mathrm{R} + \mathrm{j}T_\mathrm{J} = S_\mathrm{w}(\mathrm{j}\omega)^{-1}$ where $S_\mathrm{w}(\mathrm{j}\omega)$ is the sensitivity of the closed-loop position control [44]. It implies that the parameters are stored in a lock-up table and interpolated. In practice, a single set of parameters (T_R, T_J) is sufficient and is chosen as follows: After selection of closed-loop control pole locations,

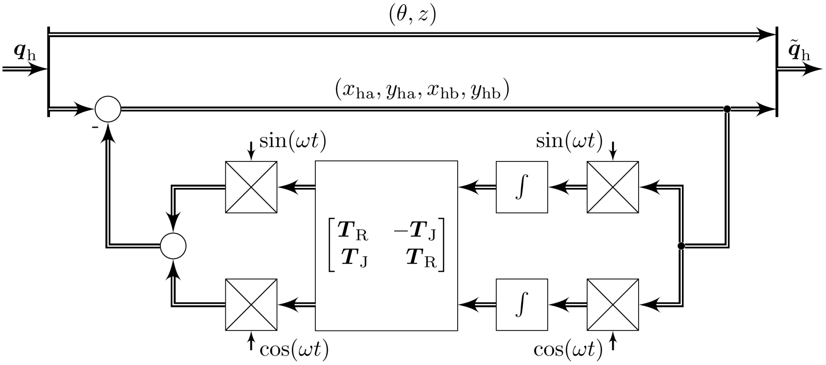

Figure 8.7.: Synchronous notch filter for imbalance force rejection [44].

for example with "natural stiffness" [4], the closed-loop transfer functions $G_{\mathrm{w}}^{\mathrm{p}}(\mathrm{j}\omega)$, $G_{\mathrm{w}}^{\mathrm{c}}(\mathrm{j}\omega)$ of the two motions (parallel and tilting motions) are evaluated as well as the corresponding sensitivity functions $S_{\mathrm{w}}^{\mathrm{p}}(\mathrm{j}\omega)$, $S_{\mathrm{w}}^{\mathrm{c}}(\mathrm{j}\omega)$. The frequency range where both the closed-loop transfer functions $G_{\mathrm{w}}(\mathrm{j}\omega)$ and the sensitivity functions $S_{\mathrm{w}}(\mathrm{j}\omega)$ have a significant gain is the "critical frequency region". Since the closed-loop transfer function plus the sensitivity function equal identity (MIMO system) or unity (SISO system), this critical frequency region always exists. In this frequency range, the control reacts against the imbalance forces (high closed-loop gain) but does it with a poor phase margin (high sensitivity gain), leading to high actuator force commands. The average phase and gain of the inverse sensitivity function $S_{\mathrm{w}}(\mathrm{j}\omega)^{-1}$ in this frequency range are evaluated and the parameters (T_{R}, T_{J}) are calculated accordingly. In order to use a single set of parameters for both motions, the two transfer functions $G_{\mathrm{w}}^{\mathrm{p}}(\mathrm{j}\omega)$, $G_{\mathrm{w}}^{\mathrm{c}}(\mathrm{j}\omega)$ should be selected to be similar. Otherwise, two distinct filters must be used. The transient response of the horizontal position and the related reference current at 9 000 rpm and no-load are recorded in Figure 8.8. The reference current $i_{2,\mathrm{d},\mathrm{a}}$ vanishes in less than 150 ms. Since the rotor displacement amplitude in Figure 8.8 is lower when the position controller does not react to rotor imbalance (32 µm $<$ 37 µm), one should expect a sensitivity gain bigger than 0 dB at 150 Hz. This result can be verified in Figure 8.9.

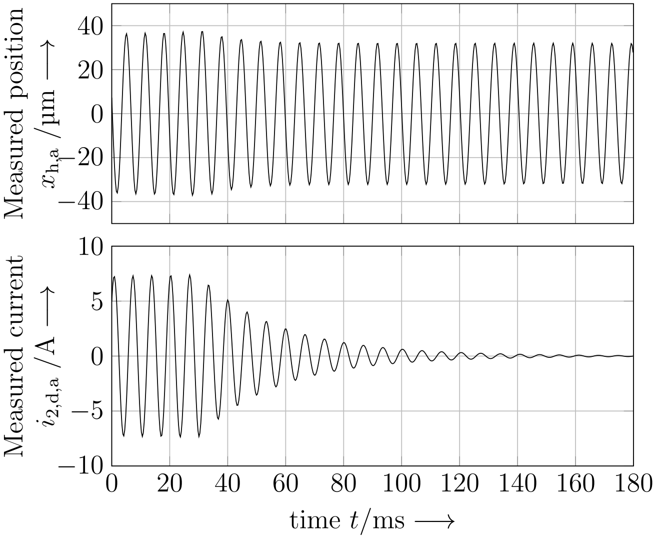

Figure 8.8.: Measured transient response of the horizontal position signal and the reference current after switching the imbalance force rejection. The reference current component at rotational frequency 150 Hz vanishes while the displacement amplitude is slightly reduced.

8.4. Evaluation of the control performances

The multi-feedback pole placement was presented in Chapter 7. In order to validate the control and the pole placement, the closed-loop transfer function of each mode, as well as the corresponding sensitivity function is evaluated on the set-up. For that, sinus position reference signals are given as input and the output positions are measured. Eleven excitation frequencies are selected from 1 Hz until 500 Hz. The input and output signals are moved to the frequency domain with fast *Fourier* transformation. The ratio of the two peaks at excitation frequency gives the closed-loop gain and the phase difference at that same frequency is the closed-loop phase. The sensitivity function is calculated at each measurement point as 1-$G_w(j\omega)$. In order to avoid that the gyroscopic effect and the force interferences alter the transfer functions, the measurement is performed

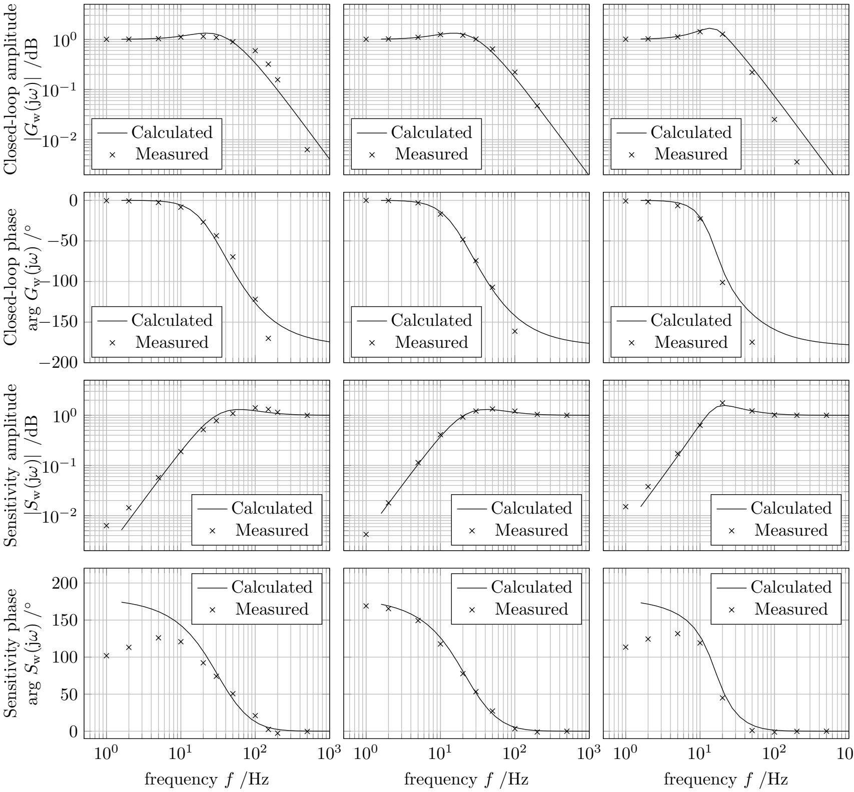

Figure 8.9.: From the left to the right: *Bode* transfer functions of horizontal common mode, horizontal differential mode and axial motion, calculated and measured at rotor stand-still $\omega = 0$. From top to bottom: Closed-loop gain $|G_{\mathrm{w}}|$, closed-loop phase $\arg(G_{\mathrm{w}})$, sensitivity gain $|S_{\mathrm{w}}|$ and sensitivity phase $\arg(S_{\mathrm{w}})$.

at stand-still. The results are presented in Figure 8.9. The closed-loop transfer functions are matching relatively well. The parallel motion seems to be stiffer in the set-up than calculated from the pole placement. The gain and phase are rolling off faster than expected at higher frequencies. This is due to the low-pass filtering action after the position demodulation in the FPGA. The sensitivity functions are not precisely obtained at low frequency since they result from the difference of two very close values. Since the axial

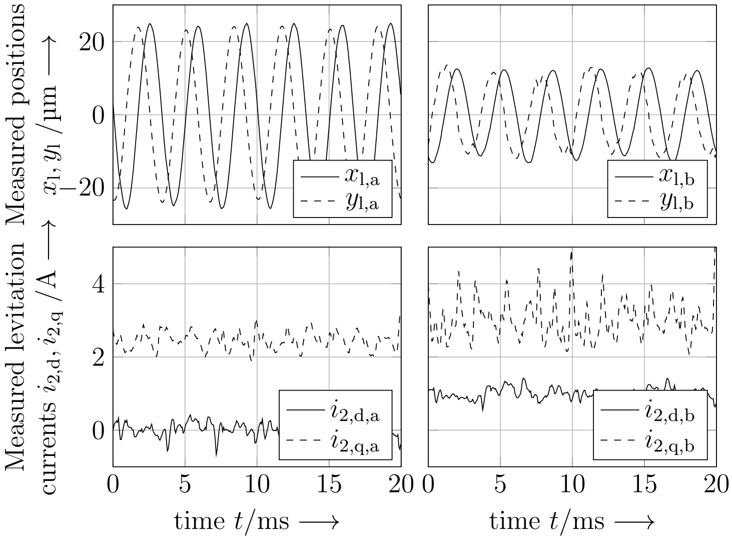

Figure 8.10.: Top: Measured radial positions in each half-motor. Bottom: Measured levitation currents in each half motor. The measurement is performed at rated speed $n_N = 18\ 000$ rpm. The position orbits are not visible in the levitation currents due to the rotor imbalance rejection.

poles were chosen with less damping (dominant poles closer to the imaginary axis), a small peak is observable in the closed-loop and sensitivity functions. With the presented set-up with pole placement control and imbalance force rejection, the prototype is able to operate until voltage limit at 25 000 rpm. The radial currents and positions are illustrated in Figure 8.10 at nominal speed n_N.

9. Summary and Conclusions

This work gives an insight of the self-bearing permanent magnet synchronous motor working principle, modelling and control. It starts by presenting the elements required to control such a motor. The choice of the sensors is addressed. The bandwidth, the resolution and the limitations of current sensors, rotor angle sensors and displacement sensors for this particular application are discussed, and recommendations are given. The necessary inverter power is calculated and compared to the one for magnetic bearings in an illustrative example. It is shown that, under transient conditions, the reactive power requirement due to the big air gap is comparable to the one of a magnetic bearing with bias-current. This is, because the rotor bias flux is generated with the motor permanent magnets. The motor modelling part starts with the analytical calculation of the motor lateral forces,the torque and the force interferences. To do so, the rotor and stator fields are calculated in a slotless permanent magnet synchronous motor by solving *Laplace*'s and *Poisson*'s equation in the motor regions for constant iron permeability. Then the lateral forces and the torque are obtained by integration of the *Maxwell* stress on a closed surface around the rotor in the air gap. It results a set of characteristic parameters, which are used to model the self-bearing motor. The parameter analytical expressions are given for the two-pole rotor magnet diametrically magnetised, a two-pole drive winding and a four-pole levitation winding. It is shown that the motor should be designed with a rotor field much bigger than the stator fields in order to simplify the motor model to the one commonly found in the literature. The control stiffness is recommended to be not too low in order for the control to be robust against non-linear force interferences or torque disturbances that result from the superposition of the fields and from the effect of radial rotor displacement. The accuracy of the parameters are verified numerically by comparison with finite element simulation results as well as with measurements. Since cylindrical self-bearing motors produce only radial lateral forces, for magnetic levitation they require a thrust bearing to be actively controlled in axial direction. A double-conical self-bearing prototype motor is presented that generates also controllable axial forces thanks to its stator and rotor conical form. The calculation of the motor parameters is analytically too difficult in this particular case, so that an approximation is presented to estimate those coefficients, when the rotor cone angle is small ($< 10°$). Unfortunately the analytical determination of the parameters for the axial forces in the motor can not be simplified, since the 3D field end-effect are dominating. Therefore, it should be determined by means of 3D finite element simulation and should be verified experimentally. In the following chapter 6, an alternative cylindrical self-bearing motor is presented with a split stator winding. It has two anti-symmetrical windings that generate both torque and lateral forces. Their respective independent control is possible with the projection of the current components in two orthogonal coordinate systems. The two-pole prototype is built and measured at its nominal speed 60 000 rpm. In principle, thanks to the force contribution of each of the two three-phase windings, the rotor can be maintained in suspension even when one three-phase inverter is switched off. In practice, this property was verified at zero speed. Finally, a model-based control scheme with motion decoupling is presented and tested on a test-bench. It is concluded that the self-bearing motor straddles synchronous machines and levitated drives with magnetic bearing. From the electric point of view, the current control is very similar to the one of a inverter-fed synchronous motor. The stator lateral force control is performed in a fictive synchronous reference frame, and the electrical circuit is equivalent to a simple resistive-inductive model. From the mechanical point of view, the position control is analogous to the one for an electrical drive with active magnetic bearings. The differences are nuances in the non-linear parts and in the presence of additional disturbance components.

As long as the stator fields are small compared to the rotor field, and as long as the position controller is set with sufficient stiffness and damping, a linear approximation of the electro-mechanical model is sufficient to obtain satisfying closed-loop control performance.

A. Annexe

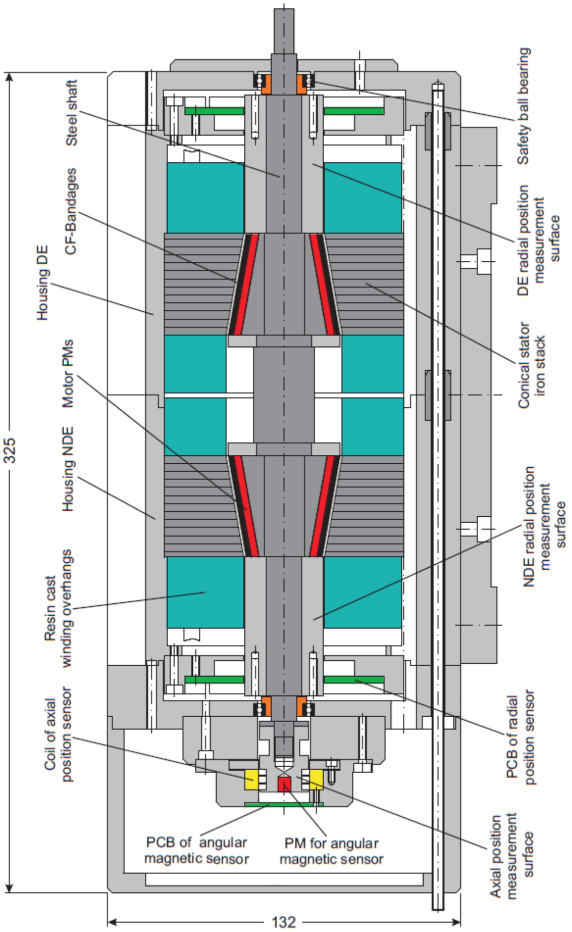

Figure A.1.: 2D assembly drawing of Conical-BM (axial cross-section) [14].

References

[1] ISO 14839-2, *Mechanical vibration - Vibration of rotating machinery equipped with active magnetic bearings - Part 2: Evaluation of vibration*, Geneva, Switzerland, 2004.

[2] L. Miller and M. Wackers, "Transrapid Maglev System Technical Readiness and Corridors of Application," *Journal of Advanced Transportation*, vol. 27, no. 1, pp. 49–64, 1993.

[3] S. Earnshaw, "On the Nature of the Molecular Forces which regulate the Constitution of the Luminiferous Ether," *Transactions of the Cambridge Philosophical Society*, vol. 7, pp. 97–112, 1842.

[4] G. Schweitzer, E. H. Maslen, and et al., *Magnetic Bearings: Theory, Design, and Application to Rotating Machinery.* Berlin-Heidelberg, Germany: Springer, 2009.

[5] A. Chiba, T. Fukao, O. Ichikawa, M. Oshima, M. Takemoto, and D. G. Dorrel, *Magnetic Bearings and Bearingless Drives.* Oxford, United Kingdom: Elsevier Linacre House, 2005.

[6] D. Vischer, *Sensorlose und spannungsgesteuerte Magnetlager.* Dissertation, Swiss Federal Institute of Technology, Zürich, Switzerland, 1989.

[7] F. Betschon, *Design Principles of Integrated Magnetic Bearings.* Dissertation, Swiss Federal Institute of Technology, Zürich, Switzerland, 2000.

[8] T. Schneider and A. Binder, "Design and Evaluation of a 60 000 rpm Permanent Magnet Bearingless High Speed Motor," in *7th International Conference on Power Electronics and Drive Systems (PEDS'07)*, pp. 1–8, 2007, Bangkok, Thailand.

[9] H. Sequenz, *Die Wicklungen elekrischer Maschinen.* Vienna, Austria: Springer-Verlag, 1st ed., 1950.

[10] J. Wang, *The Current Slope Based Position Estimation for Self-Sensing Magnetic Bearings.* Dissertation, Institute for Electrical Energy Conversion, TU Darmstadt, 2015.

[11] Kaman Precision Products, *Inductive Technology Handbook*, Colorado Springs, Colorado, USA, 2012.

[12] I. J. Mönchand, F. Bahr, and M. Melzer, "Flexible Hall Sensorics for Flux-Based Control of Magnetic Levitation," *IEEE Transactions on Magnetics*, vol. 51, no. 11, pp. 1–4, 2015.

[13] J. Visosky, *Anordnung zur Positionsmessung bei einer magnetisch gelagerten Welle.* Patent DE 10 2005 025 588 A1, 2006.

[14] G. Bergmann, *Five-Axis Rotor Magnetic Suspension with Bearingless PM Motor Levitation Systems.* Dissertation, Institute for Electrical Energy Conversion, TU Darmstadt, 2013.

[15] F. W. Carter, "The Magnetic Field of the Dynamo-Electric Machine," *Journal of the Institution of Electrical Engineers*, vol. 64, no. 359, pp. 1115–1138, 1926.

[16] Z. Q. Zhu, D. Howe, and C. C. Chan, "Improved Analytical Model for Predicting the Magnetic Field Distribution in Brushless Permanent Magnet Machines," *IEEE Transactions on Magnetics*, vol. 38, no. 1, pp. 229–238, 2002.

[17] U. Kim and D. K. Lieu, "Magnetic Field Calculation in Permanent Magnet Motors with Rotor Eccentricity: Without Slotting Effect," *IEEE Transactions on Magnetics*, vol. 34, no. 4, pp. 2243–2252, 1998.

[18] H. J. Dirschmid, *Mathematische Grundlagen der Elektrotechnik.* Wiesbaden: Vieweg, 1992.

[19] R. Belmans, A. Vandenput, and W. Geysen, "Calculation of the Flux Density and the Unbalanced Pull in Two Pole Induction Machines," *Archiv für Elektrotechnik*, vol. 70, no. 3, pp. 151–161, 1987.

[20] G. Müller, *Betriebsverhalten rotierender elektrischer Maschinen.* Berlin: VDE-Verlag, 3rd ed., 1984.

[21] F. R. Alam and K. Abbaszadeh, "Magnetic Field Analysis in Eccentric Surface-Mounted Permanent-Magnet Motors Using an Improved Conformal Mapping Method," *IEEE Transactions on Energy Conversion*, vol. 31, no. 1, pp. 333–344, 2016.

[22] T. J. A. Bromwich, *An introduction to the theory of infinite series.* New York, USA: American Mathematical Society, 3rd ed., 1991.

[23] Z. Q. Zhu and D. Howe, "Instantaneous Magnetic Field Distribution in Brushless Permanent-Magnet DC Motors, Part lll. Effect of Stator Slotting," *IEEE Transactions on Magnetics*, vol. 29, no. 1, pp. 143–151, 1993.

[24] F. Ollendorf, *Berechnung magnetischer Felder, Band I.* Vienna, Austria: Springer, 1952.

[25] Z. Q. Zhu and D. Howe, "Instantaneous Magnetic Field Distribution in Brushless Permanent Magnet DC Motors, Part ll: Armature Reaction Field," *IEEE Transactions on Magnetics*, vol. 29, no. 1, pp. 136–142, 1993.

[26] G. Munteanu, A. Binder, and S. Dewenter, "Five-Axis Magnetic Suspension with Two Conical Air Gap Bearingless PM Synchronous Half-Motors," in *International Symposium on Power Electronics, Electrical Drives, Automation and Motion (SPEEDAM)*, pp. 1246–1251, 2012, Naples, Italy.

[27] G. Wu, X. Wang, Q. Ding, and T. Ni, "Design and Analysis of a Novel

Axial Actively Regulated Slotless Skew Winding Bearingless Motor," in *IEEE International Conference on Mechatronics and Automation (ICMA)*, pp. 1864–1869, 2015, Beijing, China.

[28] J. Kučera, "Axialer magnetischer Zug bei elektrischen Maschinen," *Elektrotechnik und Maschinenbau*, vol. 59, pp. 305–315, 1940.

[29] K. J. Binns and P. J. Lawrenson, *Analysis and Computation of Electric and Magnetic Field Problems.* New York: Pergamon Press, 2$^{\text{nd}}$ ed., 1973.

[30] H. Sugimoto, S. Tanaka, A. Chiba, and M. A. Rahman, "Winding Arrangement in Single-Drive Bearingless Motor with Radial Gap," in *International Power Electronics Conference (IPEC)*, pp. 982–987, 2014, Hiroshima, Japan.

[31] H. Sugimoto, S. Tanaka, A. Chiba, and J. Asama, "Design and Test Result of Novel Single-Drive Bearingless Motor with Cylindrical Radial Gap," in *IEEE Energy Conversion Congress and Exposition (ECCE)*, pp. 2466–2473, 2013, Denver, Colorado, USA.

[32] J. Asama, Y. Hamasaki, T. Oiwa, and A. Chiba, "Proposal and analysis of a novel single-drive bearingless motor," *IEEE Transactions on Industrial Electronics*, vol. 60, no. 1, pp. 129–138, 2013.

[33] J. Pyrhönen, T. Jokinen, and V. Hrabovcova, *Design of Rotating Electrical Machines.* United Kingdom: John Wiley & Sons, Ltd, 2008.

[34] A. Binder, *Elektrische Maschinen und Antriebe.* Heidelberg: Springer, 2012.

[35] M. Mack, *Luftreibungsverluste bei elektrischen Maschinen kleiner Baugröße.* Dissertation, University of Stuttgart, Stuttgart, Germany, 1967.

[36] R. Larsonneur, *Design and Control of Active Magnetic Bearing Systems for High Speed Rotation.* Dissertation, Swiss Federal Institute of Technology, Zürich, Switzerland, 1990.

[37] J. Kautsky, N. K. Nichols, and P. V. Dooren, "Robust Pole Assignment in Linear State Feedback," *International Journal of Control*, vol. 41, no. 5, pp. 1129–1155, 1985.

[38] R. D. Williams, F. J. Keith, and P. E. Allaire, "Digital Control of Active Magnetic Bearings," *IEEE Transactions on Industrial Electronics*, vol. 37, no. 1, pp. 19–27, 1990.

[39] M. Ahrens and L. Kučera, "Cross Feedback Control of a Magnetic Bearing System: Controller Design Considering Gyroscopic Effects," in *Third International Symposium on Magnetic Suspension Technology (ISMB)*, pp. 177–191, 1995, Tallahassee, Florida, USA.

[40] A. Traxler, *Eigenschaften und Auslegung von berührungsfreien elektromagnetischen Lagern.* Dissertation, Swiss Federal Institute of Technology, Zürich, Switzerland, 1985.

[41] R. Seifert and W. Hofmann, "Completion of analytical model of active magnetic thrust bearings including asymmetric air gap field between mixed materials," *Mechanical Engineering Journal*, vol. 4, no. 5, pp. 1–11, 2017.

[42] G. Stein, "Respect the Unstable," *IEEE Control Systems Magazine*, pp. 12–25, 2003.

[43] F. Mink, *Modellierung und hochdynamische Stromregelung von PM-Synchronmaschinen unter Berücksichtigung von Sättigungseffekten.* Dissertation, Institute for Electrical Energy Conversion, TU Darmstadt, Germany, 2012.

[44] R. Herzog, P. Bühler, C. Gähler, and R. Larsonneur, "Unbalance compensation using generalized notch filters in the multivariable feedback of magnetic bearings," *IEEE Transactions on Control Systems Technology*, vol. 4, no. 5, pp. 580–586, 1996.

[45] J. Abrahamsson, J. Ogren, and M. Hedlund, "A fully levitated cone-

shaped lorentz-type self-bearing machine with skewed windings," *IEEE Transactions on Magnetics*, vol. 50, no. 9, pp. 1–9, 2014.

[46] K. Vogt, *Berechnung rotierender elektrischer Maschinen.* Berlin: VEB Verlag Technik, 3^{rd} ed., 1983.

Publications with own contributions

[47] G. Messager and A. Binder, "Analytical comparison of conventional and modified winding for high speed bearingless permanent magnet synchronous motor applications," in *International Conference on Optimization of Electrical and Electronic Equipement (OPTIM)*, pp. 330–337, 2014, Brasov, Romania.

[48] Y. Gemeinder, G. Messager, and A. Binder, "Synthetic test bench for measurements of bearing-currents in inverter fed drives," in *European Conference on Power Electronics and Applications (EPE14)*, pp. 1–10, 2014, Lappeenranta, Finland.

[49] G. Messager and A. Binder, "Evaluation of a dual half-pitched three-phase bearingless high-speed permanent magnet synchronous motor prototype," in *10th ETG/GMM-Symposium Innovative small Drives and Micro-Motor Systems*, pp. 83–88, 2015, Cologne, Germany.

[50] G. Messager, F. Mink, T. Becker, J. Wang, and A. Binder, "Control interference of electrical machines with double-star winding systems driven by independent current controllers," in *European Conference on Power Electronics and Applications (EPE15)*, pp. 1–10, 2015, Geneva, Switzerland.

[51] G. Messager and A. Binder, "Observer-based pole placement control for a double conical high-speed bearingless permanent magnet synchronous

motor," in *European Conference on Power Electronics and Applications (EPE16)*, pp. 1–10, 2016, Karlsruhe, Germany.

[52] G. Messager and A. Binder, "Derivation of forces and force interferences in a double conical high-speed bearingless permanent magnet synchronous motor," in *IEEE International Electric Machines and Drives Conference (IEMDC)*, pp. 1–8, 2017, Miami, Florida, U.S.A.

Supervised theses of students

[53] S. Balasubramanian, *Analysis and Simulation of a Double Three-Phase Half-Pitched High-Speed Bearingless Permanent Magnet Synchronous Motor with extended Field Oriented Control.* Master thesis, Institute for Electrical Energy Conversion, TU Darmstadt, 2014.

[54] P. Mouratidis, *Design and Implementation of Modern Controls for Drive and Suspension of a High Speed Double Conical Bearingless Motor on a Real-Time System.* Master thesis, Institute for Electrical Energy Conversion, TU Darmstadt, 2014.

[55] P. Kappes, *Control Design and Implementation of a Double Conical Bearingless PMSM on a Real-Time System.* Master thesis, Institute for Electrical Energy Conversion, TU Darmstadt, 2013.

[56] P. Hörner, *Auslegung und Regelung eines 40kW/40000 min-1 lagerlosen PM-Synchronmotors bestehend aus zwei Halbmotoren mit sternpunktverbundenen Tragwicklungen zur Speisung des separaten Axiallagers.* Master thesis, Institute for Electrical Energy Conversion, TU Darmstadt, 2016.

[57] J. Liebhart, *Elektromagnetische Auslegung eines 40 kW/40000 min*$^{-1}$ *konischen lagerlosen Permanentmagnet-Synchronmotor und thermische Messungen an einem 1 kW konischen lagerlosen PMSM.* Bachelor thesis, Institute for Electrical Energy Conversion, TU Darmstadt, 2012.

[58] J. Valverde, *Implementation of a bearingless motor control on a Real*

Time Application Interface. Master thesis, Institute for Electrical Energy Conversion, TU Darmstadt, 2012.

[59] Y. Nijan, *Electro-thermal modeling, design and testing of innovative converter using new technologies.* Master thesis, Institute for Electrical Energy Conversion, TU Darmstadt, 2013.

[60] Y. C. Devisscher, *Reglerentwurf und implementierung für einen doppelkonischen lagerlosen Permanentmagnet-Synchronmotor auf einem Echtzeitsystem.* Bachelor thesis, Institute for Electrical Energy Conversion, TU Darmstadt, 2013.

[61] W. Rana, *Entwurf und Simulation einer neuen Pulsweitenmodulationsart für die Regelung der Mit-, Gegen- und Nullkomponente des Stroms einer lagerlosen permanenterregten Synchronmaschine mit zwei stern punktverbundenen dreiphasigen Systemen.* Bachelor thesis, Institute for Electrical Energy Conversion, TU Darmstadt, 2016.

Curriculum Vitae

Personal data

Gael Messager
Born on 18th of May 1987 in Cannes, France

Education

10/2007-10/2011	Study for master's double-degree in electrical energy conversion École supérieur d'électricité, Paris - Technische Universität Darmstadt, Germany
09/2005-08/2007	Study for Classe préparatoire aux grandes écoles Centre Internationale de Valbonne, France

Professional career

Since 08/2017	Developing engineer LTI Motion GmbH, Lahnau, Germany
02/2012-07/2017	Scientific assistant Technische Universität Darmstadt, Germany
11/2011-01/2012	HIWI assistant Technische Universität Darmstadt, Germany